University of Strathclyde

Department of Mechanical and Aerospace Engineering

The development of a satellite-enabled tool for offshore wind resource optimisation

by

Alberto S. Rabaneda

A thesis presented in fulfillment of the requirements for the degree of

Doctor of Philosophy

2018

Author's declaration

This thesis is the result of the author's original research. It has been composed by the author and has not been previously submitted for examination which has led to the award of a degree.

Date:

Signature:

Acknowledgments

I would like to express my gratitude to my supervisor, Dr. Matthew Stickland. I really appreciate your guidance along the Ph.D. Your advice about how the research community works and how private companies are involved in research was priceless. I also appreciate the freedom I had to develop my work in order to become an independent researcher, as well as your support to choose my own research lines.

After four great years studying at the University of Strathclyde, first and MSc and finally a Ph.D., I must thank the university the support to students; especially to foreign students. It is remarkable the willingness to help students by the university staff.

This opportunity would never have existed without the external support of some sponsors. I would also like to thank the Satellite Applications Catapult, Oldbaum Services, and the Offshore Renewable Energy Catapult. Their will to initiate a research project, WindRes, was the reason for my research. I appreciate the assistance of Terri Freemantle, Andy Oldroyd, and Andrew Macdonald.

At the very beginning of this research, when I still was learning about this research field, I received guidance from some researchers in DTU Wind Energy. Hence, I wish to express my gratitude to Dr. Ioanna Karagali, Dr. Merette Badger, Dr. Charlotte Hasager and Dr. Paul Astrup for their advises in satellite remote sensing for wind retrievals.

All my work has been possible because of the previous work of many researchers; concretely, researchers from IOVWST working group, Remote Sensing Systems, ESA, and NASA. I would like to thank your efforts to publish and make freely available the satellite datasets as well as information and explanation of them for future research.

Finally, I wish to thank my friends in Glasgow and family. Especially to my mother, who always encouraged me to dream and chase my dreams. To my friends Tania, Berta, Roi and Elba, you have been the most precious support during my stay in Glasgow; the moments we shared were the recharge of energy I needed to complete this thesis.

Abstract

The actual offshore wind farms are mainly located near the shore, only tens of kilometres offshore. The development of this sector is forecasting offshore wind farms over deeper seas. This fact is complicating and increasing the cost of a wind resource monitoring campaign by meteorological masts. Hence, the industry has been searching for cheaper technologies capable to measure wind vectors on deep seas, such as floating LIDAR or satellites. The European project NORSEWInD created wind atlases from satellite measurements for the North, Irish and Baltic Seas. After that project, the creation of software to undertake wind resource assessments by satellites was aimed by a new project named WindRes. This aim was the starting point of the present thesis.

New software was created which merges knowledge from different fields, microwave remote sensing, satellite Earth Observation and wind resource assessment. The capabilities of the tool, and more important, the capabilities of satellites to match requirements by the wind industry were tested. In this initial analysis, advantages and disadvantages were identified as well as lack of knowledge. Two main points were concluded to need further research; the vertical extrapolation of wind vectors, and the creation of climatology from satellites measurements.

In a second analysis, different extrapolation methods suggested in the literature were tested. These include methods to calculate aerodynamic surface roughness length (z_0) and friction velocity, (u_*). The logarithmic law, the law to calculate wind speed in the surface layer at different heights, is dependent on these two parameters, z_0 and u_*. Since previous methodologies were found to mismatch in situ measurements, a new expression for z_0 was developed. New equations were reached by application of knowledge in oceanography and boundary layer meteorology. Although a definitive expression was not reached, the high z_0 values found under young waves conditions suggested the need of a complete logarithmic law for offshore environments. Results pointed the necessity to include the energy transfer from wind to the sea into the logarithmic law.

Preface

Different space borne devices have been measuring the wind vector over the seas using different instruments with different characteristics for several decades. Satellite wind retrievals over the ocean surface are arranged in a plane parallel to the ocean surface representing wind speed (U) and direction at 10 meters above the sea surface under neutral stability conditions. Some researchers joined together several satellite datasets thereby trying to increase the number of measurements which was too low for a confident wind resource assessment. There would be a significant advantage if operational software to perform wind atlas and wind resource assessments by satellites for potential offshore wind farms could be developed. Hence, the aim of this analysis was to check the capability of satellite remote sensing to match the wind industry requirements, identify what is required to improve the quality of the data and to develop the tool and enhance models. To carry out the analysis a database was constructed from the combined data output of several satellites (SSM/I, Quikscat, ASCAT, and Sentinel-1) in order to solve the problem of data shortage. The database allowed offshore wind assessment to be carried out at any location where satellite surface wind measurement data were available. In this study output from the software are presented for the test areas of the Firth of Forth (Scotland) and the river mouth of Ems (Germany). Also data are compared with the offshore meteorological masts, Fino-1 and Egmond aan Zee located off of the coast of the Netherlands. However, for the data to be useful, it is necessary to extrapolate the wind vectors to turbine hub height which is usually around 100 meters above sea level. The satellite extrapolated wind speed was calculated and the difference between the Fino-1 and the satellite data was found to be between 1% and 2.26% of the mean speed. The logarithmic law was fitted to measured data at the mast allowing the vertical extrapolation to hub height. This law is a function of surface roughness (z_0) and friction velocity (u_*). It was found that the enhancement of surface roughness, atmospheric stability correction parameterization and short-term calculations could improve the accuracy of the wind resource assessment. Unlike onshore locations, z_0 over the ocean is not constant. Many oceanographers have been parameterizing both, z_0 and u_*, in order to study the atmosphere-sea interaction. Since there is no consensus, a review of methods for u_* and z_0 is

presented in this study. The capability to calculate wind profile was tested for different combinations of methods. Calculated u_*, z_0 and U_{100} were compared with an offshore meteorological mast measurement at Egmond aan Zee. The best correlation was found for a wave slope dependent method with R^2, the slope of linear regression and bias of 0.8, 0.99 and 0.20 respectively. Nevertheless, u_* and z_0 were always underestimated when compared with in situ measurements. Low values of u_* and z_0 were found to compensate each other in the logarithmic law making possible a reasonable wind extrapolation even when both parameters are underestimated. None of the reviewed methods were capable of achieving high accuracy under all kinds of sea-atmosphere conditions. Furthermore, all studied methods include empirical coefficients in their algorithms which depended on the chosen datasets.

Another goal of this study was the development of an algorithm capable of determining z_0 under any condition. The main challenge was to parameterize a non-static surface. The approach used in this study was to adapt Lettau's equation for z_0 which is widely accepted for onshore locations. The proposed equation is a synergy between wind and sea parameters which does not include empirical coefficients. The method was validated by comparison with the wind profile measured by the meteorological mast Egmond aan Zee located in the North Sea. Results showed high accuracy where the correlation coefficient reached a value of 0.987. However, only 15% of the time, when z_0>0.4, was the predicted z_0 accurate enough to determine the wind speed profile successfully. The method has also been proved to achieve a remarkable accuracy when wave age, c_p/u_*, is under 5 in what are considered calm seas. The last analysis in this study was the parameterization of atmospheric stability correction. The aim was to include all observations including those under unstable, stable and neutral conditions. Then, z_0 was calculated again by the logarithmic law including the stability correction parameter and compared with the proposed z_0 method in this study. Low agreement was found under unstable conditions. Also, a complete lack of agreement was observed for stable conditions. This fact was caused by the stability correction. This parameter presented a difficulty of parameterization for the short-term basis of 50 minutes average. Fluctuations of different parameters are necessary to calculate, but a lack of frequency of

measurements led to miscalculated parameters, such as u_* and vertical heat flux. Furthermore, u_* observations by ultrasonic anemometers under neutral conditions indicated lower values than those calculated by the logarithmic law.

Nomenclature

A	Area of the domain under study	[m^2]
a_c	Wave crest amplitude	[m]
a_T	Wave trough amplitude	[m]
C	Weibull's scale parameter	[m/s]
C_d	Drag coefficient	[dimensionless]
C_{d10}	Drag coefficient at 10 metres	[dimensionless]
c_p	Phase speed	[m/s]
c_p/u^*	Wave age	[dimensionless]
cw	Composition of waves coefficient	[m]
d	Depth	[m]
e_p	Partial pressure of water vapor	[kPa]
e_s	Saturated vapor pressure	[kPa]
g	Gravitational acceleration	[m/s^2]
H	Wave height	[m]
H_s	Significant wave height	[m]
H_s/L_p	Wave slope	[dimensionless]
h^*	Effective obstacle height	[m]
k	Wavenumber	[m^{-1}]
k_w	Weibull's shape parameter	[dimensionless]
L	Wavelength	[m]
L_p	Wavelength at the peak of the spectrum	[m]
L_c	Length of the wave crest	[m]
L_s	Mounin-Obukhov length	[m]

L_T	Length of the wave trough	[m]
n	Number of obstacles	[dimensionless]
P	Pressure	[kPa]
P_0	Reference pressure	[kPa]
r	Mixing ratio of unsaturated air	[g/g]
RH	Relative humidity	[%]
s	Silhouette (cross-section area)	[m^2]
t	Time	[s]
T	Temperature	[K]
T_p	Wave period	[s]
u^*	Friction velocity	[m/s]
U	Wind speed	[m/s]
$\bar{U}$	Mean wind speed	[m/s]
$U(z)$	Wind speed at height z	[m/s]
U_{10}	Wind speed at 10 metres	[m/s]
U_{116}	Wind speed of 116 metres	[m/s]
w	Wave angular frequency	[s^{-1}]
W_A	Side length of the squared domain	[m]
W_W	Wave width	[m]
x	Position along the wave propagation	[m]
z	Height	[m]
z_r	Reference height	[m]
z_0	Surface roughness length	[m]

α	Drag coefficient exponent	[dimensionless]
α_c	Charnock's coefficient	[dimensionless]
ϵ	$(kH)/2$	[dimensionless]
θ	Incidence angle	[°]
θ_v	Virtual potential temperature	[K]
κ	von Karman constant	[dimensionless]
μ	Sea surface elevation above still water level	[m]
ν	Kinematic viscosity of air	[m^2/s]
σ	Standard deviation	
χ	Fetch	[m]
Ψ_s	Atmospheric stability correction parameter	[dimensionless]

Acronyms

CLS	Collecte Localisation Satellites
CSA	Canadian Space Agency
DB	Database
DDM	Delay Doppler Mapping
DMSP	Defense Meteorological Satellite Programm
DTU	Technical University of Denmark
EEO	Edinburgh Earth Observatory
EODA	Earth Observation Data Access
ESA	European Space Agency
GIS	Geographic Information System
GLONASS	Global'naya Navigatsionnaya Sputnikovaya Sistema
GNSS	Global Navigation Satellite System
GPS	Global Positioning System
HDDC	High Data Density Cell
IPCC	International Panel Climate Change
ISRO	Indian Space Research Organisation
JAXA	Japan Aerospace Exploration Agency
LEO	Low Earth Orbit
LIDAR	Laser Imaging Detection and Ranging
MABL	Marine Atmospheric Boundary Layer
MCP	Measure-Correlate-Predict
NASA	National Aeronautics and Space Administration
NOAA	National Oceanic and Atmospheric Administration

NWP	Numerical Weather Prediction
RMSE	Root Mean Squared Error
RSS	Remote Sensing Systems
SAR	Synthetic Aperture Radar
SODAR	Sonic Detection and Ranging
TRMM	Tropical Rainfall Measuring Mission
UAV	Unnamed Aerial Vehicle

Table of Contents

List of figures

List of tables

1. Introduction

Nowadays, the power mix in developed countries includes different types of renewable sources, [1]. One of the most mature technologies within the renewable sector is the wind power, [1]. Most of its production belongs to large wind turbines; medium and small turbines are marginal technologies, [1]. Furthermore, there are two types of wind farms; those located onshore and those offshore. Onshore wind farms are well spread along the world since this type of wind farm was the first to be developed, [1]. This source of electricity is now capable of creating an important percentage of the power mix, [1]. On the other hand, offshore wind farms are mostly located in the North Sea, [1]. The weather and bathymetry characteristics of the North Sea made this area of the world an optimal location, [1].

Offshore wind farms present some advantages and disadvantages. Overall, the wind resource in offshore environments is larger than onshore, [1]. However, the costs of offshore wind farms are also larger than onshore wind farms, [2]. The reason for an increment in costs is due to the foundations, offshore electrical substations, electrical cables to shore and larger wind turbines, [2]. Also the amount and cost of maintenance of the equipment is higher because of the corrosion and extreme weather conditions offshore, [2]. Hence, offshore wind projects require a higher investment than the equivalent onshore project. This fact represents a higher financial risk for the developer company. Hence, the wind resource over the area must be well parameterized. This concludes with the installation of a meteorological mast prior to the installation of any wind turbine. It is in this initial stage where companies assume the highest risk. Until a location has been proven to be an optimal location, there will not be any type of financial support made available from the banks, [3]. Furthermore, if the chosen location is studied and then found to be poor in wind resource, the developer will incur considerable losses. This point is important since a meteorological mast costs between £10 to £15 million to install and run, but an accurate wind resource assessment is crucial to a successful development, [3].

In order to reduce the financial risk during wind resource campaigns, the wind industry has been searching for alternatives, [2]. A possible source of extra wind measurements comes from Earth Observation. Remote sensing by satellites is still a field of active research, not only for wind retrievals but also for many environmental parameters. Although there is literature about wind retrievals by satellites, which is detailed in the following Chapters; there is no application specifically developed for the wind industry. The existence of such a tool could reduce the financial risk associated with an offshore wind resource campaign. However, although satellite data could reduce the risks associated with offshore resource assessment, this technique is not expected to replace in situ measurements.

The present thesis was created in the framework of the WindRes. This project pursued the development and completion of operational software for wind resource assessment by satellites. The project was funded by the Satellite Applications Catapult and the Offshore Renewable Energy Catapult centres in the UK and was assisted by Oldbaum Services. The WindRes project was a continuation of a previous European project called NORSEWInD, [4]. This European project provided a dependable offshore wind atlas of the North, Irish and Baltic Seas. Furthermore, the project was undertaken with a partnership of 21 institutions or companies throughout Europe.

1.1 Thesis objectives

The research, which is contained in this thesis, was initiated for a one-year project, WindRes. This project was aimed to define a programme of work for translating previous basic EU FP7 funded research into a commercial operational tool for satellite-enabled offshore wind resource optimization. The fundamental methodology that was to be employed had been developed and verified under the EU FP7 project NORSEWInD. The key challenges to developing commercial exploitation of this satellite-enabled technology were identified as:

- Translate NORSEWInD research into commercial, operational tool.
- Develop key applications for offshore wind and demonstrate impact.
- Demonstrate opportunities offered by satellite services in the Energy sector.

Following on from a Phase 1 Project that identified the willingness of international Partners, previously involved in NORSEWInD, to support the activity WindRes was to show how these challenges could be met, and a programme of work carried out that would:

- Bring the capabilities of satellite remote sensing of wind resources to the offshore renewables industry.
- Take the methodology developed under NORSEWInD and convert it into an operational tool that could be used by the offshore renewable industry.
- Highlight the benefits of satellite remote sensing to the wider Energy sector, which could enable further commercial applications.
- Achieve a full understanding of satellite remote sensing for wind measurements and in doing so identify the possibilities, advantages, and disadvantages of this technique for the wind industry.
- The project was also to identify areas which required further research which might be required before deploying the final software package.

After the end of the WindRes project and once the gaps in the knowledge were identified, research in these fields was undertaken. The objectives of the thesis were the improvement of wind retrievals by satellites and also to increase the satellite dataset's capability to match the wind industry requirement. In order to do so, these were identified as the possible fields to extend the research:

- Increase accuracy of satellite measurements.
- Extrapolate satellite wind retrievals to different heights, since satellites measure the wind speed at 10 metres above the sea level.
- Decrease the satellite data shortage problem.
- Building climatology from satellite retrievals.

1.2 Thesis structure

This chapter introduces the reader to the reasons for the research into wind retrievals from space and the thesis objectives.

Chapter 2 is an explanation of the state of the art for both wind resource assessment and satellite remote sensing for wind measurements. The reason for this chapter is to introduce satellite remote sensing to the reader from within the energy sector and introduce readers familiar with satellite applications to wind resource assessment. Therefore, the chapter is just an introduction to both fields. More information and a deeper explanation of the topics can be found in the cited references.

In Chapter 3, the development of the code is explained. It is mainly focused on how the data is processed. The chapter explains the different possibilities of the software.

In Chapter 4 the first wind resource study of this thesis is explained. The first analysis was a test of the code as well as a method to evaluate the possibilities of satellite remote sensing for the wind industry. The results of this assessment highlighted areas where there was a lack of knowledge.

Chapter 5 is an analysis of the different methods for surface roughness length and friction velocity parameterization. In the previous chapter, the lack of accuracy for both parameter methods was found. Results were also analyzed under different wave age, wave height and wind speed conditions.

Chapter 6: This chapter includes the development of a new method for surface roughness length and drag coefficient parameterizations. However, the drag coefficient method was not tested since this was not included in the thesis objectives. On the other hand, the new surface roughness method was tested and proven to be relatively successful. As in the previous chapter, this new formulation was also analyzed under different conditions.

Conclusions and recommendations for future work are contained in the last chapter of this thesis, Chapter 7.

Only part of the work was made public before the materialization of this thesis. The code of the tool has been made open source and it is accessible online. Along with the code a user manual an installation specifications were

published. These correspond to most of the material from Chapter 3 and Appendix A. Furthermore, some results have been presented in the International Ocean Vector Winds Science Team meetings of 2016 and 2017. The exposed results correspond to results from Chapters 4 and 5.

Although there is a will to publish the work in peer-reviewed journals, any article has been sent to journals. However the articles were written before the confection of this thesis. The three written articles correspond to Chapters 4, 5 and 6. Finally, Chapters 2 and 3 correspond to the work and material from the WindRes project.

2. State of art

2.1 Introduction

The goal of this chapter is to be a literature review giving an overview of the state of the art for satellite mapping of offshore wind resource. Because of the possible different background of potential readers, wind resource or remote sensing, it is necessary to introduce offshore wind resource assessment and satellite microwave remote sensing technology separately.

The literature on wind assessment and the use of satellites in wind engineering is reviewed in the first part of this chapter. A description of the processes involved in the conventional wind resource assessment is included. Although this is not the goal of this thesis, non-specialized readers will need to know the basics of wind resource assessment.

The use of satellite data for the wind industry is reviewed and the question of access to satellite data is addressed. The different types of satellite-mounted instruments for wind measurement and some of the main missions using those instruments will be described. The basics for each instrument will be explained. However, it is not a deep explanation and some aspects are missing such as instrument design, principles of radar systems and signal processing. For a deeper insight into the technology, the reader is recommended to follow the cited references.

A review of the previous work carried out in satellite based wind resource assessment is presented and a list of existing software to process wind retrievals provided. Also, there are a few lines about the work carried out by other research institutions. Finally, conclusions are drawn from this literature review including proposals for future research based on the gaps found in the published literature.

2.2 Wind resource assessment review

Wind resource assessment is the collection of technologies and analytical methods used to estimate how much energy will be available for a wind power plant over the course of its useful life. A realistic assessment of the energy production for a specific site is very important for the "bankability"

of a project. There are best practice guidelines to assess quality during the process of wind mapping, [5].

To provide the basis for an accurate estimate of energy production the wind resource must be characterized not only by the mean speed but also by variations in speed and direction in both time and space.

Temporal variation can be divided into 4 categories: inter-annual (climate variability), annual (seasonal variation), diurnal (due to differential heating of the earth surface over 24hrs) and short-term (gust and turbulence).

Spatial variation of the wind depends on the topographical and ground cover variations for a horizontal plane parallel to Earth's surface. It also includes the vertical variation of the wind or wind shear [6].

A lot of research has been carried out in the area of wind resource assessment and a recent review from G.M. Joselin Herbert et al. [7] describes in detail the research and development carried out over the last decades in the area of not only wind resource assessment but also estimating and forecasting of wind energy production. However, the New York State Energy Research and Development Authority (NYSERDA) [8] has provided a more comprehensive overview of the wind resource assessment process with a detailed description of the analysis involved with the estimating wind form energy production. This chapter is intended to give guidance to professionals practitioners on the accepted methods of wind resource assessment for utility-scale wind farms. A summary of the processes involved is reported below.

2.2.1 Wind resource assessment process

Wind resource assessment is carried out in a different range of scales for both, time and space. Thus, and according to Sempreviva et al. [9], there are two differentiated steps:

1. **Regional mapping**. Large-scale wind assessment to find out potential locations to place a wind farm. Nowadays it is common to consult a wind atlas or existing measurement and modeling approaches, [10].

2. **Micro-siting**. This is a detailed wind assessment in specific areas, usually undertaken on-site by wind developers. NYSERDA has categorized the wind resource investigation for a targeted area in 6 main stages.

2.2.1.1 Wind monitoring

The objective of a wind monitoring campaign is to obtain the best possible understanding of the wind resource across a project area. Actually, the measurement campaign could be conducted by different instrumentation:

- The most traditional is a meteorological mast consisting of cup anemometers and wind vanes, to measure wind speed and wind direction respectively. Other sensors for monitoring temperature, humidity, pressure and other parameters may also be included to determine the atmospheric stability and air density.
- Sonic anemometers. This is a different type of anemometer based on the Doppler effect. It also can be installed on a meteorological mast and can give 3D vector information.
- Remote sensing.
    - SODAR emits sound pulses to measure the backscattered part reflected from refraction index fluctuations in the atmosphere; this instrument can determine the wind profile.
    - LIDAR works in a similar way than SODAR but uses a laser instead of sound pulses.
    - Satellites, this is the newest remote sensing method in wind remote sensing which will be explained in section 2.3.

Measurement parameters might include wind speed and direction, wind shear, turbulence intensity, pressure, humidity, and temperature. Once the data from the monitoring system have been collected, the data can be validated. In this validation process, the completeness and the accuracy of the data are assessed and invalid or suspicious values are flagged within the data record.

2.2.1.2 Observed wind resource characterization

A report summarising the observed wind resource is normally produced on a monthly, quarterly or annual basis as well as at the end of the monitoring program. Summary statistics in the report might include observed mean and annualized mean speeds, mean wind shear, air temperature and air density, humidity, turbulence intensity and wind power density. A wind speed frequency distribution chart and fitted Weibull curve, [11], help to establish how much energy the site might produce at a given wind speed, figure 2.1. A wind and energy rose indicates the directional distribution of the wind resource, which will strongly influence the turbine layout.

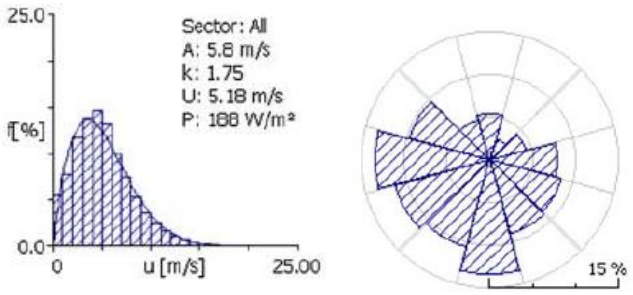

Figure 2.1. Example of Weibull distribution (left) and wind rose(right). Source: [9]

The probability of the wind speed having a value *P(U)*, is given by Eq. 2.1. Where k_w represents the shape parameter, *C* is the scale parameter and *U* is the wind speed.

$$P(U) = (k_w/C)\,(U/C)^{(k_w-1)}\,e^{[-(U/C)^{kw}]} \qquad (2.1)$$

First, to calculate *C*, it is necessary to calculate mean wind speed, $\bar{U}$, at a targeted height. Once the mean wind speed and standard deviation at hub height are known Weibull parameters are calculated using Equations 2.2 and 2.3. Standard deviation is represented by σ.

$$C \cong (2\bar{U}/\pi)^{(1/2)} \qquad (2.2)$$

$$k_w \cong (\sigma/\bar{U})^{(-1.086)} \qquad (2.3)$$

2.2.1.3 Hub height resource estimation

It is known that wind speed increases with height, but it has been observed that the wind profile is different depending on the atmospheric stability and terrain profile, figure 2.2. Since the majority of field data are collected below the hub height of modern, large, wind turbines it is usually necessary to extrapolate the wind resource data to the turbine hub height.

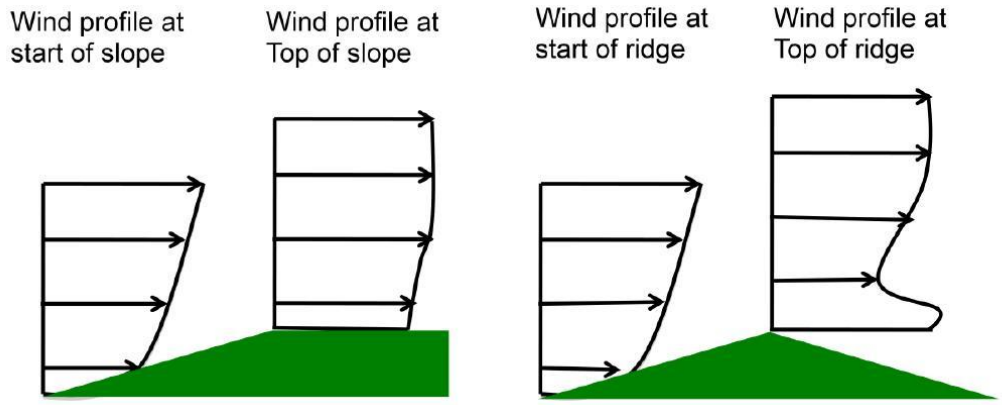

Figure 2.2. Wind profile on several terrains. Source [12]

The most common method of extrapolating wind speeds to turbine hub height is through the logarithmic law, Eq. 2.4. This is based on the logarithmic equation containing a parameter linked to the height and density of elements surrounding the tower and the friction velocity. Because some of the parameters within the logarithmic law are difficult to measure, another approach to extrapolate the wind speed is recommended. The logarithmic law under neutral stability, Eq. 2.5, can be rewritten to exclude friction velocity, as shown in Eq. 2.6.

$$U(z) = \left(\frac{u_*}{\kappa}\right)\left[\ln\left(\frac{z}{z_0}\right) + \Psi_s\left(\frac{z}{L_s}\right)\right] \qquad (2.4)$$

$$U(z) = \left(\frac{u_*}{\kappa}\right)\left[\ln\left(\frac{z}{z_0}\right)\right] \qquad (2.5)$$

$$U(z) = U\,(z_r)\left[\frac{\ln(z/z_0)}{\ln(z_r/z_0)}\right] \qquad (2.6)$$

Where $U(z)$ represents the mean wind speed at height z, u_* is the friction velocity, κ is the von Karman constant (usually 0.4), z_0 is the aerodynamic surface roughness length, Ψ_s is the atmospheric stability correction parameter and $U(z_r)$ the wind speed at reference height z_r. After Eq. 2.5, the friction velocity and aerodynamic surface roughness length can be found from wind speed measurements, U_1 and U_2, at two different heights, z_1 and z_2, as shown in Equations 2.7 and 2.8.

$$\ln z_0 = \frac{U_1 \ln z_2 - U_2 \ln z_1}{U_1 - U_2} \qquad (2.7)$$

$$u_* = \frac{\kappa(U_2 - U_1)}{\ln(z_2/z_1)} \qquad (2.8)$$

2.2.1.4 Climate adjustment process

The uncertainty in the long-term mean wind speed on a year's measurement is typically 3-5%, corresponding to around 5-10% of the mean wind plant production. Reducing this uncertainty is the primary goal of climate adjustment. The leading method for performing climate adjustment is the MCP method (Measure-Correlate-Predict) [13]. For an explanation of this method see figure 2.3. The observed winds at a target site are correlated with the observed wind recorded at a long-term reference, such as an airport weather station and, a relationship between them is established.

The key assumption underlying all MCP methods is that the wind resource in the future will be similar to what it has been in the past, in other words, the wind climate is invariable.

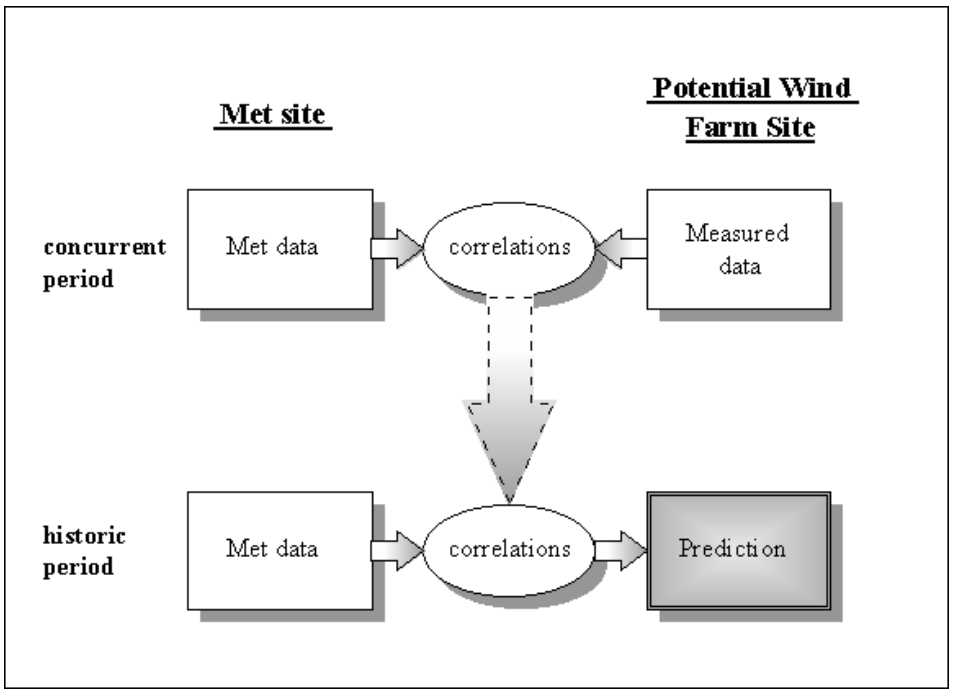

Figure 2.3. Scheme of the technique of MCP. Source: [13]

2.2.1.5 Wind flow modeling approach

The main purpose of wind flow modeling is to estimate the wind resource at every potential wind turbine location so that the wind plant's overall production can be calculated and its design can be optimized. In an ideal world, wind flow modeling would not be necessary. Wind measurements would be taken at every likely turbine location to estimate any possibility of significant error. However, for most projects, this would be an expensive proposition. Aside from estimating the variation in the wind resource across the project area, wind flow modeling must account for each turbine's influence on the operation of other turbines, the so-called wake effect.

There are several wind flow models in use by the wind industry today, which are based on a variety of numerical approaches. The models fall into 4 categories:

- Mass consistent
- Jackson Hunt
- Computational fluid dynamics (CFD)
- Mesoscale numerical weather prediction models (NWP)

The mass consistent flow model

The model solves just one of the physical equations of motion, the governing mass conservation. The models predict stronger winds on hill and ridge tops and weaker winds in valleys. However, they cannot handle thermally-driven wind patterns, such as sea breezes and mountain-valley circulations, and flow separations on the Lee phenomena side of hills or mountains.

Jackson-Hunt model

The model solves the linearized form of the Navier-Stokes equations governing fluid flow. This model came into wide use when computing resources were limited. It runs fast while performing reasonably well where the wind is not significantly affected by steep slopes, flow separations, thermally driven flows, low-level jets and other dynamic and nonlinear phenomena, [14]. The most widely used Jackson-Hunt model in the wind industry is the model contained in the software *WAsP*, see section 2.4.2. This model proceeds in 2 stages:

- The observed wind at a mast is used to derive the background wind field, which represents the wind resource that would exist in the absence of terrain. This background wind field is typically summarised in a file known as a wind atlas or library file.
- The process is subsequently reversed using the background wind as an input to predict the wind profile at other points. *WAsP* also contains several modules that address various needs in wind flow modeling, including the ability to incorporate the effects of surface roughness changes and obstacles. However, it is recognized that *WAsP* is not equipped to handle complex terrain and ignores the effects of thermal stability and temperature gradients.

CFD approach

CFD models solve a complete form of the mass and momentum equations of motion known as the Reynolds-averaged Navier-Stokes, or RANS equations, [14]. The model is capable of simulating non-linear responses of the wind to steep terrain, such as flow separation and recirculation. Although CFD models have not always proven to be a significant improvement over other modeling technique, they nonetheless can provide useful information

concerning turbulence intensities, shear, direction shifts and other features of wind flow in complex terrain. However, CFD models do not usually take into account any circulations due to temperature gradients although this is theoretically possible.

Mesoscale numerical weather prediction model

The next step in sophistication is the Numerical Weather Prediction (NWP) model, [14]. The mesoscale model solves the Navier-Stokes equation and includes parameterization schemes for solar and infrared radiation, cloud microphysics and convection. Thus, it incorporates the dimensions of both energy and time and is capable of simulating such phenomena as thermally driven mesoscale circulations (sea breezes) and atmospheric stability or buoyancy. However, the model requires enormous computing power to run at the scales required for the assessment of wind projects. The typical model resolution for most mesoscale simulations is on the order of kilometers meaning a single grid cell is a kilometre across. It is impossible to obtain a detailed picture of the wind resource within a project area at such scale. One way around this problem is to couple mesoscale models with microscale model of some kind.

2.2.1.6 Wind energy yield and Micro-sitting

After the calculation of the wind resource over the targeted area, it is time to allocate wind turbines and calculate the future energy production. There is some software for that purpose which is specified in section 2.4.2. These will calculate the optimum location for a wind turbine according to wind resource in each point of the area according to orography, and avoid the wake effect of wind turbines. One example is shown in Fig. 2.4.

In order to understand how this is calculated, and the total energy production per year forecast, it is necessary to know the power curve of the wind turbine. Different types of wind turbines will have different power curves. These are provided by the turbine manufacturers. The power curve will depend on the drivetrain, starting from blades and finishing in the applied generator. In Figure 2.5 there is an example power curve in red. Different power curves may have different cut-in and cut-out wind speeds. In Fig. 2.5, the wind turbine will reach its maximum power at 13 m/s.

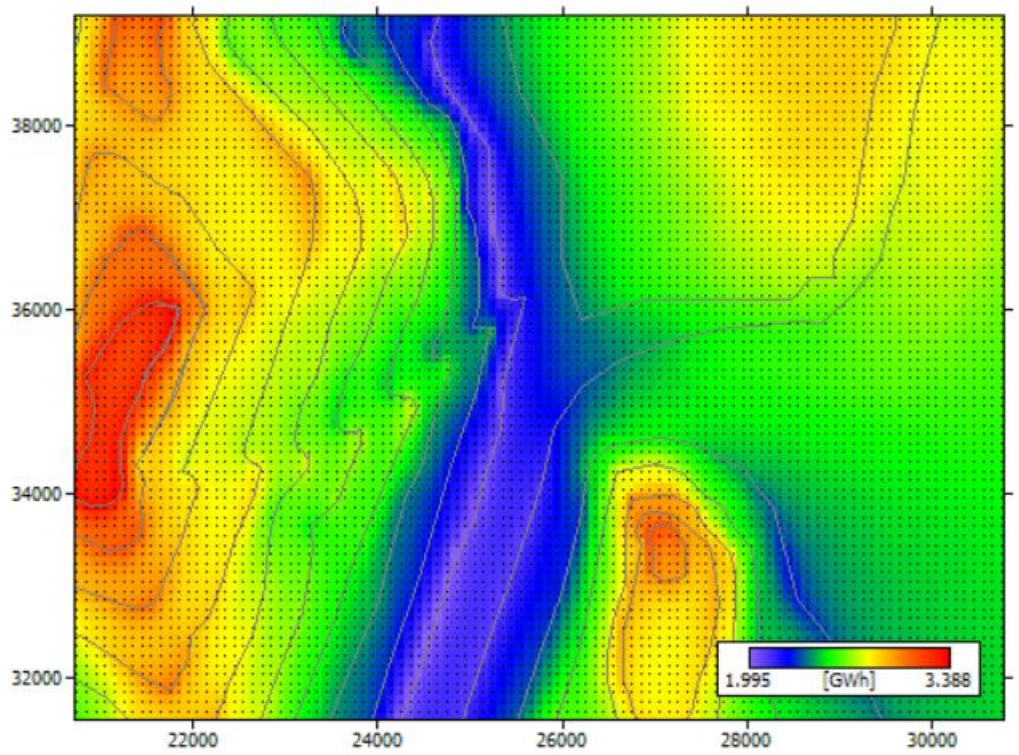

Figure 2.4. Onshore micro-sitting using WAsP. Source: [15]

The final step is to calculate the energy yield. To do this it is necessary to know the Weibull curve or probability density distribution of wind speed and the power curve of the wind turbine. Graphically, the energy produced will be the area below both curves. Figure 2.5 shows an example of such a curve. The maximum energy production will occur for 8 m/s wind conditions, since these are more frequent than 13 m/s when the maximum power is reached. Even so, it is always necessary to calculate the future energy production numerically.

2.2.1.7 Uncertainty in wind resource assessment

Wind resource estimation should be accompanied by an estimation of the uncertainty or margin error. The uncertainty present in all wind resource estimates is primarily related to the following factors: wind speed measurements, historical climate adjustment, potential future climate deviations, wind shear and the spatial wind resource distribution.

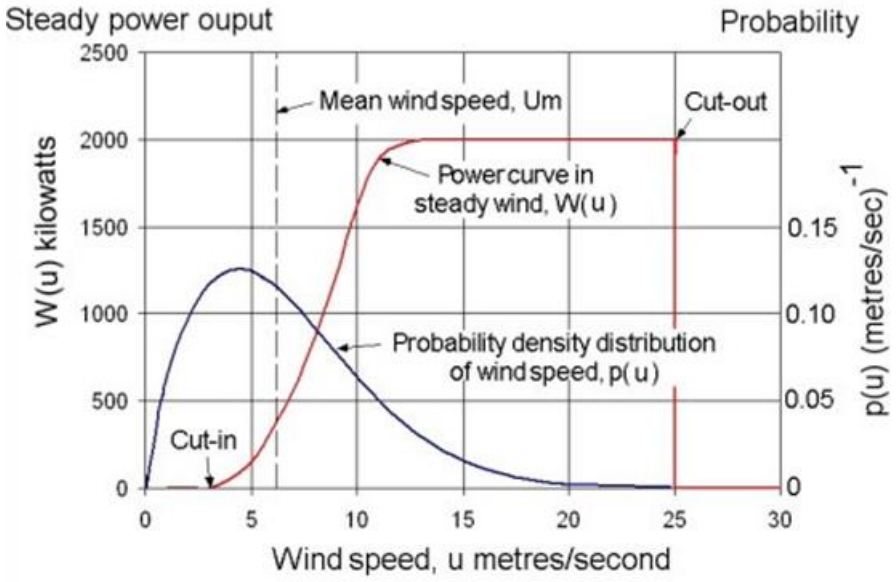

Figure 2.5. The intersection between Weibull distribution and power curve. Source: [16]

2.3 Satellite remote sensing for wind engineering review

2.3.1 Background

Satellite data are relatively new in wind engineering, but not in wind monitoring. In 1987, the first satellite on board the passive Special Sensor Microwave/Imager (SSM/I) was launched to deliver a continuous ocean wind speed time series [17]. This instrument has delivered wind data for more than 30 years. One of the disadvantages of the SSM/I is its use of passive microwave technology and can only provide time series on wind speed. A few years later, in 1991, the European Space Agency (ESA) launched a satellite equipped with an active microwave remote sensor capable of retrieving not only wind speed but also the wind vector. Since then several studies have been reported where satellite data have been used in wind resource estimation [18] to [34], some results are shown in section 2.4.4. In their review of methodologies for offshore wind resource assessment, Sempreviva et al. [9] details the various investigations involving satellite-borne remote sensing for wind resource mapping in European seas. Recently another study, Hasager et al. [34], explains wind resource assessment by the synergy of different satellite remote sensing instruments.

2.3.2 Satellite missions to measure ocean surface winds

Five types of instruments measure ocean surface winds: microwave radiometers and microwave scatterometers, Synthetic Aperture Radar (SAR), altimeters and Global Navigation Satellite System (GNSS).

- The microwave radiometer measures ocean surface roughness and correlates it to wind speeds approximately 10 meters above the water's surface. A special type of radiometer, a polarimetric radiometer, can derive wind speed and wind direction using more observations, [35].
- The microwave scatterometer sends a signal to the ocean surface which reflects off the Bragg waves on the surface of the larger scale ocean waves. The reflected energy measured by the scatterometer is translated using a geophysical model function into 10 meter neutral wind speeds and wind direction, [36].
- The SAR is a type of scatterometer which improves the method of processing the backscattered signal, and so, enhances the azimuth and spatial resolutions, [36].
- The altimeter is also similar to scatterometers, but simpler. This sends a signal directly to the surface below with an incidence angle of 0°, i.e. perpendicular to the surface. This instrument basically measures the time delay of the echo to calculate altitude. But it is also possible to calculate wind fields following the same principles as scatterometers, [37].
- The GNSS is a different type of instruments. Until 2017, this kind of satellite was only transmitting but not receiving. This was until ESA (European Space Agency) decided to send receiver satellites into low earth orbit which can measure wind speed at 10 meters over the sea by the same method as scatterometers. At the moment there are three different networks: GPS (Global Position System), GLONASS (Globalnaya Navigazionnaya Sputnikovaya Sistema) and BeiDou from the United States, Russia, and China respectively. The GNSS satellite network offers an extensive coverage of the earth which will be increased by ESA, French, Indian, and Japanese space agencies, [38].

A series of missions have been launched over the last few decades with onboard instrumentation to map wind speed and directions over the oceans. In Fig 2.6, a representation of the time in orbit of the scatterometers and radiometers monitoring the wind is shown. Also included in the figure are the types of measurement devices (scatterometers, radiometers and SAR's) on board some of the satellites. For more information check *CEOS Database* by ESA, [39]. Extra information is also contained in Table 2.1.

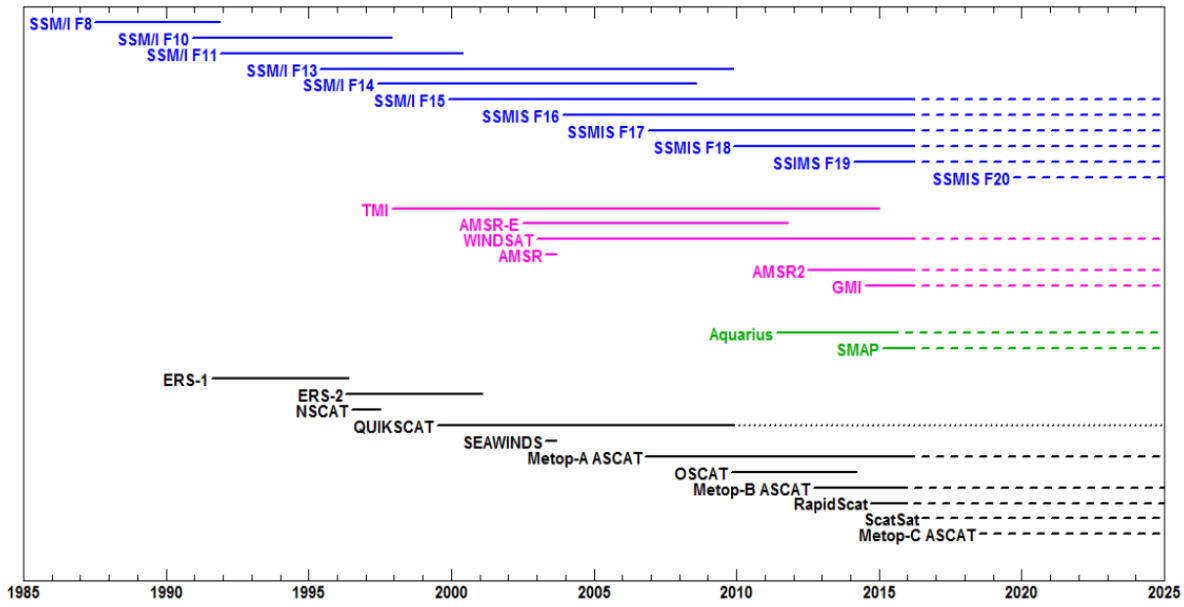

Figure 2.6. Devices measuring wind vectors from space over time. The black line represents scatterometers, blue lines are for the different radiometers of SSMI missions, pink lines are radiometers and green lines represent L-band radiometers. Source: [40]

- The European remote sensing satellite (ERS) was the ESA's first earth observing satellite program launched in 1991. ERS-1 carried a wind scatterometer used to calculate information on wind speed and wind direction. ERS-1 failed in March 2000 and was replaced by ERS-2, launched in 1995 which was in operation until 2010. The successor of ERS-2 (Envisat) was launched in 2002 but, after losing contact with the satellite, ESA announced the end of the Envisat's mission in 2012. The Envisat's mission has been replaced by the Sentinel series of satellites with the first, Sentinel 1A, launched in April of 2014. This is within the European Copernicus programme.

In 2016 Sentinel 1B will be launched, followed by other Sentinels according to the programme, [41].

- MetOp is another mission developed by ESA, EUMETSAT (European organization for the exploitation of meteorological satellite) and NOAA (National Oceanic and Atmospheric Administration) for the launch of three satellites with an ASCAT instrument on board. The first satellite MetOp-A was declared fully operational in 2007, then replaced by MetOp-B in 2103. MetOp-C is scheduled for launch in 2018 for the replacement of MetOp-B. Currently ESA is preparing the next generation of MetOp's satellites to ensure this supply of meteorological data, [42].

- NSCAT (NASA Scatterometer) was a microwave radar scatterometer to measure both wind speed and wind direction over the sea surface. This instrument was mounted and launched on the Advanced Earth Observing Satellite (ADEOS) in 1996 by the National Space Development Agency of Japan, [43].

- QuickScat was launched in 1999 with the mission of reducing the ocean-wind vectors data gap after losing the NSCAT, which failed in 1997. Basically, QuickScat followed the same mission as the NSCAT; to study the sea surface wind speed and direction. SeaWinds was the main instrument which was an active radar scatterometer mounted on the QuickScat satellite, [43].

- OSCAT is another scatterometer, but this one uses a Ku-band, conically scanning, system. It was built by the India Space Research Organization (ISRO) and Space Applications Centre (SAC), but NOAA is also working with its data products. This instrument was launched on the Oceansat-2 satellite in 2009. Similar to previous scatterometers, this one is studying wind vector retrievals but at different resolutions, [44].

- After QuickScat stopped measuring the wind in 2009, NASA worked to replace the instrument with RapidScat, which was launched in September of 2014. Unlike the others missions, this instrument was not mounted on a satellite. Instead, it was mounted aboard the International Space Station. As QuickScat, its mission is to measure the wind speed and direction on the ocean surface, [43].

- The Canadian Space Agency (CSA) also launched its own SAR in 1995 mounted in the RadarSat-1 satellite. This was launched with the mission of studying different fields, one of them oceanography and it was used by Hasager et al. [25] in their study of wind resource. The end of the mission was in 2013. The CSA also sent a second satellite with SAR into orbit in 2007, RadarSat-2, although it is not used primarily to study the wind resource, [45].

- A radiometer has been carried on board the Defence Meteorological Satellite Program (DMSP), also known as SSMI. Satellites and the data from the Special Sensor Microwave/Imager are produced as part of NASA's measurement program. The first instrument, F8, was launched in 1987 and the last instrument, launched in 2009, is the F18 and it is still in operation with the F16 and F17 at the start of 2018, [43].

- The Tropical rain Fall Measuring Mission (TRMM) satellite also from NASA (National Aeronautics and Space Administration), has on board a passive microwave radiometer (TMI) similar to SSM/I but with a better resolution of data measurement due to the lower altitude of the satellite orbit. It was launched in 1997 and is still in operation at the beginning of 2018, [43].

Agency	missions	instrument	availability
ESA	ERS-1	SAR, scatterometer	1991-2000
ESA	ERS-2	SAR, scatterometer	1995-2003
CSA	RadarSat-1	SAR, scatterometter	1995-2013
ESA	Envisat-Sentinel	ASAR (Advanced Synthetic Aperture Radar)	2002-2012
ESA	Sentinel 1	ASAR	2014-present
ESA/NOAA	MetOp-A	ASCAT (Advanced Scatterometer)	2007-present
ESA/NOAA	MetOp-B	ASCAT, scatterometer	2013-present
ESA/NOAA	MetOp-C	ASCAT, scatterometer	2016
NASA	ADEOS	NSCAT, scatterometer	1996-1997
NASA	QuikSCAT	SeaWind, scatterometer	1999-2009
NASA	(DMSP) (F16)	SSM/I, passive microwave radiometer	1987-present
NASA/JAXA	TRMM	TMI, passive microwave radiometer	1997-present
NASA	Aqua	AMSR-E, Advanced microwave radiometer	2002-2011
JAXA	GCOM-W1	AMSR-2, Advanced microwave radiometer	2012-present
JAXA	ADEOS II	AMSR-J, Advanced microwave radiometer	2002-2003
US NRL	Coriolis	Windsat, Polarimetric radiometer	2003-present
ISRO/SAC	OceanSat-2	OSCAT, scatterometer	2009-present
NASA	ISS-RapidScat	Scatterometter	2014-present

Table 2.1. Satellite missions for measuring ocean surface winds. Sources: NASA, ESA, EumetSat, ISRO, and CSA.

- Advanced microwave radiometers have been carried by a series of satellites such as Aqua, GCOM-W1, and ADEOS-II operated by NASA and Japan Aerospace Exploration Agency (JAXA). A key feature of the ASMR instrument is to see through clouds, thereby providing an uninterrupted view of the ocean. The mission

ADEOS-II had, in addition to a radiometer, a scatterometer to measure the wind speed and the wind direction. However, this satellite was in operation for only one year due to solar panel failure, [43].

- Finally, the Windsat polarimetric radiometer was developed by the Naval Research Laboratory (NRL) and launched in 2003 with the main goal to demonstrate the capability of this instrument to measure ocean surface wind vectors. Prior to this launch, the only instrument capable of measuring ocean wind vectors were scatterometers, [46].

2.3.3 Instrument performance

2.3.3.1 Microwave radiometers

Microwave radiometry has been well studied for remote sensing, [35, 47, 48, and 49]. SSM/I instruments were evaluated in 1990, and the first polarimetric measurements of sea surface brightness and temperatures were realized in 1995. The energy received by the radiometer is the sum of the energy released from the sea surface, radiation from atmosphere and energy from the sky reflected off the surface [50]. Radiometers measure the microwave emission within the field of view of its antenna: and in doing so, quantifies the energy which is known as brightness temperature. A conceptual description of this is shown in Fig. 2.7.

Following the equation shown on Fig 2.7, T_{sky} represents the brightness temperature from the sun, T_B is the temperature emitted from the Earth, T_{atm} for radiation from the atmosphere, $(1-e)T_{sky}$ is the energy reflected off the surface and eT_w is the energy from the sea surface.

Previous studies shown that microwave emissions from the ocean surface depend not only on the wind speed but also on the wind direction. Wind vectors may produce roughness on sea surface due to the increasing waves. With a rougher sea the microwave emissions increases, therefore the intensity of emission depends on the wave structure and orientation.

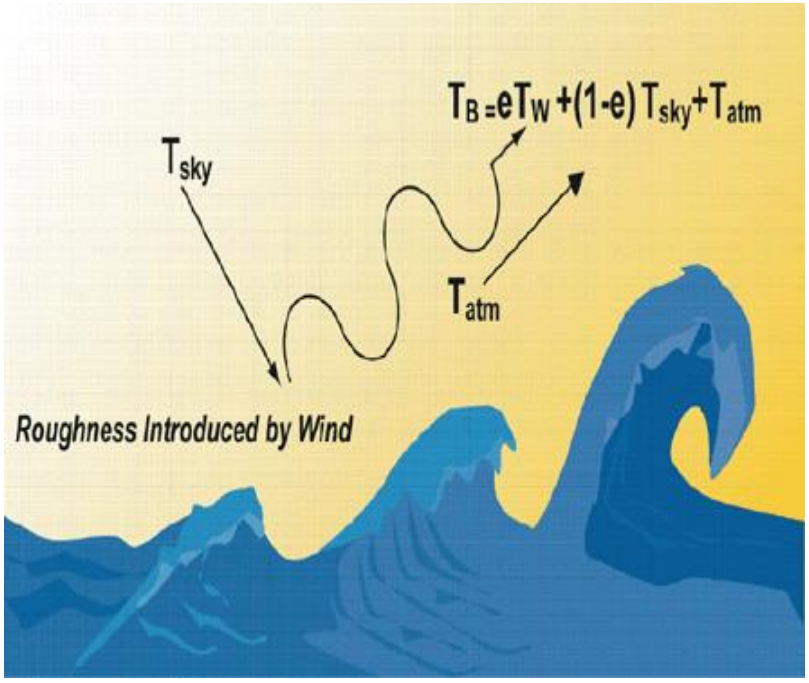

Figure 2.7. Principles of a microwave radiometer. Source: [50]

The first radiometer instruments, such as DMSP or TRMM, could only measure vertical and horizontal polarization, but the last radiometer released to space, WindSat, can measure vertical, horizontal and cross-correlation of the vertical and horizontal polarizations.

2.3.3.2 Microwave scatterometers

There are several different types of scatterometer; SAR, ASAR, ASCAT, RAR (Real Aperture Radar), but all of them work following the same principle. They are mounted on a moving platform, such as satellites, and transmit pulses of energy to illuminate a section of the Earth surface. They work in the microwave spectrum, but not all instruments work on the same wavelength, Table 2.2 shows the five different bands. The most common is band C. In scatterometry only bands with centimetric wavelength are used. It is also important to know that the higher the frequency, the higher the resolution.

The wave polarization can be vertical or horizontal, but always perpendicular to the direction of propagation [29]. These pulses can penetrate clouds, light rain or fog; thus scatterometers can acquire data in adverse weather conditions. Therefore images can be acquired taking into account the time delay, the angle of incidence and Doppler shift of the returned radar signal.

Band	Wave length [cm]	Frequency [GHz]
L	15-30	1-2
S	8-15	2-4
C	4-8	4-8
X	2.5-4	8-12
Ku	2.5-1	12-18

Table 2.2. Wavelength and frequency for scatterometers according to the band. Source: [29]

It is also important to know the geometry of scatterometers signals, as Fig. 2.8 illustrates. Spatial resolution depends not only on the distance between the satellite and the surface, but but also on the slant range, the spectral resolution depends on the bandwidth only.

In Fig. 2.8 a special kind of scatterometer is represented; the windscatterometer. This is different because it uses multiple look angles (a minimum of three). Comparing asymmetry in the backscatter of each angle can define wind direction with an ambiguity of 180°. There is another way to get different look angles, using a conical scanning as shown in Fig 2.9. Some windscatterometers use this technique but, another beam is required to have a minimum of three look angles. With conical scanning, it is only possible to achieve two measurements with different angles.

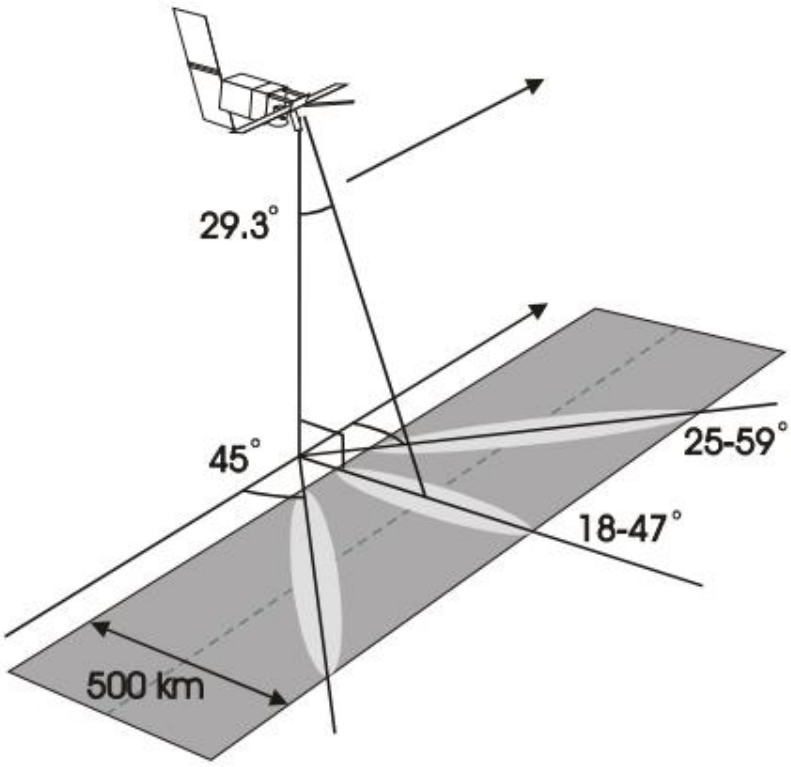

Figure 2.8. ERS windscatterometer geometry. Source: [36]

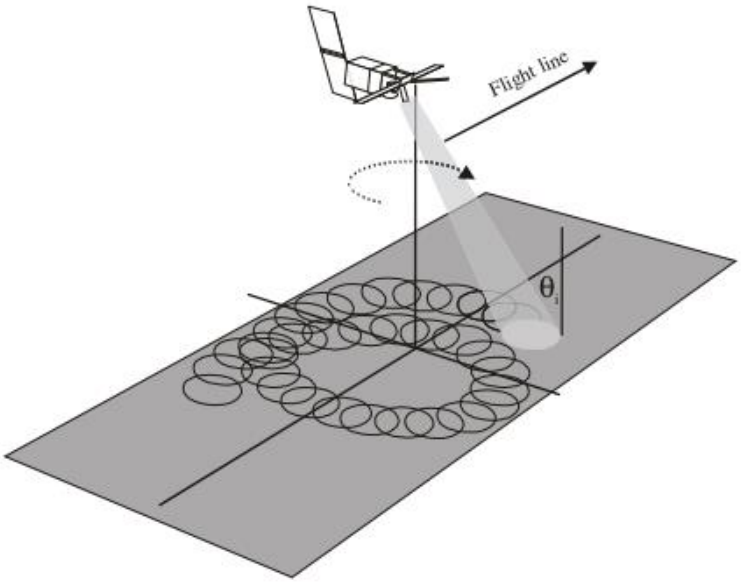

Figure 2.9. A conical scanning as used by QuikSCAT. Source: [36]

Another mechanism to understand is backscattering because, depending on the reflection of the signal, it is possible to create wind retrievals. Fig. 2.10 shows how backscattering works for different surfaces. A calm sea surface situation is like a smooth surface and it is considered as the direct scatterer. When there is an obstacle, such as a corner reflector, the back signal is very strong as shown in Fig 2.10. Finally, there is a lot of dispersion for rough surfaces such as land. For this reason, it is not possible to receive a clear signal from land.

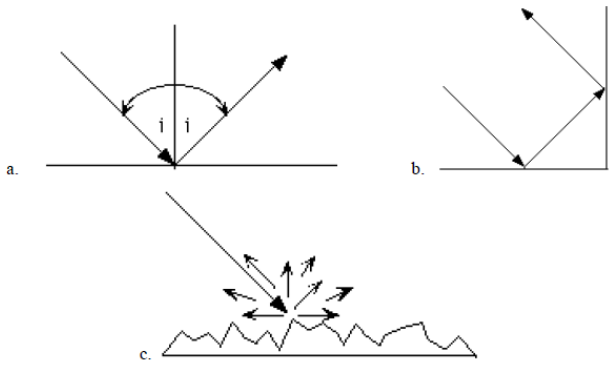

Figure 2.10. Scattering from a) smooth surface, b) corner reflector, c) rough surface. Source: [29]

Thus, scatterometers measure the backscatter, the alteration of which is physically related to the wind stress over the sea, [51]. This backscatter it is translated to wind speed through a Geophysical Model Function (GMF). The C-band V-polarisation GMF is also called CMOD. Nowadays, the most widely used GMF for scatterometers is CMOD5.N which allows the calculation of 10-metres height neutral wind speed. All CMOD models use an empirical functional relationship where the normalized backscatter is a function of 10-metres wind speed, incidence angle and wind direction relative to the antenna azimuth look direction, [52]. The expression is solved by iterations in order to find the wind speed for a measured backscatter. The incidence angle is always known because the position and angle of the antenna are always known. Thus, a key parameter to calculate the wind speed is the wind direction. If no wind direction is provided or measured by the scatterometer, the wind speed cannot be found. The general CMOD expression is shown in Eq. 2.6.

$$\sigma_0(\theta, v, \emptyset) = B_0(\theta, v).[1 + B_1(\theta, v)\cos(\emptyset) + B_2(\theta, v)\cos(2\emptyset)]^p \qquad [2.6]$$

Where σ_0 is the normalized backscatter, θ is the incidence angle, v is the wind speed at 10 metres, $\emptyset$ is the wind direction relative to the azimuth look direction. The rest of terms, B_0, B_1, B_2, and p, are empirically derived.

2.3.3.3 Altimeters

As explained before, altimeters are a type of scatterometer but simpler due to their geometry, as shown in Fig 2.11. Altimeters are the most frequently used radar system as they are installed in many aircraft and satellites. There is no angle of incidence because the beam is almost vertical.

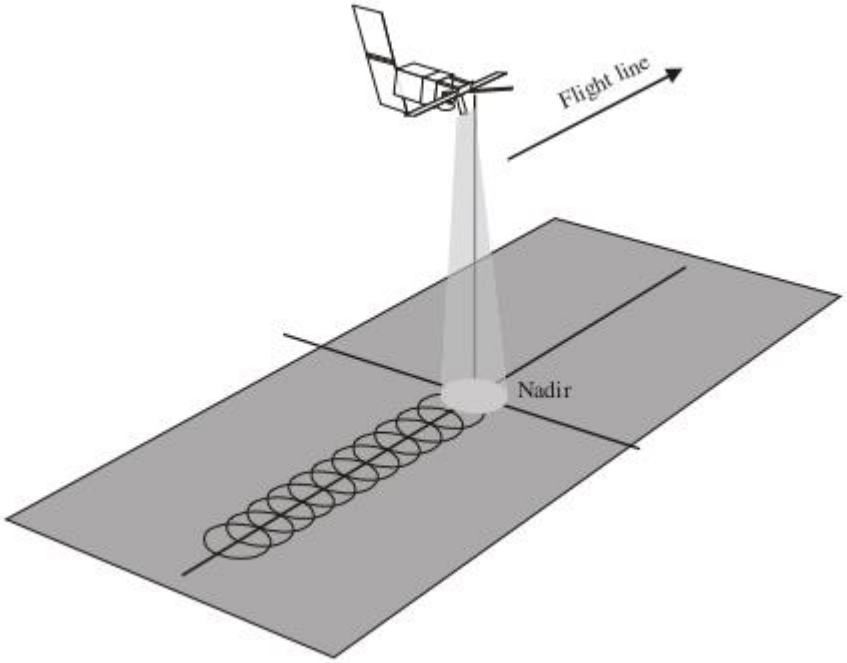

Figure 2.11. The basic geometry of a simple altimeter. Source: [36]

They have been used to determinate the distance to a target or surface. The performance of an altimeter is simple, the device sends the signal and counts the time delay before reception of the echo, knowing the speed of the waveform and the time taken it is possible to calculate the distance. Height measurement is slightly more complicated over the sea because it is necessary to take into account the sea surface height, the geoid, and ellipsoid as shown in Fig. 2.12.

Geoid is the shape that the surface of the oceans would take under the influence of Earth's gravity and rotation alone. On Fig. 2.12, h_g is the geoid height, h_d is the height between geoid height a sea surface height, H is the satellite orbit height, and h is the range or distance from orbit to sea surface.

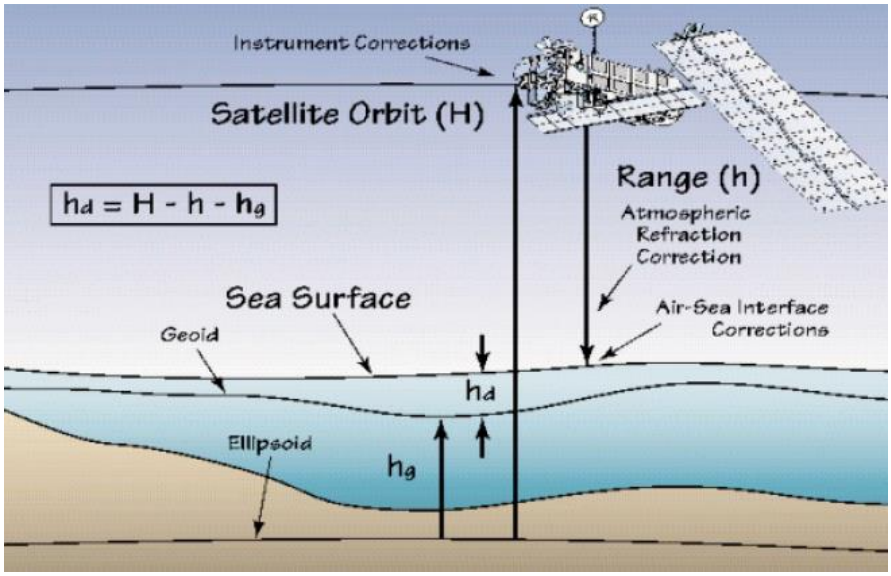

Figure 2.12. The principle of altimetry measurements. Source: [53]

With some more complicated analysis of the signal returned it is possible to use altimetry to measure wind speed. Determination of wind speed is based on the measurement of backscattering with the maximum angle of incidence, i.e. near the boundary of the beam where there is a significant angle of incidence. Comparing this with the vertical value of backscattering and applying the algorithm of Witter & Chelton [37], it is possible to determinate wind speed at 10 meters above the sea.

There are two problems with altimeters; firstly the swath is very narrow in comparison with windscatterometers and secondly it is not possible to determine the wind direction.

2.3.3.4 Synthetic Aperture Radar

SAR's are instruments similar to scatterometers but designed to have high resolution. As explained before, resolution is higher with high frequencies. But this is not the case for SAR's, which work in the C-band. The azimuth

spatial resolution is dependent on neither the distance from the instrument to the target nor the wavelength of the radar. A summary of its performance is shown in Figure 2.13.

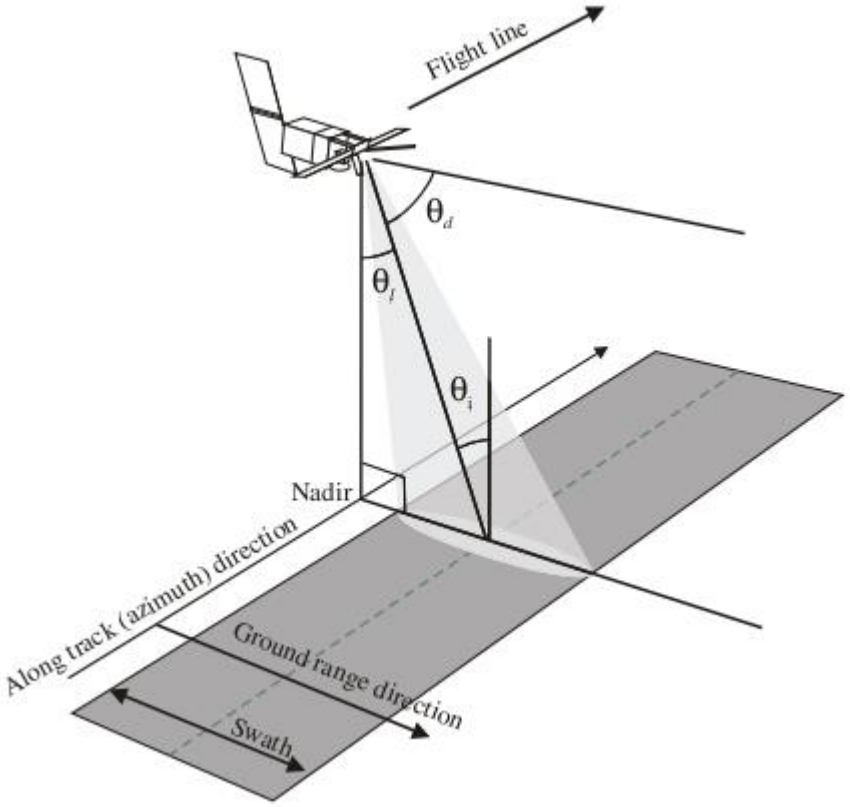

Figure 2.13. Side-looking airborne radar geometry. Source: [36]

The most straightforward explanation is that SAR's work by improving the analysis of the Doppler Effect. SAR's large antenna is made of small antennas working sequentially instead of simultaneously. By the joining of the echoes is possible to synthetize a large antenna. The Doppler shift is not detectable on individual echoes, but it is possible for a sequence of many successive echoes. This is possible not for the echoes frequency, but for the echo phase change. The echo is divided into bins according to the Doppler Effect and so it is possible to analyze a very wide beam by bins. The last step is that by using wide beams the footprints overlap and the antenna will receive different signals of low resolution from the same point of the earth surface,

see Fig. 2.14. By combining many footprints it is possible to achieve a high-resolution signal.

Thus, SAR's obtain high-resolution images over a wide swath. There is also another reason, regarding its geometry but this is complex to explain and beyond the scope of this thesis. For more information consult [36] and [51]. From here the process and principles to achieve wind vectors are exactly the same as scatterometers.

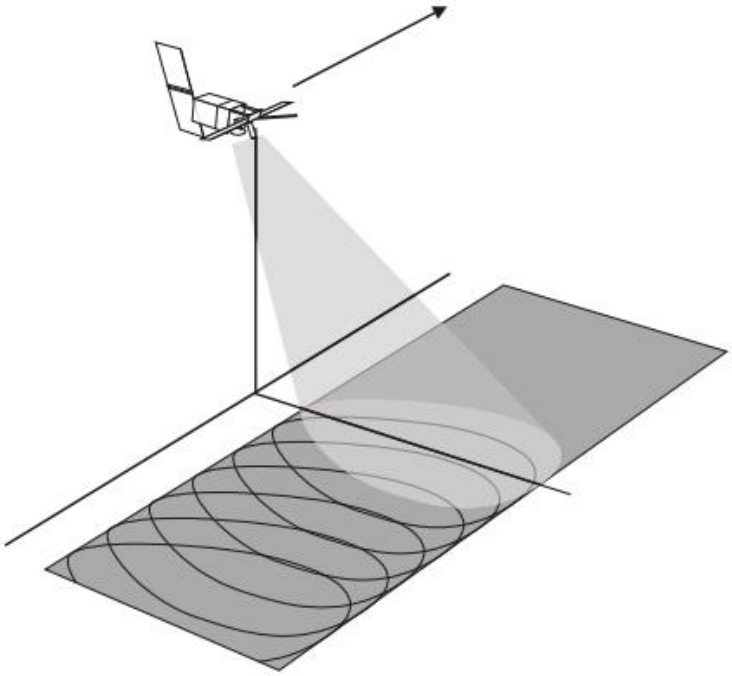

Figure 2.14. SAR geometry. Source: [36]

2.3.3.5 GNSS-R

There is an important difference between this system and previous systems, which are monostatic (the same antenna is transmitting and receiving). GNS satellites are always transmitting, so it is necessary to have a separate receiver, this is referred to as a bi-static system.

Satellite	Status	Developed by
UK-DMC	Finished	UK
Techdemosat-1	Operating	UK
PARIS	Proposed	ESA
CYGNSS (8 satellites)	Launched in October 2016	NASA
GEROS-ISS	Under study	ESA
Cat-2	Launched in 2015	UPC, Spain
CubeSat	Launched in February 2016	Europe

Table 2.3. GNSS-R remote sensing missions.

The GNS signal is also a microwave signal, but consists of two monochromatic carriers, with two different L-band frequencies. Actually, there are many GNS satellite transmitters in space, 24 by GPS, 24 by GLONASS and 15 by BeiDou. Recently, ESA launched 30 satellites more known as Galileo.

The problem with this system is that there is only actually one Low Earth Observation (LEO) satellite receiver operating. In Table 2.3, there is a list of previous and upcoming missions, according to the table, there was twelve LEO receiver satellites operating by the end of 2016. These satellites are able to capture reflected L-band signals from GPS and Galileo constellations, some of them could also use GLONASS and BeiDou constellations. Each LEO satellite will do at least four simultaneous measurements, each one from a different GNSS satellite as Fig. 2.15 shows.

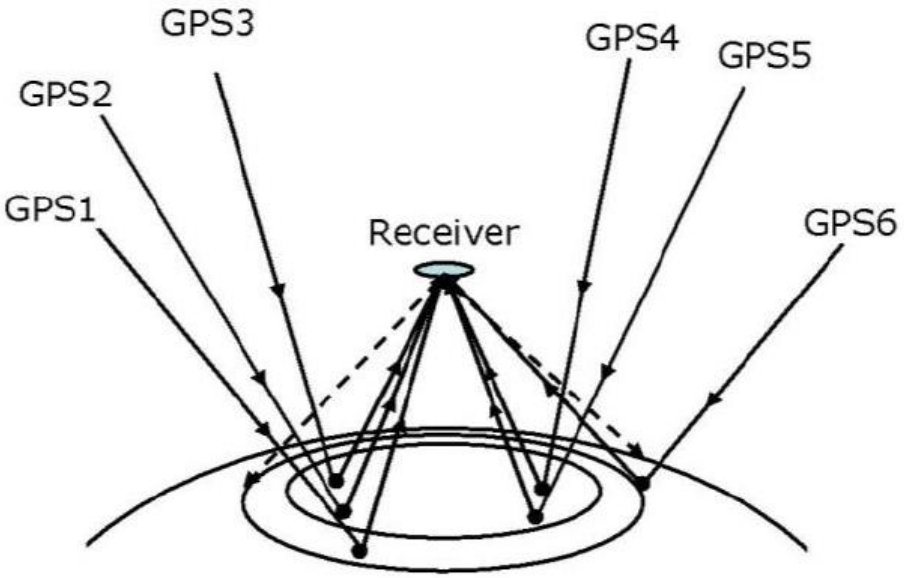

Figure 2.15. Simultaneous signals from different GPS satellites. Source: [38]

GNS signals can be refracted or reflected, and a LEO satellite can receive both (depending on the orientation of antennas), but these signals measure different parameters. Refracted signals (GNSS-RO) measure atmospheric parameters such as water vapor, temperature, pressure, and humidity; reflected signals (GNSS-R) measure land and ocean surfaces, including sea surface roughness and therefore wind vectors. There are some papers which have assessed the capability of GNSS-R to determine wind vectors, [54] to [61], with successful results. In order to measure the wind, a technique called Delay Doppler Mapping (DDM) is used which is based on the same principles used by scatterometers.

Although in this section wind resource assessment by satellites has been explained, using GNSS signals aircraft could be used. In fact, with reflected signals only the receiver is missing so instead of mounting a receiver on a LEO satellite there is the option of mounting it on aircraft. In [56] a receiver was mounted on a balloon but it would also be feasible to mount a receiver on a small airplane or unmanned aerial vehicle (UAV) or drone. This could open many possibilities where each offshore wind farm could have their own UAV/drone. This option is much cheaper than any meteorological mast or LIDAR.

2.3.4 Instrument characteristics

Satellite data have different spatial resolutions, locations, and temporal sampling. Pryor et al. [62] have demonstrated that approximately 250 independent wind observations or images are required to estimate the Weibull scale and shape parameters. It is important to know the spatial and temporal characteristics of the different space-borne instruments. It will help to assess the potential of these instruments for wind resource assessment.

Missions	Instrument	Swath width (km)	Resolution (km)	Revisit cycle (days)
ERS-1to 2	SAR	500	5	35
Envisat-Sentinel	ASAR	50-100	2	35
Sentinel 1	ASAR	20-400	1-2	6
MetOp-A to C	ASCAT	500	12.5	29
ADEOS	NSCAT	600	25	41
QuikSCAT	seaWind	1800	26	4
(DMSP) (F16)	SSM/I	1400	25	6
TRMM	TMI		25	
Aqua and GCOM-W1	AMSR-E or 2	1450	5-50 (dependent on frequency)	16
ADEOS II	AMSR-J	1800	25	4
Coriolis	Windsat	1000	25	8
OcenaSat 2	OSCAT	1400	25	2
ISS	RapidScat	1100	17.3	5

Table 2.4. Example of spatial and temporal characteristics of some space-borne instruments. Source: NASA, ESA, EumetSat, ISRO, and CSA.

The repeat cycle of the satellite is the period between 2 successive identical orbits and the swath width is the total width of the area covered by the sensor on the ground. With a repeat cycle of 4 days, the sampling period of Quikscat is approximately one day. However, the resolution of this instrument is low compared to the ASAR instrument. The high spatial resolution of ASAR is associated with a low temporal sampling (sampling period greater than 150 hours). This is due to the low swath width of this instrument, [63].

In order to take advantage of the synergy between high-repetitiveness low-resolution scatterometer data and low-repetitiveness high-resolution synthetic aperture radar, a data fusion method has been proposed, [64]. Another method for data synergy is proposed in this thesis as explained in Chapter 4.

Some studies have shown the synthetic aperture radar is an adequate tool for local wind resource assessment and mapping in coastal and offshore areas. The wind statistics can be evaluated from scatterometer satellite data (e.g. QuikScat) from a nearby location [24] and [65].

2.3.5 Instrument data

Raw sensor data are collected by the ground station and dispatched to processing dedicated facilities as the images require a large amount of processing before they are usable. The amount of processing done to the images is commonly classified into levels [66]. It is important to get a good understanding of these levels of processing before ordering satellite data from one of the agencies which supply it.

Level 0 — The data is raw as collected at the sensor. There are some fundamental corrections to be applied to the data before they are usable. Therefore, most agencies will not distribute Level 0 imagery.

Level 1A — Data is corrected for detector variations within the sensor.
A remote sensor has many light detecting devices or detectors. So it is important that the brightness measured by each detector on a sensor is recorded uniformly across the scene. A series of data calibrations involving the pre-launch value and in-flight measurements are carried out to equalize the detector response. The in-flight readings come from pointing the sensor at targets with known brightness levels: an onboard calibration lamp, the blackness of deep space and/or the brightness of the sun. Absolute calibration coefficients are posted in the ancillary data and can be used to convert pixel values into real radiances measurements.

Level 1B Due to the movement of the satellite in orbit above the earth's surface and the rotation of the earth beneath the satellite, the sensor's view of the surface can be more oblique towards the edges of the scene and create distortions in the geometry of the imagery. These distortions are predictable and are corrected to improve its geometry qualities to give Level 1B data.

Level 2A Images from level 1B are mapped into a standard cartographic map projection based on a prediction where the satellite was when the image was acquired. With systematic geometry correction application, these images still have expected location errors.

Level 2B In order to create a precise geo-referenced product, the image analyst registers the image to an existing base map by selecting pairs of well-defined ground control points from both the image and the map. With a sufficient number of ground control points accurately identified, the image can be geo-referenced. The position accuracy of the level 2B image generally matches the spatial resolution of the original data (Location resolution from 30 m down to 10 m depending on the satellite).

Level 3A In an area of high local relief, the location errors for level 2B data remain high as the relief displacement is not accounted for. To reduce these errors, a digital elevation model is applied to level 2B imagery to obtain level 3A images that match the spatial resolution of original data, including areas of high local relief.

Level 3B If the region of interest is very big, level 3A images can be mosaicked together. Therefore these images have the same attributes as level 3A scenes, but they cover a large area.

An overview of the processing applied to the raw satellite data is shown in Fig. 2.16.

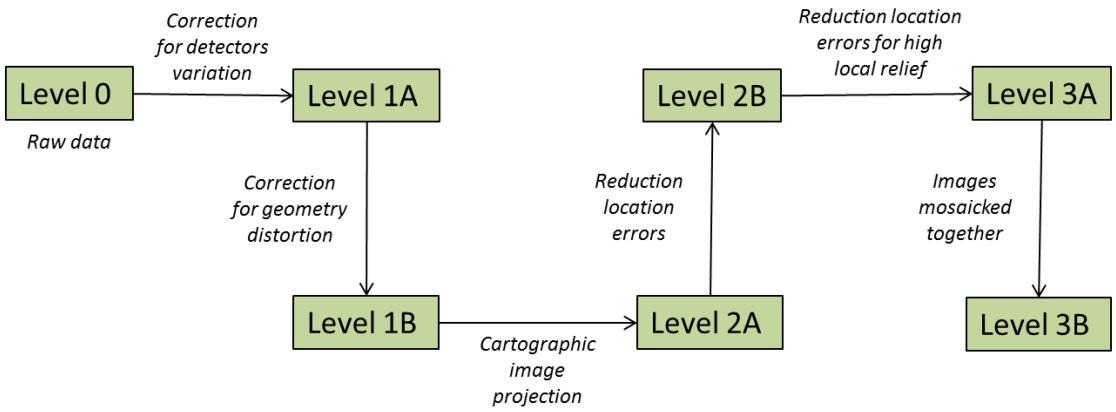

Figure 2.16. The processing applied to each level of satellite data. Source: [66]

Data from any of the automated processing levels such as level 0 to level 2A generally costs the same price. When the processing requires an analyst's intervention, the prices begin to jump by around 25% between levels 2A and 2B and an additional 25% when going from level 2B to 3A.

With some image experience and access to a remote sensing image analysis system or a robust GIS (Geographic Information System) with geometric correction capabilities, then level 1B data can be a good starting point for remote sensing applications. However, if there is no access to the necessary software and time to process the imagery, then level 2B or 3A data are required. These images will import directly into a GIS and be ready for use.

2.3.6 Example of processing

The NORSEWInD project is an example where satellite data have been used to develop a wind map of the Baltic Sea, Irish Sea, and the North Sea. In this study, wind observations from space have been retrieved, processed and analyzed in order to quantify the wind resource, [67].

These satellite observations were focused on 4 sensors (Envisat ASAR, QuikSCAT, ASCAT coastal, SSM/I). The study gives a good understanding of the processing chain from satellite data to 10 m wind speeds or to a final product such as a wind resource map. An overview of the processing chain is reported below for data from Envisat ASAR sensors, see Fig. 2.17.

- L0 data acquired by the network of ESA.
- L0 data processed into L1 products by ESA. The product is made available to Collecte Localisation Satellites (CLS).
- The L1 product is processed into the L2 product by CLS using the software Maestro developed by CLS.
- L2 products processed in near-real-time can be downloaded by users utilising the Soprano web interface.
- Use algorithm for the reprocessing of the data for wind map production at 10 m above sea level.
  (A version of the algorithm is described by Dagestad K.F. et al. [68]. It is worth noting that a new algorithm, at the time of writing this thesis, is currently under investigation by Mouche et al. [69] and it has been stated by the author that this work will be reported in the near future).
- Data used in WAsP for wind resource calculation. (Final product is a Weibull wind speed distribution for 12 bins each representing a 30 degrees wind direction sector).
- Wind data lifted from 10 m to hub height using information on vertical wind profiles at high levels as reported by Peña et al., [70] and [71], and Weather Research and Forecasting parameter [72]. However, this process is still in a stage of development and more work is required before getting an acceptable model as it will be explained in this thesis.

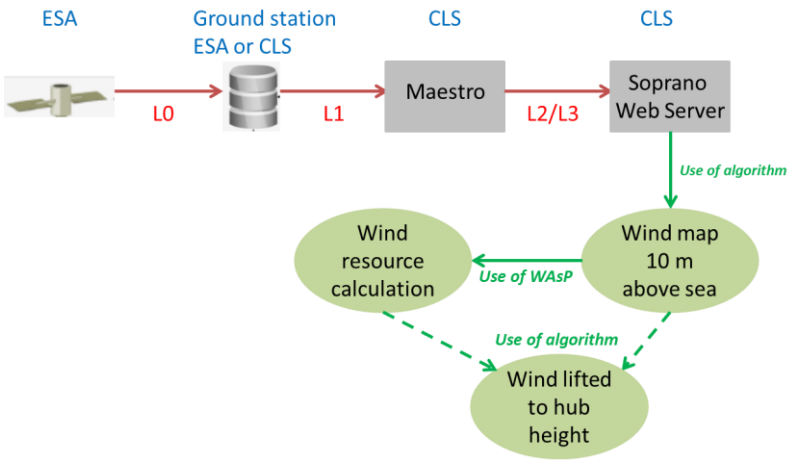

Figure 2.17. Process chain involving Envisat ASAR data. Source: [68]

2.3.7 Difficulties and influences on wind retrievals

At the present time satellite instruments are not as accurate as on-site instruments such as meteorological masts or even other types of remote sensing such as LIDAR or SODAR. Hence, every wind resource assessment by satellites should be accompanied by an accuracy study. In many of the published articles in this field, researchers have remarked on the difficulties of carrying out a wind assessment using satellites. Barthelmie et al., [73] and [62], have undertaken a sensitivity analysis of these difficulties, which are:

- Average periods of observations.
- The time between measurements.
- Data density.
- Temporal biases. Diurnal and seasonal variability are difficult to see.
- Truncation of wind speed distribution due to limitations of measurement instruments, in situ or remote.
- Criteria for image processing.
- Calibration on wind retrievals.
- Lift of wind speed data to hub height.
- Merging of wind retrievals from different satellites.

There are also some studies [25], [62], [73], and [74] where it is intended to determine the minimum number of images required to carry out a wind assessment with enough accuracy. This research is aimed primarily at trying to resolve the issues related to low data density. At present there is still no consensus among researchers regarding the feasibility of satellite resource measurement due to this problem. This problem will be returned to in the following sections.

The used GMF in the translation of radar backscatter to wind speed is also a source of uncertainty. This could be englobe as criteria for image processing because radar backscatter images are translated to wind maps. As explained, the backscatter backscatter is related to wind stress instead of wind speed. Even so, all CMOD models link backscatter with wind speed; plus the sea state is not taken into account. Furthermore, CMOD models are empirical relationships. For all these reasons, the GMF is expected to introduce uncertainty in wind retrievals.

Other problems of remote sensing are related to some phenomena in the Marine Atmospheric Boundary Layer (MABL) and also some oceanic influences. For example, in the MABL, researchers should take into account:

- Internal boundary layers
- Thermal internal boundary layers
- Atmospheric stability
- Convective cells and roll vortices
- Lee phenomena
- Gap flows and barrier jets
- Rain cells

On the other hand, oceans affect wind measurements due to surface waves, internal waves, currents and bathymetry, and also surface slicks.

2.3.8 Methodology for vertical wind extrapolation

Like conventional wind resource assessment, it is necessary to extrapolate to wind speeds at hub height since satellite wind retrievals are given at 10 meters over the ocean. With satellite data it is not possible to follow the same methodology as used with meteorological masts because there is no second measurement at different height to calculate surface roughness and hence extrapolate. Wind measurements are also too low, at 10 meters, when compared with traditional meteorological masts where the highest measurement is near the hub height. This fact has pushed researchers to find an alternative method to extrapolate winds from 10m to hub height. In Badger et al., [72], a reasonably successful methodology for extrapolation was proposed. Fundamentally this involved applying the logarithmic law for neutral stability but by keeping the friction velocity, Eq. 2.5, and Charnock's equation, Eq. 2.9, it was possible to calculate the friction velocity by iteration and thereafter extrapolate the wind speed. In Eq. 2.9, α_c represents the Charnock's parameter and g is the gravitational acceleration.

$$z_0 = \alpha_c \frac{u_*^2}{g} \qquad (2.9)$$

When calculating the friction velocity, neutral stability should be assumed since satellite wind retrievals at 10 meters corresponds to neutral wind speeds if the CMOD5.n GMF was applied. Knowing U_{10} from satellites it is

possible to extract the friction velocity and surface roughness, once this is done, applying again Eq. 2.4 the wind speed at any height may be calculated. However, at the moment of measurement by satellites, the stability might not be neutral or zero. So here are two alternative ways of extrapolating wind speeds:

1. Assuming neutral stability.

2. Calculating a stability correction. For this, it is necessary to use Weather, Research, and Forecasting data to extract the friction velocity, air temperature, and surface heat flux.

The first method is obviously the simplest but not as accurate as the second. The difference between wind extrapolated values is roughly 0.5 m/s as shown in [72], but this difference would increase in warmer seas. The complete methodology to apply stability correction is also explained in [72].

2.3.9 Combination of different instruments

In order to solve one of the main problems of satellite instruments, specifically data density, there are three studies [26], [34] and [75], where satellite synergetic data were used. In the most recent study, [34] in 2014, researchers found a couple of advantages in comparison with the use of a single satellite.

1. Obviously the greater the number of samples the greater the accuracy.
2. Increase in overpass data gives a better representation of the diurnal variation in wind speed.
3. Possibility to develop more detailed wind maps.
4. Inter-calibration of wind retrievals between different satellites in order to have solid, valid and high-quality data, [76].

2.3.9.1 Methodology to merge different instruments

Once the winds are extrapolated to hub height, they can be merged, but never before lifting, since some of the parameters to lift winds change along with the time and location. Here again, there are two methods for merging:

1. **Grid selection**. This is the straightforward method.
    I. First, it is required to choose the resolution of the grid for the final wind map.
    II. Divide lower resolution cells into small cells until they fit with the chosen resolution. With this method, it must be known that mixing different datasets at different resolution can produce a loss in resolution. To solve that, instead of taking values for all divided small cells, it is better to take values only from central small cells and around the centre.
    III. Calculate the average for each cell. For this reason, high-resolution data can be lost, when creating the average with low-resolution datasets.

2. **Power spectra density**. This method is more complex and requires more calculations. Basically, the power of the wind is calculated but, instead of on a time-scale basis, it must be calculated on a spatial-scale basis i.e. by different grid sizes. Traditionally, the power spectra density it is calculated on a time-scale basis since met masts provide data every 10 minutes or more frequently if required. But, with satellite data, this is not possible. However, it is feasible on a spatial-scale since it is possible to choose the grid resolution because satellites provide data over a wide area.

Nowadays, experts are still arguing about which method it is better, and how they should be applied.

2.4 Starting point for novel research

2.4.1 Access to satellite data

Some of the most widely used satellite in the study of ocean wind vectors are listed in Table 2.5 including their data access and the processing level.

Instrument	Data access	Type of data
ERS 1&2	website https://earth.esa.int Go to data access/browse data product Earth topic = ocean and coast Mission = Envisat Instrument = ASAR Typology = Radar imagery	Processing level = 0 / 1 / 1B / 2
Envisat ASAR		
NSCAT	ftp://podaac-ftp.jpl.nasa.gov/OceanWinds/	L2 product
QuikSCAT	RSS website http://www.remss.com/	L2 product
ASCAT	ftp://podaac-ftp.jpl.nasa.gov/OceanWinds/	L2 product
	RSS website http://www.remss.com/	L2 product
SSM/I	RSS website http://www.remss.com/	10 m above sea level Daily / 3-day / weekly / monthly data
WindSat		L2 product
AMSR		
TMI		
OSCAT	ftp://podaac-ftp.jpl.nasa.gov/OceanWinds/	Level 2B product
Sentinel-1	https://sentinel.esa.int/web/sentinel/sentinel-data-access/access-to-sentinel-data/	L0 or L1 products
RapidScat	ftp://podaac-ftp.jpl.nasa.gov/OceanWinds/	L2 product

Table 2.5. Satellite data accessibility.

2.4.2 Software

Since the amount of data received from satellites is huge, some researchers have developed specific software to facilitate the data processing. Some of the wide range of software used in wind assessment by satellites are:

- ***WEMSAR***: Developed by Risø and the Nansen Environmental and Remote Sensing Center (NERSC) in 2000-2003. This software was designed to manage wind retrievals from calibrated ERS-2 SAR, only wind speed but not wind direction. Previously called RWT.
- ***WiSAR****:* Developed by GKSS Reseach Center in Germany. It is a tool to find the wind direction from SAR datasets, [77].
- ***ANSWRS****:* Developed at the Johns Hopkins University, it is software to enable near real-time calibration and wind retrieval from RADARSAT-1 and ASAR, [78].
- There is a software package from BOOST Technologies, which processes SAR images to wind maps, but users have to load wind directions from another source, [79].
- ***BEST****:* Software developed by ESA, this one is used to calibrate raw images from SAR images, [41].
- ***Satellite WAsP****:* Another tool developed by Risø, which can extract the wind field of a specific area and calculate wind statistics. As with previous tools, it was used for SAR processing.
- ***Sentinel 1 Toolbox****:* This software has been developed by ESA taking as a base the other previous software. The user can use more SAR satellites and will work with any C-band SAR. Actually, this is the most important software on the list, [41].

Also well-known mathematical/wind analysis software can be used for wind resource assessment such as *Matlab, WAsP, Windpro or Windfarmer*. But none of them is open-source so their source code is not available for modification and also they were designed to carry out wind assessment from on-site measurements.

2.4.3 Research teams working in satellite wind retrievals

Before organizing the research line of this thesis, and following the literature survey, the work of other research teams working in satellite wind retrievals was consulted. NASA and ESA agencies have been launching satellites for Earth observation in the past decades. They also made datasets available to scientific community. Furthermore, there were some researchers improving the accuracy of remote measurements. However, possible applications were not only studied by NASA and ESA, but also by other institutions,

companies or research teams. In the following subsections, the most relevant European research teams working in wind satellite retrievals are introduced. Remote Sensing Systems was the only American company included here due to its important datahub which was used to undertake the present research.

2.4.3.1 Edinburgh Earth Observatory

The Edinburgh Earth Observatory (EEO) it is a multidisciplinary research entity including Geography, Ecology, Meteorology, Geology & Geophysics. Their strengths are remote sensing and GIS modeling, measuring and modeling land-atmosphere fluxes of traces gases, modeling atmospheric transmissivity and stratospheric ozone, seismology, and hydrocarbon detection. The EEO aims to address a range of interdisciplinary science issues, such as the carbon cycle, atmospheric composition and human health, land use change, rapid climate change, vegetation change, long-term trends in the biological activity of the planet. But they have also carried out some studies on offshore wind mapping by SAR, [80].

In their studies, they were trying to prove the accuracy of SAR measurements and show its high resolution. But also, they tried to develop a Directional Wind Speed Algorithm (DWSA) for SAR. They compared the results of that algorithm with results a Unified Mesoscale Model (UMM), the union of both methods and in-situ measurements. However, they used the CMOD5 algorithm to retrieve SAR wind speed which does not retrieve neutral wind speed like the CMOD5.N; and in-situ measurements were placed on the coast, not offshore. That methodology implies a low accuracy in validation due to the nature of the wind retrievals.

2.4.3.2 DTU Wind Energy

DTU Wind Energy is a department of the Technical University of Denmark, previously known as Risø, the National Laboratory for Sustainable Energy. DTU has carried out the major part of wind energy research in Denmark, becoming one of the most important research entities for wind energy in the world. DTU integrates research, education and public/private sector consulting. Their goal is to develop new opportunities and technology for global and Danish exploitation of wind energy, [81].

DTU developed the most widely used software for wind energy assessment, *WAsP*. In their offices, there is one team focused on the study of wind by remote sensing. As shown in previous paragraphs, they also developed two tools for wind assessment by SAR, *WEMSAR* and *Satellite WAsP*. The newest and most interesting one is *Satellite WAsP*, which can calculate the wind field, Weibull curve, and parameters. Even so, the software only works with SAR's, SAR imagery must be included one by one and wind retrievals are placed at sea level.

2.4.3.3 IFREMER

IFREMER is the French Research Institute for Exploitation of the Sea, and one of the most important institutes in ocean research. Their areas of research include climate change effects, marine biodiversity, pollution prevention, seafood quality among others. Also in IFREMER, there is a laboratory for oceanography from the space named CERSAT. Their scientists contribute to several major international projects about climatology, sea waves, sea ice, sea surface temperature and so on, [82].

They are not specifically involved in any project about offshore wind, but there is an interesting project about SAR's and oceanography. The project is called GlobeICE and is focused on the Arctic sea ice. In the project, they also use Quikscat and SSMI satellites.

2.4.3.4 KNMI

The Royal Netherlands Meteorological Institute (KNMI) is the Dutch national weather service. Their primary tasks are weather forecasting and monitoring, but it is also the national research centre for meteorology, climate, air quality, and seismology. KNMI also contributes to the process and reports of the International Panel on Climate Change (IPCC), [83].

KNMI and ECMWF developed the C-band geophysical model functions CMOD5 and CMOD5.N. These algorithms were initially designed for ERS and ASCAT but they can be applied to any C-band SAR. In order to calculate winds, they developed software, *NWP SAF*, which is capable to process ASCAT, ERS, Seawinds, OSCAT, HSCAT and RapidScat data. Furthermore, they developed *IDL*, *Fortran,* and *Python* packages to calculate wind vectors.

2.4.3.5 RSS

Remote Sensing Systems (RSS) is a world leader in processing and analyzing microwave data from satellites. Their work involves algorithm development, instrument calibration, ocean product development, and product validation. They work with more than 30 satellites, mainly radiometers, and scatterometers. With all these satellites they are measuring brightness temperature, atmospheric water vapor, CCMP, cloud liquid water content, rain rate, sea surface temperature, upper air temperature and wind, [84].

Another important task carried out by RSS is their freely available data hub. They process satellite data applying their own algorithms or freely available algorithms to calculate atmospheric and meteorological parameters; plus, they inter-calibrate measurements from satellites in order to obtain confident measurements. RSS is a very important source of data in satellite microwave remote sensing of the Earth.

2.4.3.6 CLS

Collecte Localisation Satellites (CLS) is a subsidiary of IFREMER and CNES. CLS provides services for environmental monitoring, sustainable management of marine resources, marine security and telematics. CLS works with 40 different satellites carrying in total more than 80 instruments. They provide expertise in location and environmental data collection, monitoring land and maritime activities, geolocation of land vehicles and ocean observation, [85].

One of the most relevant works is EODA, Earth Observation Data Access; which is a free online service. In order to select the data an online GIS tool is available, but there is no possibility to export or save maps. The capabilities of the tool are:

- Near-real-time ocean surface wind measurements: showing some (but not all) images from RadarSat-2 were wind vector was calculated in less than 10 minutes.
- Global swell monitoring from space
- Offshore wind energy - resource assessment: This was a work partnering DTU and under the NORSEWInD project. Here it used

historical data from Envisat-ASAR satellite to produce wind maps of the North Sea.

- Offshore wind energy – wake from space: Also partnering DTU, here is shown the wake effect downstream of some offshore wind farms.
- Early warning system for oil spill threats to sensitive areas and wildlife
- Ocean surface current measurements
- Oil spill aging and polluter identification

2.4.3.7 ECMWF

The European Centre for Medium-Range Weather Forecast (ECMWF) is an independent intergovernmental organisation supported by 34 states. This institute offers operational services as well as undertakes research in meteorology and weather forecast. The ECMWF uses and develops Numerical Weather Prediction models and global forecasts, [86].

The most interesting fact about ECMWF related to this thesis is the reanalysis datasets ERA and CERA. Both datasets represent old datasets achieved years ago which are recalculated by combining new models with observations to improve accuracy for the monitored parameters. These datasets contain atmospheric parameters, such as wind, pressure, humidity and temperature, and surface parameters, such as rainfall, soil-moisture, roughness, etc. It is remarkable the amount of sea, land, climate and atmosphere parameters included in their datasets.

2.4.4 Previous results in wind scatterometry and radiometry

The study of ocean wind vectors from space is not a new field or technology. As explained, the first radiometer was launched in 1987, and the first scatterometer in 1991, see section 2.3.2. Although, there is still research ongoing for all five type of instruments capable of measuring the wind which appear in section 2.3.2. Obviously, the level of confidence of these technologies has been tested before. Most of the time, the validation device for ocean winds was a buoy in the middle of the sea. A few studies used a meteorological mast to check the uncertainty in satellite retrievals. Results from these studies are shown in Table 2.6. Since buoy data was not used in

this thesis, only studies where meteorological masts were included appear in Table 2.6.

Met. mast	Instrument	Height (m) (mast/sat)	R	Std. Dev. (m/s)	Reference
Horns Rev	Quikscat	15/10	-	1.3*	[17]
Fino-1	SSM/I	100/100	0.72	1.75	[87]
Egmond aan Zee	Envisat ASAR	10/10	0.86	-	[34]
Horns Rev	Envisat ASAR	10/10	0.79	-	[34]
Horns Rev	Envisat ASAR + ERS-2	10/10	0.86	1.34	[18]
Horns Rev	Quikscat	10/10	0.93	1.32	[88]
Fino-1	Quikscat	10/10	0.96	0.96	[88]
Greater Gabbard	Quikscat	10/10	0.92	1.43	[88]
Hainan 59765	Envisat ASAR	10/10	0.74	2.00	[89]
Hainan M1328	Envisat ASAR	10/10	0.81	2.37	[89]
Hainan 59765	ASCAT	10/10	0.79	1.77	[89]
Hainan M1328	ASCAT	10/10	0.82	2.13	[89]

Table 2.6. Results from previous studies where meteorological masts were used as validation device. *standard error

2.5 Summary

In order to define the wind resource assessment of a targeted site, the process should start with on-site assessment for a minimum of one complete year. This short-term analysis will be related to a wind climate from long-term measurements at nearby sites or from model outputs to identify whether the

measured wind speed is representative on the timescales the wind farm is expected to be producing electricity (20 to 30 years). However, in-situ offshore observations of wind speeds are sparse due to the cost of the installation of measurement system offshore. Satellite-borne system can help solving this issue of lack of data. The principal advantage in the use of satellite data is in spatial coverage that they provide over a large area. The next chapter of this report describes the characteristics of the data collected from space observations.

The goal is to collect information such as monthly average or diurnal average wind speeds, wind speed distribution (or Weibull distribution) and wind roses from the satellite observations. From this information and the power curve of the wind turbine, an annual production output can be estimated.

Satellite observations provide ocean wind maps valid at 10 meters above sea level only (see section 2.3). An extrapolation of this information to higher height to obtain a hub height resource assessment is required. This extrapolation is currently the subject of a lot of research.

Despite a large number of missions to study the wind from space, and the well-identified process to convert raw data; there are still difficulties which mitigate against the use of satellite data for wind resource assessment. In most of the papers, the accuracy when compared with measurements in situ is the main issue. However, this may become less of a problem due to the number of missions planned for the near future.

Due to the different types of instruments with different characteristics, it is obvious that the balance between data density and data quality (or resolution) is not well defined. Probably with higher resolution images fewer samples will be required. But the minimum number of samples required is still and area of study. The manner of how to combine different types of satellite datasets is also a field of research that is requires considerable work. Also, the effect of the use of different algorithms or criteria to analyze the data from satellites needs to be considered.

Software currently available software has not been designed to compute scatterometers, radiometers and SAR's data together. Furthermore, this software does not meet the requirements of the wind industry. The analysis

software was designed to compute one satellite image or a few images at once. In order to undertake a wind resource assessment it is necessary to analyse a very large amount of data, therefore there is a requirement for software capable of processing a large amounts of satellite images and producing wind resource assessments.

The aims and objectives of the thesis, as explained with detail in section 1.1, were selected to solve the gaps in knowledge explained in previous paragraphs, which are:

- Decrease the satellite data shortage problem.
- Bring the capabilities of satellite remote sensing of wind resources to the offshore renewables industry.
- Increase accuracy of satellite measurements.
- Extrapolate satellite wind retrievals to different heights, since satellites measure the wind speed at 10 metres above the sea level.

3. Development of a tool for wind resource optimisation by a different type of instrument

3.1 Introduction

This chapter is a synopsis of the structure and capabilities of the software that has been developed. The main goal of the tool is to process satellite data to achieve a wind map as a product. Although nowadays there are wind maps from satellite data, see section 2.4.3, these represent the mean wind speed at 10 meters over the sea and cover very large areas of the world, such as the North Sea. The present software was designed to cover small areas and so be able to carry out a wind resource assessment for a potential offshore wind farm. The other difference present in this software is the calculation of winds at the chosen hub height. Therefore, the main outputs of the tool are a wind map for a targeted area with winds at hub height and a data density map, but this is not the only output. Although not present in the current software output, energy or wind direction maps could be easily implemented. Development of the resource assessment software leads to further research which is explained in chapter 4. Validation of the data produced is paramount and therefore correlation between satellite and ground devices was included in the assessment.

The main characteristics of the software are:

- The tool has been developed in *Python*, an open-source programming language.
- The input or data source is a database (DB) composed of satellite data.
- The DB was developed to cover the entire world and work efficiently with a huge amount of data. Future users of the software will only need to handle a small portion of the database for their chosen area.
- By the end of 2015, the DB included data from 9 different satellites: Sentinel-1, Windsat, Quikscat, ASCAT, OSCAT and SSMI (only f08, f10, f11, f13). All data are freely available through different data hubs, see section 2.4.1. Therefore only freely available data for those missions, from the beginning of their mission until December of 2015,

were included in the DB. The analyses included in this thesis only comprise the data present in the DB.

3.2 Database

Although satellite datasets are available online, freely for many devices, the datasets are not arranged in the same format. Each data hub has its own format. Hence, it was necessary to transform the data to a standard format. Furthermore, because of the nature of the different devices, this new format had to be capable of including all instruments; radiometers, scatterometers and SAR. Altimeters and GNSS-R were discarded because of their narrow swaths. The main difficulty with this was the combination of different resolutions.

The first step was to set a format. For wind resource assessment, the more data that is included in an analysis, the better the accuracy. Hence, the DB was devised to host the data from complete missions when possible. This meant a very large amount of data would need to be manipulated, i.e. satellite Big Data. For that reason, and in order to decrease the amount of data to compute simultaneously, the DB was composed of 1,200 tables. These tables represent a UTM square as shown in Fig. 3.1. Exceptions were located in the *X* and *V* rows which were removed and divided in a similar form as the rest of the rows. Thus, all boxes have the same size.

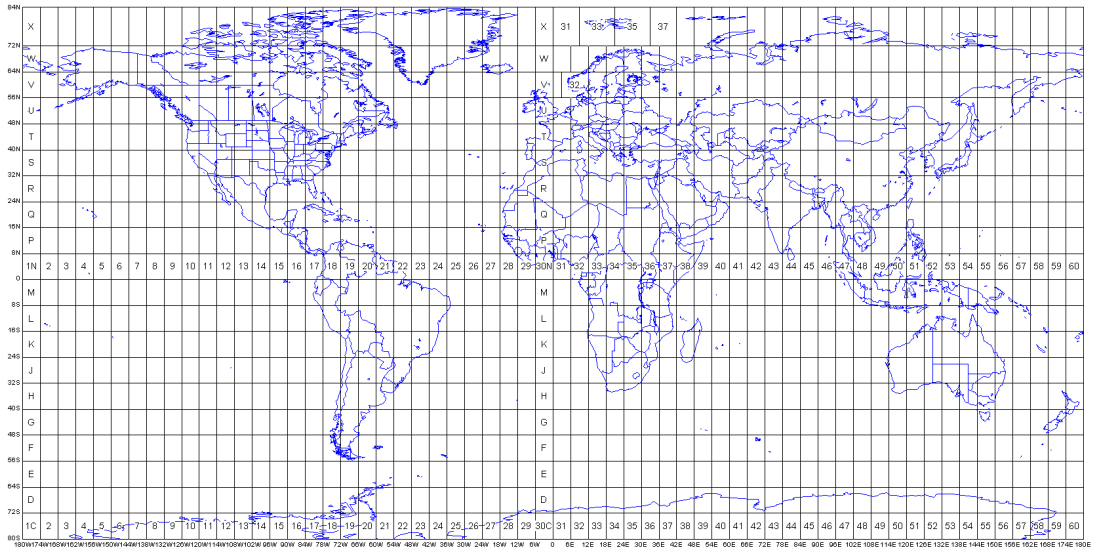

Figure 3.1. World map with UTM division.

Satellite datasets are arranged by daily products for radiometers and scatterometers. Each product includes the different measurable parameters for the entire globe. Where the satellite was not observing, non-valid values are found. This fact leads to an unnecessary multiplication of data. The case for Sentinel-1 is different since their datasets are arranged by single images. Thus, the first scripts to be written were designed to read each kind of satellite dataset, removing the non-valid data and inserting the remaining data into the appropriate table of the DB.

As explained previously each device has its own resolution. In order to place data from different satellites into the same table, four different fields for geolocation were added. These are low and high longitude, plus low and high latitude. Along with these fields, Satellite name, Type of Instrument, Date and Time, Wind speed and direction, and Rain were also included. Once all data was inserted into the DB, the scripts to read and select data from the DB were written. Since the tool was designed to be focused on small areas, there was no need to work with all tables at once. Thus, the tool is capable of selecting the data according to the location and date, and export it to a *csv* (comma separated values) file. The benefits of this process are minimum work with the DB and again a decrease in the amount of unnecessary data being processed. As a result, the speed at which the whole tool operates was kept as high as possible.

3.3 Data analysis design

In order to explain all of the capabilities and structure of the software, the whole analysis process is explained. The process is also represented in Fig. 3.2 to ease comprehension.

1. **Working with or without satellite data**. Although the goal was to use satellite data, the software is able to do a wind assessment with only in situ or satellite measurements or both at the same time. However, users must provide in situ data when this option is selected. At this point, the software only reads in situ data in one format of data table. Extra scripts were written to create a specific template according to user preferences. Thus, users can transform their data in order to be readable by the tool.

2. **Acquiring satellite data**. As explained, satellite datasets are contained in a DB. Once the target area is set, the tool exports a file containing all satellite wind measurements for the specified location. Since the tool was designed for small areas, a maximum of four UTM squares were allowed as an area definition. The software works with a coordinate system in degrees; from −180° to 180° for longitudes, and from −90° to 90° for latitudes.

3. **Filtering data.** This filtration removes missing values, and it is done according to some optional parameters that the user can choose, such as:

    - Rain rate.
    - Satellites to work with.
    - Instruments (or type of devices) to work with.
    - Atmospheric conditions.
    - Overlaps between ground and satellite measurements.
    - Period of study. This option is very flexible since it is not just a selection of the start and end date. Different temporal analyses can be undertaken; by year, by months of one year or by the same month but different years, by day and night and also by selected time for different days.

4. **Setting grid or resolution.** This option depends entirely on the user's selection of satellites because the resolution on the wind map is exactly the same as the resolution of the satellite data. By default the highest resolution is chosen automatically. For example, SAR satellites have the best resolution with pixels of 2km x 2km, whereas the most common resolution is 25km x 25km. Satellite data is adapted to the grid.

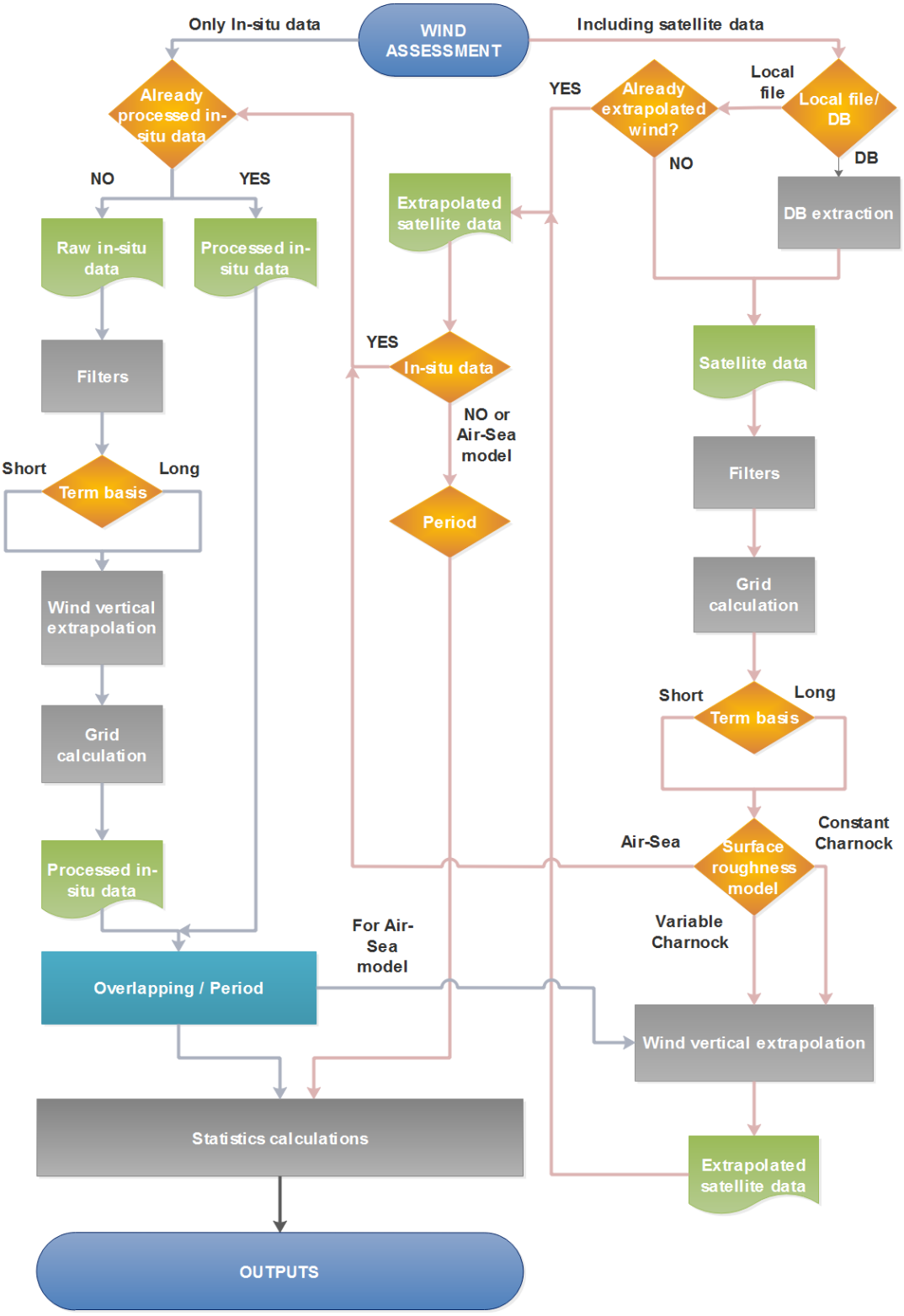

Figure 3.2. Flowchart of the software structure. Grey line represents in situ data, red lines means satellite data.

In this process, a problem was considered, which was named "data spreading". This problem consists of the increase in the number of measurements when low-resolution data is fitted to the high-resolution grid. Since low-resolution pixels cover a larger area than high-resolution pixels, the low-resolution data could be represented in many high-resolution pixels. Fig. 3.3 is a representation of data spreading. If every high-resolution pixel contains the values from low-resolution data, the low-resolution data is multiplied by a factor of (low resol. / high resol.)^2, this factor is 25 in Fig 3.3. Furthermore, this fact will automatically be a loss of resolution and, when represented, high-resolution pixels will not be observed.

In order to solve data spreading, every single low-resolution pixel was inserted in only one high-resolution pixel from the grid. A single pixel in microwave remote sensing represents the average wind speed over that area. The maximum representativeness of the measurement is expected to be the centre of such a pixel. Hence, the high-resolution pixel hosting the measurement from a low-resolution pixel is the one closest to the centre of the low-resolution pixel. As it is explained in chapter 4, this method leads to the production of cells or pixels with a huge amount of data called HDDC (High Data Density Cells).

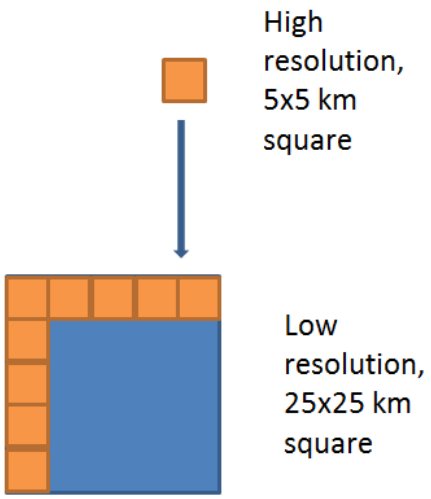

Figure 3.3. Representation of data spreading.

5. **Vertical wind extrapolation.** Here winds at hub height are calculated. The user must choose the hub height. It is possible to work on a long or short-term basis. There are three different models for shifting the wind; from simple to complex data analysis:

    - Iteration with constant Charnock parameter
    - Variable Charnock parameter and friction velocity
    - Air-sea interaction models to calculate surface roughness

    Methodologies for vertical extrapolation of the wind speed are explained and analysed in chapters 5 and 6.

6. **Choosing output parameters.** Users can select what it is going to be represented. The software can do comparisons between different years, months or day and night; and so, observe yearly seasonal and diurnal variations. Hence, the software is capable of producing different maps. Otherwise, the user may select to make one wind map with all available data and higher data density. It is also possible to select those satellite measurements that overlap in time with in-situ measurements and so be able to undertake a fair comparison and correlation between satellites and ground devices.

7. **Calculating statistics.** According to which parameters were chosen in the previous step not only are the mean, minimum, maximum wind speed and standard deviation calculated but also Weibull parameters. At this point, it could easily calculate power density, turbulence intensity, etc. However, these were not included in an analysis as explained in chapter 4. The reason for this is that the most important parameter to be studied is the wind speed.

8. **In-situ measurements**. There is an option to include in-situ measurements inside the area under study, and so be able to do an accuracy study. This data will be processed under the same parameters as the satellite data. In order to use in-situ data, it is necessary to adapt the data to the templates used by the software thereby allowing the analysis software to read it.

3.4 Outputs

As explained previously, at the moment the main output is a wind map. However, in the future, it could be possible to include more outputs such as energy yield, turbulence intensity, extreme winds and risk calculations. If the user selects a set of coordinates inside the map, the software can release the following:

- Wind roses.
- Weibull curves.
- Bar charts of comparison for wind speed, temperature, pressure, and humidity. The last three parameters were included for in-situ measurements only.
- CSV file with all parameters for each pixel of the map.
- CSV file is pre-formatted to be an input for a GIS tool. This is useful when a user needs a better layout of the wind map.
- Regression analysis for wind speed at calculated height and surface roughness between satellites and in-situ devices.

Some of these outputs are discussed in this thesis, but not all of them. Examples and interpretations of some of them are explained in chapters 4, 5 and 6.

3.5 User manual

Previous sections in this chapter already explained the software architecture. Basically, the software can be divided in two blocks. The first block is the code for database creation, and the second block is only related to wind resource assessment. Outputs of the software are also included in the second block.

Since the software has not been deployed and the user interface has not designed, future users will need to launch the code from the scripts. This means users are required to have minimum IT skills for its use. As explained, the software was written in *Python*, version 2.7 to be precise. All the work was developed under a *Linux OS* environment, in this case *Ubuntu 14.04 LTS* was chosen. All the instructions are based on the use of the same operating system and can be found in detail in Appendix A.

3.5.1 Software installation

First at all, it is mandatory to install the same database, *MySQL*. This could be done by the use of the *Ubuntu Software Center*. Installing the *MySQL Workbench* may be useful for beginners to database programming. After *MySQL* installation, the password for user "root" will be set initially. It is recommended that the username and host name as given by default, "root" and "localhost" respectively are not changed. Also, the password must not be changed.

Once the database software is installed, some *Python* libraries must be installed. The *Python* version must be the same; if this is not the case it will be necessary to install it. Here is the list of the *Python* packages included in the software; *pandas, numpy, scipy, MySQLdb, netCDF4, xml, gzip, openpyxl, windrose, matplolib* and *basemap*. All these packages are available through *PiPY*, the online repository for *Python*.

One of the packages, *MySQLdb*, is especially important. This is the bridge between *Python* and *MySQL*. By default, the data directory is set to a folder created during installation. It is possible to change the data directory. The change is convenient due to future DB size, thus the operating system and DB can be placed on different hard drives. Setting a new data directory for *MySQL* is not straightforward. It is necessary to edit a few files from the operating system. Further details for software installation are given in the Appendix A; all the steps of this section are included.

3.5.2 User interaction

Once the software is installed, there is no requirement for programming skill with *Python*. However, since there is no user interface, it will be necessary to run *Python* scripts from the command line, as well as a very basic knowledge of *Unix/Linux*. Before running any script, all the database scripts must be kept in the same folder. It is the same case for the wind assessment scripts. Database scripts and wind assessment scripts are completely independent. Thus, it is better to separate both script groups into different folders. All the code is open source and already available through *Github* platform; more information in Appendix A.

Once the command prompt is opened, the directory must be changed to the folder containing the scripts. This is done by simply writing:

cd path/to/the/folder

After, the script can be summoned easily by writing:

python name_of_script.py

There are only two scripts to remember, one for each software block; database creation and wind assessment. Once any of these two scripts are called, the processes will start asking the user to make some choices and/or set some parameters as shown in Figure 3.4.

The script name to be called for starting the database creation is *Insertion_process.py*. On the other hand, the script name to begin the wind assessment is *sat_options.py*. It could be helpful to follow the flowcharts from Figures 3.6 and 3.2 for database creation and wind assessment respectively.

After any of these two scripts are run, the user will only interact with the command line window for making choices and decisions, setting some parameters and inserting the path to specified files. The software has been designed to be easily used from the command line. There is an exception, every time an output, such as a map, graph, or wind rose, is reached, a new window will be displayed. That window is created by the *Python* package *matplotlib*. A few options will appear on the window such as zoom, grid and more important save file as a picture. An example of an output window is shown in Figure 3.5. Furthermore, in Figure 3.4 is shown the example of the software interface for the output represented in Figure 3.5.

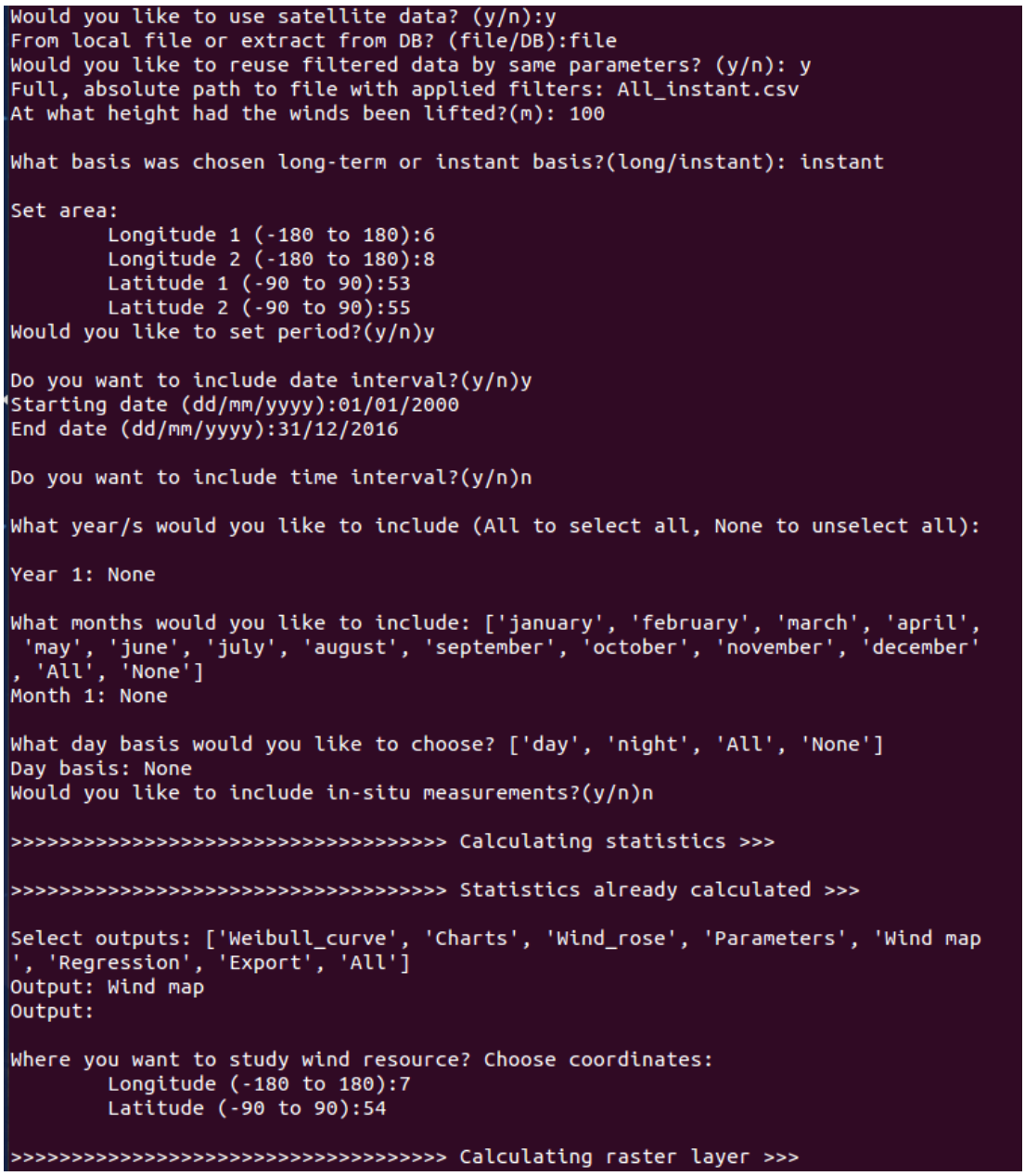

Figure 3.4. Software interface used to achieve the output from Figure 3.5.

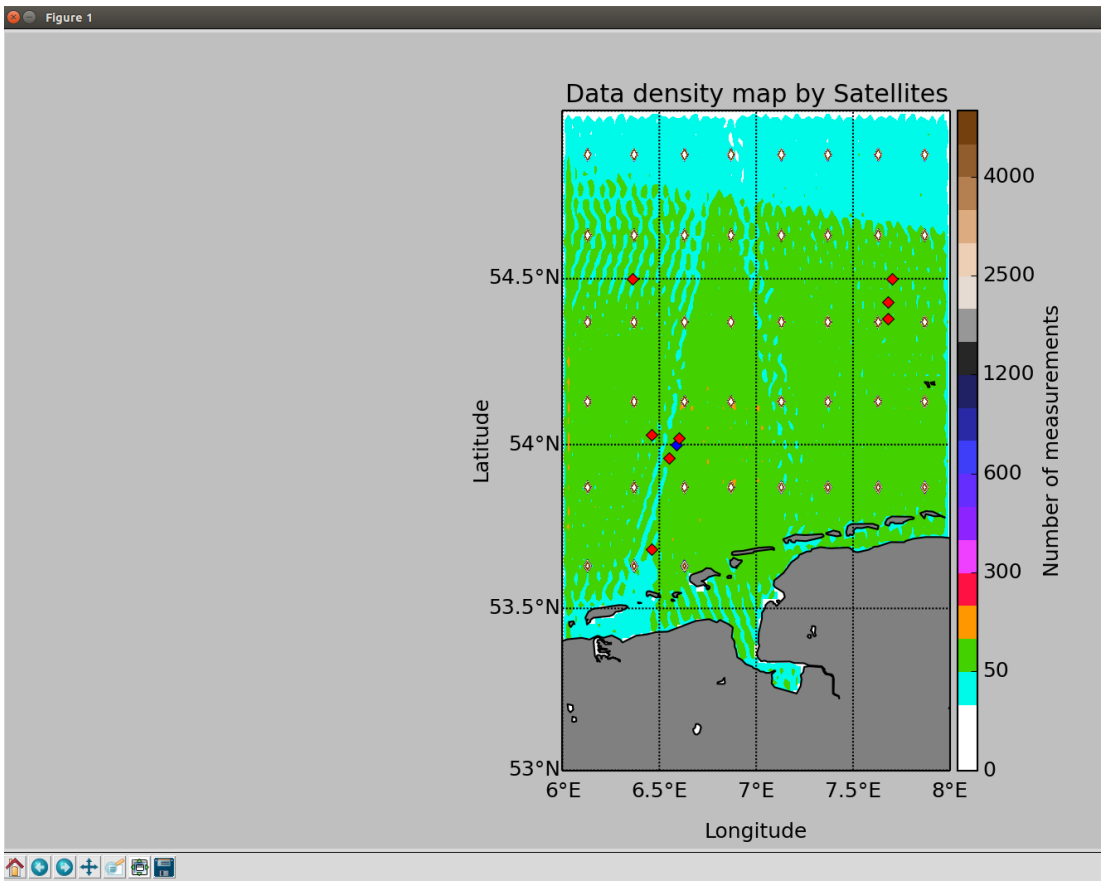

Figure 3.5. Software output window example, in this case for a data density map.

3.5.3 Database creation

Before the database, the first step is to download the satellites datasets. The datahub websites were already shown in section 2.4.1. It is recommended that a full mission of a satellite is downloaded before inserting the data into the database. Datasets can be kept in the same folder or directory tree. After, the datasets can be transformed into a new format, *CSV* files. At this point datasets are ready for insertion into database. Parallel to satellite data transformation, the database with its 1200 tables must be created. Scripts to carry out all of these processes have been created. The whole DB creation process is shown in Figure 3.6.

Although the code was designed to have high performance, some routines are slow. Scripts were written to handle only one satellite mission at time. Thus, the risk of a process being interrupted, and therefore data lost, was reduced. However, an advanced user may try to modify the code to automate the process or to work in parallel. For any user, here are some recommendations when preparing a computer to host the DB:

- Hard drive larger than 3 TB.
- Memory RAM larger than 32 GB.
- Process each satellite mission separately or independently. Satellite datasets can be processed in parallel strings, but insertion into DB must be a single string.
- Build indexes only when all satellite data has been inserted into DB.

3.5.4 Wind assessment

This process is much faster than the database creation. Since the tool was designed to undertake wind assessments for small areas, the amount of data is drastically reduced once the domain under study is set. In fact, the extracted file from database could be shared with or sent to other computer where the wind assessment would take place. There is no need for special hardware requirements for the second computer or laptop. In this case, it is not necessary to install the *MySQL* database since no database would be required.

All processes required to run a wind assessment have already been well explained in section 3.3.

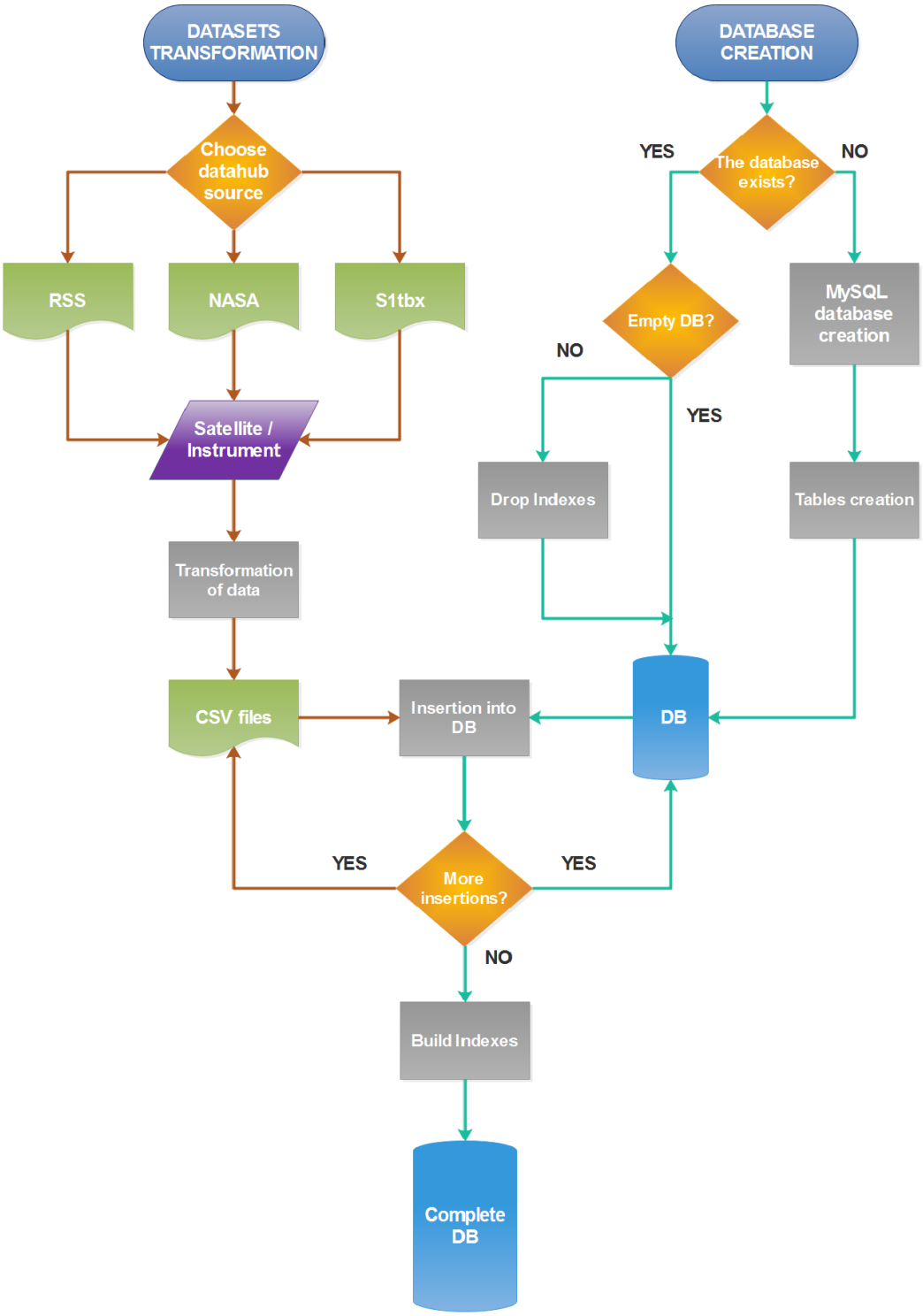

Figure 3.6. Full process for the creation of the database. Brown lines represent satellite data; green lines represent database management.

3.6 Summary

The tool was designed to handle an extremely large amount of data although, in this study, only some satellite missions were fully or partially included. In all steps, from insertion into the DB, exporting from the DB and the whole process of data analysis, the possibility of working with large datasets or Big Data was considered. Therefore, computational speed was measured and processes were enhanced to increase speed. This was one of the reasons *Python* was chosen as the programming language since nowadays the majority of Big Data applications are written in *Python.* The other reason was the possibility of making the code freely available as open source software.

The method used to avoid data spreading was developed to prevent taking into account an unrealistic number of measurements and keep a high resolution. However, a significant assumption has been made due to the measured wind speed of microwave remote sensors being biased towards that located in the centre of the measured area. Because of this the wind speed measured by these microwave remote sensors over the area of a pixel is biased toward the real wind speed at the centre of each pixel. This assumption is a source of inaccuracy that must be remembered in the analysis.

The best summary of the whole data analysis process is the Fig. 3.2. There are two parallel processes, one for in situ data and the other for satellite data. As shown, both processes are completely independent with one exception, when models including air-sea interaction are selected. Furthermore, the tool allows a comparison between results from the ground and remote sensors. This is a critical and necessary function to validate not only the tool but also satellite measurements and vertical extrapolation methods.

As explained in section 1.2, the code has been published along with some material of the present chapter. More information and the link to the code were included in Appendix A.

4. Satellite-enabled wind resource optimisation analysis

4.1 Introduction

Usually, an offshore measurement campaign is conducted by meteorological masts located near the coast. However, the cost of an offshore met mast can exponentially increase with deeper waters, [90]. In order to reduce costs, the wind industry is introducing remote sensing instruments in measurement campaigns such as Sonic Detection and Ranging (SODAR), Light Detection and Ranging (LIDAR) and satellites, [91]. Satellite data are relatively new in wind engineering, but it is not in wind monitoring. In 1987, a satellite with an onboard passive, microwave sensor was launched to deliver continuous ocean wind speed time series, the Special Sensor Microwave/Imager (SSM/I). Since then many studies have been reported where satellite data was used in wind resource estimation, [17, 23-28]. Recently, another study [34] explained how wind resource assessment could be carried out by the combination of different satellite remote sensing instruments. Five types of instrument can measure ocean surface winds from satellites; the microwave radiometer, altimeter, scatterometer, Synthetic Aperture Radar (SAR) and Global Navigation Satellite System Reflection (GNSS-R) receivers.

Satellite measurements are not as accurate as on-site instruments such as meteorological masts, LIDAR or SODAR, therefore, every wind resource assessment by satellites should be accompanied by an accuracy study. In many of the published articles in this field, researchers have noticed the difficulties of carrying out a wind assessment using satellites. Sensitivity studies for those difficulties have been undertaken, [62, 73]. Difficulties were found, such as the time between measurements, data density, diurnal and seasonal variations, truncation of wind speed measurements due to the limitations of measurement instruments, criteria in image processing, calibration of wind retrievals, vertical extrapolation of winds and merging wind retrievals from different satellites. There are also some studies [25, 62, 73, and 74] where it was intended to determine the minimum number of images required to carry out a wind assessment with sufficient accuracy in order to resolve the low data density problem. However, there is still no consensus among researchers regarding the required minimum data density.

Other problems of remote sensing are related to phenomena in the Marine Atmospheric Boundary Layer such as internal boundary layers, thermal internal boundary layers, atmospheric stability, convective cell, roll vortices, lee phenomena, gap flows, barrier jets and rain cells. Also, some Oceanic influences such as surface waves, internal waves, currents, bathymetry and surface slicks may create distortion on the backscattered signal that leads to an underestimate or overestimate of the wind speed. On the other hand, satellite remote sensing presents a significant advantage in being able to take multiple measurements over large areas of the world's oceans every day.

The aim of this chapter is a study of the application of satellite remote sensing for the wind industry at the wind resource assessment stage. The study will also investigate satellite capabilities and methodologies and test these according to wind industry requirements thereby highlighting their strong and weak points and allow suggestions for future studies. A combination of many different satellite data could improve the accuracy and coverage of wind maps and wind resource assessment by satellites. To test this capability the creation of wind maps using satellite data, not only for large areas but also for small areas such as an offshore wind farm, was undertaken. At the small, wind farm, scale a resolution of 1 or 2 km is desirable to see possible wake effects and to cover coastal areas. A secondary capability, to undertake a basic wind resource assessment at a specific point of the area under study and carry out a posterior comparison with ground-based measurements, was also carried out in order to validate the tool. A comparison with an offshore met mast was undertaken for the area located north of the river mouth of Ems (on the border between Germany and the Netherlands) and the results are presented.

4.2 Materials and Methods

4.2.1 Fino-1 data processing

The selected in situ device to check accuracy for satellite measurements and post-processing was the Fino-1 platform located 45 km offshore of Borkum, Germany (6.59°E, 54°N) as shown in Fig. 4.1. In 2001, the German government adopted the objective of the construction of research platforms in the North and Baltic Seas. The first platform erected was Fino-1, built and

operated by GL Garrad Hassan Deutschland GmbH. The present platform provides meteorological, technical, biological and oceanographic measurements for the analysis of environmental conditions leading to the exploitation of wind energy, [92]. Fino-1 became operational from the autumn of 2003 until the present and data are available through two different databases; Fino-1 database and the NORSEWIND database. Only the NORSEWIND database was used in this study, [4].

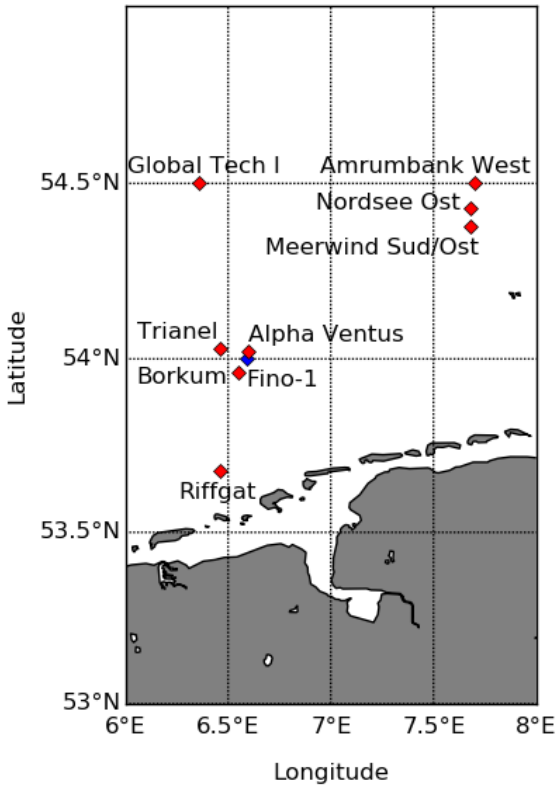

Figure 4.1. Location of Fino-1 (blue point) meteorological mast, and offshore wind farms (red points) with wind turbines already installed by October of 2015 near the river mouth of Ems in the North Sea.

In the present analysis, only wind speed and direction measurements at different heights are considered. The necessity of data at different heights is the reason to use Fino-1 instead of buoys for which wind speed needs to be extrapolated to 10 meters. Many cup and ultrasonic anemometers were mounted on Fino-1 as well as vanes. However, due to device performance over the years, only some of them were included in this analysis. In the present study cup anemometers and vanes at 33 and 90 meters were used.

The data from NORSEWIND covers from January of 2004 until November of 2011. Once data was downloaded this was filtered according to two conditions. First, valid data must be from the highest processing level in order to use already corrected measurements. Second, data was only considered when there were valid data at 33 and 90 meters simultaneously, since measurements at two heights were needed to calculate surface roughness. In order to obtain surface roughness, the logarithmic law for neutral stability with two different heights instead of friction velocity was used, see Eq. 2.5. The same equation was used for vertical extrapolation. However, in this chapter, the in situ data was not filter according to the atmospheric stability.

4.2.2 Satellite data processing

In order to work with a range of different satellites, it was important to use inter-calibrated datasets and also to work only with neutral wind speeds. Inter-calibrated datasets have been reprocessed using a consistent methodology to develop their particular GMF's with another satellite as a calibration target, [76, 93, and 94]. For this reason, the Remote Sensing Systems (RSS) data hub was ideal. They have inter-calibrated some missions such as Quikscat, ASCAT, WindSat, SSM/I and TMI. Also, they have processed wind retrievals to achieved neutral wind speeds over the ocean surface. From the RSS data hub, the entire missions of Quikscat, ASCAT and SSM/I were downloaded with all available data until March of 2015.

Actually, there is no SAR inter-calibrated data, therefore, when different missions are merged, this needs to be noted. The applied GMF was CMOD5, as it is implemented in the Sentinel-1 toolbox, which does not retrieve equivalent neutral winds. Due to the use of different GMF's differences or bias can be expected between Sentinel-1 and other devices. Sentinel-1 data is downloaded through the Sentinel Data Hub by ESA. Their datasets are not daily gridded data, as Remote Sensing Systems products are, so it is necessary to calculate neutral winds. All available extra and interferometric wide swath images were downloaded and processed for the area around FINO-1. Thus, wind vector measurements by position were obtained and the dataset gridded. In the end, almost 100 Sentinel-1 images were processed from the beginning of the mission to October of 2015.

Data were filtered according to rain rate, default missing values and satellites and instruments to work with. In this study, only rain-free measurements for SSM/I, Quikscat and ASCAT were selected. In the case of Sentinel-1, there is no rain flag. Although Sentinel-1 can measure winds under all-weather conditions, it is thought that there is some bias under rain conditions. Another important difference between Sentinel-1 and the other satellites is the number of images. One hundred images were taken from Sentinel-1 while a few thousands of images were taken for each of the other missions. Due to rain presence and the limited number of SAR images, a strong bias between Sentinel-1 and the other satellites was expected. Satellite data can have different spatial resolutions. Therefore it was necessary to formulate a method to merge different datasets and avoid data spreading. In section 3.3 there is an explanation of the method.

Like conventional wind resource assessment, it is necessary to calculate wind speeds at hub height since satellite wind retrievals are given at 10 meters over the ocean. Here, it is not possible to follow the same methodology because there is no second measurement to calculate surface roughness and extrapolate. Wind measurements are too low in comparison with traditional met masts where the highest measurement is close to hub height. This fact has pushed researchers to find another method to extrapolate winds. In Badger et al. (2016), a method for extrapolation to hub height was proposed, [95]. Basically, the logarithmic law for neutral stability was applied but keeping friction velocity, see Eq. 2.5, and Charnock's equation, Eq. 2.9. The Charnock's parameter, α_c, was considered 0.0144 in the long term. Since the algorithm applied represents the neutral wind speed, Ψ_s is neglected and U_z is the satellite wind speed and z is 10 meters. Then it becomes a system of two equations with two unknowns. The friction velocity and surface roughness can be calculated by iteration. Once surface roughness and friction velocity are known, z can be switched to 100 meters, or any desired height, in order to calculate wind speed. The simplest way to extrapolate winds, and the one used in the present study, is to always assume neutral stability and so the atmospheric stability correction is neglected. However, this is not realistic since the atmosphere can be unstable, stable or neutral. The way to apply stability correction on a long-term basis is also described by Badger et al. (2016) [95], where it is necessary to know heat fluxes and temperatures.

At this point, there are two possibilities; long-term basis or short-term basis. The first one, the long-term method, calculates the average, neutral wind speed at 10 meters for each square of the grid and afterward the vertical extrapolation is applied. The second one, the short-term method, applies the vertical wind extrapolation for every single measurement and afterward the average wind speed is calculated at 100 m. In this study, both long and short methods are applied and compared using different parameters such as wind speed, surface roughness length, standard deviation, Weibull parameters.

In order to compare the results with in-situ measurements, Fino-1 data is also included in the grid according to its location. However, due to the limited amount of data from Sentinel-1, Fino-1 is only compared with the nearest HDDC, which is located at 6.63°E, 54.13°N.

Before comparing in situ and satellite data, data is selected only when the time stamp coincides. Then wind speed and wind direction averages are calculated for Fino-1 over a period of 50 minutes. Since satellites retrieve the mean wind vector over an area, it is more representative to make a comparison with average, in situ measurements over a period of time than with instantaneous measurements. There is the exception of SAR's due to their high resolution. However, Sentinel-1 is not compared with Fino-1 in this study.

All satellite missions were processed separately for both short and long methods. The results were compared to in situ observations. The same process was undertaken for all satellite data merged together.

4.2.3 Methodology for wind resource parameters

Conventional wind resource assessment is undertaken with large datasets from meteorological masts, LIDAR's or SODAR's with wind measurements every ten minutes for various years of observation. With a large amount of data, it is possible to realize a confident assessment by directional sectors. This is not the case with satellite wind resource assessments. Even when different missions were merged there was not enough data due to the various filters applied and posterior matching between Fino-1 and satellite data. For this reason, in the present study, the assessment was only undertaken for all wind directions at the same time.

Once winds are vertically extrapolated and the wind grid is calculated a wind map can be produced. Weibull parameters and curves are obtained through the mean wind speed and standard deviation. Wind roses are also produced but only on a short-term basis under the assumption that wind direction will remain the same from 10 meters to 100 meters. Wind direction can change with height; possible reasons are effects of surface friction, tidal streams, Coriolis Effect, Ekman spiral, currents or inertial oscillations, [96]. It is not possible to produce wind roses for the long term since there is only one available wind speed value at 100 meters. In order to check accuracy, all parameters were compared and a regression between satellites and Fino-1 was undertaken for both wind speed at 100 meters and surface roughness length.

All data processes, calculations of parameters, wind maps, wind roses and other graphs were made by the use of the designed tool. This tool was explained in detail in chapter 3. It is worth to remember that the tool was an essential part of the research showed in this thesis.

4.3 Results

Two of the main outputs of the tool is the wind map and data density map which is made to show the number of samples involved in the wind map. Excepting a posterior application of a numerical weather prediction model, there is no way to spread wind speed over an area as satellites are capable to measure. Hence, wind maps are only compared with in situ data on the exact point where the met mast is located. Even so, wind maps are compared for the selected satellites. Furthermore, due to the use of density maps, the strong relationship between a number of samples and quality of wind map is shown.

Some previous studies [25, 27, 34 and 73] show the accuracy of satellites for both instant measurements and average wind speeds with very good results for rain-free measurements. However, all of them compare satellite wind speed at 10 meters with offshore masts or buoys. In the present analysis, wind speed data are compared after vertical extrapolation for both, satellite and offshore mast. Weibull parameters, standard deviation and surface roughness length between devices are also compared. Vertical extrapolation

depends on surface roughness and friction velocity calculations due to the extrapolation method used. Therefore, surface roughness is an indicator of accuracy and can be used for validation of the method.

The last comparison is between long and short term. Here, the same parameters are compared. Stability correction was not applied for long-term [95]; however, through the analysis of the standard deviation and Weibull parameters, some conclusions were reached.

4.3.1 Comparison of wind maps

Wind speed maps are the most common output in wind analysis by satellites over the ocean. In all cases, they represent wind speeds at 10 meters over the sea for either average or instant wind speed. Most of them also include the wind direction. In this analysis, all wind maps represent average, extrapolated, winds at 100 meters but wind direction is missing. The wind maps cover a period from January of 2004 to November of 2015.

Because only a small area has been studied poor maps by satellites with low resolution may be expected as shown in Fig. 4.2. Quikscat, ASCAT and SSM/I show similar wind speeds, around 9 m/s, with some differences. The differences are produced by small speed differences for some low resolutions squares. By contrast, the data density maps are very different. For Quikscat there are between 4000-4500 samples, 1500-2000 samples for ASCAT and finally between 2000-2500 samples for SSM/I f13. Unlike the others, ASCAT presents a homogeneous density. The case of Quikscat is similar. However, some points near the coast lost measurements due to coastal disturbance, land-sea pixels masked out of satellite products. The SSM/I density map is completely different. First the gap between coast and measurements is bigger (~25 km or ~0.25°) and second, there is a gradual loss of data toward the coast and west. This map is missing many details on wind speed since the resolution for SSM/I is 0.25°, even so, there is a gradual reduction of samples from 2000-2500 in the open sea to 100-200 images near the shore.

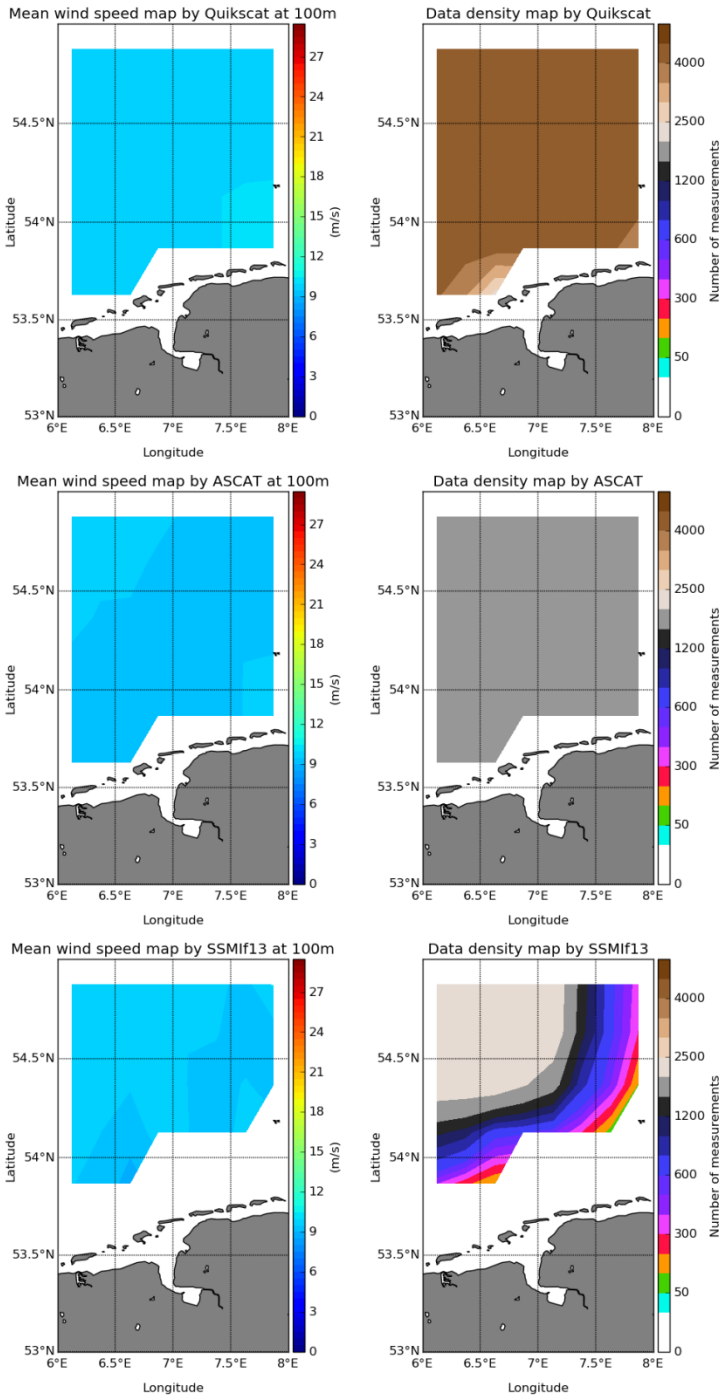

Figure 4.2. Wind maps at 100 meters for Quikscat, ASCAT at 50 km and SSM/I f13 at left and corresponding data density maps to the right. The area represented is the river mouth of Ems.

With the inclusion of SAR data at 2km resolution, the wind map is drastically improved in Fig. 4.3 because of its high resolution and coverage near the coast. The mean wind speed map seems to be divided in two, east and west

of meridian 7°E. Due to the small amount of data, 100 images, the mean wind speed is very sensitive to bias by a few images. This is supported by comparison with the data density map, because it is possible to observe the same patterns on both maps, such as the vertical, straight lines in dark blue. However, it is possible to see the wake effect produced by the islands located in the north of the main land. Furthermore, the wind speed gradient from coast to open seas is represented as could reasonably be expected; low speed near the coast increasing to open waters. There are two anomalies, located at 54.5°N 6.4°E and 54.5°N 7.7°E, these locations match with the position of some offshore wind farms, Global Tech I, Amrumbank West, Nordsee Ost and Meerwind Sud/ Ost. However, the presence of other offshore wind farms, are not observed in the wind map. Comparing the wind maps in Fig. 4.3 to the wind maps in Fig. 4.2, there are wind measurements near the coast due to the higher resolution of SAR; even the wind speed in the river mouth of Ems is measured.

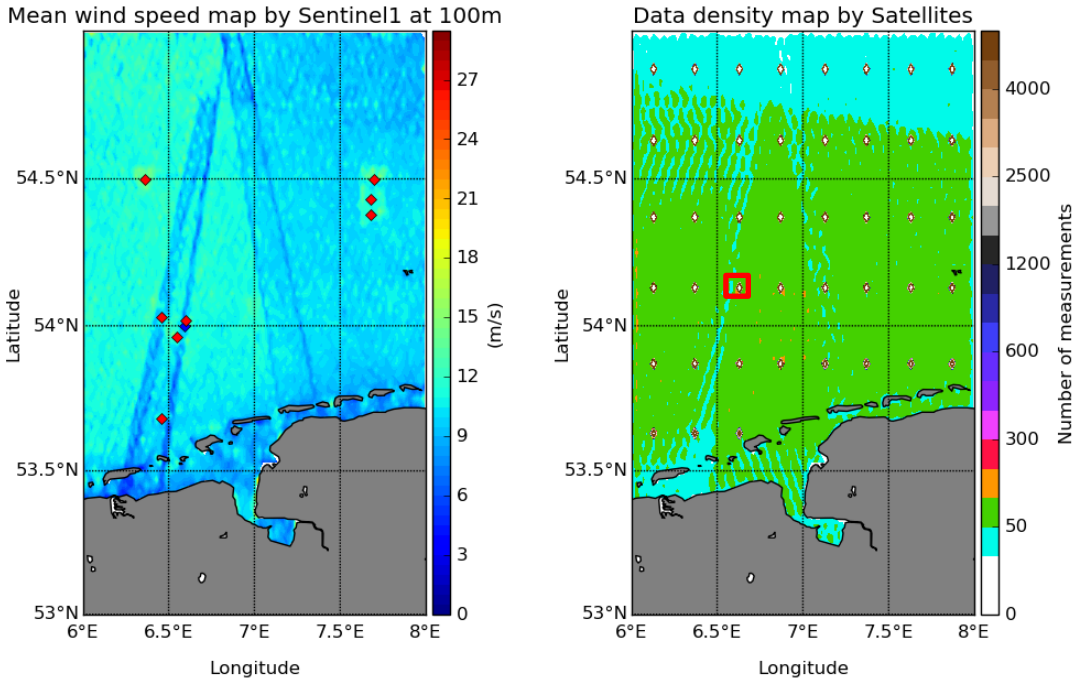

Figure 4.3. Wind maps at 100 meters by satellites on the left. Data density to the right. These maps are the product of a merging between Sentinel-1, Quikscat, ASCAT and SSM/I data. The area represented is the river mouth of Ems. In the wind map, blue point is Fino-1 and red

The data density map of Fig. 4.3 includes red and white rhombuses which are the HDDC points as explained in the methodology. These points, separated by 0.25°, are samples from Quikscat, ASCAT and SSM/I and a few images from Sentinel-1. HDDC's have a white colour because they are out of scale on the map since there are approximately 30,000 samples in each. Even so, there are differences between HDDC's near the coast and west HDDC's and HDDC's located in open seas. The white area inside the HDDC's is smaller or non-existent for those points near the coast than HDDC's in open seas. The rest of the points on the map have between 50-100 images (green area) except near the coast and north (blue areas) where there was between 20-50 images.

4.3.2 Comparison of wind assessment parameters

The chosen HDDC for comparison is the nearest to Fino-1, inside the red square in Fig. 4.3, as explained in methodology. It is located at 54.13°N 6.63°E, approximately 13 km away from the met mast. There was another HDDC as near as the one selected located to the south of Fino-1 but it was discarded due to the absence of enough data overlapping in time.

The results shown in Table 4.1 have Quikscat, ASCAT and SSM/I results included. Sentinel-1 was excluded in the wind resource assessment due to the low number of samples. The results from each satellite were compared with Fino-1 always using the same number of measurements for both and only those measurements were taken with less than one minute difference in time. Differences in low wind speeds were expected since it is a comparison between 10 and 33 meters therefore FINO-1 results are always a bit higher than the satellite data. Due to the wind profile characteristics it is usually expected to have a higher wind speed at greater heights. Here there is no difference between long and short-term data. Unlike data at low height, results at 100 meters should not differ if measurements and methods are precise. However, from the data in Table 4.1 it may be seen that there is a significant bias, always positive in the short term basis and negative for the rest in a long-term basis. These differences are higher for long-term calculations.

	Instrument	$U_{10/33}$ (m/s)	U_{100} (m/s)	Weibull k	Weibull C	σ(m/s)	N
Long term	Quikscat/Fino-1	8.03(-1.35%)	9.65(2.55%)	2.33(3.05%)	10.89(2.54%)	3.68	3787
	ASCAT/Fino-1	7.55(-4.43%)	9.05(-3.72%)	2.09(-6.28%)	10.22(-3.76%)	3.82	1464
	SSMIf13/Fino-1	7.51(-1.83%)	9.00(-4.25%)	1.95(-10.55%)	10.16(-4.33%)	4.05	595
Short term	Quikscat/Fino-1	8.03(-1.35%)	9.70(2.21%)	2.24(1.38%)	10.95(2.24%)	4.61(0.65%)	3787
	ASCAT/Fino-1	7.55(-4.43%)	9.12(0.22%)	2.02(-7.45%)	10.29(0.10%)	4.76(7.20%)	1464
	SSMIf13/Fino-1	7.51(-1.83%)	9.07(1.91%)	1.88(-11.3%)	10.22(1.69%)	5.07(13.45%)	595

Table 4.1. Comparison between Fino-1 30 minutes mean and satellites when there was overlap between measurements. Average wind speeds at a low height ($U_{10/33}$, 10 meters for satellites and 33 meters for Fino-1) and 100 meters (U_{100}), number of samples (N) and standard deviation (σ) are included. Percentages on the table represent the difference with Fino-1 results when overlaps specifically with each satellite. Weibull k and C, and σ are calculated at 10 m for long term, and 100 m for short term.

One interesting parameter is the standard deviation, σ, because Weibull parameters, mainly Weibull K, depend on its value. Here there is a significant difference between long and short-term datasets. In long term, it is not possible to calculate standard deviation at 100 meters because there is only one value at that height and it was therefore calculated at 10 m. For that reason, results were not compared with Fino-1 and the percentage difference is missing in Table 4.1. Unlike long-term, on a short-term basis there is the same number of values at 10 and 100 meters, thus standard deviation difference at 100 meters with Fino-1 was calculated as shown in Table 4.1. The higher the number of measurements, the lower difference in standard deviation with in situ measurements. Looking at Weibull parameters, it was found that scatterometers achieve better accuracy for Weibull K. This parameter shows an obvious correlation with standard deviation differences for short term. On the other hand, Weibull C differences show correlation with hub height wind speed differences for both short and long terms. Short-term results achieved slightly better accuracy for scatterometers but not for SSM/I. However, hub height wind speed and Weibull C are better calculated

when short-term data is applied. Overall, Quikscat is the best satellite for accuracy in both cases, short and long-term.

Another parameter not included in Table 4.1 is wind direction. In order to represent wind direction, it is commonly presented in a wind rose. In Fig. 4.4 Fino-1, Quikscat, and ASCAT wind roses are shown. SSM/I data is missing because there is no wind direction measurement from radiometers. For all roses, the most predominant wind direction was south-west. This was clearer for Fino-1 than for the satellite data. The frequency for each sector was not equal to Fino-1 but, for most of the sectors, was similar for winds above 12 m/s. Unlike Quikscat, ASCAT measured practically the same frequencies. Even so, there was no match between devices for winds below 6 m/s; between 6 and 12 m/s a better match was observed.

Although Weibull parameters were shown in Table 4.1, it is useful to see them graphically expressed through the Weibull distribution equation to calculate wind probabilities by wind speed, as shown in Fig. 4.5. Long and short terms have been separated in order to appreciate and highlight the difference between satellites and the met mast. As observed in Table 4.1, Quikscat is more accurate and draws a similar line to the Fino-1 data. ASCAT and SSM/I draw similar lines; both show higher frequency for winds between 0 and 10 m/s. For all curves in Fig. 4.5 the peak is reached between 14 m/s and 18 m/s. Fino-1 peak reaches similar probability than satellites in long term. In short-term, Fino-1 reached the highest probability with significant difference.

In order to compare short and long terms, Fino-1 data were analysed for both terms independently of satellite measurements, i.e. for more than 300,000 measurements. The result is shown in Fig. 4.6. Basically, they are very similar curves to Weibull curves for Fino-1 which appears in Fig. 4.5. Therefore, the difference between term methods is observed without the possible uncertainty or bias from satellites and also without the necessity of atmospheric stability correction. The difference between them is only caused by the surface roughness calculations. As in Fig. 4.5 the probability between 0 and 12 m/s is higher for short-term and after 12 m/s, long-term presents higher probability.

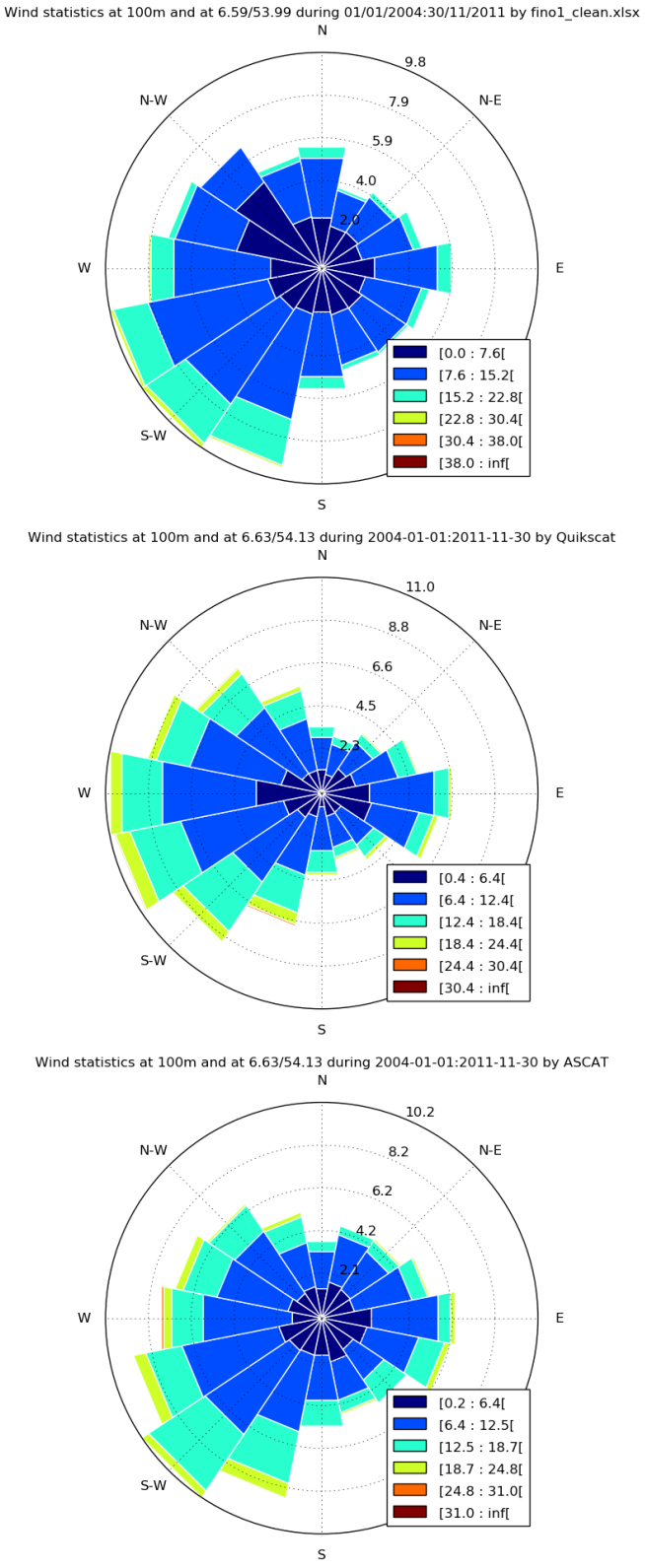

Figure 4.4. Wind roses for Fino-1, Quikscat, and ASCAT at Fino-1 location. Legend of colours represents wind speed (m/s), and each internal circumference represents the frequency of winds (%).

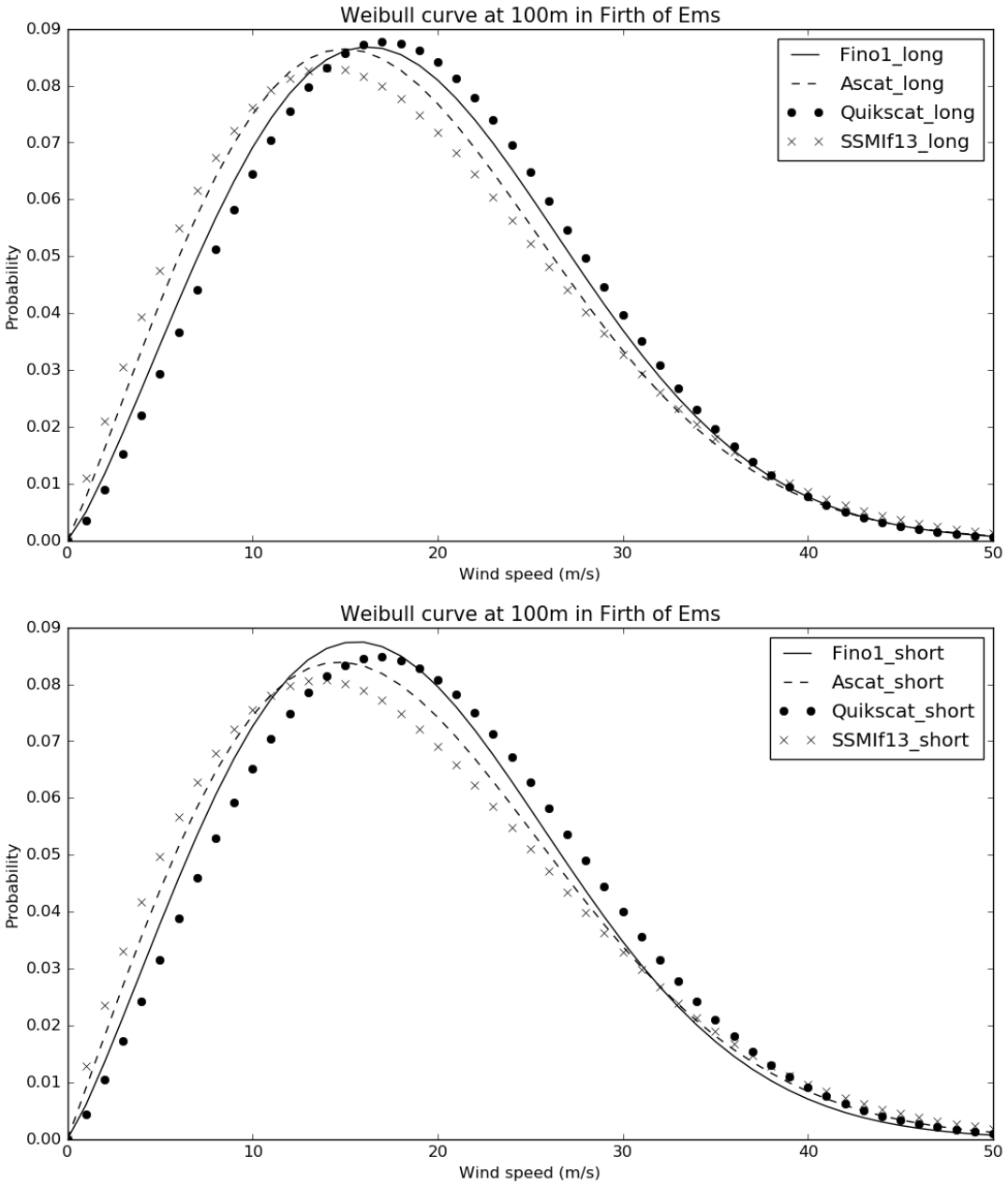

Figure 4.5. Weibull curves for Fino-1, Quikscat, ASCAT and SSM/I f13 by long and short basis, right and left respectively.

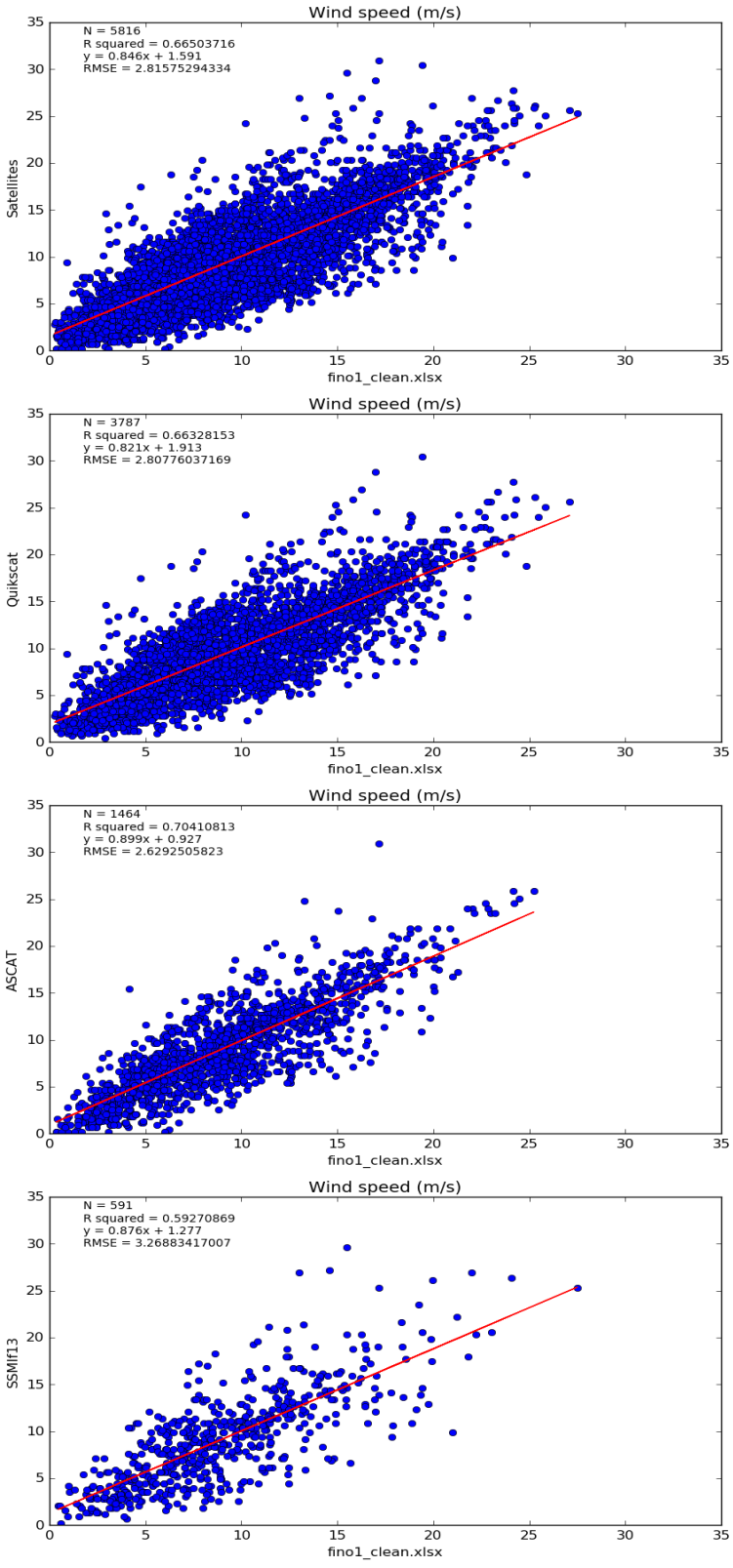

Figure 4.6. Regression graphs for wind speeds at 100 meters on a short-term basis. Satellites calculations are compared with Fino-1 calculations. It is included N as a number of measurements, R^2, the equation of trending line and RMSE.

4.3.3 Comparison of regression graphs

In order to know if satellites are being accurate enough it is necessary to compare not only averages but also instant measurements. Hence, wind measurements and surface roughness are studied. Since there are some previous studies comparing different satellites with buoys or met masts at sea level in this thesis wind speeds at 100 meters were compared. It must be highlighted that the accuracy of measurements is not only related to instrument performance and signal processing for satellites but it is also dependent on the vertical extrapolation method. For this reason, the effect of surface roughness is also studied the accuracy of which is an indicator of the precision of the vertical extrapolation method.

For long term, it is not possible to undertake a regression analysis since extrapolated wind speed and surface roughness are a single, averaged value. Regression analysis has been done for satellites as a group and separately as shown in Fig. 4.7. Furthermore, a trend line has been drawn and some parameters have been calculated such as R^2, Root Mean Square Error (*RMSE*) and the equation for the trend line. Wind speed regression shows a very low correlation in all cases where R^2 is around 0.65. Here a value of 0.9 should be reached in order to conclude that there is good precision in the measurement. RMSE is also very high with values around 3 m/s. This represents a large uncertainty in energy production by wind farms. Apparently, regressions are better for Quikscat and ASCAT than SSM/I according to results on Fig. 4.7. Satellites as a group achieved practically the same results as Quikscat itself. ASCAT achieved the lowest RMSE, the highest R^2 and also the highest slope of the trending line.

That trend is also observed in Fig. 4.8 where surface roughness regressions are shown. In this case, the regression shows a very low level of correlation. The trend line has a negative slope in all cases excepting SSMI when the ideal slope should have a value of one. Also, R^2 has values under 0.1 in all graphs, and RMSE is around 0.5, which is a significant uncertainty since surface roughness values usually lie in the range between $2x10^{-2}$ and $3x10^{-4}$ m, only in case of a storm or extreme weather conditions is this value exceeded in offshore locations. Satellite surface roughness calculations are always between 0 and 0.02 m. However, meteorological mast calculations are higher

around 20% to 30% of the time. Despite this, Weibull curves were surprisingly accurate as shown in Fig. 4.5 and 4.6.

In all surface roughness regressions, there was an accumulation of points near the 0 value for Fino-1 values. A big proportion of points were located in this area. If points above 0.002 meters for Fino-1 were removed, it is possible to find a correlation. Under this possibility, a new regression with logarithmic scale was calculated as shown in Fig. 4.8. Again there was an accumulation of points around low magnitude values. The last regression was showing that the method to calculate aerodynamic surface roughness length was only agreeing with the meteorological mast when z_0 is very low.

4.4 Discussion

The capability of satellites to measure ocean winds has been well documented and studied but using satellite datasets for wind industry applications is still requiring further study. In the case of offshore wind farms, there is one main challenge; the extrapolation of wind speeds from sea level to hub height in order to know wind probability distribution at different heights. Once the distribution is known, a wind farm can be designed and the expected energy production calculated. This wind distribution depends on Weibull parameters and average wind speed at hub height. However, during the design of a wind farm, other wind parameters are required such as extreme wind speed distribution, return period, standard deviation and turbulence intensity at hub height. These parameters are used to select the optimal wind turbine for the area under study. Therefore, a complete wind resource assessment by satellites must include all of these parameters.

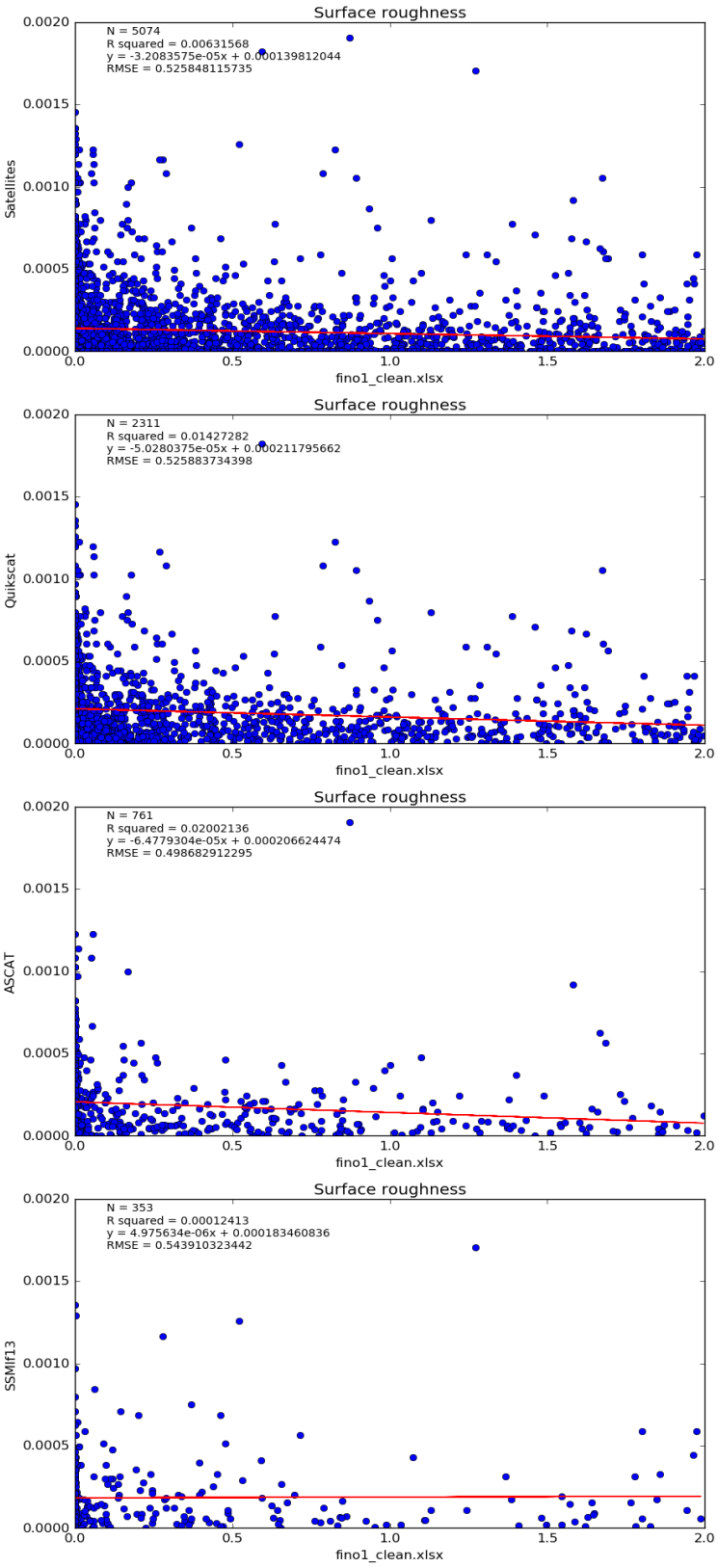

Figure 4.7. Regression graphs for surface roughness length (m) in short-term basis. Satellites calculations are compared with Fino-1 calculations. It is included N as a number of measurements, R^2, the equation of trending line and RMSE.

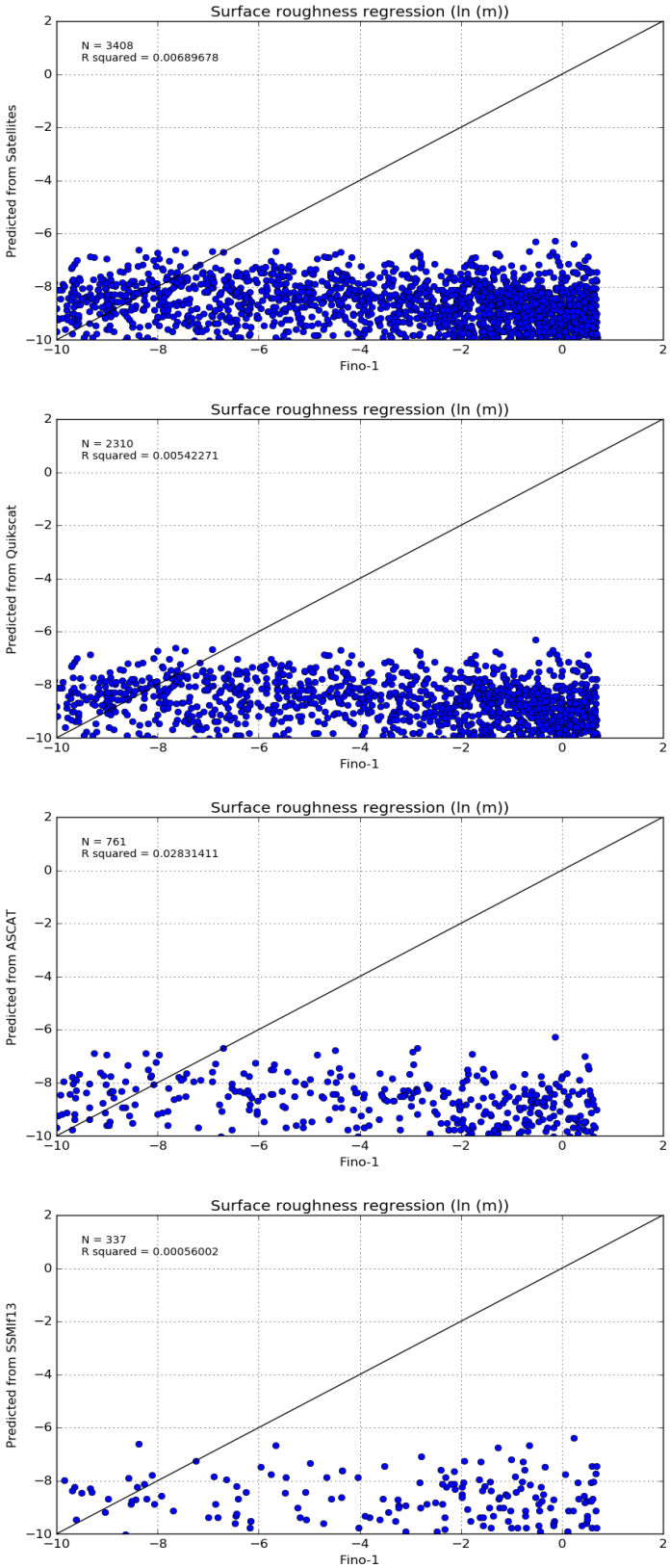

Figure 4.8. Regression graphs for surface roughness length (m) in short-term basis with logarithmic scale. Satellites calculations are compared with Fino-1 calculations.

Another challenge for the application of satellites into the wind industry is the use of wind maps to locate wind turbines in their proper positions according to wind conditions. This process is called micro-siting. It is always necessary to calculate wind conditions over an area to find the best positions and also to avoid wake effects from other wind turbines. In order to spread wind conditions measured at one point to an area, computational fluid dynamics is commonly used. This can be a slow process depending on the model applied. Since satellites can produce wind maps, these have been studied to check their capability for micro-siting but also to study the wake effect.

The present study is not a complete wind assessment as only Weibull parameters, average wind speed and standard deviation were calculated and compared with in situ measurements. Following the hypothesis that increasing the amount of satellite data would improve the quality of wind parameters and wind maps, datasets from several different satellites were combined. The first problem found was the availability of overlapping measurements. In order to validate satellite measurements with consistency, only data overlapping in time between satellites and Fino-1 was used. This fact reduced drastically the number of samples. Even so, because many satellites were included, 5816 overlaps in total were found. In order to corroborate the hypothesis three points are discussed, wind maps, the comparison between satellites and Fino-1, and finally, the comparison between long and short-term datasets.

Wind maps from Fig. 4.2 and 4.3 showed the big difference between low and high-resolution datasets. Obviously, only SAR's are able to draw a map with precision in coastal areas according to wind industry requirements where the optimal is between 0.5 and 1 km. The presence of a shore nearby produces loses of measurements by scatterometers and radiometers as observed in Fig. 4.2. This fact was already found [34] where the Envisat ASAR satellite was used instead of Sentinel-1; with more samples, but wind maps covered big areas such as the North and Baltic Seas. As commented, the problem of SAR's is the lack of inter-calibration and error model. Another problem for SAR's is the shortage of data, in comparison with scatterometers and radiometers, covering open seas since they use to be designed to study the shore or inland locations. In order to use a wind map for wind farm design

more SAR data will be required which presents the highest resolution and so produce maps without data density influence as was observed in Fig. 4.3. This SAR data can come from Envisat ASAR, PALSAR, Radarsat-2 or some other SAR's. Another point to highlight is the presence of HDDC's. These points are the centre of the area of representativeness for low-resolution products. However, it does not necessarily mean that wind speeds at that point are exactly what is measured by satellites since a satellite measurement represents the average of an area. Nevertheless, HDDC data could be used in computational fluid dynamics to spread winds measurements over the area and perhaps achieve better resolution maps, [97].

When differences between satellites and Fino-1 are shown as a percentage or Weibull curve, these do not seem to be relevant, but when regressions are plotted differences are easily observed. This is obvious for regression graphs, mainly surface roughness, but important discrepancies were also found between satellites and between satellites and Fino-1. Thus, Quikscat with more samples than ASCAT and SSMI achieved the most similar Weibull curves and the best regression in comparison with Fino-1. The reason is the reduction of the statistical error due to the increase in the amount of data. Also due to the same reason the Weibull K was more similar to Fino-1 results. However, ASCAT achieved better wind mean speed at hub height and by extension better Weibull C. This is a fact to remember for future studies in other places to check if it occurs again.

Some other researchers [25, 34, 62, 73, and 74] also studied the bias between satellites and in situ devices, including wind roses, at 10 meters with similar results, or percentage of difference, than the present study, see Table 2.6. Some of these studies tried to determine the minimum number of samples required, but there is no consensus. The percentage difference between 10 and 100 meters can have two origins, first bias between devices and second the methodology to extrapolate the winds from sea level. For a few satellites, such as Quikscat and ASCAT, this bias is well documented. In previous studies [26] the difficulty of wind retrieval by satellites for high winds from 15 m/s and above was explained. This fact is another reason that there may be differences in standard deviation and wind averages. Even so, it would require a sensitivity study to show its relevance to the final results.

Due to the limited amount of satellite data, the wind resource was not analysed by sector. Even so, wind roses can give an approximated idea. ASCAT and Fino-1 presented similar frequencies by sector in general, unlike Quikscat. However, comparing frequencies by sector and wind interval, the results differ significantly. Hence, if wind resource was studied by sectors, it would be expected to find higher differences in wind speed and Weibull parameters between satellites and Fino-1. Wind roses were also calculated with very small differences which are caused by the difference in the periods studied, [34].

There are two parameters with a high influence on the vertical extrapolation methodology; atmospheric stability correction and surface roughness. The first one was not included in this analysis as it was in Badger et al. (2016) [95] where the correction represented an addend of 0.5 m/s. However, their study was based on long-term average wind speed instead of instantaneous measurements or short term. This fact led to finding a close to neutral stability because unstable and stable conditions override each other since stability correction was calculated over a long period. This issue can produce a big difference in some parameters at hub height such as average wind speed, Weibull C, standard deviation, turbulence intensity and extreme winds distribution.

The problem with surface roughness calculation is similar to stability correction because it is based on the long-term i.e. averaged roughness. In onshore wind assessment, it is common to work with averaged wind speeds to calculate surface roughness. This method is realistic onshore, where orography and vegetation are not expected to change significantly and neither is the surface roughness. Nevertheless, in offshore areas, this is no longer true because the surface is in constant movement. Therefore, surface roughness and Charnock's parameter are changing constantly in a time scale of minutes or hours. Furthermore, the methodology to calculate surface roughness cannot be extrapolated to short-term because; using the present methodology, roughness is only dependent on wind speed. Certainly, wind speed produces sea waves but it is not the only phenomena that can produce waves. Hence, the sea state, i.e. waves, should be the variable to take when calculating surface roughness. This fact is also highlighted in some previous studies, [98] and [99]. As occurs with the atmospheric stability correction, an

averaged surface roughness will lead to bias in many wind parameters. This issue is also relevant even if a wind resource assessment is realized with offshore met mast data.

4.5 Summary

As explained in section 4.2, the preparation of data before analysis was essential and one of the main processes. Cleaning and filtering of large datasets were necessary to obtain valid and valuable data. The synergy of different type of datasets was also an issue. An extra complexity was found when data from different kinds of sensors was mixed. In order to do it properly, it was necessary to acquire knowledge the performance of all the sensors included.

Some of the possible outputs of the developed tool have been showed here. Three different tools have been tested in this chapter. Spatial coverage by satellites in the form of wind speed and data density maps was the first. The second tool was the calculation of Weibull parameters which are essential to building a wind climate. The last tool studied was the vertical extrapolation of wind speed. Furthermore, an analysis of wind direction as a comparison between satellites and mast measurements was also undertaken.

This chapter represents the first look at wind resource assessment by satellites. The main objective of this first study was to identify strong and weak points of this technology. It was a test for the developed software. Thus, once the lack of knowledge was known, research was focused on solving two main issues. The first is the vertical extrapolation of wind speed and surface roughness length parameterization. The second is the insertion of atmospheric stability in the vertical extrapolation method.

5. Review of methods for vertical extrapolation of wind speed over the ocean for satellite retrievals

5.1 Introduction

Before an offshore wind farm is designed it is necessary to undertake a wind resource assessment over a target area. The main goals of such assessments are to describe the wind profile and climatology of the location under study. The wind resource campaign can be executed using different instruments. The most common is a meteorological mast with anemometers, vanes, thermometers and hygrometers among other sensors. However, there are more instruments capable of measuring wind vectors, such as LIDARs or SODARs. Also, in recent decades, spaceborne instruments have been proven to be accurate in the measurement of wind speed and direction over the ocean, [17]. Altimeters, radiometers, SAR's, GNSS-R, and especially scatterometers have been analysed successfully by researchers, [26], [27] and [34]. The inclusion of satellite wind data into wind resource assessments by the wind industry has become interesting for offshore wind farm developers. The main advantages are the reduction of costs during wind resource measurement campaigns and the acquisition of data over large parts of the world. Nevertheless, two main challenges must be overcome before the application of satellite wind data becomes acceptable in the wind industry. The first one is building climatology from limited daily data, and the second is wind vertical extrapolation. The second challenge was already addressed in [95], where friction velocity (u_*), the surface roughness (z_0) and atmospheric stability parameterizations were studied. However, that study was undertaken under long-term premises, with constant Charnock parameter and averaged u_* meaning constant z_0. Hence, that study is considered highly idealized.

Over the ocean, the interaction between the air and the sea must be understood in order to study u_*, z_0 and atmospheric stability. Unlike onshore, the complexity of the subject is higher due to the non-static sea surface and dynamics under the sea surface. Both, u_* and z_0, have been studied by many researchers when wind stress and drag coefficient parameterizations were attempted, [100] to [105]. Even so, there is no consensus yet on the best method to calculate the drag coefficient or z_0. Most

authors tried to calculate z_0 through the well-known Charnock's equation. All of them pointed to the difficulty in determining Charnock's parameter and its dependence on wave age (c_p/u_*). In other cases, Charnock's parameter has been related to the neutral wind speed at 10 meters or wave slope (H/L_p). However, all methods included empirical coefficients making the equations dependent on the datasets being used. Previous methods worked well under certain wave age conditions, as stated by the authors [106, 107, and 108]. One cause is the presence of swell or conditions where the sea is swell-dominated since the wind speed is low. Another cause is the presence of young waves which appear when the fetch or duration of wind are not long enough to develop completely under certain wind speed conditions [109]. On the other hand, when the sea is fully developed and wind dominated over deep seas, different authors found their best results [106 and 107].

The second variable included in the logarithmic law is u_*. In this thesis, different methods for calculating u_* are also compared. Unlike z_0, u_* can be calculated from direct measurements if horizontal and vertical wind speeds are known from in situ measurements. In their absence some authors suggest other methods for calculating u_*; wind speed dependent, [110], or wave parameters dependent, [111] and [112]. Nevertheless, these methods also rely on empirical coefficients in the same way as the z_0 calculation methods.

The aim of this chapter is to analyse and compare the different methodologies for friction velocity and surface roughness calculations which are necessary for the extrapolation of sea level satellite data to hub height. Due to a lack of consensus on z_0 parameterization between researchers, it is necessary to make a comparison of the methods under different sea and wind conditions. Usually, studies are compared with measurements from instruments mounted on buoys for validation. However, in this study offshore meteorological mast data is used since the accurate modeling of the wind profile is the ultimate goal. For the comparison, the meteorological mast located at Egmond aan Zee was used.

5.2 Material and methods

In this study satellite data and in situ data were used, descriptions of datasets are explained in the following sections. Both datasets were filtered separately

and non-measurable wind and wave parameters were calculated for in situ data. Once filtering was done, only overlapping measurements were taken. Afterwards, u_* and z_0 were calculated for all different methods. The first regressions and tests between methods were u_* and z_0 regressions against in situ values. Finally, satellite wind retrievals were vertically extrapolated following Eq. 2.4. More regressions for extrapolated winds were then undertaken. The last results were the same regressions but under different wave age, wave height and wind speed intervals.

5.2.1 Satellite data

Between the different spaceborne instruments, capable of measuring winds, the wind scatterometers Quikscat and ASCAT were chosen. Scatterometers are an active, monostatic, instrument mounted on a moving platform and transmitting pulses of energy to illuminate a section of the Earth's surface. This energy reflects off of the Bragg waves on the surface of the larger scale ocean waves. The reflected energy measured by the scatterometer is translated, using a Geophysical Model Function (GMF), with 10 m wind speeds and wind direction assuming neutral atmospheric stability, [113]. The monostatic scatterometer does not provide information about the wind direction. A special type of scatterometer, the windscatterometer, uses multiple beams, which achieve multiple look angles making possible the calculation of the wind direction, [36].

Quikscat was a satellite launched in June of 1999 with the mission of measuring winds near the sea surface. This NASA satellite was operating until November of 2009. Quikscat was the third Ku-band windscatterometer, working at 14 GHz, from the NASA SeaWinds instrument series. Its GMF for Ku-band has been improved over the years as discussed by [114]. However, the data from Quikscat still presents two main difficulties; contamination of the measured data by the presence of rain and validation of wind data at speeds in excess of 15 m/s. Quikscat delivered wind speed and direction at 10 meters over the sea for ten years. In order to solve rain contamination, Remote Sensing Systems (RSS) added a rain flag to Quikscat measurement data by using radiometers such as TMI, and SSM/I f13, f14 and f15 on board different satellites. Quikscat has a spatial resolution of 50 km, but samples of 25 km were used in the study as it is delivered by RSS.

The other windscatterometer used in this study, ASCAT, was developed by EUMETSAT. Although ASCAT represents two instruments on board different satellites, MetOp-A and MetOp-B, due to limitations in the availability of data from MetOp-B, only MetOp-A data is used. MetOp-A is a C-band scatterometer working at 5.2 GHz, [115] which makes its data less susceptible to contamination by rain than Ku-band scatterometers at high wind speeds. MetOp-A and MetOp-B were launched in October of 2006 and September of 2012 respectively and both are still operating at the time of writing this thesis. The GMF used to process MetOp-A retrievals is C-2013 GMF [94], with which it is possible to calculate ocean surface wind speed and ocean surface wind direction. Like SSM/I and Quikscat, ASCAT has a spatial resolution of 25 or 50 km, samples of 25 km were used.

5.2.2 Egmond aan Zee meteorological mast

Ground-based, in situ, data came from meteorological masts and LIDARs in the NORSEWIND database, [4]. Among all of the instruments in this database, only two of them included wave height and wave period or length. These parameters are required for some z_0 and u_* methodologies, as explained in sections 2.4 and 2.5. The two possible instruments were the meteorological masts of Fino-1 and Egmond aan Zee. However, the quality of data for sea parameters was too low in the Fino-1 dataset; there are too many gaps between measurements. From this process of elimination Egmond aan Zee was selected to become the validation instrument. This meteorological mast is located 13.7 km offshore of Bergen, Netherlands (4.419°E, 52.606°N) as shown in Fig. 5.1. The mast was installed in November of 2003 by NoordzeeWind and it has been monitoring wind data until the present. In 2006, 36 wind turbines were constructed at the same location and Egmond aan Zee offshore wind farm has been in operation since then.

In this analysis cup anemometers and vanes, located at 21, 70 and 116 meters above the mean sea level were used. Temperatures from sea and air were also taken at -3.8 meters and 21 meters respectively. Egmond aan Zee data from the NORSEWIND database covers a period from May of 2006 until December of 2008. The sea depth at the location of the meteorological mast is 18.5m.

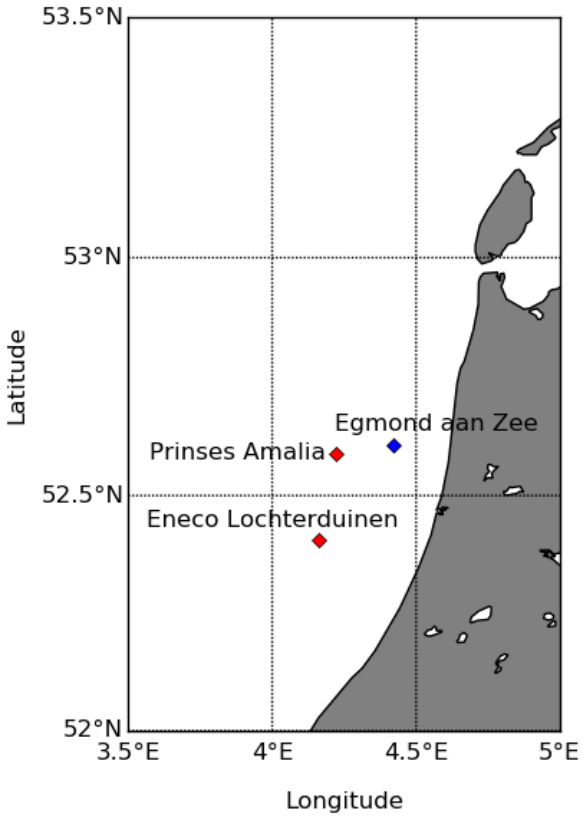

Figure 5.1. Egmond aan Zee meteorological mast location in blue. Red points represent offshore wind farms. Egmond aan Zee offshore wind farm is also located in the blue point.

5.2.3 Data processing

Both, satellite and mast data needed to be filtered in order to avoid device errors and erroneous measurements under certain conditions. Before applying these filters it was necessary to take into account how to mix two datasets created by different instruments. The satellite's revisit cycle is about 1-2 days; on the other hand, the mast takes measurements every 10 minutes for wind vectors. Every single measurement by a satellite represents a spatial average at 10 meters, assuming an atmosphere with neutral stability over an area of 25 by 25 km. A parcel of wind at 8 m/s wind speed, roughly the average for Egmond aan Zee, will take 52 minutes to cover this 25 km. Based on this residence time mast measurements, usually, 10-minute average data, must be recalculated to 50 minutes average to allow them to be compared with satellite data.

In situ data were firstly filtered to avoid gaps between measurements, not only for every single sensor but also between sensors. Thus, only simultaneous sensor measurements from all selected sensors were considered valid data. The maximum time gap allowed between sea and wind sensors was 30 minutes. Wavelength (L_p) was calculated for deep water from the wave period (T_p) at the peak of the wave spectrum, gravitational acceleration (g) and depth (d), following the dispersion relationships shown in Eq. 5.1 and 5.2.

$$L_p = \frac{g * {T_p}^2}{2\pi} \qquad (5.1)$$

$$c_p = \frac{L_p}{T_p} \qquad (5.2)$$

The phase speed at the peak of the spectrum (c_p) could be calculated once L_p and T_p were known. Surface roughness length could be calculated from the wind profile measured by the meteorological mast. Since wind speed at different heights, 21 and 116 meters were used here, the logarithmic law for neutral stability was applied, Eq. 2.5.

The last filter for in situ data was the selection of measurements only under neutral conditions. This may be considered to occur when the sea surface and air temperature are roughly the same. A difference between $T_{-3.8m}$ and T_{21m} of less than 1°C was considered to be required for the atmosphere to be near neutral.

Satellite data was also filtered and only rain-free measurements were used in the analysis. Only those wind retrievals within the same time period of Egmond aan Zee mast were included. As expected, at this point there was more data available from the mast than from the satellites. The last filter applied to the data was to select in situ data only when data acquired from the met mast overlapped with satellite data. The application of these filters provided a dataset of concurrent 50 min-averaged mast data and satellite data.

Because satellite wind retrievals only measure the neutral wind speed at 10 meters above sea level a second measurement, at a different height is missing, and Eq. 2.5 is not applicable. To solve this problem the logarithmic law with the inclusion of u_*, as shown in Eq. 2.4, could work for satellite

data. Since only neutral conditions measurements were used in this study, Ψ_s was neglected.

5.2.4 Friction velocity parameterization

In total, six methods to calculate u_* were compared. The first one, for in-situ measurements, is based on a combination of Eq. 2.5 and 2.9. Once z_0 was calculated, u_* was found through the logarithmic law under neutral conditions. This method in combination with in situ data was selected as validation for the rest of the friction velocity methods. The two other methods are a function of wind speed at 10 meters, U_{10}. The first of them, from [110], is **Wu's method** shown in Equations 5.3 and 5.4.

$$C_{d10} = \left(\frac{u_*}{U_{10N}}\right)^2 \qquad (5.3)$$

$$C_{d10} = (0.8 + 0.065U_{10N}) * 10^{-3} \qquad (5.4)$$

Where C_{d10} is the drag coefficient, also called wind-stress coefficient, acting on the sea surface and U_{10N} is the neutral wind speed at 10 meters over the sea. By combining Eq. 5.3 and 5.4, u_* becomes a function of U_{10N}. This calculation method is acceptable as only neutral winds are considered in this paper. Another U_{10N} dependent method was suggested in [116] and uses Eq. 5.3 and 5.5 to 5.8; this is **Hersbach's method**. Unlike Wu's method, this one is also a function of Charnock's parameter (α_c) and the kinematic viscosity of the air (ν).

$$C_{d10} = \left(\frac{\kappa}{b_n}\right)^2 \qquad (5.5)$$

$$b_n = [(b_\nu)^{-12} + (b_\alpha)^{-12}]^{1/-12} \qquad (5.6)$$

$$b_\nu = -1.47 + 0.93 \log\left(\frac{z}{0.11\nu}(\kappa U_{10N})\right) \qquad (5.7)$$

$$b_\alpha = 2.65 - 1.44 \log\left(\frac{\alpha_c}{gz}(\kappa U_{10N})^2\right) - 0.015\left[\log\left(\frac{\alpha_c}{gz}(\kappa U_{10N})^2\right)\right]^2 \qquad (5.8)$$

In this study, both ν and α_c were considered to have constant values of $1.5*10^{-5}$ m^2s^{-1} and 0.018 respectively, [116]. It should be noted that the Wu and Hersbach methods require the inclusion of empirical coefficients in their equations. The friction velocity can also be calculated based on sea

parameters as published in [111] and [112]. **Maat's method** is dependent on the significant wave height (H_s) and phase speed, as shown in Eq. 5.9. On the other hand, **Toba's method** is a function of significant wave height and wave period Eq. 5.10.

$$u_* = \frac{g^2 * H_s^2}{B^2 * c_p^3} \qquad (5.9)$$

$$u_* = \frac{H_s^2}{B_T^2 g T_p^3} \qquad (5.10)$$

Where B and B_T are empirical coefficients, 1.04 and 0.602 respectively. The last method includes Charnock's equation, Eq. 2.9 or Eq. 5.11.a, and the logarithmic law without atmospheric stability correction as shown in Eq. 2.5 and Eq. 5.11.b. With both, Eq. 5.11.a and 5.11.b, friction velocity and surface roughness can be solved by iteration as long as Charnock's parameter, α_c, is known. This last method creates different possibilities for the calculation of the friction velocity. A constant α_c may be set as was done for the **Iteration method** with α_c=0.0144. Alternatively, α_c may be calculated by other methods as explained in section 5.2.5.

$$z_0 = \alpha_c \frac{u_*^2}{g} \qquad (5.11.a)$$

$$U(z) = \frac{u_*}{k}\left[\ln\left(\frac{z}{z_0}\right)\right] \qquad (5.11.b)$$

5.2.5 Surface roughness length parameterization

There are many different methodologies in the literature for the calculation z_0. These can be divided into four different categories according to their dependency: wave age, wind speed, wave slope and iterated methods. These are discussed in detail later in this section. All of them were combined with each u_* method and used for vertical extrapolation of wind speed in this study. Most of the methods used to determine z_0 are an expression to calculate α and solve for z_0 through the use of Eq. 2.9. However, u_* must be known a priori. Hence, z_0 methods need to be combined with u_* methods with a few exceptions.

5.2.5.1 Wave age expressions

The first two methods for calculating α_c are from [100] and [117] and are fundamentally the same. The only difference between the two is their empirical coefficients. This is due to the use of different datasets in their research. Eq. 5.12 is for **Smith's expression** and Eq. 5.13 is **Toba's expression**.

$$\alpha_c = 0.48\left(u_*/c_p\right) \qquad (5.12)$$

$$\alpha_c = 0.025\left(u_*/c_p\right) \qquad (5.13)$$

Another straightforward method is suggested in [106]. Since this is not the only expression suggested in the same publication, this method is named the **"Edson Age" method** and is shown in Eq. 5.14. Unlike the two previous expressions for α_c, here there are two empirical coefficients.

$$\alpha_c = 0.114\left(\frac{u_*}{c_p}\right)^{0.622} \qquad (5.14)$$

The final method was suggested in [107]. As with previous wave age equations, α_c is a function of the inverse wave age. However, their expression is more complex and uses more empirical coefficients than the previous models as shown in Eq. 5.15. Furthermore, in their study, they calculated the inverse of wave age as a function of U_{10} and fetch (χ), Eq. 5.16. This expression sets the relationship between wave age and wind. Consequently, Eq. 5.16 was only expected to be accurate under fully developed, wind generated, waves over the deep sea without the presence of swell.

$$\alpha_c = 1.89\left(\frac{u_*}{c_p}\right)^{1.59}\left[1.0 + 47.165\left(\frac{u_*}{c_p}\right)^{2.59} + 11.791\left(\frac{u_*}{c_p}\right)^{4.59}\right]^{-1} \qquad (5.15)$$

$$\left(\frac{u_*}{c_p}\right) = \frac{3.5}{2\pi}\left(\frac{U_{10}^2}{\chi g}\right)^{\frac{1}{3}} \qquad (5.16)$$

Two methods were developed from Eq. 5.15 and 5.16. The first, called **"DTU Age" method**, calculates α_c from the wave age as in previous methods described in this section. For the second, known as the **Fetch method**, Eq. 5.16 is combined with Eq. 5.15. To employ this method the distance to shore was measured for each 10° sector of the Egmond aan Zee mast location. Then fetch was calculated depending on the wind direction.

5.2.5.2 Wind speed expressions

Two methods are included in this section, Eq. 5.11 and 5.17. If U_{10} and u_* are known, z_0 can be solved with the logarithmic law shown in Equations 5.11.a and 5.11.b; this method was called **"Log law" method**. U_{10} was taken from satellite retrievals, and u_* calculated according to the selected u_* method explained in section 5.2.4. The second wind speed dependent method was proposed in [106] and is called the **"Edson Speed" method**. Empirical coefficients are included as shown in Eq. 5.17.

$$\alpha_c = 0.017U_{10N} - 0.005 \qquad (5.17)$$

5.2.5.3 Wave slope expressions

The first wave slope equation was also suggested in [106], Eq. 5.18. This equation includes a numerical constant and a non-empirical coefficient, unlike previous expressions. Again, Charnock's parameter is calculated by the method called **"Edson Wave" method**.

$$\alpha_c = 0.09H_s\left(\frac{2\pi}{L_p}\right) \qquad (5.18)$$

Another expression was proposed in [108]. Unlike other methods, with Eq. 5.19, surface roughness was calculated directly and Charnock's equation, Eq. 2.9, was not necessary. Even so, this **Taylor method** still includes empirical coefficients.

$$\frac{z_0}{H_s} = 1200\left(H_s/L_p\right)^{4.5} \qquad (5.19)$$

5.2.5.4 Iterative methods

All iterations are based on the combination of Eq. 2.9 and 5.11. Using satellite data U_{10N} is known and, if Charnock's parameter is known, u^* and z_0 may be solved by iteration. The different methods are related to the different methods used to calculate α_c. As explained in section 5.2.4, the first method was to set α_c=0.014 and is named **"Iteration"**. A second method, named "Fetch iteration", is where α_c is calculated according to the fetch by Eq. 5.15 and 5.16. Another is the **"Edson speed iter"** method where α was calculated according to Eq. 5.17. The **"Wave iter"** method was the last set of equations iteratively solved where α_c relies on Eq. 5.18. The last method included in this

section is the **"Taylor iter"**. However, it was not necessary to calculate z_0 by iteration since this could be solved using Eq. 5.19. Thus, in this case, Eq. 5.11 was only used to calculate u_*. All methods that were dependent on u_* to calculate Charnock's parameter, α_c, were excluded.

5.2.6 Wave age, Wave height, and Wind speed analysis

Once z_0 was known this was combined with each u_* method and so the wind speed at 10 meters could be extrapolated to hub height, at 116 meters in this study, by Eq. 5.11. In order to validate the methodologies the extrapolated wind speed was compared with real measurements. The target height of 116 meters was the highest anemometer on the Egmond aan Zee mast. A different target height could have been selected but, in such a case, the wind speed from meteorological mast would have also needed to have been extrapolated which would have incorporated more uncertainties. Linear regressions for wind speed at 116 meters were the choice for validation and comparison between methodologies.

The next step was to analyse each regression under certain conditions. According to many authors in the literature, their methods have wave age limitations. Hence, three different sea conditions were studied; calm sea ($c_p/u_*<5$), growing sea ($5\leq c_p/u_*\leq 32$) and decaying sea ($c_p/u_*>32$). Since wave slope was also included in two methods, wave height H_s effects were also studied. In this case, the following H_s intervals were selected; $H_s<1$ m, 1 m$\leq H_s<2$ m, 2 m$\leq H_s<3$ m, $H_s>3$ m. The effects of wind speed were also analysed. The reason was the relative inaccuracy of satellite devices to measure low wind speeds (<5 m/s) and high wind speeds (>15 m/s). Intervals for wind speed were the following: $U_{116}<5$ m/s, 5 m/s$\leq U_{116}\leq 15$ m/s and $U_{116}>15$ m/s.

5.2.6.1 Wave age against fetch

In previous research, for example [107] and [118], the aerodynamic surface roughness length is obtained through expressions which include the fetch. An example has been shown in Eq. 5.16. If z_0 depends on the sea state, then the generation of waves must be an important process for z_0 determination. Fetch, understood as the length of water over which the wind has blown, should have an important role. However, fetch it is not the only important

parameter in the generation of waves. Even if swell is neglected, there are three relevant parameters in wave generation. The first one is fetch; the second one is duration, and the third one is wind speed. Duration is related to the time that a given wind has been blowing towards a certain direction. There could be situations where there is a long fetch, but the wind direction varies before the minimum fetch to observe a fully-developed sea is reached. The wind speed is also important since the higher wind speed the longer minimum fetch will be needed. Therefore, an analysis on fetch must be always accompanied by an analysis on duration and wind speed. Otherwise, the analysis could be meaningless. Due to the high variation in wind speed and direction, this hypothetic analysis over 3 simultaneous parameters becomes very complex.

At the end, a correct effective fetch, calculated according to duration and wind speed, will only be an indicator of the wave age. Young waves are expected for short fetches and fully-developed seas are expected to be observed for long fetches. Using fetch to control the wave age will obligate to know the wind history over a location plus the calculation of effective fetches. Nowadays, oceanographers use a simpler method. The relation between the phase speed of waves and the friction velocity (or wind speed) is widely agreed to be the wave age. The reason is that at certain wind speed or friction velocity, the waves will reach certain phase speed when these are fully developed. Thus, the relation between phase speed and friction velocity or wind speed is also an indicator of the wave age.

Since an analysis on the wave age, c_p/u_*, is included in this research, an analysis on fetch is not necessary. An example of this can be found in [118] where there is no significant difference in results between the wave age method and the fetch method.

5.3 Results

All of the results shown in this study are either a friction velocity, wind speed or roughness length regression. As explained previously, the control u_* for the regressions was the u_* measured in situ. In the case of z_0, the control roughness was the one calculated from the wind profile, using cup anemometers at 21 and 116 meters, Eq. 2.7. Finally, for wind speed, the

anemometer at 116 meters on the met mast was the validation sensor. For all three types of regression, the control values from Egmond aan Zee are named "egmond_wave" as it appears in Fig. 5.2 to Fig. 5.11.

Also, in all regressions four statistics were calculated, the linear regression equation, R^2, normalized root mean squared error (NRMSE) and bias. Due to the number of figures produced by all possible combinations between z_0 and u_* methods, regression was shown for only the best four combinations. The rest of results were grouped together in Tables 5.1 to 5.4. Table 5.1 regressions plus the correspondent z_0 regression are included in Appendix B.

5.3.1 Friction velocity regressions

Regressions from non-iterative methods are included in Fig 5.2. The first two graphs, upper graphs, were almost equal. These were the U_{10} dependent methods, Hersbach and Wu, first and second graph respectively. The other two graphs in Fig. 5.2 corresponded to sea state dependent methods, Maat and Toba, third and bottom. Unlike wind dependent methods there was a big difference between them. The Maat method presented the slope nearest to the ideal value of 1 of the trend line with 0.426. On the other hand, Maat produced a lot of scatter with R^2=0.055. The Toba method was the opposite, low scatter with R^2=0.039 but a very low value for the slope at 0.021. Wind-dependent methods are located in-between since they presented lower scatter than Maat but higher slope than Toba.

Iterative methods were included in Figures 5.3 and 5.4. Here the iterative methods for z_0 and u_* calculation presented plus a control regression where the in situ u_* is plotted against the in situ u_*. This control graph is located bottom on Figure 5.4 proving the success of overlapping. The rest of the regressions in the figure can be grouped as Iterated, Fetch_iter, and Wave_iter in one side, and Speed_iter and Sea_shape_iter on the other side. These last two methods achieved a higher slope and lower NMRSE and bias but more scattered.

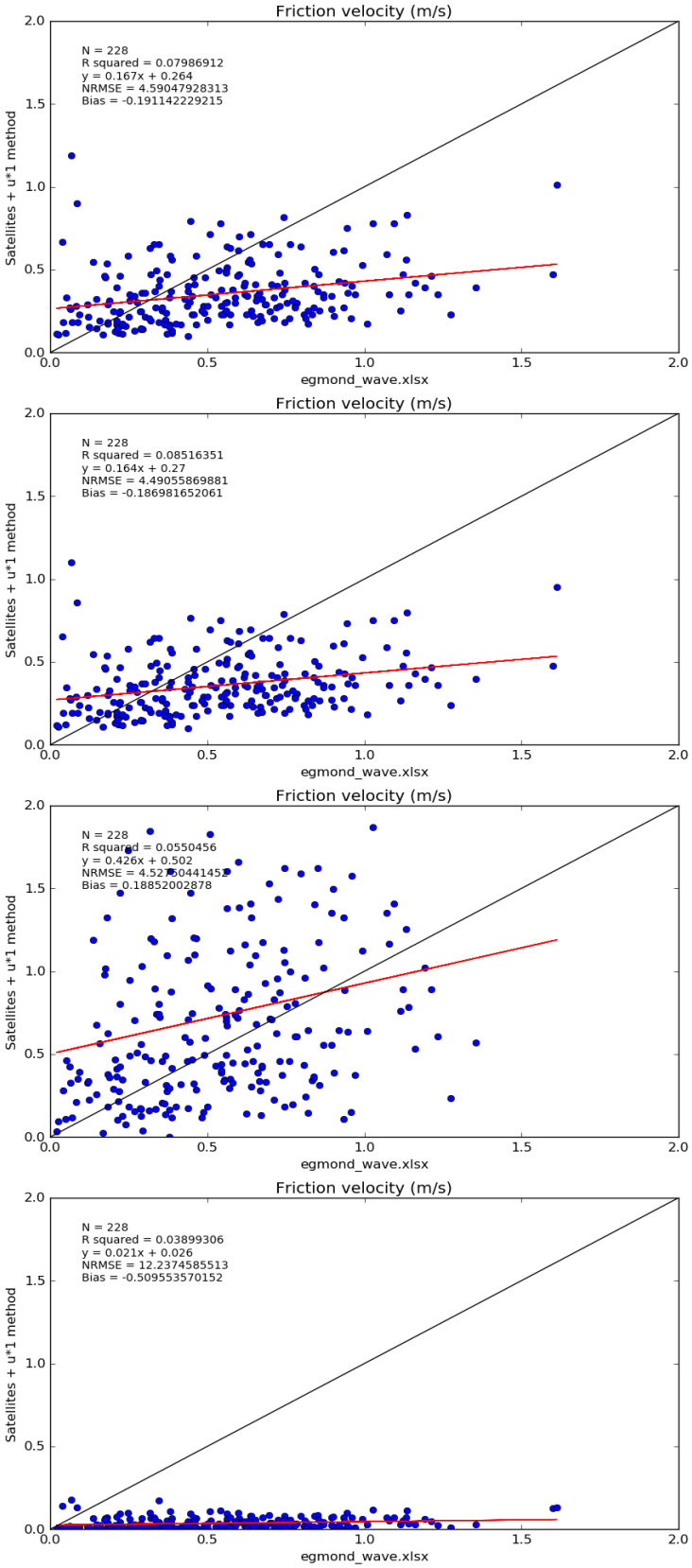

Figure 5.2. Friction velocity (u_*) regressions for methods: Hersbach (first), Wu (second), Maat (third) and Toba (bottom).

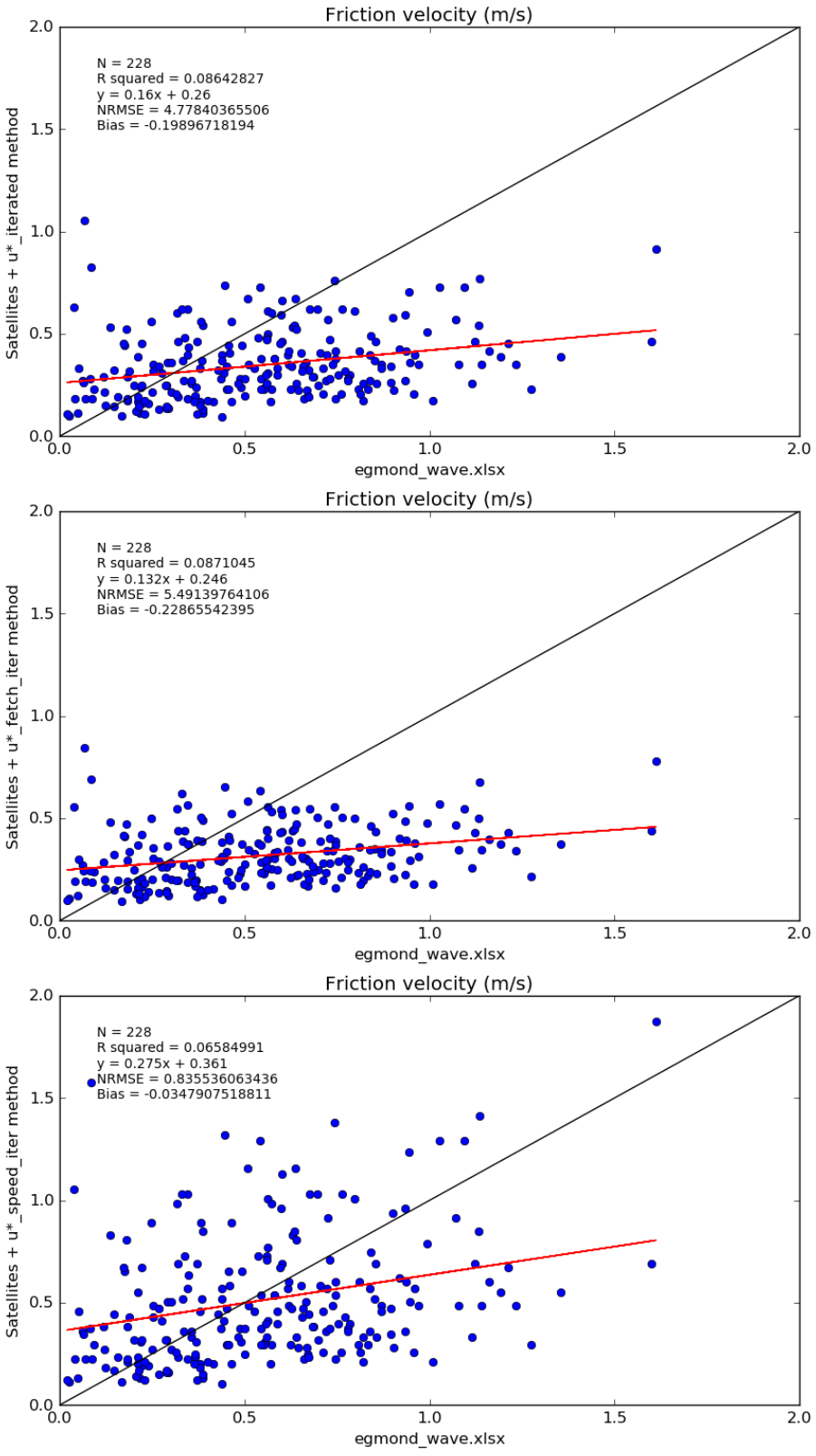

Figure 5.3. Friction velocity (u_*) regressions for methods: Iterated (upper), Fetch_iter (middle), Speed_iter (bottom).

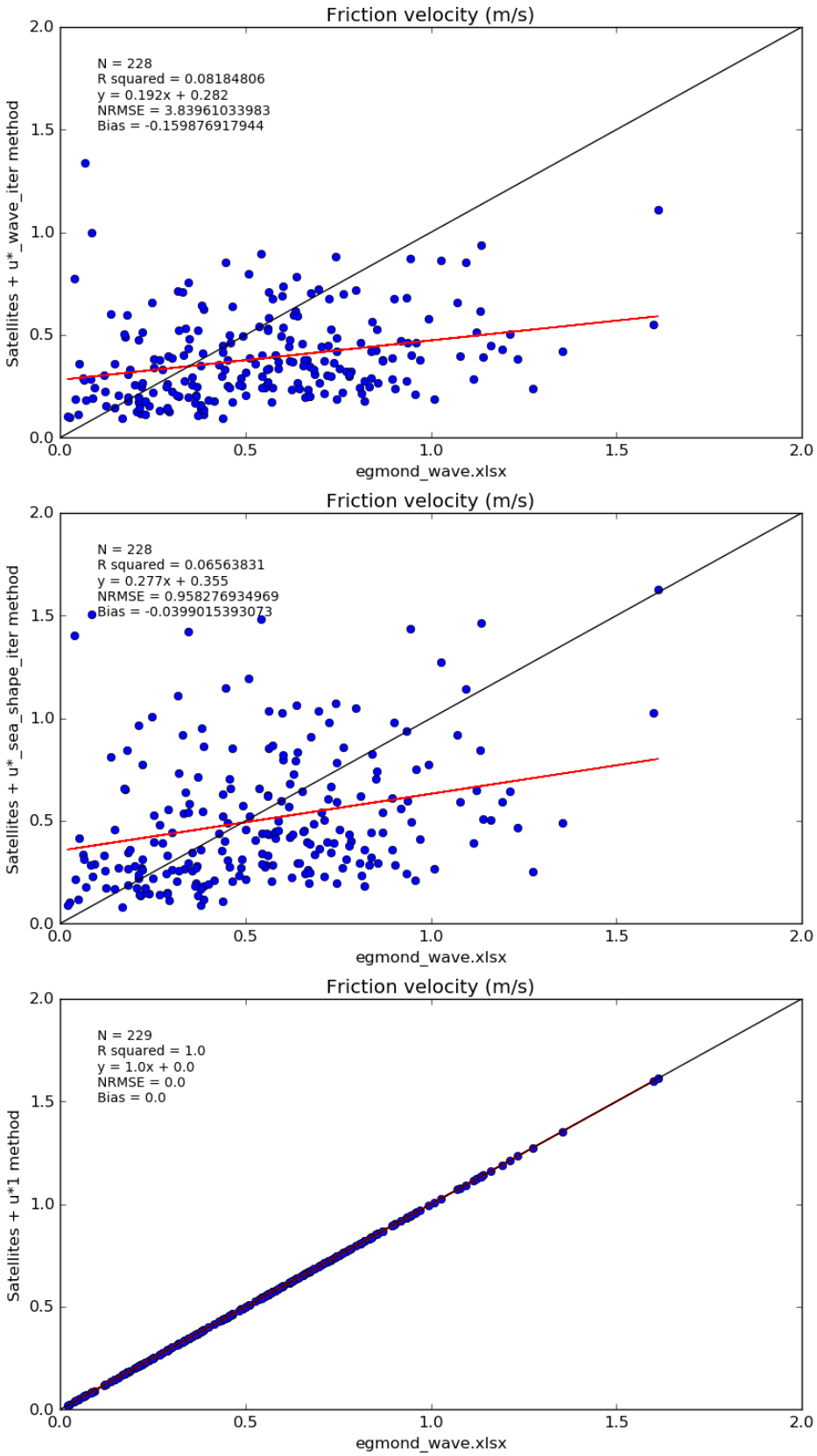

Figure 5.4. Friction velocity (u_*) regressions for methods: Wave_iter (upper), Taylor_iter (middle) and Insitu (bottom).

Overall, the highest R^2 was achieved with a Fetch_iter method, 0.087, which obtained a very low slope. The Maat method reached the highest slope, 0.426, or the nearest to 1, even so, it could be considered far from optimal since R^2 was 0.055. The Speed_iter method obtained the best results for NMRSE and bias, with 0.835 and -0.034 respectively.

5.3.2 Wind speed and roughness regressions

With a total of 50 combinations, Table 5.1 shows the results for all wind speed regressions. All of them were contrasted with a cup anemometer at 116 meters. Comparing results by z_0 method and excluding Iteration and Taylor methods, there was no significant difference in R^2 between methods. Slope, NRMSE, and bias presented certain differences, although these were small. Looking at R^2, the method with highest values was Log_law, even when the Speed and Wu combination obtained the highest value, 0.804. Analysing NRMSE and bias, the lowest values were found in Smith, Edson_age, DTU_age, and Log_law methods. According to the slope, Edson_age, DTU_age, and Log_law obtained the nearest to 1 again.

Comparing u_* methods in Table 5.1, Hersbach and Wu methods are approximately equal. R^2 values were slightly higher for the Wu method than any other u_* method. Hersbach and Wu methods obtained lower NRMSE and bias and higher slopes, but there was no a big difference in these statistics between both methods. Maat and Toba methods, which are sea state dependent, gave lower R^2 results than the wind speed dependent methods, Hersbach and Wu. Nevertheless, Maat achieved higher R^2 than the Toba method. The last method, Insitu, where u_* was calculated from in-situ anemometers, showed the lowest R^2 results of all u_* methods in all statistics with one exception. When Insitu method is combined with the Log_law method, its highest R^2 was obtained, 0.9, and also a slope close to 1, 0.988.

Within a selected, u_* method, any possible tandem with a z_0 method obtained similar results with the exception of the Taylor and Log_law methods. Those methods represent the lowest and highest R^2 results of Table 5.1 respectively between all z_0 methods. Even so, its results followed the same trend than the rest. Hersbach and Wu results were very similar, Insitu results were the

lowest R^2 and Maat and Toba results showed smaller R^2 than the wind speed dependent methods for u_*. The only difference is related to R^2, where there is no a relevant difference excepting for Insitu regression. Iteration results obtained high R^2 and low bias and NRMSE in comparison with the other u_* methods. All Iterative methods achieved an R^2 over 0.78, slope close to 1, between 1.135 and 0.903, plus a bias under 1. Statistics showed the best results for Iteration, Fetch_iter and Wave_iter methods.

Due to the number of regressions, only four combinations are shown in this chapter. Those combinations are Wave_iter, Wu plus Log_law, Iteration, and Fetch_iter. Wave_iter obtained the slope nearest to 1 in Table 5.1, the third highest R^2, and NRMSE and bias below 1. Also, this method is interesting since z_0 was calculated through the wave slope. The u_* method with highest R^2 was Wu and the same for z_0 method was Log_law. Hence the combination Wu plus Log_law was a logical choice. The cases of Iteration and Fetch_iter are something different since these methods do not need any in-situ measurement from either sea or atmosphere. Also, their results reflected high R^2.

As shown in Fig. 5.5 the number of points after filtration and overlapping was 229. Even when all four regressions showed slopes very near to 1 and very low bias and NRMSE, the R^2 was still far from 1. All of them had an R^2 under 0.8, with too much scatter. Nevertheless, there is correlation unlike z_0 regressions in Fig. 5.6. Also for z_0 it was expected a correlation 1:1 for the perfect regression. However, all four slopes are close to 0. In all four the calculated z_0 from numerical methods was always significantly lower than z_0 from the wind profile.

Another interesting combination is the Insitu u_* plus Log_law methods, which reached the highest R^2 with 0.900 and relevant slope with 0.988. Wind speed and surface roughness regressions are shown in Fig. 5.7. Even when the results in Fig. 5.5 showed similar slopes, this combination achieved less scatter i.e. higher R^2. Surface roughness regression in Fig. 5.7 is worthy of highlighting since it achieved some correlation, which is completely missing in Fig. 5.6. However, statistics showed a low correlation; low R^2, 0.648, and high NRMSE, 4.252.

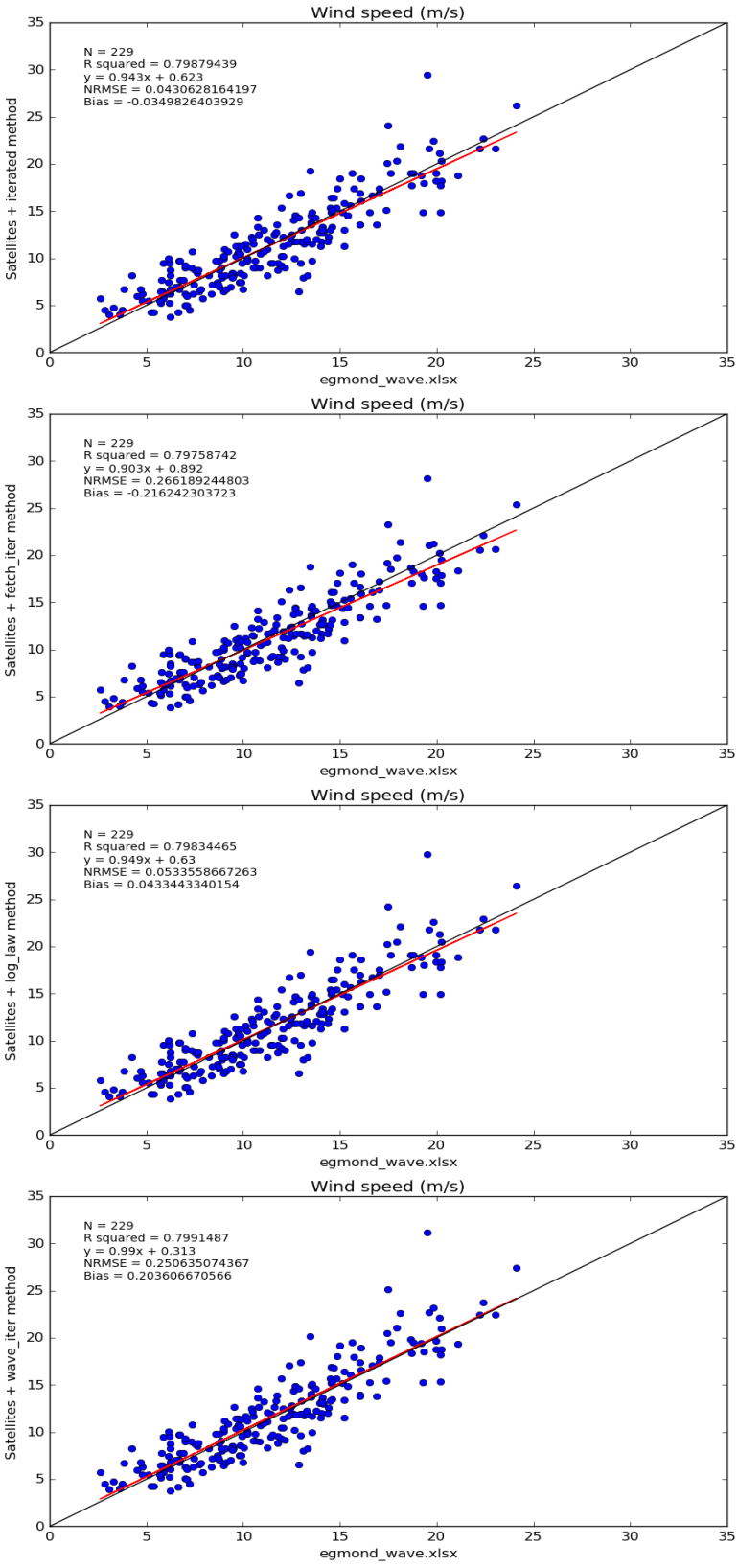

Figure 5.5. Wind speed regression for methods: Iterated (upper-left), Fetch_iter (upper-right), Log_law & Wu combination (bottom-left) and Wave_iter (bottom-right).

		z_0 METHODS									
u* METHODS		Iteration	Fetch	Smith	Toba	Edson Speed	Edson Age	DTU_Age	Log_law	Edson Wave	Taylor
Hersbach	R^2	-	0.771	0.792	0.794	0.799	0.791	0.790	0.796	0.788	0.646
	slope	-	1.166	0.865	1.181	0.708	0.928	0.864	0.958	1.132	0.564
	NRMSE	-	2.370	0.626	2.298	2.505	0.190	0.301	0.021	2.597	2.995
	bias	-	1.925	-0.508	1.867	-2.035	-0.155	-0.244	0.017	2.110	-2.433
Wu	R^2	-	0.778	0.797	0.799	0.804	0.797	0.794	0.798	0.795	0.631
	slope	-	1.119	0.833	1.136	0.679	0.893	0.831	0.949	1.089	0.528
	NMRSE	-	2.565	0.471	2.511	2.358	0.029	0.146	0.053	2.790	2.818
	bias	-	2.083	-0.383	2.040	-1.916	-0.024	0.119	0.043	2.266	-2.289
Maat	R^2	-	0.696	0.689	0.680	0.656	0.681	0.666	0.784	0.679	0.686
	slope	-	2.905	1.858	2.631	1.669	2.107	1.927	1.355	2.605	1.842
	NRMSE	-	15.595	7.886	14.405	5.811	9.513	8.429	2.877	14.548	7.355
	bias	-	12.668	6.406	11.702	4.720	7.728	6.847	2.337	11.819	5.975
Toba	R^2	-	0.643	0.627	0.616	0.629	0.627	0.618	0.799	0.626	0.614
	slope	-	0.249	0.235	0.238	0.182	0.234	0.237	0.772	0.283	0.100
	NMRSE	-	11.944	12.206	12.195	12.458	12.208	12.197	2.346	11.921	12.964
	bias	-	-9.703	-9.916	-9.907	-10.120	-9.918	-9.908	-1.956	-9.684	-10.532
Insitu	R^2	-	0.319	0.352	0.348	0.271	0.344	0.352	0.900	0.348	0.101
	slope	-	1.232	0.878	1.199	0.722	0.959	0.881	0.988	1.177	0.569
	NRMSE	-	9.566	4.042	8.817	2.250	5.047	4.313	1.429	8.984	3.717
	bias	-	7.799	3.296	7.189	1.834	4.115	3.517	1.165	7.325	3.030
Iterated	R^2	0.798	0.797	-	-	0.781	-	-	-	0.799	0.797
	slope	0.943	0.903	-	-	1.125	-	-	-	0.990	1.135
	NRMSE	0.043	0.266	-	-	1.190	-	-	-	0.250	1.158
	bias	0.034	0.216	-	-	0.967	-	-	-	0.203	0.941

Table 5.1. Wind speed regression statistics for all combinations of z_0 methods (columns) and u_* methods (rows), including iterated methods. Bias in m/s.

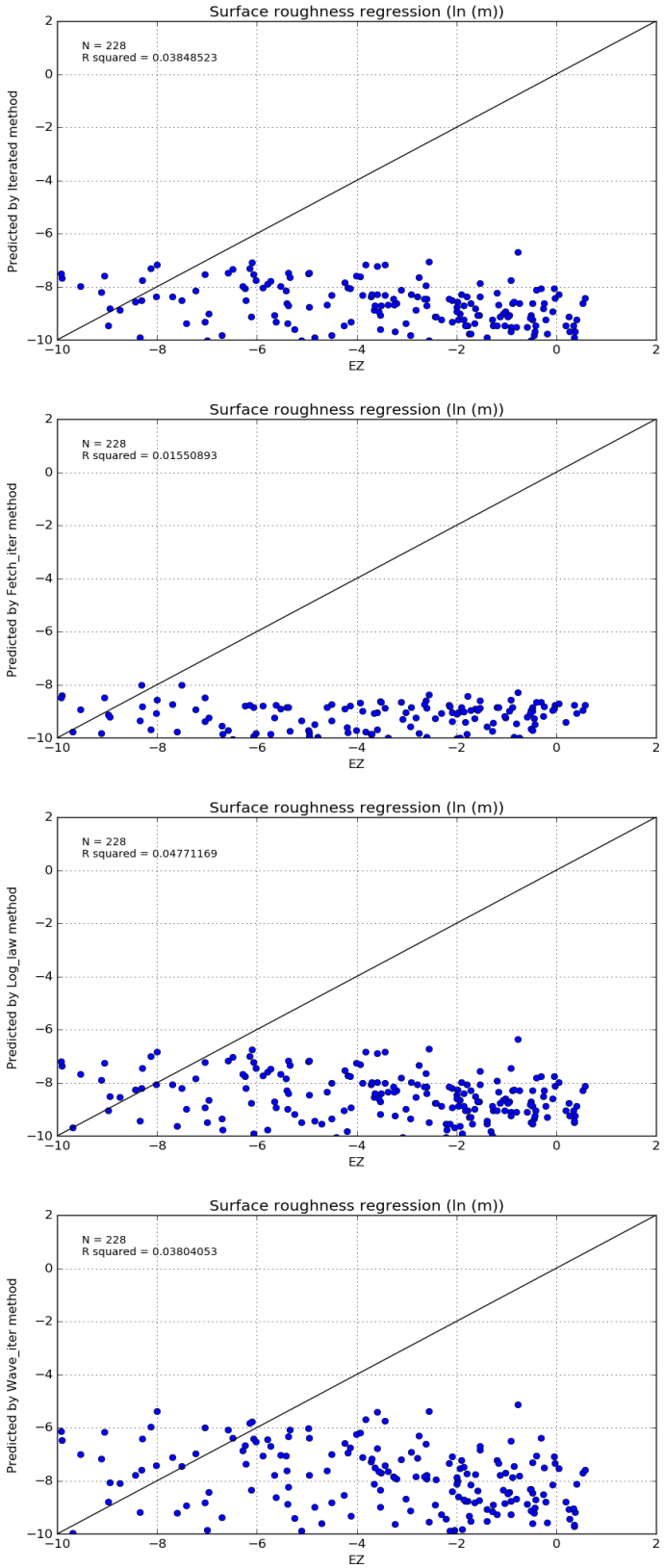

Figure 5.6. Surface roughness (z_0) regression for methods: Iterated (upper), Fetch_iter (second), Log_law & Wu combination (third) and Wave_iter (bottom).

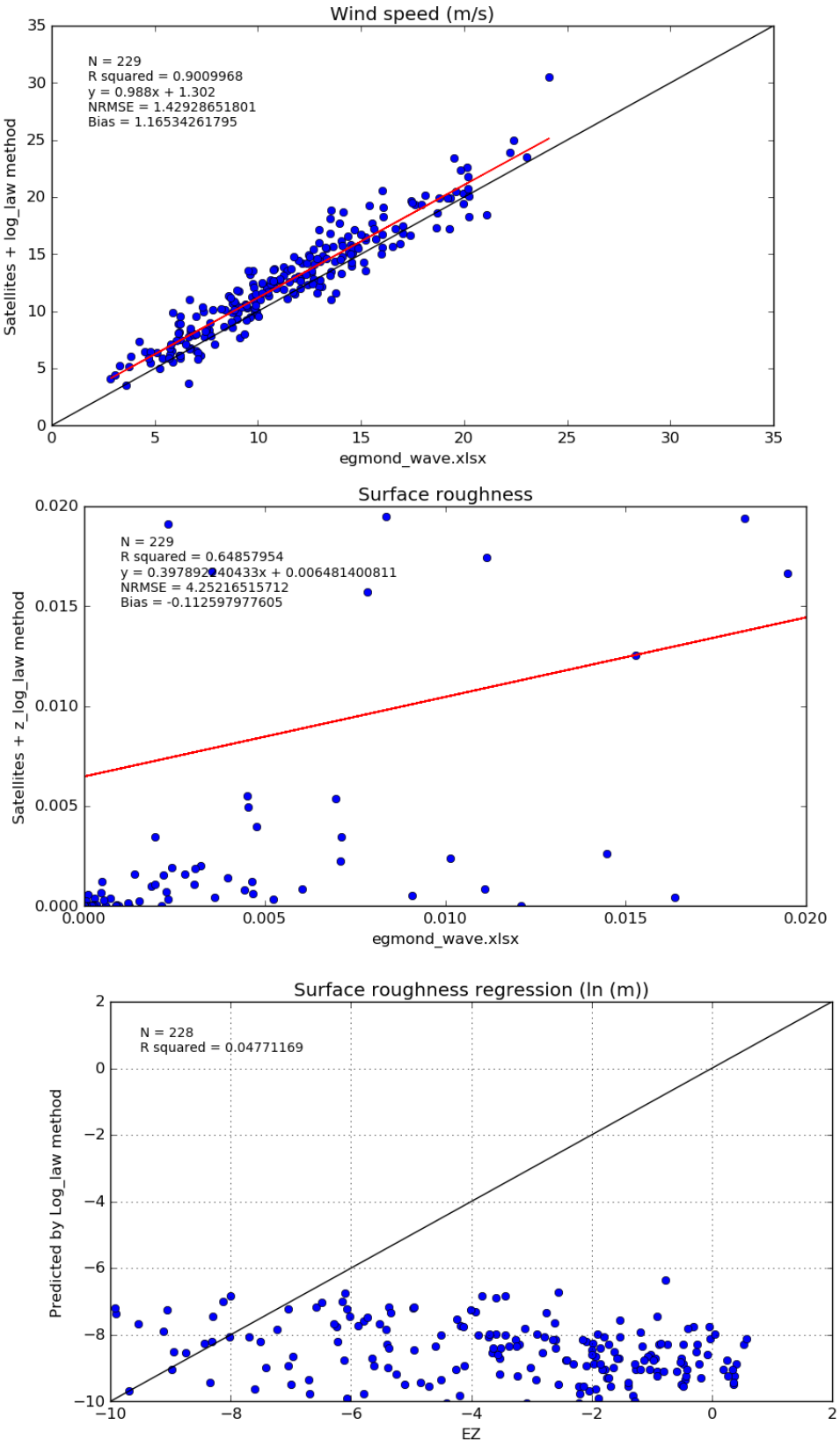

Figure 5.7. Wind speed and surface roughness regressions for Insitu u_* plus Log_law combination.

5.3.3 Regressions for different wave ages

As explained in section 5.2.6, regressions were tested under different wave age conditions. These were calm sea, growing sea, and decaying sea as appears in Table 5.2. Only the selected four combinations between z_0 and u_* were studied. All combinations achieved similar results.

		calm sea $c_p/u_*<5$	growing sea $5\leq c_p/u_*\leq 32$	decaying sea $c_p/u_*>32$
Iteration	R^2	0.877	0.834	0.901
	slope	1.129	0.967	1.308
	NMRSE	0.533	0.323	1.344
	bias	-2.252	-0.301	2.165
Wu_Log_law	R^2	0.877	0.834	0.900
	slope	1.140	0.973	1.318
	NMRSE	0.513	0.239	1.392
	bias	-2.171	-0.223	2.242
Fetch_iter	R^2	0.883	0.832	0.903
	slope	1.088	0.926	1.253
	NMRSE	0.577	0.529	1.266
	bias	-2.438	-0.493	2.039
Wave_iter	R^2	0.881	0.838	0.898
	slope	1.203	1.016	1.383
	NMRSE	0.472	0.064	1.480
	bias	-1.995	-0.059	-2.384
Number of points		12	184	32

Table 5.2. Wind speed regression statistics for different wave ages. Bias in m/s.

Comparing the three different wave age intervals, the best correlation was found for decaying seas, obtaining the highest R^2 in all cases where its value is around 0.9. This value was also the nearest to one in this study. R^2 values for calm and growing seas are just slightly lower than decaying sea R^2. Slope results were above one for calm and fully developed seas unlike growing sea slope with values around one. NRMSE was lower than unity for growing and calm seas, unlike decaying sea. Bias reached values between one and minus one only for growing seas. In other cases, bias was above two or below minus two. A relevant fact is the number of points for each case. Most of the points represented growing sea, leaving only 12 and 32 points for calm and decaying sea respectively. Even so, all R^2 values in Table 5.2 are higher than the results shown in Table 5.1. Regressions for wind speed and z_0 under decaying seas conditions are shown in Fig. 5.8 and Fig. 5.9 respectively. Unlike wind speed regressions, R^2 values were always under 0.37 for z_0 regressions.

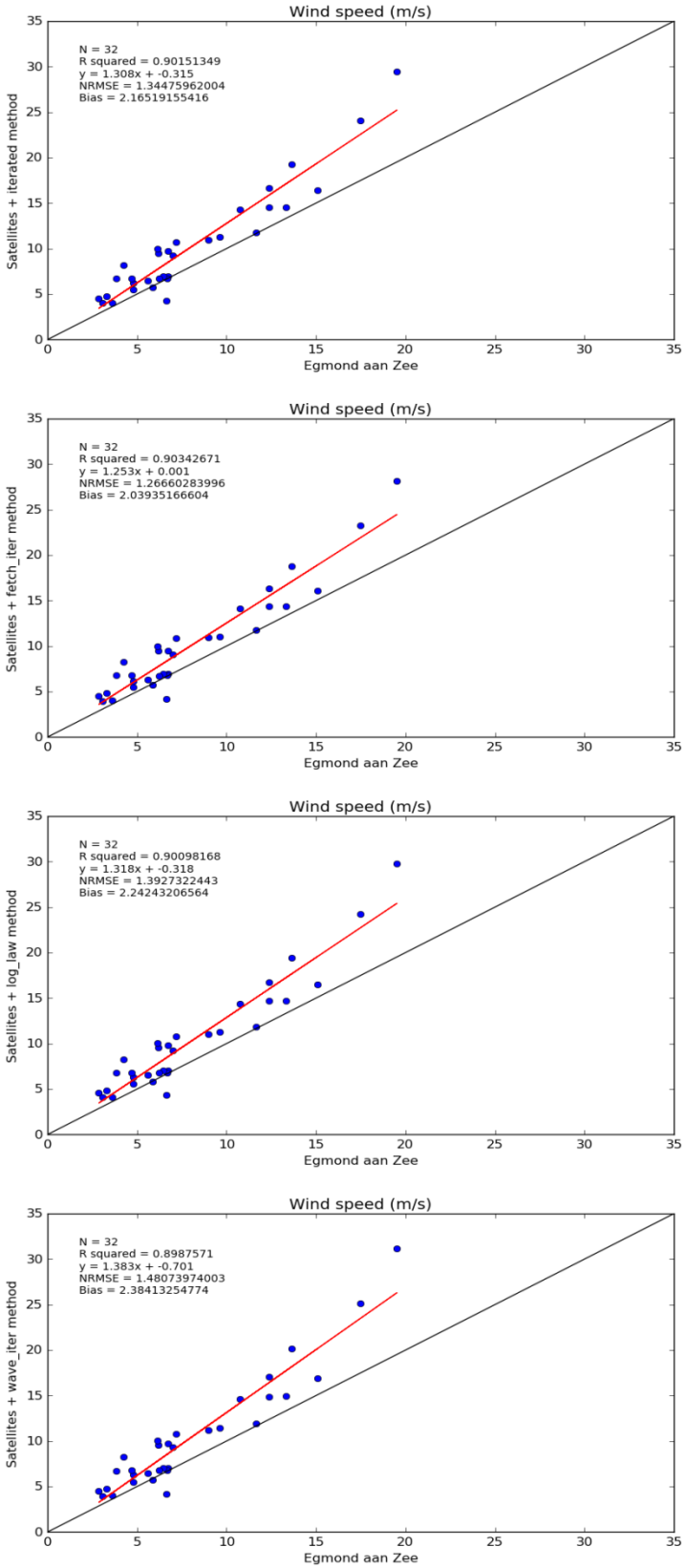

Figure 5.8. Wind speed regression when wave age >32 for methods: Iterated (upper), Fetch_iter (second), Log_law & Wu combination (third) and Wave_iter (bottom).

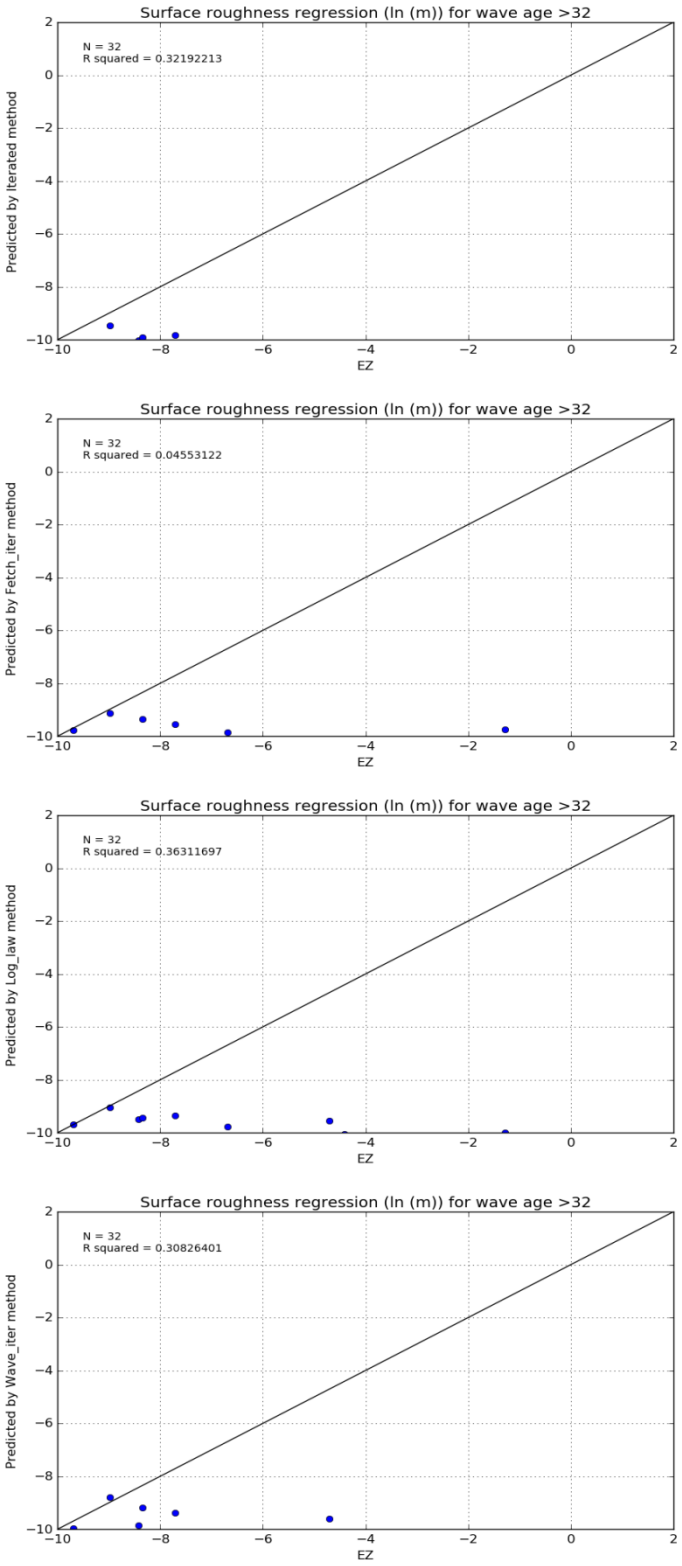

Figure 5.9. Surface roughness (z_0) regression when wave age >32 for methods: Iterated (upper), Fetch_iter (second), Log_law & Wu combination (third) and Wave_iter (bottom).

5.3.4 Regressions for different wave heights

Same combinations of methods were also studied under different wave heights, see Table 5.3. Again, the Wave_iter method found higher R^2 and Fetch_iter the lowest R^2 in the table. Even so, all four combinations showed similar statistics. Regressions for wave height between 1 and 2 meters were the highest R^2. For H_s between 2 and 3 meters, the agreement found was certainly lower than for 1-2 meters. However, it was not as low an agreement as for wave heights under 1 or over 3 meters. The column with highest R^2 in Table 5.3 was also shown in Fig. 5.10 were 87 measurements were found. In this case, statistics R^2 and slope represented a lower correlation than regressions with all sea conditions. The correlation in Fig. 5.11 for z_0 showed again a lower calculated z_0 than values extracted from the wind profile.

		Hs<1m	1m≤Hs<2m	2m≤Hs<3m	Hs>3m
Iteration	R^2	0.528	0.722	0.657	0.252
	slope	0.610	0.783	0.748	0.633
	NMRSE	0.427	0.171	0.161	0.424
	bias	-0.399	0.223	0.422	2.317
Wu_Log_law	R^2	0.528	0.722	0.657	0.252
	slope	0.612	0.787	0.755	0.641
	NMRSE	0.365	0.115	0.203	0.454
	bias	-0.341	0.149	0.532	2.481
Fetch_iter	R^2	0.522	0.723	0.634	0.251
	slope	0.583	0.742	0.677	0.588
	NMRSE	0.536	0.281	0.036	0.316
	bias	-0.500	-0.365	0.095	1.730
Wave_iter	R^2	0.537	0.726	0.662	0.249
	slope	0.632	0.815	0.797	0.679
	NMRSE	0.349	0.006	0.346	0.583
	bias	-0.326	-0.008	0.905	3.187
Number of points		90	87	39	12

Table 5.3. Wind speed regression statistics for different wave heights. Bias in m/s.

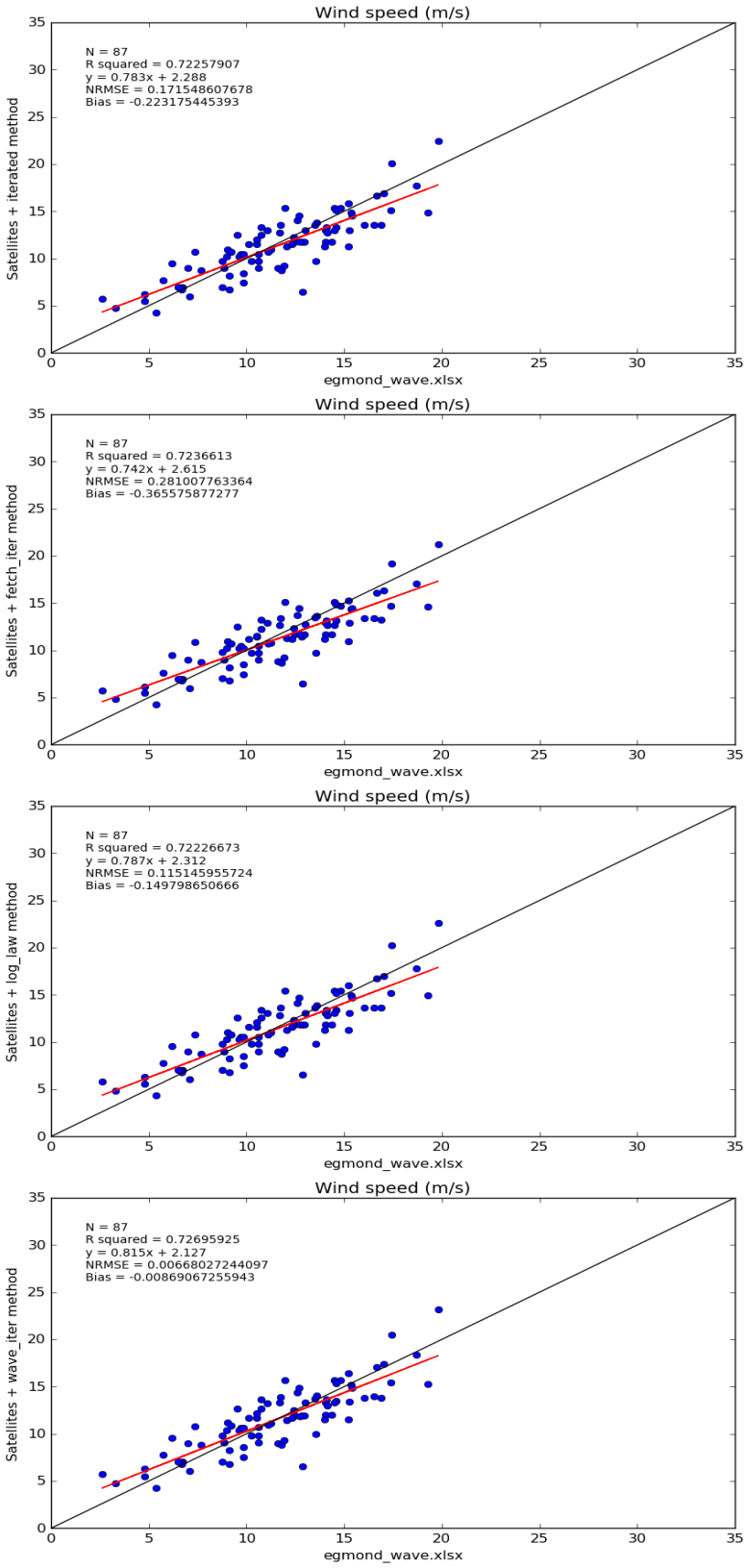

Figure 5.10. Wind speed regression when wave height was between 1 and 2 meters for methods: Iterated (upper), Fetch_iter (second), Log_law & Wu combination (third) and Wave_iter (bottom).

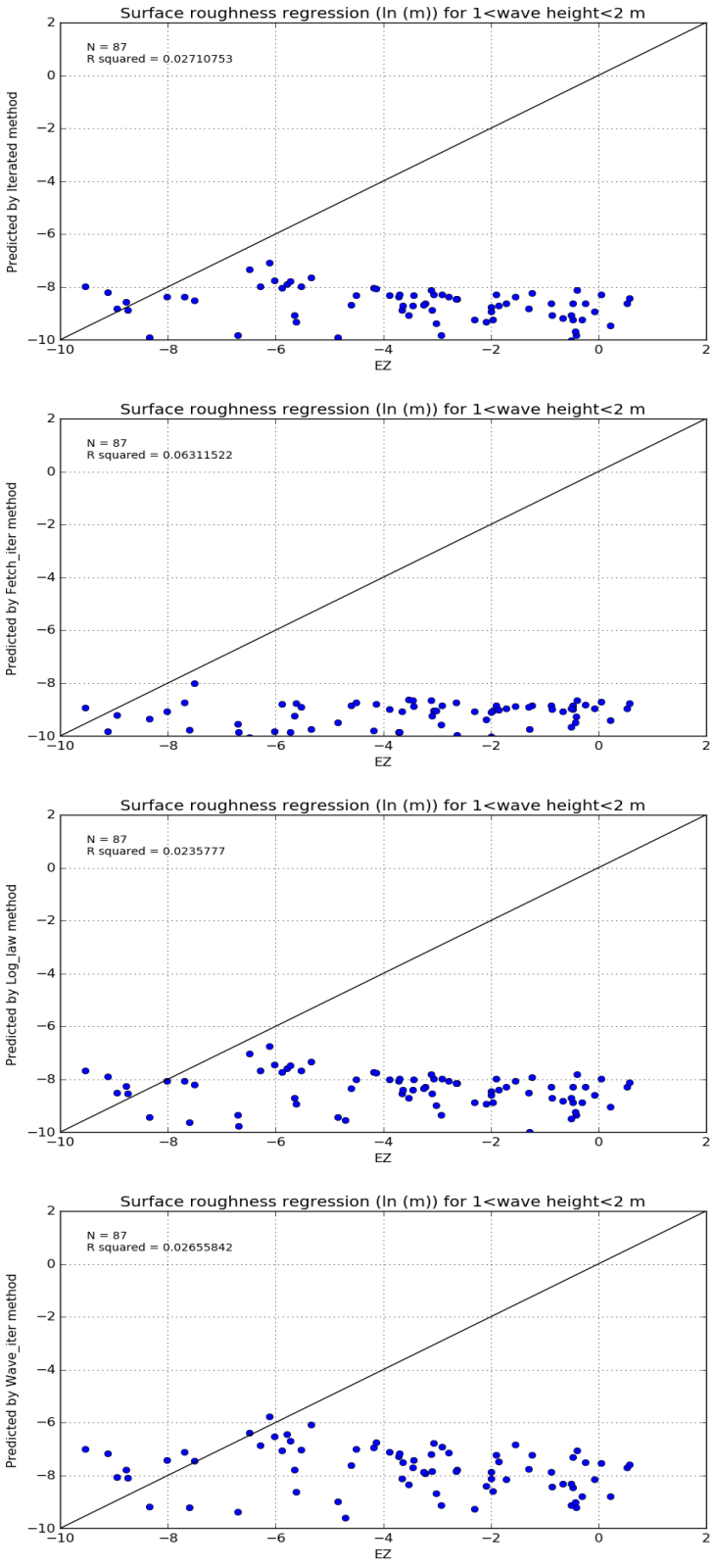

Figure 5.11. Surface roughness (z_0) regression when wave height was between 1 and 2 meters for methods: Iterated (upper), Fetch_iter (second), Log_law & Wu combination (third) and Wave_iter (bottom).

5.3.5 Regressions for different wind speeds

The last regressions were those realized under different wind speed conditions. The same trend from Tables 5.2 and 5.3 was observed in Table 5.4. Differences between methods were exactly the same and followed the same pattern. Wave_iter reached a slightly higher correlation and Fetch_iter reached the lowest R^2 of all four different combinations. The main difference with other regressions was the low value of R^2. The highest results in that sense were for wind speeds between 5 and 15 m/s, with an R^2 around 0.6. Regressions under such conditions were shown in Fig. 5.12 and 5.13. As expected z_0 graphs followed the same pattern than previous z_0 results. On the other hand, wind speed regression was just a portion of the Fig. 5.4, but only measurements excluding points less than 5 m/s and over 15 m/s.

		U_{10}<5m/s	5m/≤U_{10}≤15m/s	U_{10}>15m/s
Iteration	R^2	0.101	0.600	0.417
	slope	0.512	0.892	1.020
	NMRSE	1.428	0.174	0.016
	bias	1.530	-0.141	-0.044
Wu_Log_law	R^2	0.101	0.599	0.416
	slope	0.513	0.897	1.032
	NMRSE	1.476	0.091	0.031
	bias	1.582	-0.074	0.085
Fetch_iter	R^2	0.099	0.598	0.410
	slope	0.508	0.870	0.946
	NMRSE	1.431	0.307	0.203
	bias	1.533	-0.249	-0.558
Wave_iter	R^2	0.101	0.603	0.418
	slope	0.520	0.931	1.095
	NMRSE	1.442	0.020	0.207
	bias	1.545	0.016	0.569
Number of points		14	170	45

Table 5.4. Wind speed regression statistics for different wind speeds. Bias in m/s.

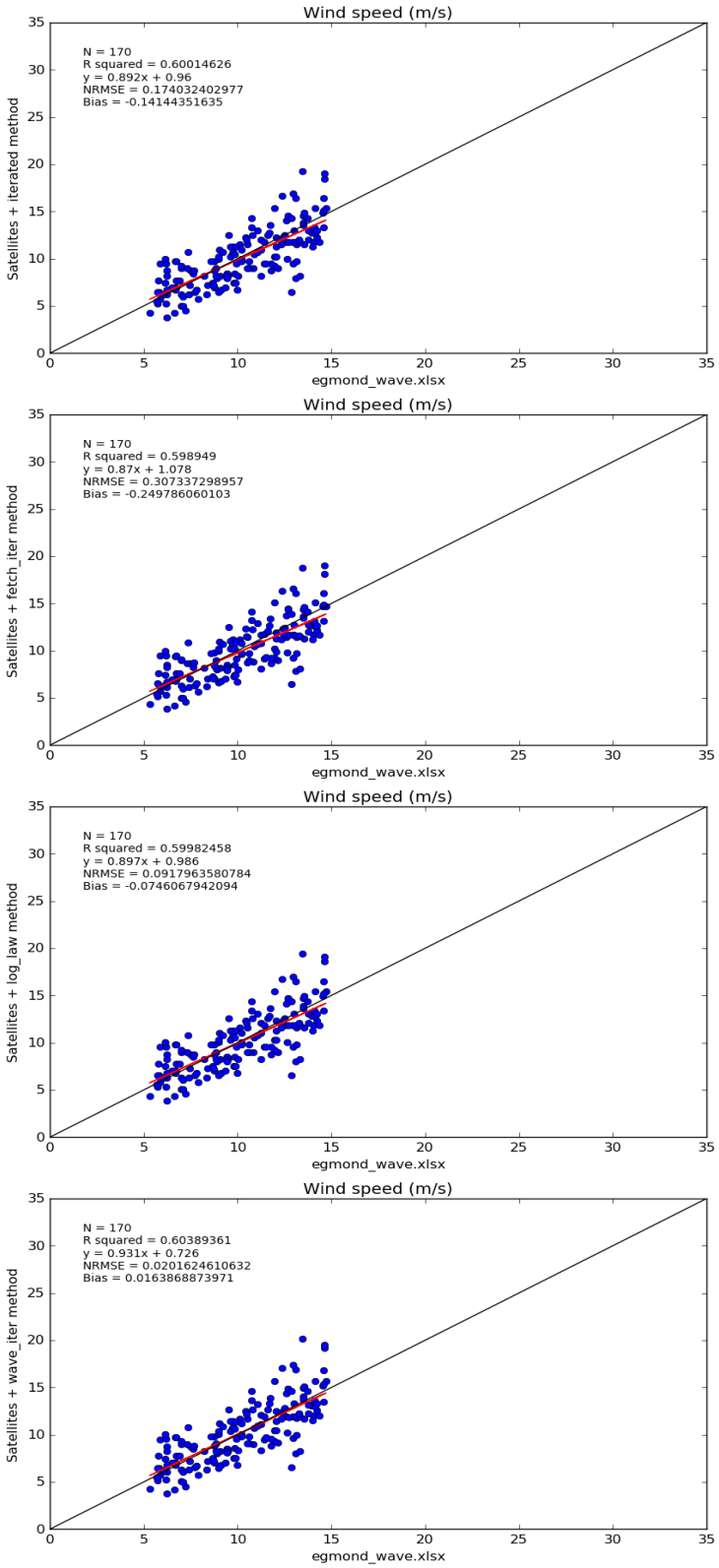

Figure 5.12. Wind speed regression when wind speed was between 5 and 15 m/s for methods: Iterated (upper), Fetch_iter (second), Log_law & Wu combination (third) and Wave_iter (bottom).

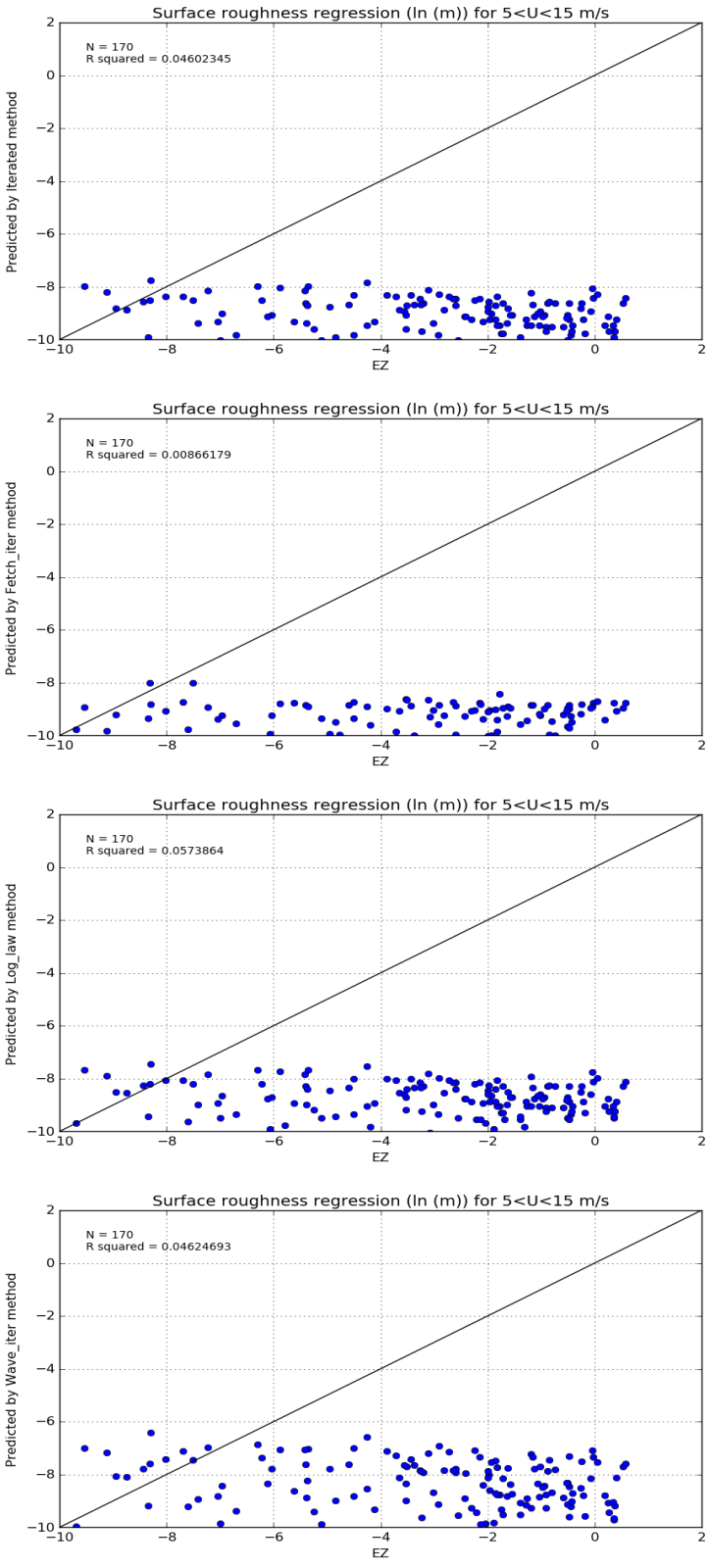

Figure 5.13. Surface roughness (z_0) regression when wind speed was between 5 and 15 m/s for methods: Iterated (upper), Fetch_iter (second), Log_law & Wu combination (third) and Wave_iter (bottom).

5.3.6 Surface roughness crosscheck

In previous figures where z_0 was represented, high values were observed. Over the ocean, the z_0 is expected to remain lower than 0.01 metres. However, in this thesis higher values were found when z_0 was calculated over a period of 50 minutes. These values were obtained by the logarithmic law under neutral conditions using two cup anemometers at 21 and 116 metres. This methodology for z_0 parameterization is the most frequently used within the wind energy sector and therefore there was the most confidence in the values determined by this method. In order to be sure there was no a miscalculation or measurement errors, a crosscheck was proposed using other anemometers mounted on the Egmond aan Zee meteorological mast.

Unlike the other results in this chapter, meteorological mast observations were not overlapped with satellite observations. The reason for this was to obtain a more representative dataset. Instead of only 229 points, around 14,000 points were used in this crosscheck. These points were assumed to be under neutral conditions since the difference between T_{air} and T_{sea} was lower than 1°C.

First, it is important to clarify how often z_0 values are higher than expected. In this subsection and in the results from Chapter 6, too many points were represented in the graphs and the data density was not clarified. Data density was calculated directly from the dataset. The majority of the data, 55%, the values were lower than 0.01 metres and most of the data, 80%, z_0 did not exceed 0.1 metres.

For the crosscheck, cup anemometers at 21, 70 and 116 metres were used, plus an ultrasonic anemometer at 21 metres. By different combinations of two anemometers, the z_0 was calculated and compared. In Figure 5.14 the different z_0's were compared for a timeline of 22 days, missing values were filtered out. Two main aspects were observed. The first one was that the combination 70/116 metres almost always produced much higher values than the other four combinations. The second aspect to highlight is the trend for all five lines; the trend is the same for of all them. There was one exception, the line 70/116 dropped after measurement 300 when the rest of the lines increased dramatically. Since 22 days cannot be fully representative, some extra comparisons were undertaken as shown in Figures 5.15 to 5.20.

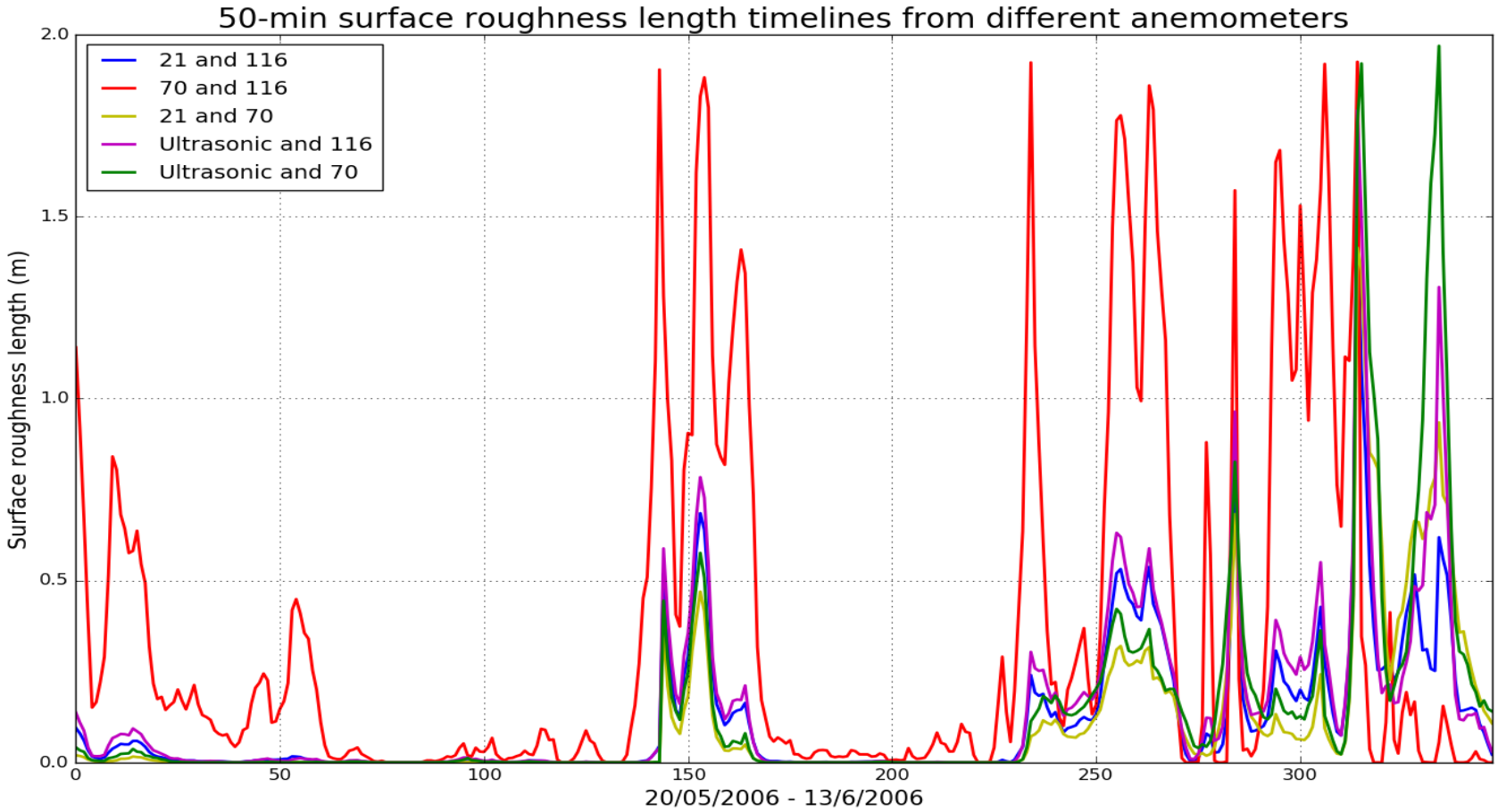

Figure 5.14. 50-min sea surface roughness timelines calculated according to the neutral logarithmic law by different combination of cup anemometers (21, 70 and 116 m) and a ultrasonic anemometer at 21 m.

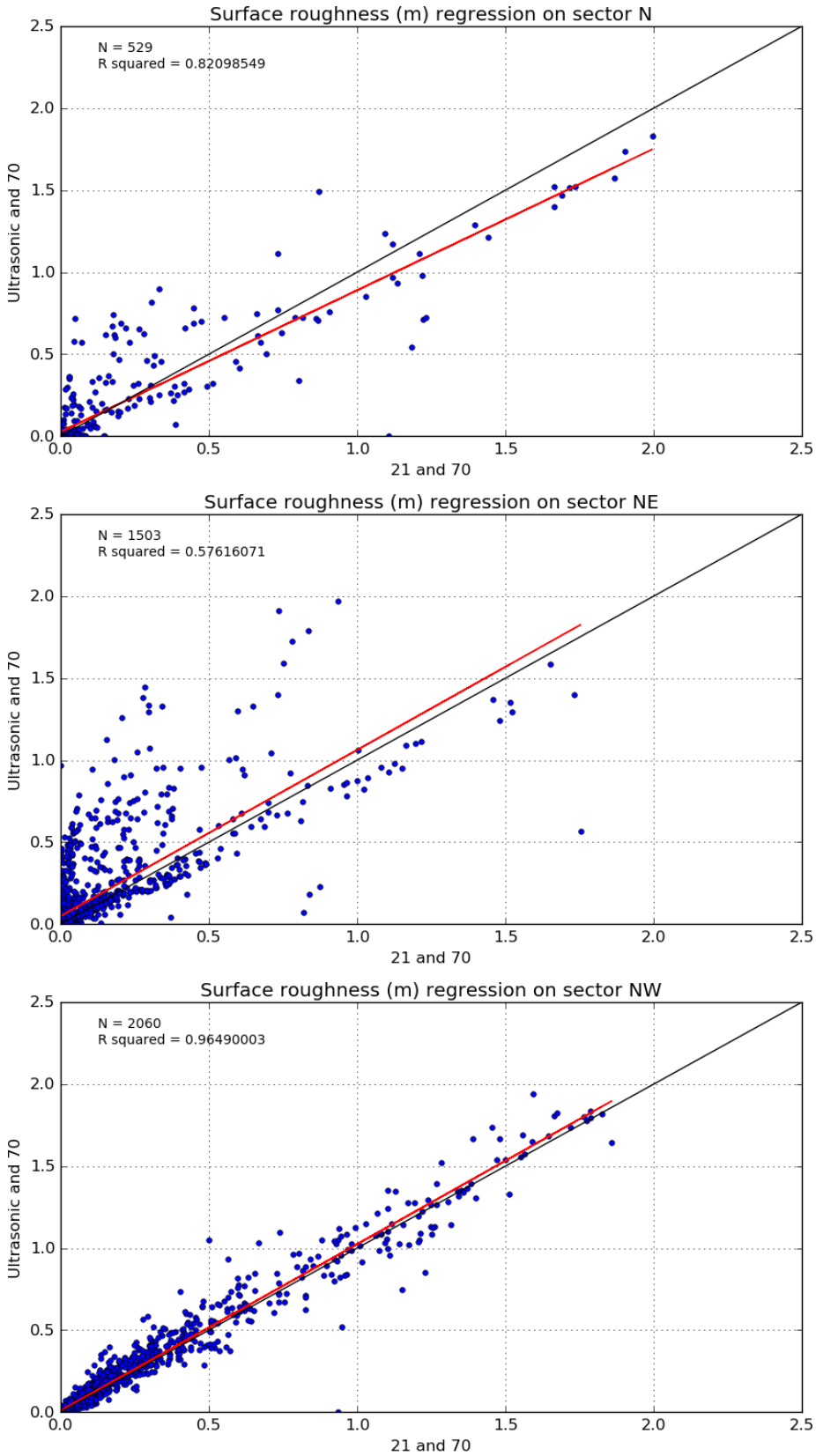

Figure 5.15. Comparison of logarithmic law z_0 between cup anemometers at 21 and 70 m, and ultrasonic anemometer at 21 m and cup anemometer at 70 m. Northern sectors.

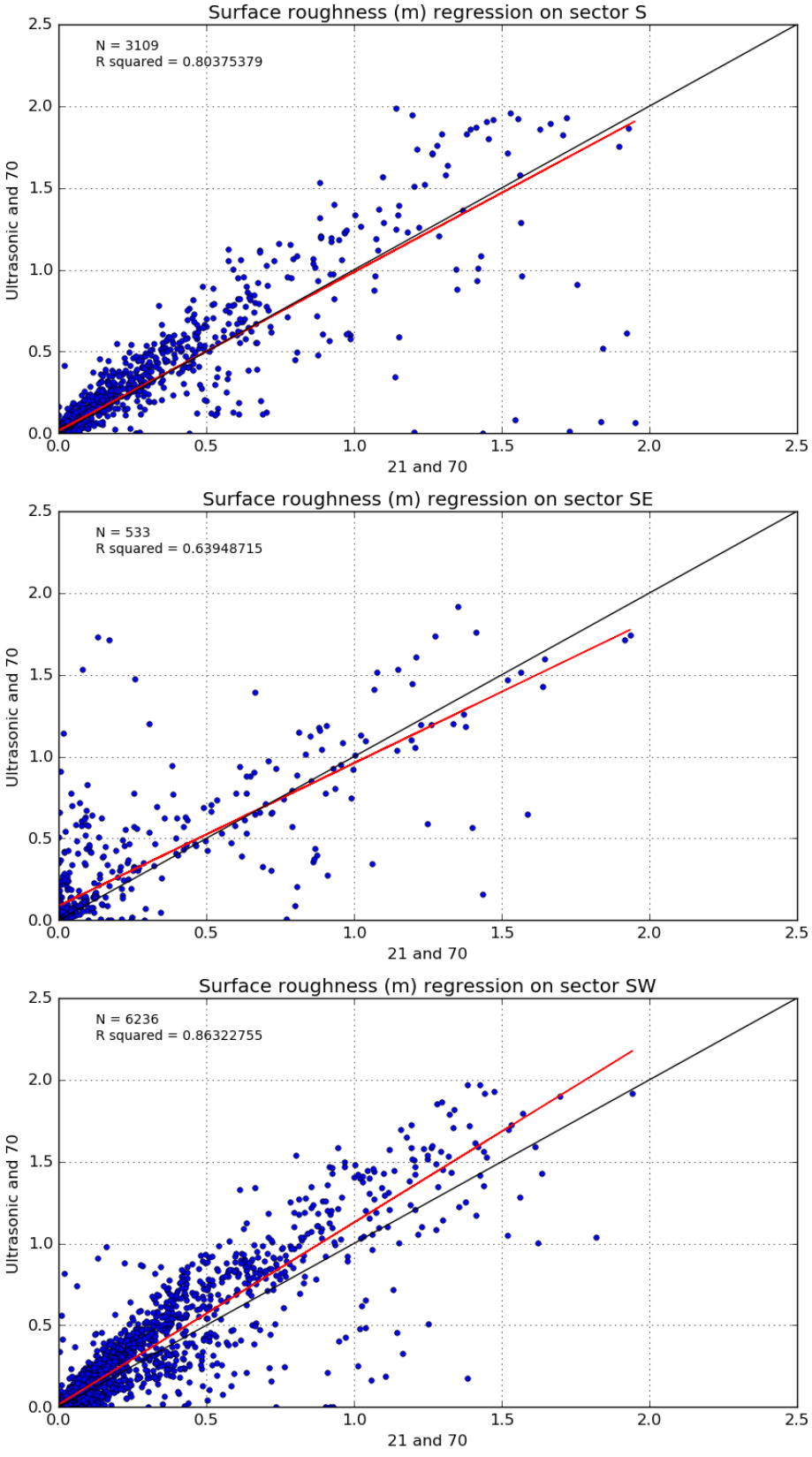

Figure 5.16. Comparison of logarithmic law z_0 between cup anemometers at 21 and 70 m, and ultrasonic anemometer at 21 m and cup anemometer at 70 m. Southern sectors.

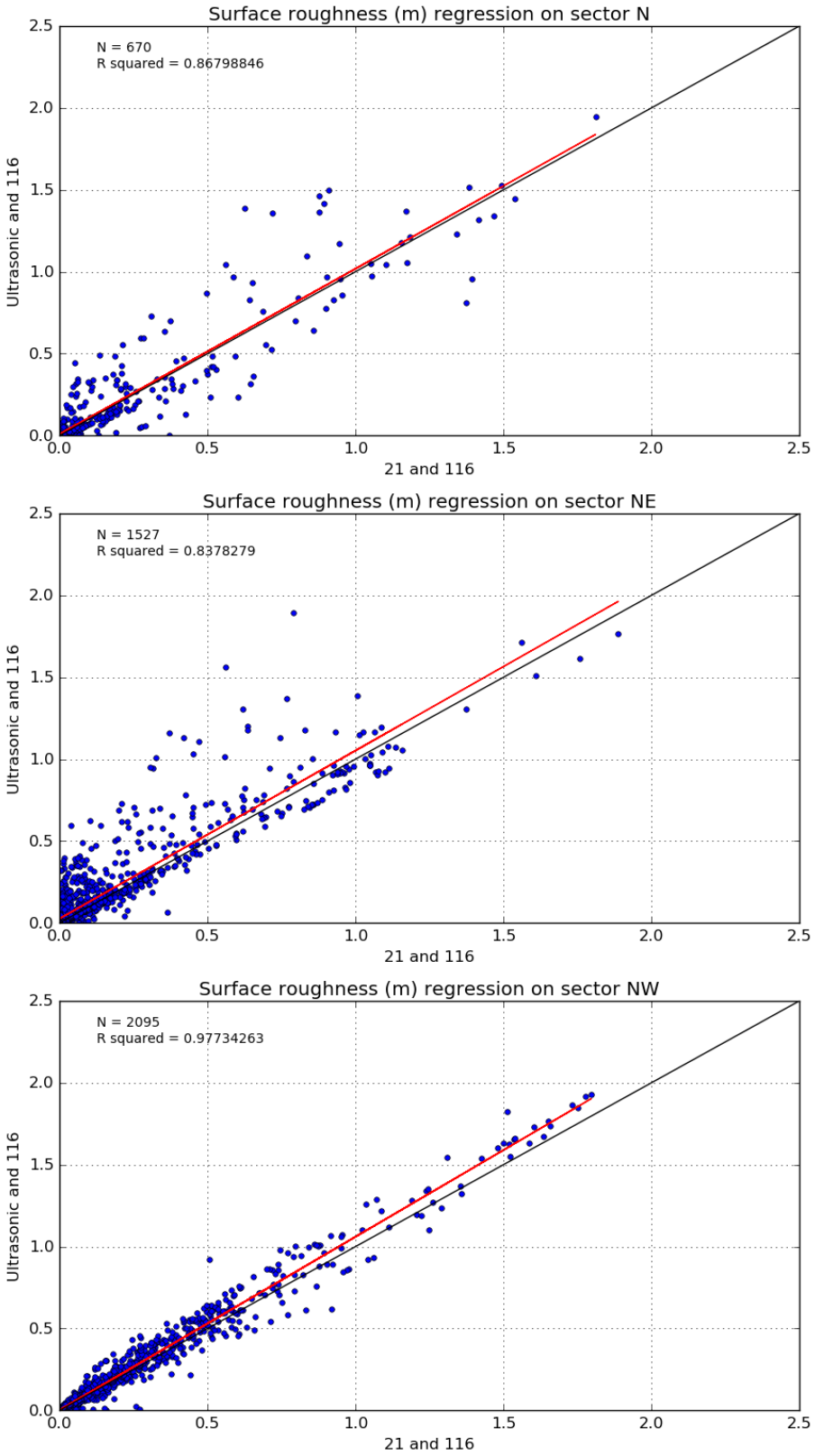

Figure 5.17. Comparison of logarithmic law z_0 between cup anemometers at 21 and 116 m, and ultrasonic anemometer at 21 m and cup anemometer at 116 m. Northern sectors.

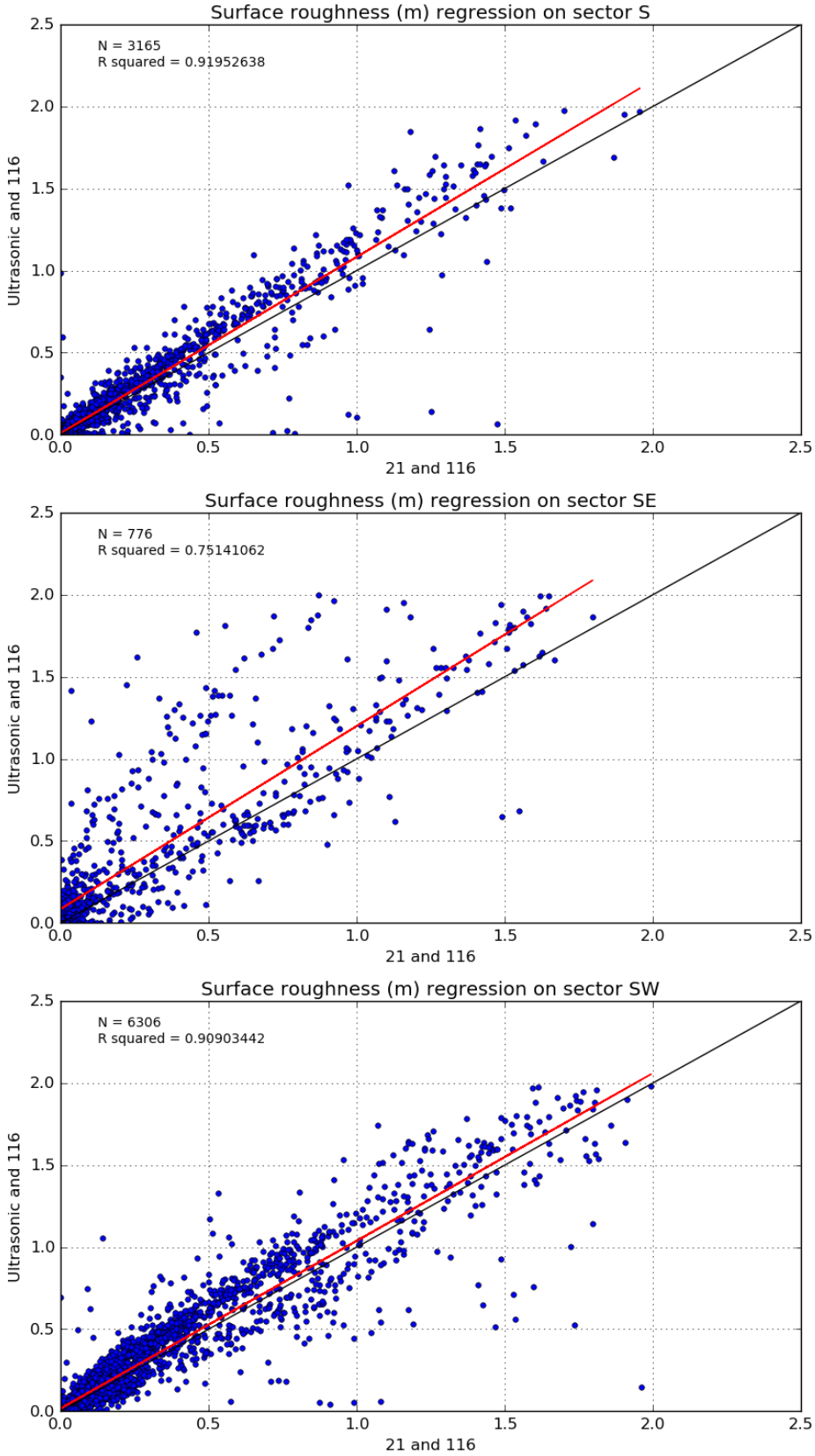

Figure 5.18. Comparison of logarithmic law z_0 between cup anemometers at 21 and 116 m, and ultrasonic anemometer at 21 m and cup anemometer at 116 m. Southern sectors.

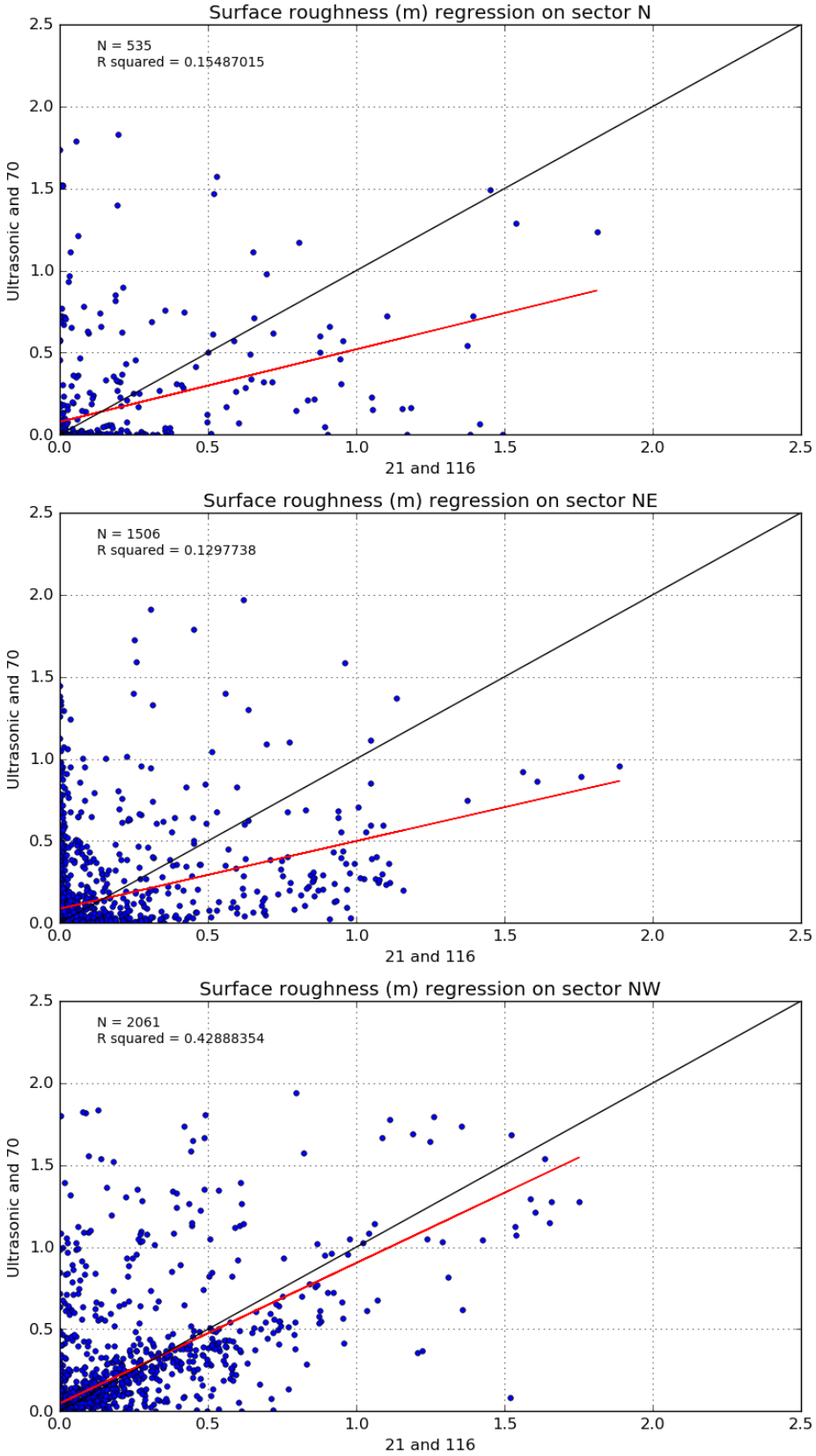

Figure 5.19. Comparison of logarithmic law z_0 between cup anemometers at 21 and 116 m, and ultrasonic anemometer at 21 m and cup anemometer at 70 m. Northern sectors.

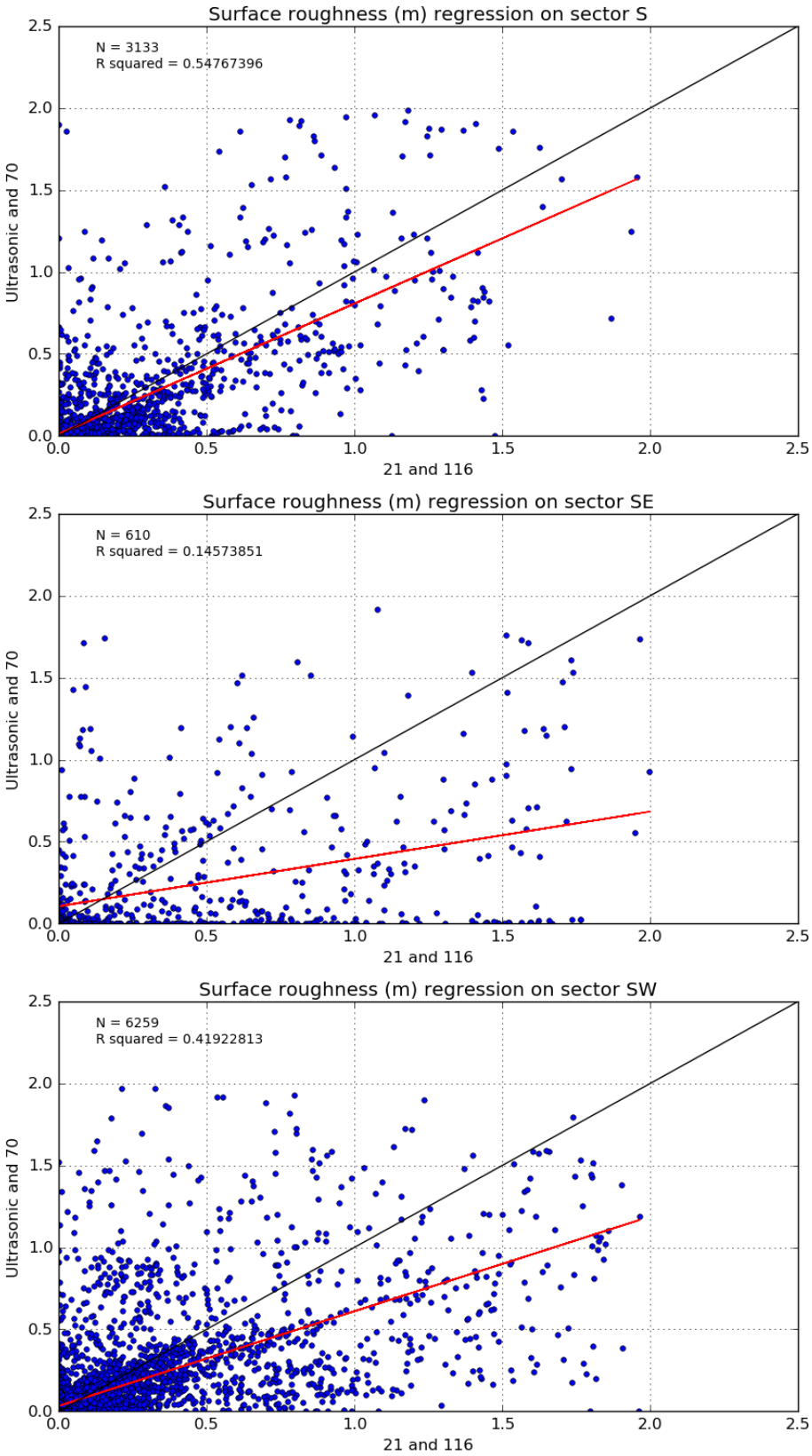

Figure 5.20. Comparison of logarithmic law z_0 between cup anemometers at 21 and 116 m, and ultrasonic anemometer at 21 m and cup anemometer at 70 m. Northern sectors.

The combinations 21/70, 21/116, Ultrasonic/70 and Ultrasonic/116 surface roughness lengths were compared between them in different regressions by sectors. First, in Figures 5.15 and 5.16, 21/70 and Ultrasonic/70 were tested. For all the sectors the regressions line was close to the line 1:1. The correlation coefficient was above 0.8 excepting the NE and SE sectors where R^2 was 0.57 and 0.63 respectively. In all sectors, z_0 reached high values, above 0.1 m.

The regressions between 21/116 and Ultrasonic/116 in Figures 5.17 and 5.18 showed similar results than Figures 5.15 and 5.16. For all sectors R^2 was above 0.8 excepting the SE sector with 0.75. The regression line was again close to draw a line 1:1. High z_0 values were observed in Figures 5.17 and 5.18; these were slightly higher than values observed in 5.15 and 5.16.

The last two figures, 5.19 and 5.20, represent a comparison between 21/116 and Ultrasonic/70 surface roughness lengths. In this case, the correlation coefficient was always below 0.6. The regression line pointed to higher z_0 for 21/116 than Ultrasonic/70. However, high z_0 values were still present.

Results from Figures 5.15 to 5.20 showed disagreement in the number of points per sector. This information was summarised in Table 5.5. Although the number of points was not the same by sector, they all are in the same range. The total number showed lower values when the cup anemometer at 70 m was used. Thus, Figures 5.15, 5.16, 5.19 and 5.20 contained fewer points than Figures 5.17 and 5.18 where the cup anemometer at 70 m was not used.

	Fig. 5.15 & 5.16	Fig. 5.17 & 5.18	Fig. 5.19 & 5.20
N	529	670	535
NE	1,503	1,527	1,506
NW	2,060	2,095	2,061
S	3,109	3,165	3,133
SE	533	776	610
SW	6,236	6,306	6,259
TOTAL	13,970	14,539	14,104

Table 5.5. Number of points from Figure 5.15 to 5.20 by sectors.

5.4 Discussion

Satellite remote sensing techniques over the ocean are able to retrieve wind vectors. These represent neutral wind speed at 10 meters over the sea level. This affirmation is true as long as a convenient GMF is used since not all of them retrieve neutral winds. The fact that neutral wind speed is obtained does not mean measurements were taken under neutral atmospheric stability conditions. Hence, only data under neutral conditions were included in this chapter. A calculation of atmospheric stability correction would be necessary to include the full dataset in the analysis.

Another issue is the necessity to extrapolate wind speed to hub height if satellite datasets are going to be used by the wind industry. Following the well-known logarithmic law, Eq. 2.5, wind speed could be extrapolated. In order to do so, surface roughness length, z_0, and friction velocity, u_*, must be parameterized. A compilation of methods was explained and tested for both u_* and z_0. Results were contrasted with ground measurements through linear regressions.

The first parameter under discussion is u_*. It was assumed that the friction velocity calculated from the wind profile was a correct measurement. Hence, all different methods of u_* parameterization were compared with that u_*. Once u_* was calculated, it was expected to find a correlation 1:1 or similar, i.e. slope of linear regressions equal to 1. The results obtained are far from the ideal slope. The Maat method reached the highest slope with 0.426. For the rest of the methods, the slope was lower than 0.36. Even when the existence of a linear correlation was obvious, it was clear there was a lack of agreement with in-situ measurements. All regressions did not reach a high R^2, with a maximum of 0.087 for Fetch_iter. All methods were underestimating u_* according to anemometer measurements.

Extrapolated winds were calculated through Eq. 2.5, meaning a directly proportional relationship between wind speed and friction velocity. Consequently, a lower calculated wind speed at 116 meters than the real wind speed measured by a cup anemometer at the same height could be expected. However, that was not the case according to Table 5.1 with wind speed regression results. Although R^2 values were not higher than 0.804 excepting the combination of Log_law with Insitu u_*, slopes near unity were

achieved. As expected, there was a direct relationship between u_* slopes and wind speed slopes. The best slopes were found when u_* was calculated through Wave_iter, Hersbach, Wu, Iterated or Fetch_iter, by this order. Those slopes were 0.990, 0.958, 0.949, 0.943 and 0.903; which were related to u_* regression slopes of 0.222, 0.193, 0.184, 0.179 and 0.152 respectively. This relationship was also observed for the rest of the u_* methods. In Table 5.1 Insitu and Maat obtained very high slopes since their u_* slope was high; in the case of Toba it was exactly the opposite.

When in situ u_* was used the lowest R^2 and the highest NRMSE and bias were found. This was not expected since u_* was directly measured. In fact, using in-situ u_* should have reached the best results of the table. Nevertheless, the best regressions were found with u_* regression slope between 0.16 and 0.2. The reason for this was explained by observing z_0 regressions. Calculated z_0 from these methods should have also reached similar values than z_0 extracted from the wind profile through Eq. 2.7. This was not observed in Fig. 5.6. Calculated z_0 was always low with slopes close to 0. Thus, all z_0 methods underestimated the real z_0. This fact is compensating an underestimated u_* when wind speed was extrapolated. According to Eq. 2.5, the higher u_*, the higher the extrapolated wind speed. Also, the lower z_0, the higher extrapolated wind speed. Then with a low, u_* it was expected to calculate a low U_{116}, but, because z_0 is also low, the final U_{116} calculated by the different methods is similar to the one measured by the meteorological mast. Even when both methodologies for u_* and z_0 were wrong, an accurate slope in wind speed regression was achieved by compensation. This effect can be assumed for all the z_0 methods even for those where the z_0 regression was not shown because all z_0 methods achieved similar results. Significant variations in the results were only observed between different u_* methods. This means their calculated z_0 was as low as the methods shown in Fig 5.6. For that reason, it is also expected to find similar results in age methodologies for z_0 where it is combined with Eq. 2.5 and solved by iteration.

There was one exception to all explained in the previous paragraph. Following the same explanation of Eq. 2.4, the Log_law was the best method for z_0 parameterization showing the maximum R^2, 0.9, combined with in situ u_*. Through this equation, z_0 was adjusted to compensate for the

underestimated u_*. That is the reason Log_law always achieved an R^2 over 0.7 and slope near to one. Even so, it does not mean the calculated z_0 is the real surface roughness length. For this reason, the combination of Log_law and Insitu u_* reached a similar regression than a comparison of wind speed at 10 meters. According to [96], regressions between ASCAT and in-situ measurements in the South China Sea achieved a correlation coefficient between 0.8 and 0.92 at 10 meters. In this study, a correlation R^2 of 0.9 at 116 meters was achieved. The location of both studies and heights were different, winds were not extrapolated in the previous study, but the same (or the same type of) remote and ground devices were used in both analyses. Therefore the lack of accuracy by Log_law and Insitu u_* could be produced for the same reasons than in [96]. These are lack of accuracy by spaceborne devices, ground devices, algorithms for signal processing and GMF; but not by this combination of methods to extrapolate winds. Plus this proved Insitu u_* as an acceptable control for u_* methods. Even so, it cannot be considered the best wind speed regression due to NMRSE and high bias values. This position was achieved by the Wave_iter method.

An interesting comparison is between Iteration and Fetch methods and the rest, i.e. methods without sea parameters and those using sea measurements. Since the availability of quality data is low, methods with fewer parameters in their equations are preferred. In Table 5.1 and regressions were shown that Iteration and Fetch_iter obtained the best statistics or were near to the best. The Iteration method should be the chosen one over Fetch_iter since this does not need to know the fetch. A part of that, the weak point of Fetch and Fetch_iter methods are in Eq. 5.16, where the inverse of wave age was calculated as a function of fetch and wind speed. Duration of the wind is also a parameter to take into account in order to know the wave age. The sea needs a minimum period of time to achieve a fully developed sea. The duration of wind should be also included in Eq. 5.16. Nevertheless, in this study it was assumed to have a fully developed sea when Fetch and Fetch_iter methods were used. According to Table 5.2, this was only true for 32 measurements out of 229.

Previous studies did not compare z_0 from wind profile and z_0 calculated from their own methods. Instead, comparisons or regressions of drag coefficients were shown. All of them obtained a fair correlation for every single method

explained in material and methods section. When authors compared different equations, they found small differences, [103] and [106]. Excepting [95], not one of the mentioned studies used measurements from a meteorological mast. Unlike this study, researchers used buoy data. Since they did not monitor the wind profile they could not extract z_0 from it. Here it was proved that all methods underestimate z_0. However, since all previous studies did not take place in Egmond aan Zee, all empirical coefficients may need to be recalculated.

When regressions were plotted according to different wave ages some interesting points were found, see Table 5.2. First, the best agreement with in situ data was found under decaying sea conditions. This situation is the easiest to parameterize since it is wind dominated and swell becomes less relevant. All four methods achieved a correlation around 0.9 but high values for NRMSE and bias. The slope of linear regression was slightly higher than general results, but this could be due to a small amount of data points, only 32. Under a calm sea, all results were very similar to the general results. Better slopes were observed but lower R^2 in comparison with decaying sea results. According to previous studies, under growing sea conditions parameterizing z_0 is very challenging. There are two reasons for this, first the possibility of finding a swell dominated sea; second, the growing sequence of wind-generated waves. Under growing seas, waves change their profile with time, unlike calm or decaying seas where the wave profile is constant in absence of swell. None of the methodologies for z_0 was found to fit perfectly for all wave ages by authors. As a proof, results for growing seas in Table 5.2 showed less correlation than any other sea condition. NRMSE and bias were smaller for growing seas due to a low number of measurements for other sea conditions. Nevertheless, there was still missing a correlation in z_0 regression for the best case, fully developed sea, as shown in Fig. 5.9.

Results were also divided by different wave heights as shown in Table 5.3. Unlike wave age results, Table 5.3, there was no improvement in regressions statistics. This was the case even for Wave_iter. This method incorporated wave slope, and hence wave height, in its equation. Due to this fact, it was expected to observe no relevant difference between different wave heights. However, this was not reflected in the present results. All four z_0 methods followed the same trend for each wave height. Again, as with previous

regressions, z_0 graphs in Fig. 5.11 showed no correlation. Calculated z_0 was always too low in comparison with the wind profile z_0 as calculated by Eq. 2.7.

The last regressions shown in Table 5.4 were classified by wind speed at 10 meters. Researchers found a lack of precision for satellite retrievals under low and high winds, <5 m/s and >15 m/s respectively. Therefore it was expected to find an improvement in wind speed correlation after removing low and high winds. Nevertheless, a deterioration in regressions parameters R^2 and slope was observed. On the other hand, NRMSE and bias remained under acceptable values, lower than one. Even so, regressions for mid wind speeds, 5-15 m/s, found much better agreement than low and high speeds. There was no relevant difference between z_0 methods. Regressions for z_0 in Fig. 5.13 showed the same trend as all previous results with low and almost constant z_0. Considering all regressions from Tables 5.2, 5.3 and 5.4, the only improvement was found when wind speed was extrapolated under fully developed sea conditions. However, the fact that u_* and z_0 are always underestimated calls into question the improvement.

The final results were a surface roughness length crosscheck since uncommon high z_0 values were observed. Four different anemometers from Egmond aan Zee were used to calculate z_0 through the logarithmic law. In Figure 5.14, the pair of anemometers at 70 and 116 metres was overestimating z_0, although followed similar trend than the other four pairs of anemometers. From Figure 5.15 to 5.18, regressions were made between pair of anemometer where only the lowest anemometer was different; i.e. a cup anemometer or ultrasonic anemometer at 21 metres both. The fair agreement found in those figures means a good agreement between the cup and ultrasonic anemometers at 21 metres. The last two figures, 5.19 and 5.20, did not show the same agreement. If the agreement between the low anemometers was proved, the lack of agreement must come from anemometers at 70 and 116 metres. Furthermore, this could be the reason for an overestimated z_0 in Figure 5.14 when the pair 70/116 metres was used to calculate z_0. The disagreement in the number of points by sector between Figures 5.15 to 5.20 was due to the filtering out of missing values. Since the dataset by the anemometer at 70 m presented more gaps than the rest, Figures 5.15 and 5.16 had fewer points than 5.19 and 5.20 where the

anemometer at 70 metres was used only in one pair of anemometers. When the anemometer at 70 m was not used, Figures 5.17 and 5.18, the maximum number of points was observed.

5.5 Summary

The logarithmic law, as shown in Eq. 5.11 and widely used within the wind energy sector, is dependent on two parameters, friction velocity, and surface roughness length. As explained, different methods to calculate them have been suggested by many researchers. Before developing the satellite wind resource software further, it was important to identify the best methods for parameterization. Hence, in this chapter, all found methods in the literature review for u_* and z_0 were tested. Predicted parameters were compared with those calculated from the measured wind profile by an offshore meteorological mast, Egmond aan Zee.

First, the analysis compared both parameters, u_* and z_0, separately between those predicted by methods and calculated from the wind profile. Afterwards, the different methods were combined to extrapolate the wind speed. Thus, the accuracy in these methodologies could be compared with a measurable parameter instead of calculated u_* and z_0. In the end, 52 different combinations were analysed. Since many researchers found reasonable agreement for their methods under certain circumstances, the best four combinations were also analysed under different conditions. These were different wave age, wave height, and wind speed conditions.

Some reasonable regressions for extrapolated wind speed were achieved. However, this did not prove to validate any methodology. All the reviewed methods in this chapter showed a complete lack of correlation for z_0, even the selected best four methods. The methods for u_* also showed low correlation. None of the reviewed methods can be considered reasonable or acceptable.

6. Development of a method for surface roughness length parameterization over deep seas in absence of breaking waves

6.1 Introduction

Atmosphere-ocean exchange and interactions have become a relevant field of study for both the meteorology and the oceanography community. There is a clear consensus among researchers, air-sea interactions must be understood and modeled in order to describe ocean and atmosphere dynamics. Wind input on wave mechanics has been widely studied and there is a large amount of literature about it; [103], [109], [117], [119] and [120]. Even so, many questions in this field are yet to be solved. The effect of the sea state over the wind has also been studied; [101], [104], [105], [106], and [121]. Heat fluxes at the boundary layer, drag coefficient (C_d), surface roughness length (z_0) and wind stress parameterizations have been described on many occasions by researchers; [100], [106], [107], [111] and [112]. However, there is not a widely agreed formulation for them. The reason is the oceans complexity due to its non-static surface, unlike onshore theories. Thus, z_0 can be considered constant over the land but it is variable over the sea.

Some researchers studied different formulations for z_0. Most of these studies were based on Charnock's equation and the coefficient for z_0 parameterization. Over long periods Charnock's coefficient can be considered as constant, but there is a wide consensus on its variability and dependency of this coefficient on wave age; [106], [122] and [123]. Thus, researchers found rougher seas for young waves than for fully developed waves, [106]. Nevertheless, all methods described in the literature have been proven to underestimate z_0 in chapter 5. Plus, all of them incorporate empirical coefficients which were calculated from selected datasets in each study. These facts show the existence of a lack of knowledge for this field. Following previous studies where C_d and z_0 formulations were suggested, it was always necessary to know wave parameters. Most of the previous studies used single height wind vectors, usually from buoys at 3 meters height from still water level and after these were extrapolated to 10 meters. A complete wind profile was never included in these studies. Only a few

studies, [89], [95] and [124], where researchers were trying to extrapolate wind speed from low to high heights included wind measurements at different heights tracing the wind profile variability. However, in these cases, wave parameters were never included in their analysis. Consequently, wind and wave profiles were never combined into the same formulation.

Surface roughness is a key parameter to calculate the wind profile since the logarithmic law relies on it as does friction velocity (u_*). Under neutral atmospheric conditions, the logarithmic law is expressed as Eq. 2.4. This formula is widely accepted for both, ocean and land, at least under atmospheric neutral conditions, Ψ_s=0, and within the atmospheric boundary layer. Therefore, a universal formulation for z_0 over the ocean is necessary before using the logarithmic law to extrapolate wind speed to different heights. At present there is not a widely agreed formulation for z_0. This parameterization is relevant not only for oceanography and meteorology community but also for the offshore wind industry and wind scatterometry.

In scatterometry a confident model to parameterize z_0 could change the method to calculate wind retrievals from satellites. Instead of using a wind speed dependent GMF, a friction velocity or wind stress dependent GMF could be used. It is expect to reduce uncertainty since the backscatter is related to the wind stress instead of wind speed. Once the z_0 is known, the logarithmic law could be applied to calculate wind vectors at 10 metres. This new method could reduce the uncertainty related to the GMF. Furthermore, it will allow the calculation of the wind profile from satellites wind retrievals.

This chapter presents the development of a new formulation for z_0. The aim is to avoid empirical coefficients as much as possible. The present research was initiated as a development of a tool for offshore satellite-enabled wind resource optimisation, although satellite measurements were not included here. However, due to satellite data with spatial samples at 10 meters, ground data with measurements at different heights but the same point, has been adapted to be compared with them.

6.2 Datasets: description and processing

In order to validate new formulations for both, z_0 and C_d, two different meteorological masts were chosen. These were Egmond aan Zee (EZ) and Fino-1 (F1), both are included in the NORSEWIND database, [4]. There are more available meteorological masts, but only EZ and F1 have been monitoring wave and sea parameters, and atmospheric and wind conditions at different heights. Wind, waves and sea parameters at different heights and depths are not commonly monitored for the same location. Hence there were no other feasible locations to undertake the validation. Furthermore, due to the application of filters to the datasets, the amount of data can be drastically reduced. Another common issue is accessibility to data since this can be commercially sensitive. All these facts create complications regarding the availability of data to accomplish the required validation.

6.2.1 Egmond aan Zee neutral stability

The first meteorological mast was EZ, located in front of the Netherlands coast (4.419°E, 52.606°N). This mast, installed by NoordzeeWind, has been monitoring wind, waves, and sea since November of 2003. Offshore wind farms around EZ can produce wake effects and turbulence in the wind vector. In Figure 5.1 three offshore wind farms are represented. Prinses Amalia and Eneco Lochterduinen are both too far from EZ to create a problem. The third offshore wind farm was constructed at the same location of the meteorological mast. Since 2006, 36 wind turbines were erected and have been operating until the present.

In this study, only data from July of 2005 to December of 2008 was used. The selected cup anemometers were those placed at 21 and 116 meters above still water level. Temperature (T), pressure and humidity were also monitored at those heights. Sea temperature was measured at different depths. Since it was necessary to know sea surface or low depth temperature, measurements at 3.8 meters depth were chosen. Obviously, wave parameters such as wave period and significant wave height (H_s) were also included in the study. The water depth of its location is 18.5 meters; therefore the location can be considered deep water as long as the wavelength of spectral peak frequency (L_p) is lower than 37 meters. These conditions were observed most of the time

(90% of the time) or only slightly exceeding the wavelength limit (10% of the time). Therefore deep water conditions were assumed at all times.

The logarithmic law, as presented in Eq. 2.4, was simplified to avoid parametrizations of atmospheric stability correction which would add more complexity as shown in Eq. 2.5. Under neutral stability conditions, correction is null. There are different methods to recognize neutral conditions. The simplest method is a comparison of the sea and air temperatures, for neutral conditions $T_{SEA} \approx T_{AIR}$. In this study, $T_{-3.8}$ was compared with T_{21m} allowing a difference of 1 °C to be considered neutral conditions. Another filter that was applied to the datasets was that only measurements were considered valid when there were no blanks or missing values for any parameter included in this study at the same time. Wind parameters were monitored every 10 minutes. However, sea and wave parameters were obtained every 30 minutes. Therefore it only a difference of 20 minutes between wind and sea measurements was allowed in order to be considered simultaneous values. In the end, 14,690 valid measurements were found.

Some parameters need to be calculated after filtering since these are not possible to measure directly on the field or were not monitored. These were wavelength at the peak of wave spectrum (L_p), z_0 and u_*. Commonly, for simplification and neutral conditions, Eq. 2.5 is written avoiding u_* and replaced by a second height wind measurement as appears in Eq. 2.6.

Surface roughness length was found through Eq. 2.7 for periods of 50 minutes and after u_* was calculated according to Eq. 2.8 for the same period. In this chapter, u_* from mast measurements was applied instead of calculated u_* from formulations with empirical coefficients. These obtained u_* and z_0 were considered as in situ and real values and therefore used as a control in this analysis.

6.2.2 Egmond aan Zee plus Satellites

Egmond aan Zee plus Satellites (EZS) dataset was based on the EZ dataset. The difference was the necessary overlapping in time with the Satellites datasets. In this study, only data from Quikscat and ASCAT were considered. Wind measurements from these two scatterometers were not used, only the retrieval time was taken into account. The reason to do this

overlapping is to compare with the methodologies previously studied in chapter 5. The methodology for filtering data and overlapping was already explained in chapter 5. Even so, only z_0 regressions are comparable with results from chapter 5 since different low-level measurements have been extrapolated. Wind vectors from satellites were extrapolated in chapter 5 unlike the present chapter were in situ measurements were extrapolated. Therefore, the extrapolated wind speed will differ between studies, when this is not the case for z_0.

Another consideration that must be taken to build and process this dataset is that the nature of satellite data and in situ data is different. Whilst satellite data is a spatial single height wind measurement, met mast measurements are wind vectors at the same place with different heights. With a satellite data resolution of 25 km and an average wind speed of 8 m/s (from EZ), the wind will need 52 minutes to travel this distance. Hence, it is more representative to compare 50 minutes averages from masts with satellite data. This fact caused problems in finding data without gaps or missing values, in order to find valid measurements. Even so, the final number of valid measurements with enough valid values including average measurements from 30 to 50 minutes was 239.

6.2.3 Fino-1 neutral stability

The other meteorological mast included in the validation was Fino-1 (F1). This mast is also located in the North Sea (6.59°E, 54°N). As shown in Fig. 4.1, there are 8 offshore wind farms in the area of F1. Due to the distance to the mast, only three of them must be considered as turbulence sources; Trianel, Borkum and more importantly Alpha Ventus. F1 was erected by GL Garrad Hassan Deutschland GmbH and it has been operational since 2003. However, in this study, only data from January of 2004 to November of 2011 was included. Different available device heights than EZ were selected for F1. Cup anemometers, vanes, thermometers, hygrometers and barometers at 33 and 90 meters were selected. In the case of sea temperature, 3 meters depth was chosen, F1 was also monitoring H_s and wave period. The meteorological mast is located in a place with 30 meters depth, meaning that for L_p<60m it is considered deep waters. According to measured period and calculated L_p, only 32% of the time measurements were taken under deep

water conditions. Processing and filtering data followed the same steps as for EZ, which were explained in section 2.1. Finally, a total of 980 valid measurements were found.

6.3 Background

6.3.1 Lettau's equation

Knowing the wind profile, or at least wind speed at two different heights allows the calculation of z_0 through the logarithmic law. When this is not possible a different method must be chosen. Over the ocean, Charnock's equation is usually selected even when Charnock's coefficient remains difficult to determine. Overland and based on a visual site survey Lettau's equation is a good approximation, Eq. 6.1, [125].

$$z_0 = C_d h^* s(n/A) \qquad (6.1)$$

Where C_d is the drag coefficient which took a constant value of 0.5 in studies, [125] and [126]. The effective obstacle height is h^*, s stands for silhouette or cross-sectional area perpendicular to wind direction, n is the number of obstacles and A is the area or domain under study. Note that $s(n/A)$ is named roughness density in [127]. Following Lettau's equation, only obstacles of the same shape can be included. In [125], the predicted z_0 is compared with the wind profile z_0 from other studies with a fair agreement. Furthermore, in [126], different methods for z_0 were compared to dust emitting surfaces. In the study different places were monitored and grouped together to plot regressions against wind profile z_0. Lettau's method did not achieve the best correlation for natural logarithm of z_0; however, it reached an R^2 of 0.756. All parameters included in this equation can be translated to wave parameters once wave geometry or shape is known.

Another method to calculate z_0 over land and widely used in the wind industry is the computation of orography of the area. Determining a Digital Elevation Model and slope of each point is possible in order to calculate z_0. Nevertheless, the selected method in this study was Lettau's equation.

6.3.2 Wave geometry versus wave age

According to the fundamentals of wave mechanics, waves present asymmetry every time wave steepness (H_s/L_p) increases or as waves approach the shore. Considering only deep waters, horizontal asymmetry can be neglected, which is only present when a wave experiences a reduction in phase speed (c_p) due to decreasing water depth. Only vertical asymmetry is present in deep waters. Because mature waves or fully developed seas do not present increments on wave steepness, these can be considered to be symmetric waves. On the other hand, young waves or growing seas can increase their wave steepness and so, present vertical asymmetry in wave geometry. Therefore, wave age indirectly defines the wave geometry.

As explained, many previous studies determined Charnock's coefficient as a function of wave age (c_p/u_*) and there is a good reason for this. Charnock's z_0 has been demonstrated to be $(u_*)^2$ dependant [128] and z_0 varied with wave age [129]. The highest z_0 was found for young waves and decreasing once the wave was fully developed. Some other studies used wave steepness to define Charnock's coefficient or directly z_0. Both, wave age and steepness parameters are ways to define wave geometry. However wave steepness is ambiguous, because it could reach the same values at different ages for different waves, depending on significant wave height and wave period (T_p). Plus it is not indicative of the presence of vertical asymmetry. In order to know the presence or absence of asymmetry it is necessary to calculate the wave profile which is possible if H_s and L_p are known. This is relevant because the presence of vertical asymmetry could be the cause of higher surface roughness for young waves.

6.3.3 The small amplitude and Stokes theories

The wave profile can be calculated through Stokes finite amplitude theory, [130]. This theory presents different orders, the higher order the more detailed and accurate the wave profile. The first order is also called small-amplitude theory, Eq. 6.2. This is applicable to symmetrical waves.

$$\mu(x,t) = \frac{H}{2} \times \cos(kx - wt) \qquad (6.2)$$

Where μ is the surface elevation above still water level, H is wave height, k is the wavenumber $2\pi/L_p$, w is the wave angular frequency $2\pi/T_p$, x is the position along the wave propagation, t is time and L is wavelength. Since the present study analysed z_0 on a short-term basis, plus was searching the full wave profile and not the position of a particle along time; Stokes theory for steady waves where t was neglected was considered. This simplification was also applied to second and fifth order formulas, Eq. 6.3 and 6.4 respectively. The easiest way to apply Stokes theory was published in [130].

$$k\mu(x) = \in \cos kx + \frac{1}{2} \in^2 \cos 2kx \qquad (6.3)$$

$$k\mu(x) = \in \cos kx + \frac{1}{2} \in^2 \cos 2kx + \frac{3}{8} \in^3 (\cos 3kx - \cos kx) + \frac{1}{3} \in^4 (\cos 2kx + \cos 4kx) + \frac{1}{384} \in^5 (-422\cos kx + 297\cos 3kx + 125 \cos 5kx) \qquad (6.4)$$

Where $\in$ is $kH/2$. According to [131], each theory has its range of application depending on H/gT_p^2 and $depth/gT_p^2$. For deep waters only the range of H/gT_p^2 is necessary to be known; from 0 to 0.001 for small amplitude theory (Eq. 6.2), from 0.001 to 0.0075 for Stokes 2nd order theory (Eq. 6.5), from 0.0075 to breaking waves point, H/L>1/7, for Stokes 5th order theory (Eq. 6.4). The maximum μ or surface elevation point is reached when $cos(kx)$ equals 1. H and L can be replaced by any other wave height or wavelength measurements in the above formulations. For cases where L is unknown but T_p is known, the dispersion relationship is used to calculate L (Eq. 6.5). For deep waters,

$$L = \frac{gT_p^2}{2\pi} \qquad (6.5)$$

Differences between these three theories are shown in Fig. 6.1. Small amplitude theory follows a symmetrical wave where L_T (length of wave trough) equals L_C (length of wave crest) and a_C (amplitude of wave crest) equals a_T (amplitude of wave trough). The 2nd and 5th Stokes theories represent asymmetrical waves where $L_T > L_C$ and $a_C > |a_T|$. Comparing between Stokes theories, the 5th order wave reaches higher a_C and L_T and lower a_T and L_C than 2nd order waves. It was expected to find different values of z_0 for the different waves represented in Fig. 6.1 even when they had same wave height and length. Presumably the aerodynamics of the wind flow should

behave differently in each case. It was assumed that the higher L_T and/or a_C, the bigger the wave area that would be impacted by the wind.

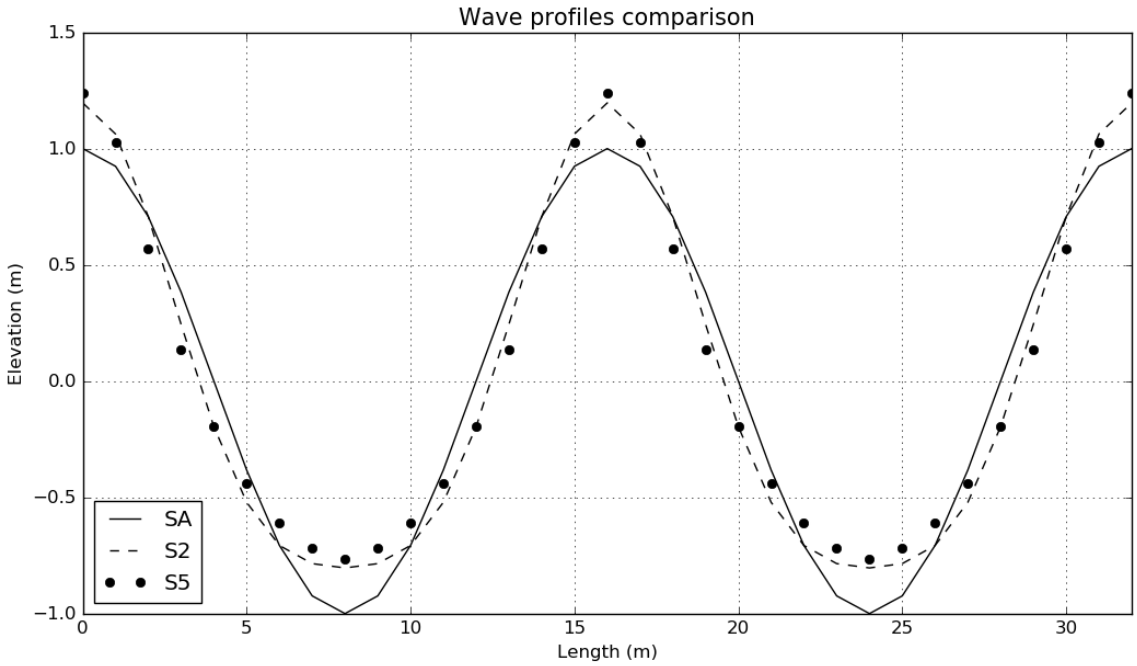

Figure 6.1. Comparison of wave profiles for small amplitude (SA), 2nd (S2) and 5th (S5) order Stokes theories.

6.4 Development of equation

6.4.1 Logarithmic law

In wind climatology assessment the logarithmic law is well known. Under neutral conditions, this is represented by Eq. 2.5 with Ψ_s=0 and replacing u_* becomes Eq. 2.6. In order to validate the methodologies for z_0 and u_* calculations in Equations 2.7 and 2.8, these have been tested for the EZS dataset. According to [127], u_* from wind profile is usually overestimated due to the adopted von Karman constant. Even if the correct κ is used, the reliability of the u_* calculation depends on the reliability of the z_0 parameterization. After both parameters were known, wind speed at 116 meters (U_{116}) was calculated following Eq. 2.5. Then, a regression between measured and predicted U_{116} was plotted as shown in Fig. 6.2. Linear regression, bias and Normalised Root Mean Square Error (NMRSE) were calculated. The correlation coefficient was 0.96 and slope of regressions line

was 1.006. Both parameters are representing a good agreement since they were very near to its perfect value, 1. NMRSE and bias were also near to 0, the best value, and there was just a minimal amount of scattering in Fig. 6.2. Hence, it was demonstrated that wind profile was calculated with accuracy through the logarithmic law with u_* and z_0 calculated values. Therefore, z_0 produced by application of Eq. 2.5 with in-situ measurements can be assumed to be the real values for wind speed. In the next sections, these in situ z_0 will be used to validate the predicted z_0.

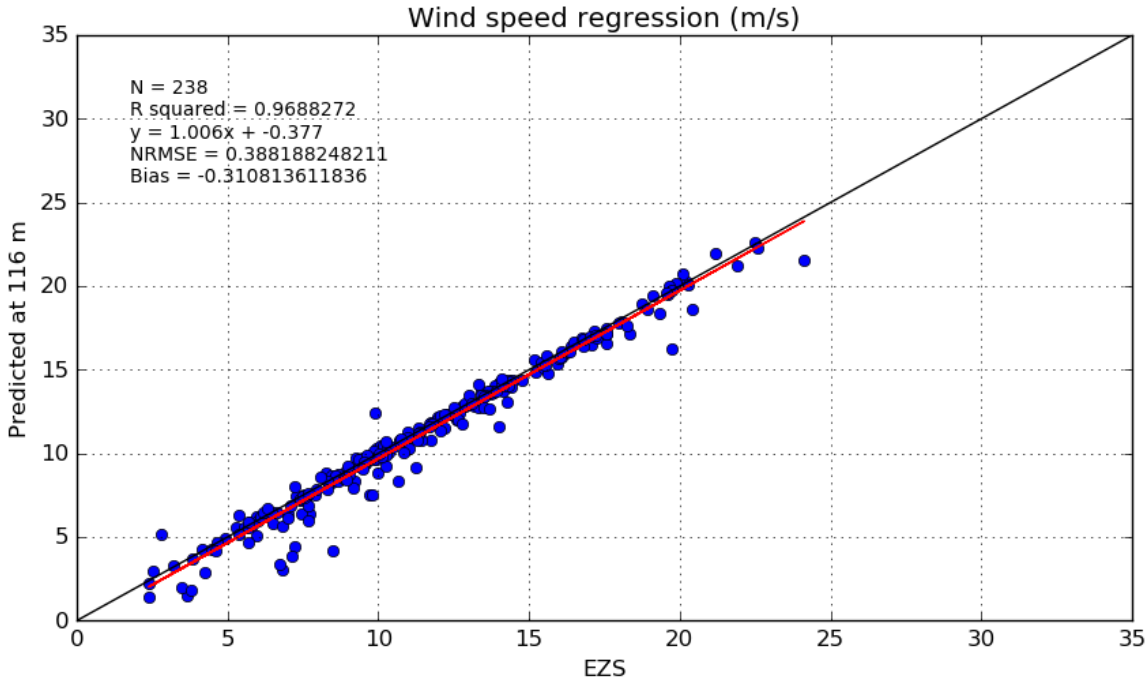

Figure 6.2. Wind speed regression at 116 meters between measured wind and predicted wind (Eq. 2.5) by in situ z_0 (Eq. 2.7) and u^* (Eq. 2.8). Red line is the regression line.

6.4.2 Adaptation of Lettau's equation to ocean waves

Once the wave profile is calculated, Lettau's equation can be translated or adapted for a square domain of area equal to W_A^2. The number of waves inside the domain will be equal to W_A/L_p. The silhouette, s, or cross section is the wave height per the wave width, $H \times W_w$. Instead of simply wave height, significant wave height, H_s, it was used. Over deep water, waves can be considered to exist in straight lines since there is no lateral displacement, along the crest. Also, wave refraction does not affect the shape since the

water depth is greater than $L_p/2$, only these cases are included. Therefore all points along the crest will have the same phase speed meaning that the wave will keep being a straight line. Thus, W_w=W_A if wave propagation is parallel to two sides and perpendicular to the other two sides of the squared domain. Substituting W_w by W_A and the rest of the wave parameters in Eq. 6.1 gives

$$z_0 = C_d \times H_S \times H_S W_A \times \frac{W_A}{L_p W_A^2} = C_d \frac{H_S^2}{L_p} \qquad (6.6)$$

In Eq. 6.6 it is implicitly considered that h^*= H_s, and this is probably not true as explained in the wave finite theories comparison section. The truth is that h^* is a function of wind speed, L_p or L_T, and H_s or a_C. In fact, the use of a_C instead of H_S is adequate in order to make a difference between symmetric and asymmetric waves, i.e. young and mature waves. Even so, there is a relevant uncertainty to determine h^*. Over the ocean it is widely assumed by researchers that C_d is a function of squared u_*, and the squared wind speed at 10 meters over the sea, U_{10}, Eq. 6.7. Then z_0 can be expressed as shown in Eq. 6.8. Note that roughness density is now equal to a_c/L_p.

$$C_d = \frac{u_*^2}{U_{10}^2} \qquad (6.7)$$

$$z_0 = \frac{u_*^2}{U_{10}^2} \frac{a_C^2}{L_p} \qquad (6.8)$$

6.4.3 Incidence angle correction

As long as wind direction and wave direction are equal then Eq. 6.8 is true. Since gravity waves are generated by wind it is not unreasonable to expect similar directions most of the time. However, by the presence of swell, a sudden change in wind direction or just Ekman's spiral [132], a relevant disagreement between both directions can be observed. In such cases z_0 can be strongly affected, z_0 will be reduced reaching its minimum for an incidence angle (θ) of 90° or 270° when waves present null cross-section area. Following Lettau's equation, Eq. 6.1, the silhouette is the cross-section area of obstacles along the wind direction. Hence, the wind direction was taken as the reference direction. As explained, for a straight wave s=$a_C W_A$ when both directions are equal.

As represented in Fig. 6.3, the perpendicular cross-section of a wave will not be W_A, it will be A or in other terms $W_A \cos\theta$. Then, adding the incidence angle correction into Eq. 6.8, Eq. 6.9, Lettau's adaptation, becomes Eq. 6.10.

$$z_0 = C_d \times H_s \times H_s W_A \cos\theta \times \frac{W_A}{L_p W_A^2} = C_d \frac{H_S^2 \cos\theta}{L_p} \qquad (6.9)$$

$$z_0 = \frac{u_*^2}{U_{10}^2} \frac{a_C^2}{L_p} |\cos\theta| \qquad (6.10)$$

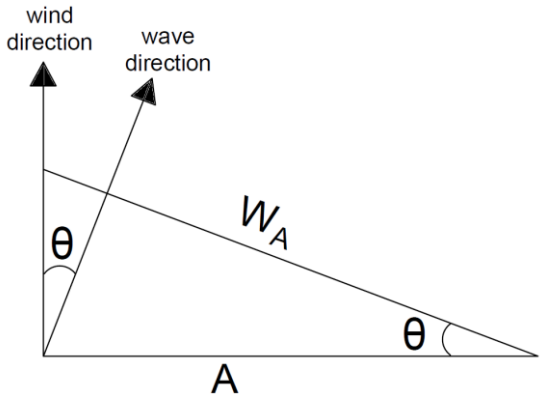

Figure 6.3. Incidence angle representation. W_A is equal to wave width and A is the cross-section perpendicular to the wind direction.

6.4.4 Total roughness equation

Different regimes for z_0 are known. These are smooth, transitional and rough regimes. In Fig. 6.4, the three regimes are shown, plotted against friction velocity. The rough line follows Charnock's equation with 0.018 as the Charnock coefficient. In most cases, the total z_0 is given by Eq. 6.11.

$$z_0 = z_0(smooth) + z_0(rough) \qquad (6.11)$$

Transitional roughness is normally neglected for practical applications. As shown in Fig. 6.4, smooth z_0 will only be relevant under very low wind conditions, when rough z_0 is almost null. Adding transitional z_0 is just an improvement for a small interval of u_*, but it can virtually increase z_0 for smooth and rough conditions. Hence, transitional z_0 was discarded in the present study. The rough regime equation in Fig. 6.4 should be substituted by Eq. 6.10.

Nevertheless, it is expected that Eq. 6.10 will follow a similar trend to Charnock's equation since both formulas are directly proportional to $(u_*)^2$.

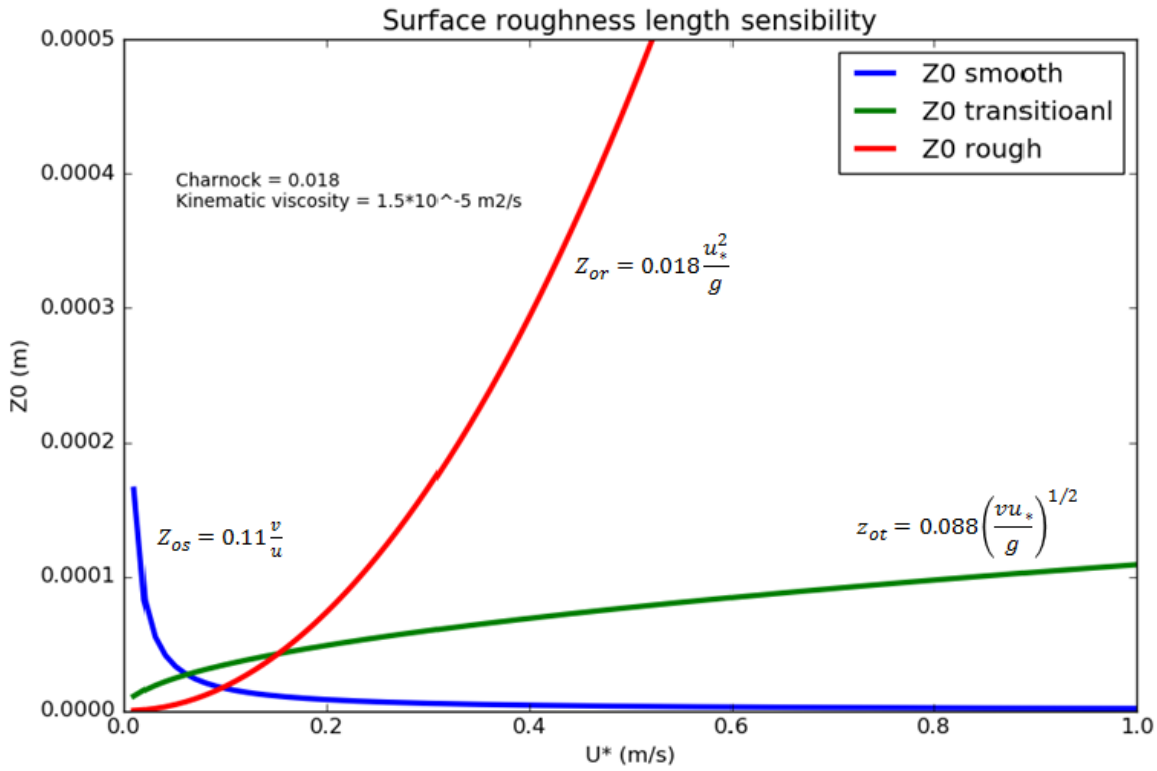

Figure 6.4. Surface roughness length against friction velocity for smooth (z_{0s}), transitional (z_{0t}) and rough (z_{0r}) regimes.

Thus, the complete equation for total z_0 is given by Eq. 6.12, where ν is the kinematic viscosity of air.

$$z_0 = 0.11\frac{\nu}{u_*} + \frac{u_*^2}{U_{10}^2}\frac{a_C^2}{L_p}|\cos\theta| \qquad (6.12)$$

Regressions for Eq. 6.12 showed a very low z_0 as shown in Fig. 6.5. Here z_0 was underestimated as it was by all of the other methods studied in chapter 5. Unlike the previous study where R^2 was below 0.05 (with the exception of one discarded case by the presence of compensation), here an R^2 of 0.75 was found. On the other hand, NRMSE was far from 0, considered the optimal value. The slope of regression line could be considered 0. Wind speed regression also did not show a relevant correlation. R^2 was too low, 0.489, even so, Eq. 6.12 reached a better correlation than previous methods when

compared with the results for in-situ u_* in chapter 5. The rest of the statistic parameters of the regression followed the same trend as the previous study.

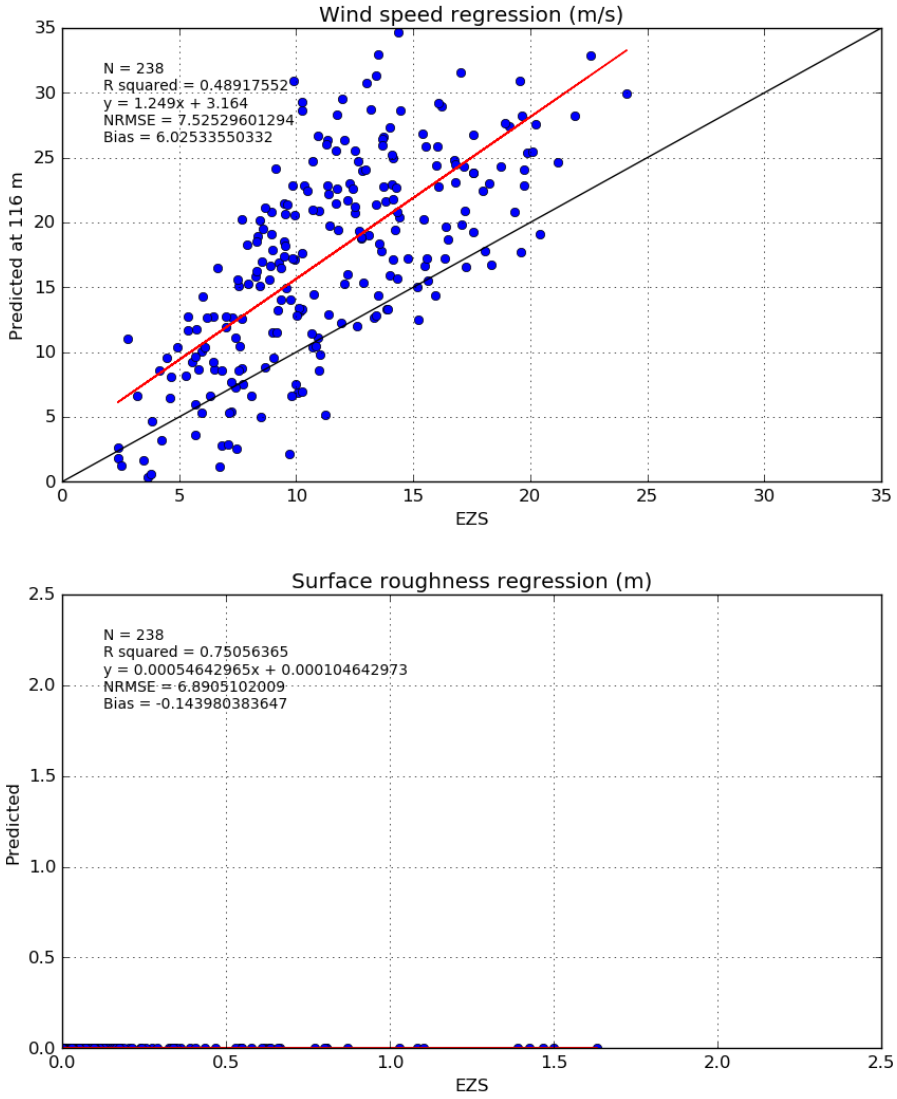

Figure 6.5. U_{116} and z_0 regressions for Egmond aan Zee overlapped with satellites dataset, according to Eq. 6.12.

Although it was not expected, a strongly underestimated z_0 was found, but the R^2 of the z_0 correlation was a step in the right direction, slightly confirmed by R^2 from the wind speed correlation. After the results in Fig. 6.5 it was obvious that something was missing. In terms of Lettau's equation, the cross-sectional area or silhouette could be underestimated and consequently z_0 would also be underestimated. The first reason for this could be the composition of the wave's effect. Sea surface shape is the sum of many

different sinusoidal waves, as can be observed in Fig. 6.6. Each singular wave can have different wave direction, H_s, L_p, and c_p.

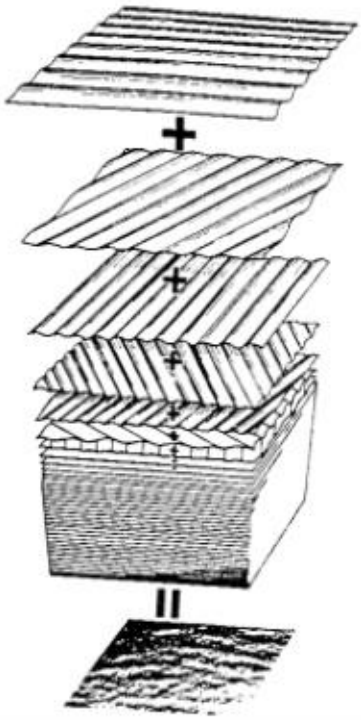

Figure 6.6. The composition of waves. Source: [133].

Considering a single, dominant wave, the composition of waves could increase slightly the total silhouette. But over a large area of the ocean, this effect may increase relevantly the total silhouette or i.e. roughness density. Another point is the existent homogeneity of the composition of waves even when the sea surface is non-static. This fact suggests the possibility of a constant, or almost constant, parameter to include the composition of waves, *cw*. Taking in-situ z_0, the coefficient *cw* can be found through Eq. 6.13.

$$z_0 = 0.11\frac{\nu}{u_*} + \frac{u_*^2}{U_{10}^2}|\cos\theta|\left[\frac{a_C^2}{L_p} + cw\right] \qquad (6.13)$$

Over the same number of measurements, 238, that were included in regressions; an average *cw* of 9.16 metres was obtained. Maximum, minimum and standard deviation found were 35.70, -21.34 and 10.87 respectively. The value of the standard deviation means that *cw* is not constant; on the contrary, it is indicative of high variability as maximum and minimum *cw*

confirmed. Even so, regressions with cw=9.16 metres were worthy of analysis. These are shown in Fig. 6.7 for both z_0 and U_{116}. Using this equation and value for cw a remarkable regression for z_0 was found. R^2 rose from 0.750 to 0.952, and the same trend was observed for the slope from almost 0 to 0.271. The slope was still far from 1 but the improvement was obvious. This enhancement was reflected in the U_{116} regression. R^2, NRMSE, and bias showed better values than before due to the reduction of scatter. The exact value of the coefficient cw did not affect the results since there was considerable variability in its selection but it did introduce an improvement into the regression. Hence, a sensibility analysis of the cw coefficient was undertaken in order to find the optimal value.

6.5 Sensitivity analysis

6.5.1 1st analysis on *cw*

As logic, the first sensitivity analysis was for the value of the cw coefficient, but this time including all three different datasets. In Fig. 6.7, where cw was equal to 9.16, the correlation coefficient R^2 was near unity i.e. near the best possible correlation. However, the slope was too low and far from its optimal value of one. This meant z_0 was underestimated by Eq. 6.13 with cw=9.16 m. Hence, the chosen interval of cw to study was between 4 and 38. z_0 all regressions are not shown due to their number. Instead, R^2 and slope values from z_0 regressions were plotted against cw coefficients in Fig. 6.8 thereby summarising all regressions. The first graph in Fig. 6.8 shows R^2 variability. As observed R^2 values remained constant for all three different datasets. This means cw has a very small or no effect on R^2 for the chosen interval. This is not the case for slope variability. Slope value is directly proportional to the cw value as shown in the second graph in Fig. 6.8. The intersection point of different datasets with the horizontal line for slope=1 was different for each dataset. The optimal values of cw were reached at 34, 36 and 33 for EZS, EZ, and F1 respectively.

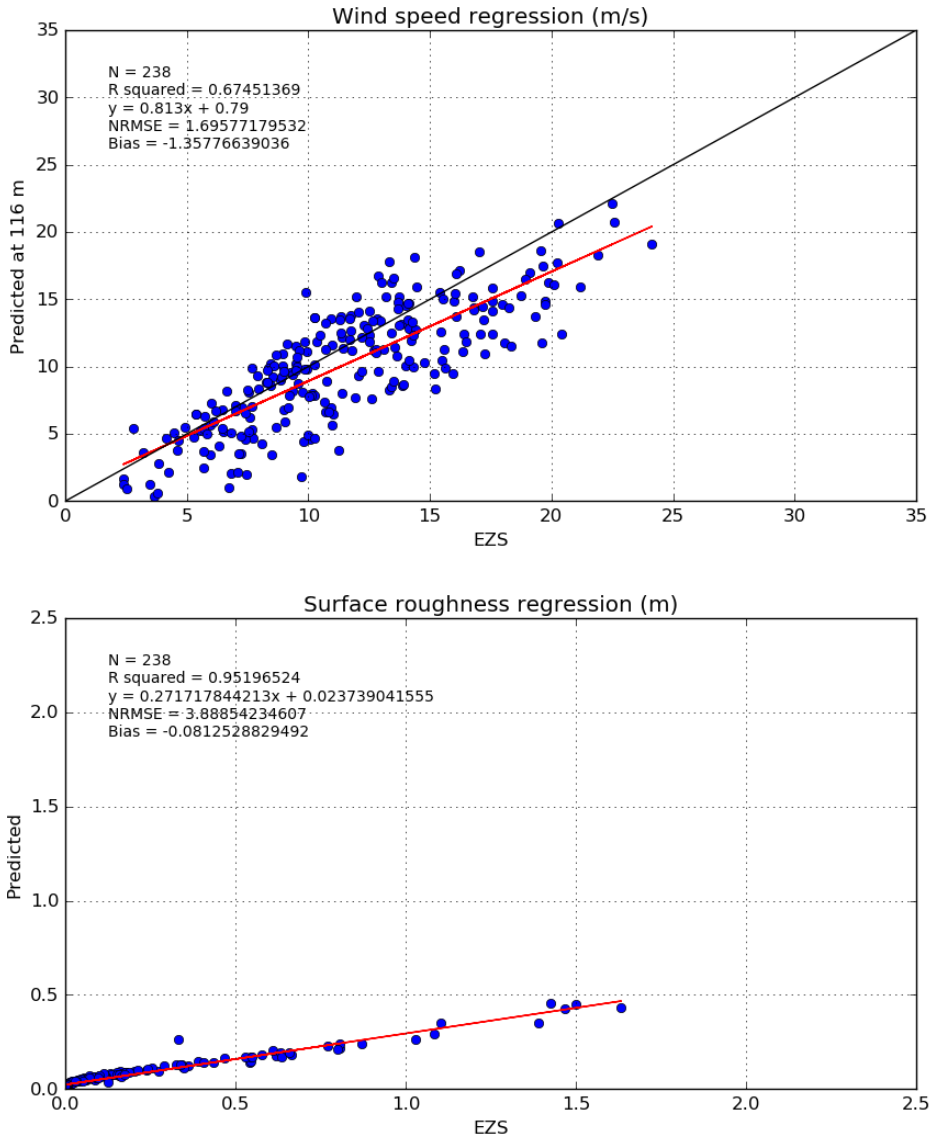

Figure 6.7. z_0 **and** U_{116} **regressions for Egmond aan Zee plus satellites dataset, according to Eq. 6.13 with** cw**=9.16 m.**

It should be noted that the optimal cw are much larger than ac^2/L_p. Hence ac^2/L_p can be neglected, and thus Eq. 6.13 can be simplified as shown in Eq. 6.14.

$$z_0 = 0.11\frac{\nu}{u_*} + \frac{u_*^2}{U_{10}^2}|\cos\theta|\, cw \qquad (6.14)$$

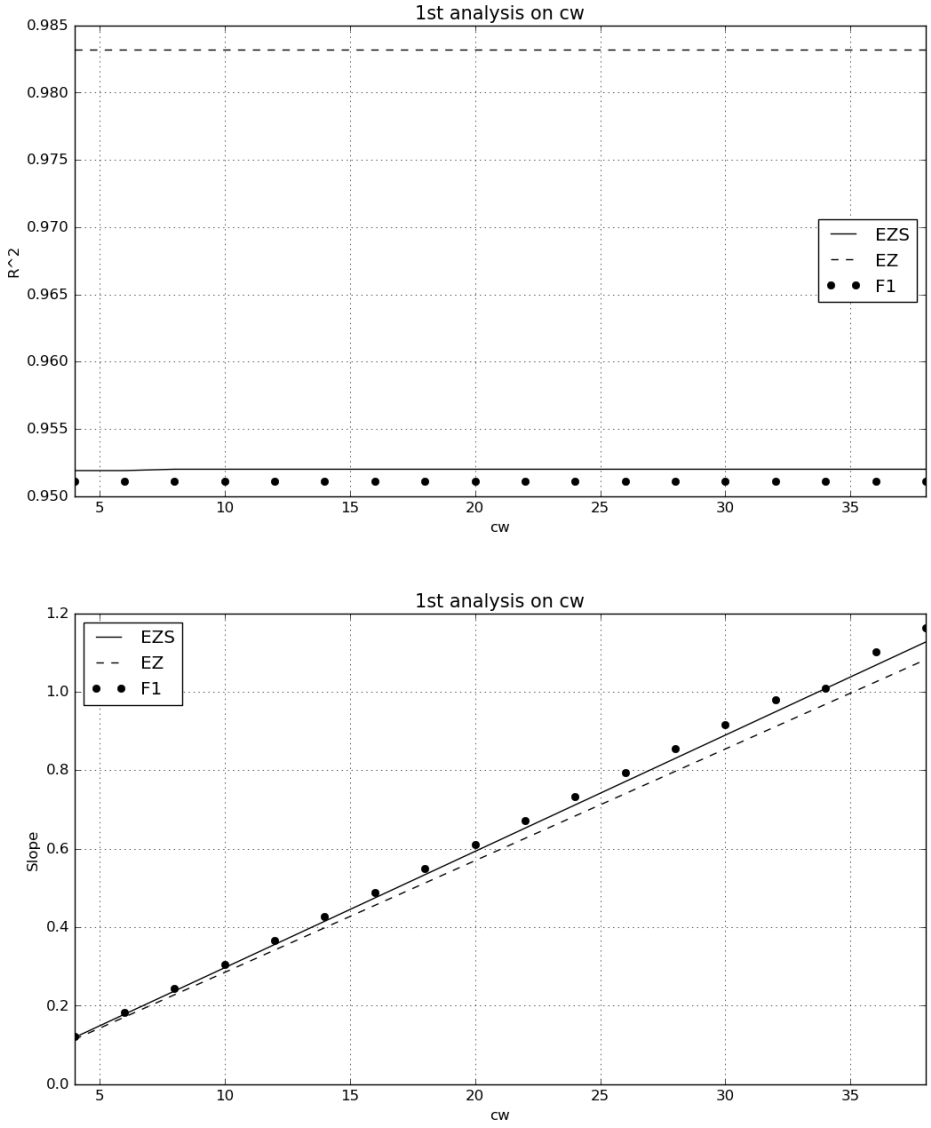

Figure 6.8. 1st sensitivity analysis on *cw* coefficient and its impact on R^2 and slope.

Each different dataset found a different optimal *cw*. Even so, this was inside a small interval, from 33 to 36. Calculated z_0 through Eq. 6.14 plus their optimal *cw* were compared with in situ z_0 in a regression again as shown in Fig. 6.9. A remarkable correlation was achieved where R^2 was above 0.95 in all three cases. As expected, all three slopes were very close to 1. The main difference was the presence of a small amount of scatter for Egmond aan Zee plus satellites. This scatter was not observed in the other two regressions.

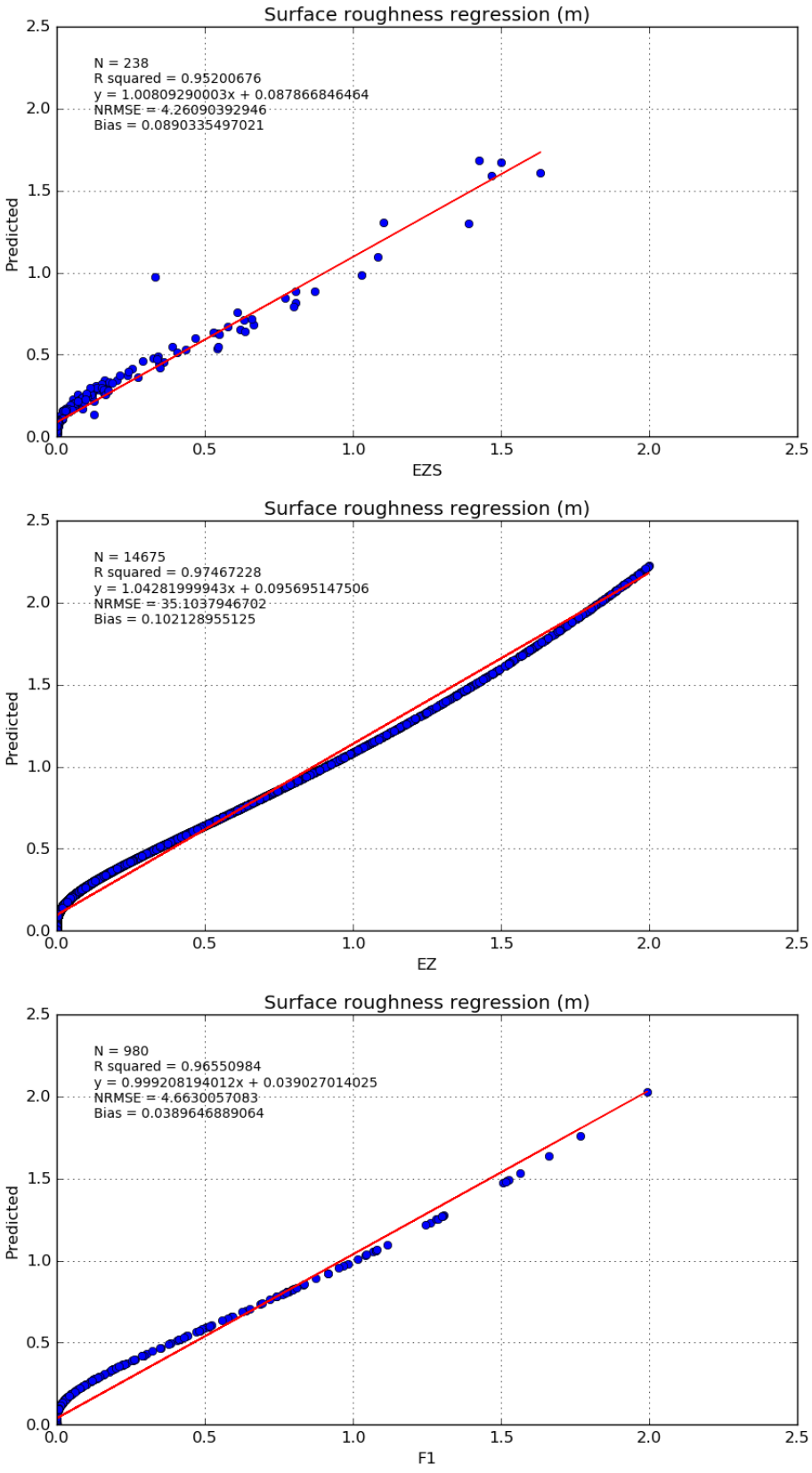

Figure 6.9. Surface roughness regressions between in situ z_0 and Eq. 6.14 model with optimal cw for three different datasets: EZS, EZ, and F1.

The reason was related to the nature of the datasets. Unlike EZS, data were consecutive in time for EZ and F1; furthermore in situ data was processed differently for EZS as explained in the datasets section. It was expected that regressions should follow a straight line $y=x$, but this was not the case. All three regressions showed a different function, which was $y^2=x$. This fact lead to a relevant disagreement for low values of z_0, where $z_0<1$. Small changes in this region are capable of producing a significant effect on extrapolated wind speed. Following the logarithmic law, the lower z_0, the higher extrapolated wind speed. This means that low extrapolated winds, in comparison with in-situ measurements, were produced because the predicted z_0 was overestimated. This condition occurred for $z_0<0.4$ as was shown in Fig. 6.9. It must be highlighted that this is the region with a higher density of measurements. Hence the importance of good correlation in that area. In order to solve this effect, a sensitivity analysis was undertaken for the exponent in the drag coefficient, which commonly takes 2 as its value.

6.5.2 Analysis of drag coefficient exponent

Another expression for Eq. 6.14 can be written with α as the drag coefficient exponent, see Eq. 6.15.

$$z_0 = 0.11\frac{\nu}{u_*} + \left[\frac{u_*}{U_{10}}\right]^{\alpha} |\cos\theta|\, cw \qquad (6.15)$$

Eq. 6.15 with the optimal *cw* coefficient for each dataset was studied in this section. The interval selected to study the drag coefficient exponent was from 2.00 to 3.00. Results of this sensitivity analysis are shown in Fig. 6.10. Following the same reasons as the previous sensitivity analysis, only results for R^2 and slope of z_0 regressions are presented. Unlike the *cw* analysis, R^2 did not remain constant. As observed in Fig. 6.10, there was an optimal C_d exponent in each case according to the value of R^2. Obviously, this optimal point was the maximum value of R^2. These points were 2.35, 2.35 and 2.65 for EZS, EZ and F1 respectively. In both cases for Egmond aan Zee datasets, the improvement was 0.01 in R^2 values. However, for Fino-1, the difference was larger with an enhancement of 0.03 in the R^2 value. The slope graph, Fig. 6.10, showed a decrease with a higher exponent. Hence once the drag exponent was replaced by the optimal value found in Fig. 6.10, another sensitivity

analysis for the *cw* coefficient was necessary. Otherwise, the slope would be below 1 again.

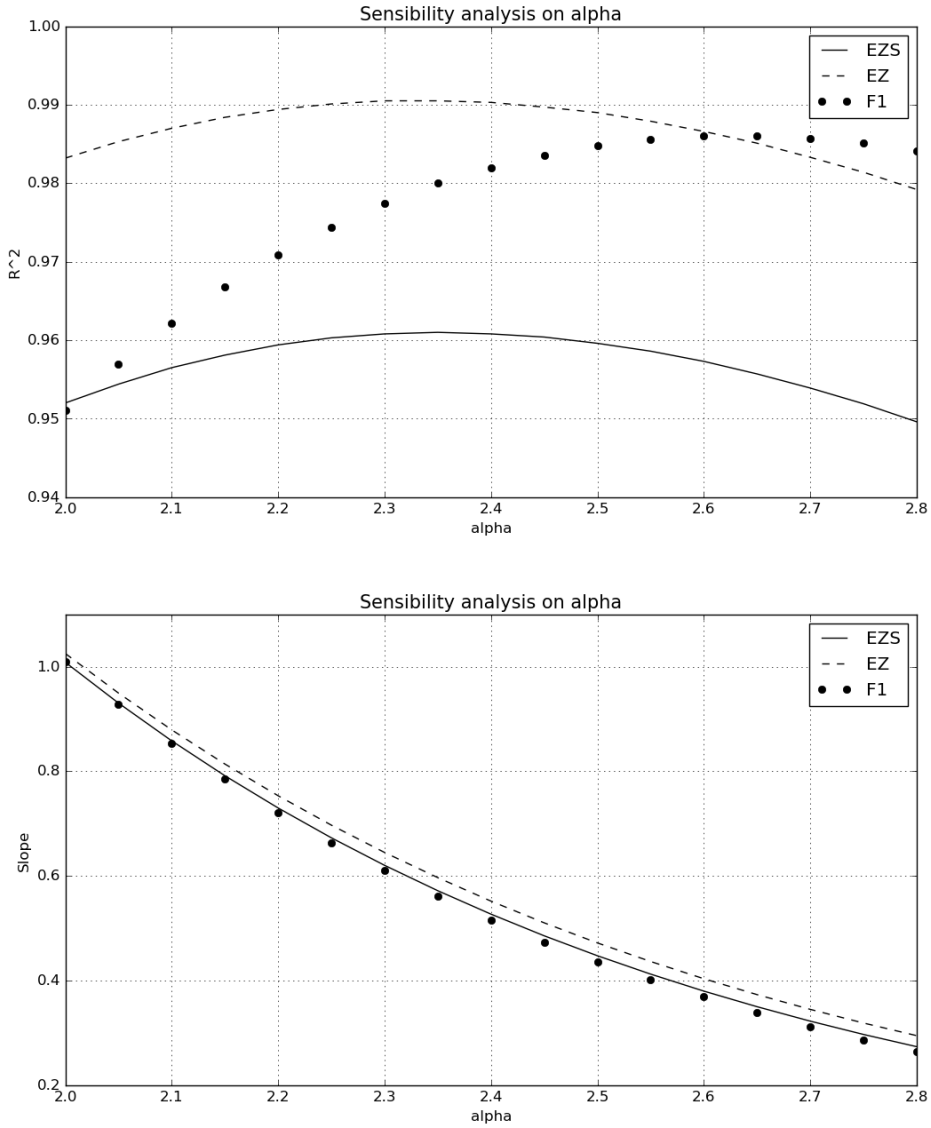

Figure 6.10. Sensibility analysis on α coefficient and its impact on R^2 and slope.

6.5.3 2nd analysis of *cw*

In this last analysis, the optimal *cw* coefficient was analysed again. z_0 was calculated through Eq. 6.15 with the best values found for drag coefficient exponent in previous sensitivity analysis. The same trend was observed in Fig. 6.8 and 6.11; R^2 was constant in all cases. The *cw* coefficient did not affect the correlation coefficient. Again as seen in Fig. 6.10, slope correlation from

Fig. 6.11 showed direct proportionality to the *cw* coefficient. However, there was a substantial difference between results from Fig. 6.8 and 6.11. This was the intersection point with a horizontal line for slope=1. In Fig. 6.11 these points were found at 60, 60 and 97 for EZS, EZ and F1 respectively. Intersection points were lower in Fig. 6.8 for all three cases. Also, these points were similar in the previous analysis, between 33 and 36, meaning a difference of only 8%. Now, following the results in Fig. 6.11, the difference between Egmond aan Zee and Fino-1 was a 61%. This was indicating that *cw* depends on the chosen dataset.

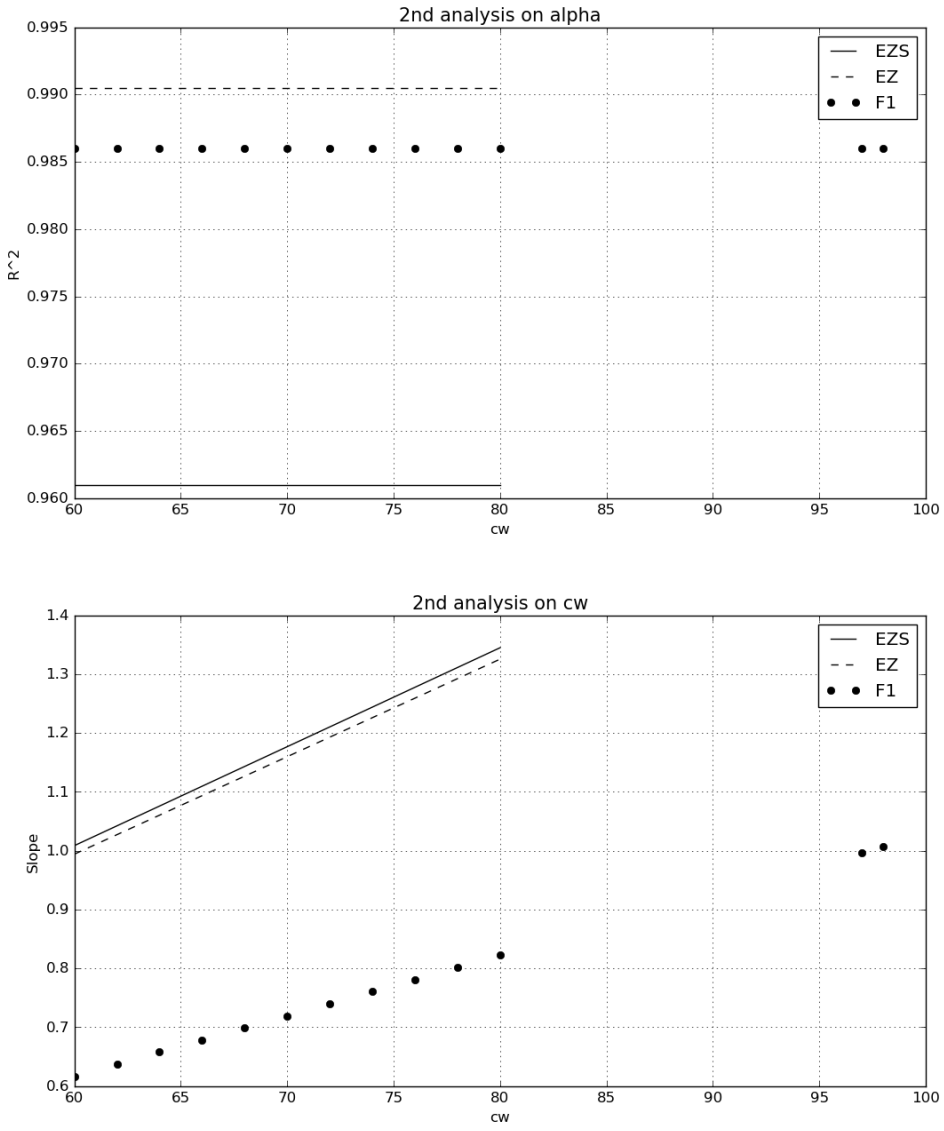

Figure 6.11. 2nd sensibility analysis on *cw* coefficient and its impact on R^2 and slope.

According to Eq. 6.15 and introducing the optimal α and cw found in Fig. 6.10 and 6.11 respectively, z_0 was recalculated and plotted against measured z_0 in Fig. 6.12. All slopes of the linear correlation were almost 1. The main and the most relevant differences between Fig. 6.9 and 6.12 were R^2 and the intercept coefficient. Achieved R^2 was higher in Fig. 6.12 with an increment of 0.01 for Egmond aan Zee cases and 0.03 for Fino-1. On the other hand, intercept values decreased until half of its value from Fig. 6.9. This means a better correlation for low z_0 values. As explained before this is important since most of the points were located when z_0<0.5. In the two cases where satellite data processing was not applied, R^2 was higher. However, regressions points are showing an overestimation of z_0 for values above 1.5. This fact is not a real problem since z_0 values over the ocean do not usually exceed z_0=1. The three regressions of Fig. 6.12 showed a high correlation since all R^2 coefficients were over 0.96

Such good correlation was not observed in Fig. 6.13 for the U_{116} regression, where the maximum R^2 was 0.77 for EZ. The slope in all three cases was below 0.8 and the nearest bias to 0 was -2.7 again for EZ. Egmond aan Zee results showed better correlations in all statistics with the exception of NRMSE. The lower amount of data the lower NRMSE was observed. As it was shown in Fig. 6.7, U_{116} was underestimated again. The reason was an overestimation of z_0 at very low levels, where most of the points grouped. This fact was showing the importance to parameterize z_0 under 0.5 where around 85% of points are located in EZ case.

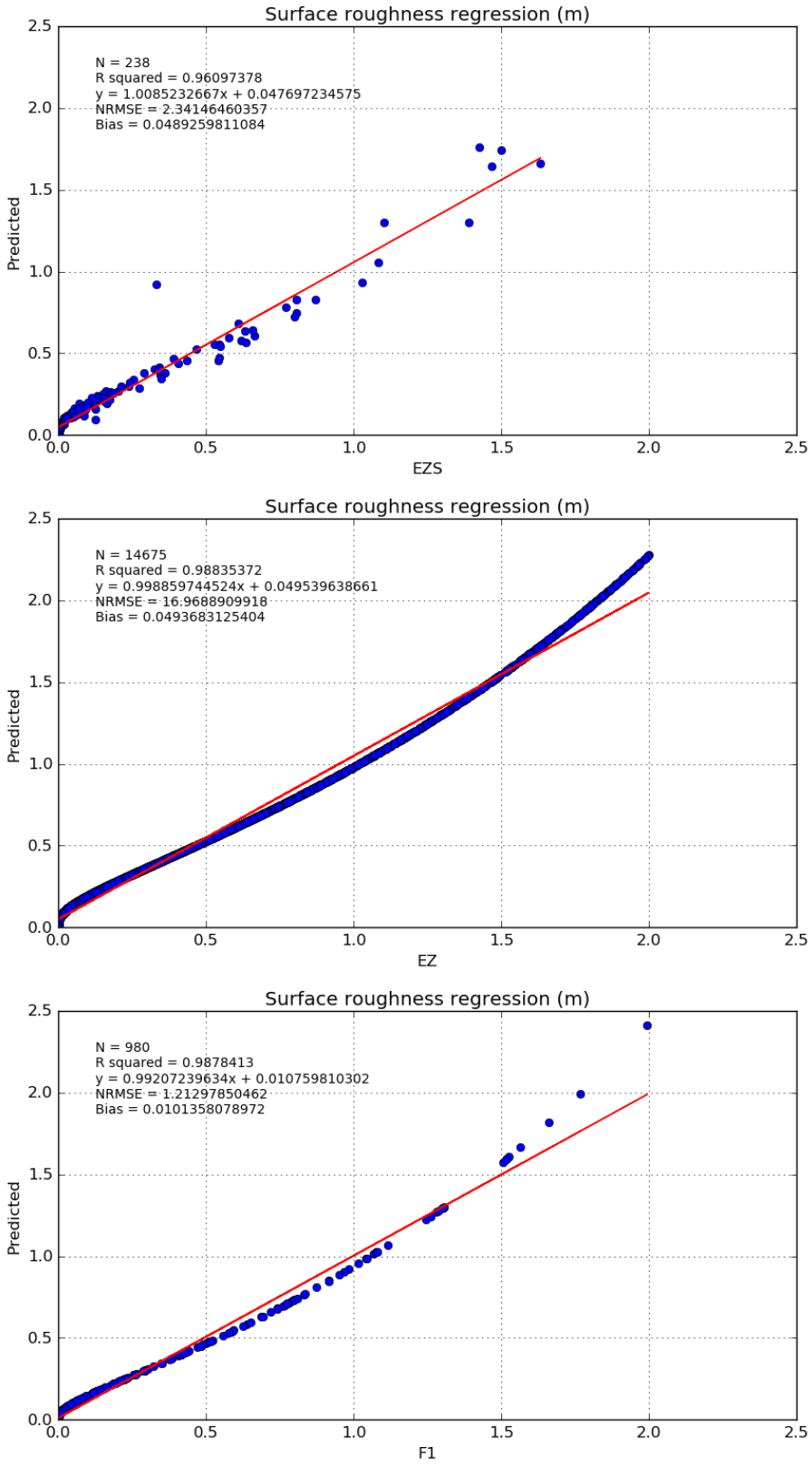

Figure 6.12. Surface roughness regressions between in situ z_0 and Eq. 6.15 model with optimal α and cw coefficients for three different datasets: EZS, EZ, and F1.

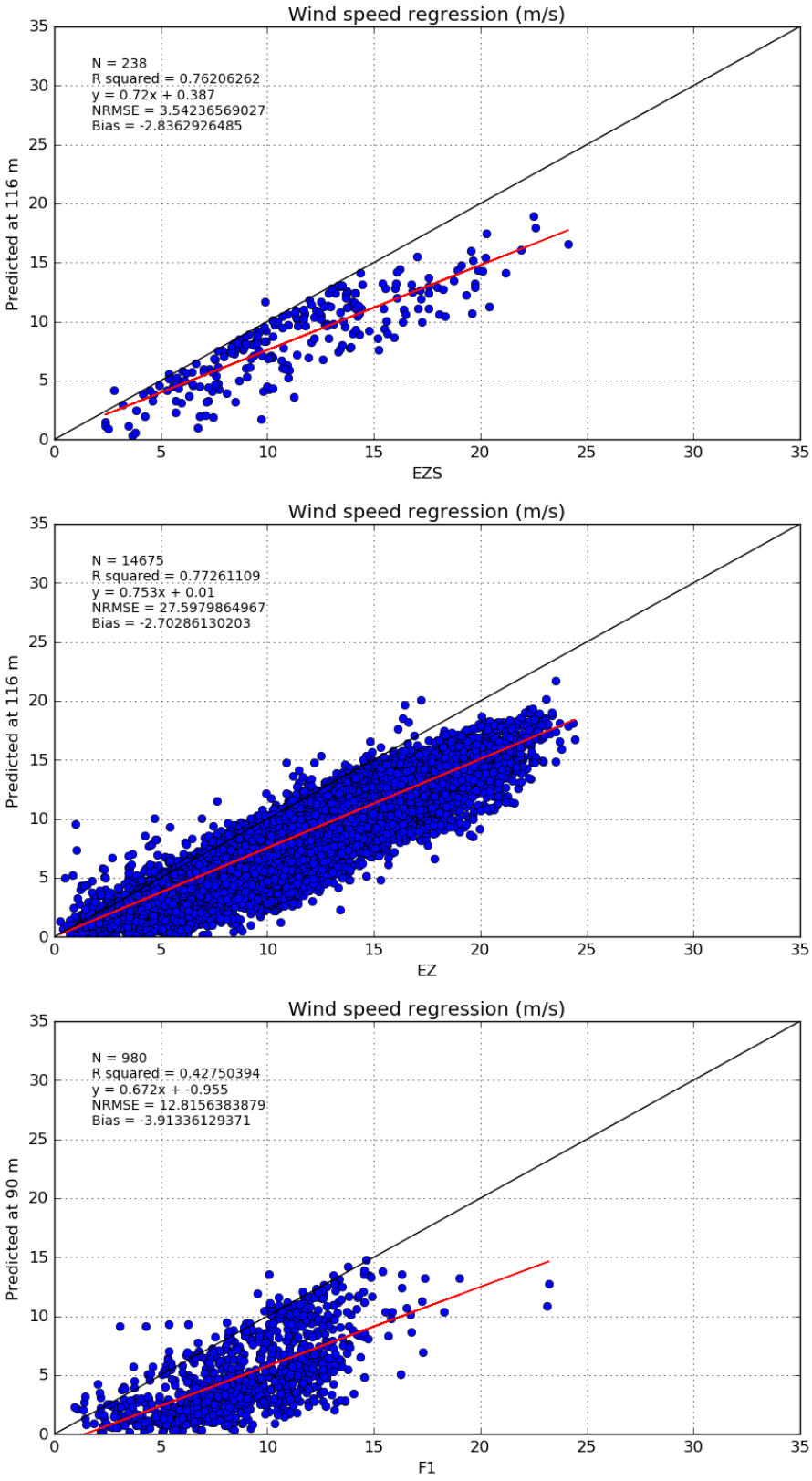

Figure 6.13. Extrapolated wind speed regressions between in situ z_0 and Eq. 6.15 model with optimal α and cw coefficients for three different datasets: EZS, EZ, and F1.

6.6 Substitution of empirical coefficients

Even when wind speed regressions in Fig. 6.13 showed lower correlation than z_0 regressions in Fig. 6.12, z_0 results showed higher agreement than any other z_0 method in comparison with the results from chapter 5. Therefore, Eq. 6.15 with the optimal empirical coefficients α and cw was considered to be the best method for calculating z_0. However, one of the aims of this study was to develop a method without the presence of empirical coefficients. Both, α and cw, are empirical coefficients and showed differences between locations. In the case of cw, these differences can be large as shown in section 6.4.3. Following all sensitivity analyses, the inclusion of physical parameters into the methods was proposed. For each case, the pertinent regressions were undertaken.

6.6.1 Analysis by similarity theory

The knowledge in boundary layer physics is still insufficient for certain situations. The similarity theory provides a method to analyse and merge variables, which helps to understand the physics involved. Similarity theory is based on the organization of variables into dimensionless groups. The right choice of groups can allow the discovery of physical relationships, [134].

There are four different steps in developing similarity theory:

1. **Select or guess the relevant variables for the situation.**

   For the logarithmic law, the chosen variables were $\bar{U}$, u_*, z and z_0. The goal was to describe the wind profile. In this thesis, the goal is to find the z_0 equation for offshore environments. Following Lettau's equation, Eq. 6.1, z_0 is dependent on drag coefficient. Hence, z_0, U_{10} and u_* variables were chosen. After the sensitivity analyses, the empirical parameters cw and α will be substituted by a physical parameter by guessing as the similarity theory indicates.

   The first sensitivity analysis was based on Eq. 6.14 where cw was analysed. The first tip for substituting cw was its units. According to Eq. 6.14, cw must have same units than z_0, i.e. it has the dimensions of length, i.e. meters. cw does not have to be necessarily a single physical

parameter; it could be the product of different parameters. Nevertheless, the optimal *cw* values found in Fig. 6.8 indicated an interval for *cw* between 33 and 36. These values were near the average wavelength in Egmond aan Zee with average L_p=23.7 m. Since L_p is also a length, the first option was to substitute *cw* directly by L_p.

The next step was the substitution of the coefficient α. As observed in Fig. 6.10, the optimal values of α were found between 2.35 and 2.65. This is not a wide interval of values, plus this coefficient must be dimensionless. The proposed approach is related to the von Karman constant, κ. Usually κ=0.4, then $1/\kappa$=2.5; thus the inverse of κ is near to the optimal α found. Furthermore, researchers found different values for κ, as it appears in [127]. According to the literature, κ could take values from 0.35 to 0.435 and therefore its inverse varies from 2.29 to 2.86. Both optimal values for α were inside the possible interval for inverse κ.

Finally, the chosen variables were: z_0, U_{10}, u_*, L_p and κ. Although κ is dimensionless and presumably constant, it was included after the sensibility analysis on α.

2. **Organize the variables into dimensionless groups.**

   At this point, the dimensionless groups are obvious since two variables are lengths, and the other two are velocities. Hence, the first group was z_0/L_p. The second group was, in fact, the expression for the drag coefficient with a different exponent, $(u_*/U_{10})^{1/\kappa}$. It was also considered the common expression for the drag coefficient, $(u_*/U_{10})^2$, for comparison.

3. **Perform an experiment; gather the data from previous experiments to determine the values of the dimensionless groups.**

   The datasets EZ and F1 were chosen in this point.

4. **Fit an empirical curve or regress an equation to the data in order to describe the relationship between groups.**

   The regressions are shown below for both datasets and for both drag coefficient expressions.

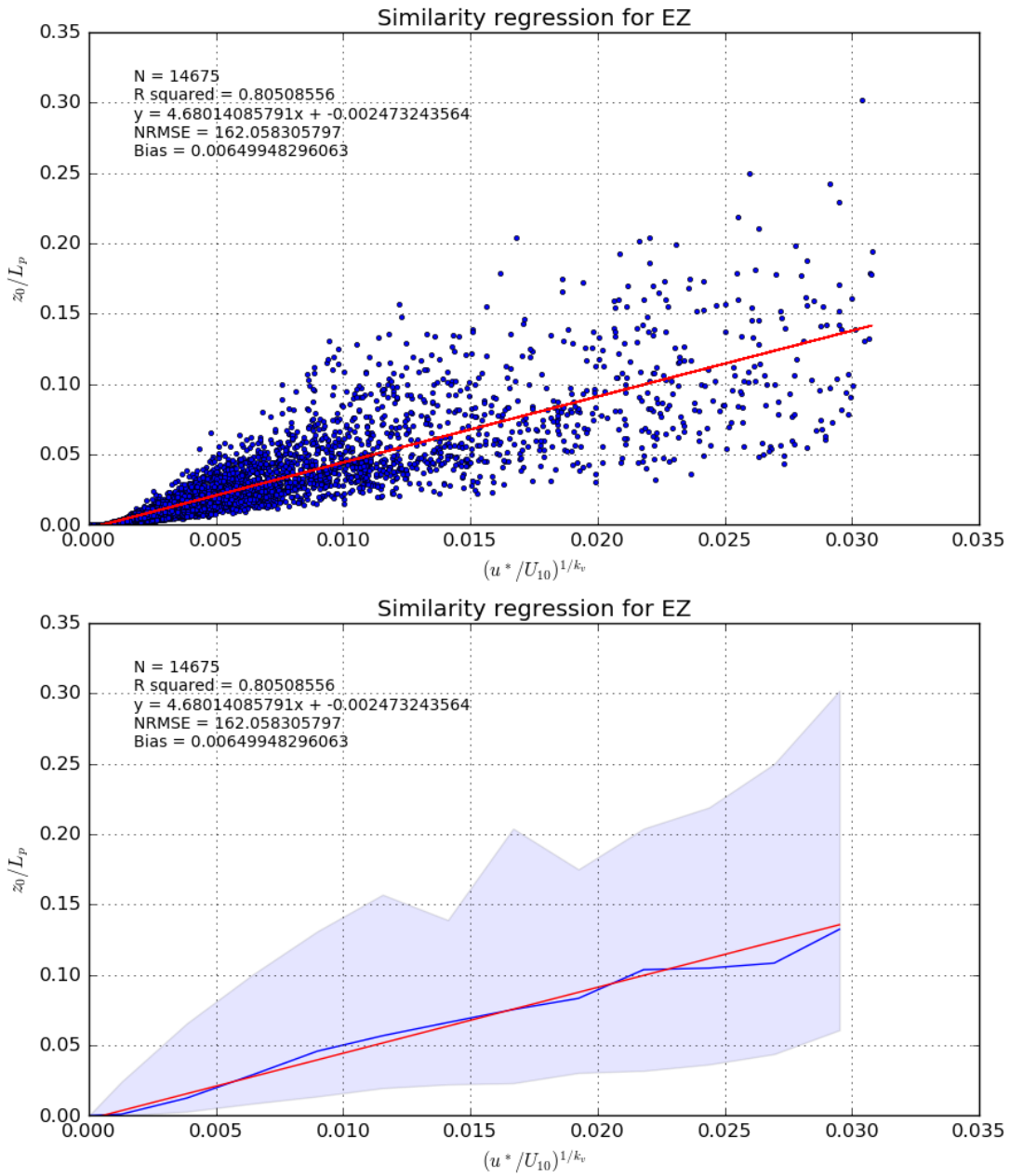

Figure 6.14. Regression for EZ with von Karman constant as k_v. The red lines are the regression lines, and the blue line is the mean value for each bin. The purple light area shows the interval of values for each bin.

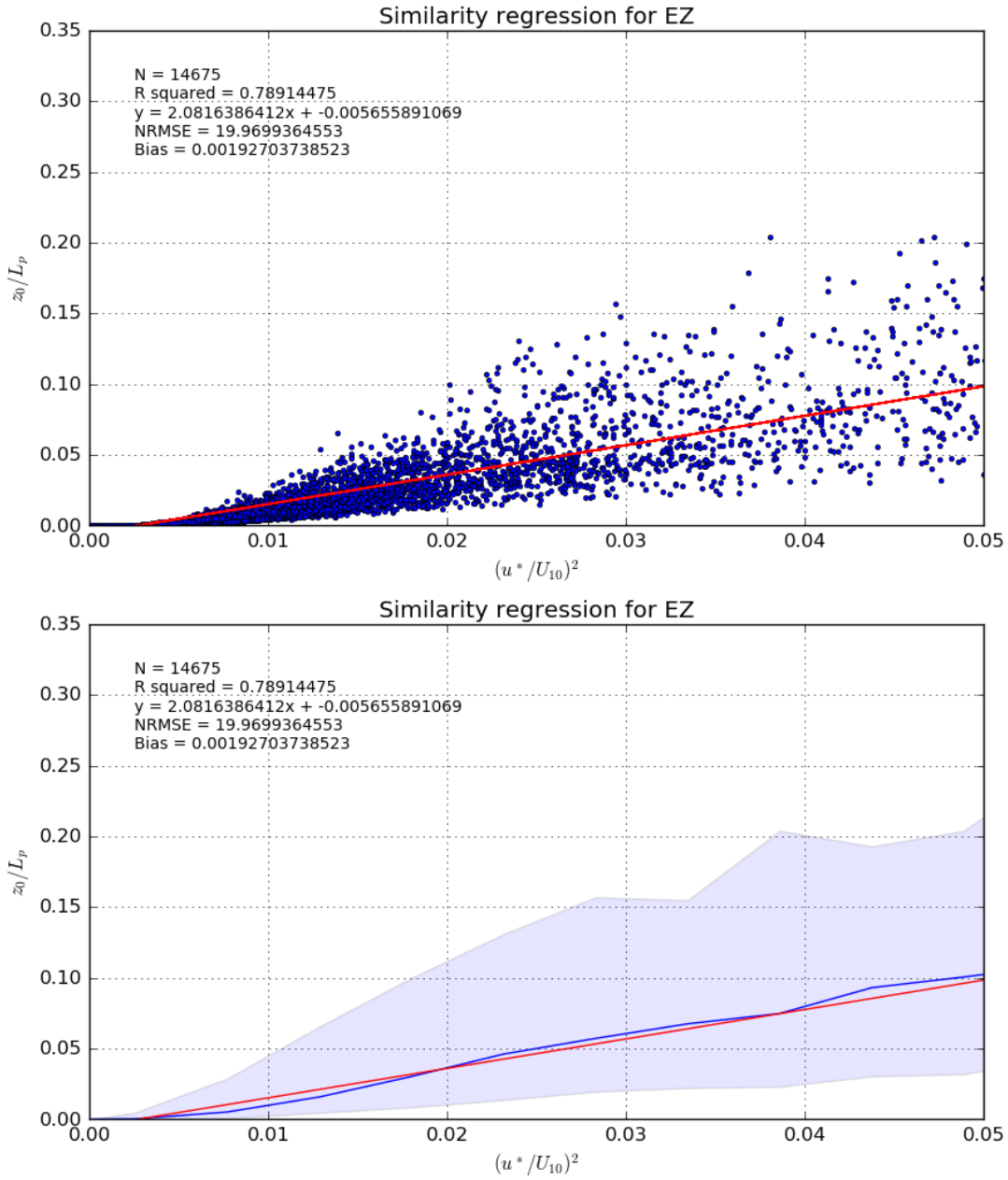

Figure 6.15. Regression for EZ without the von Karman constant. The red lines are the regression lines, and the blue line is the mean value for each bin. The purple light area shows the interval of values for each bin.

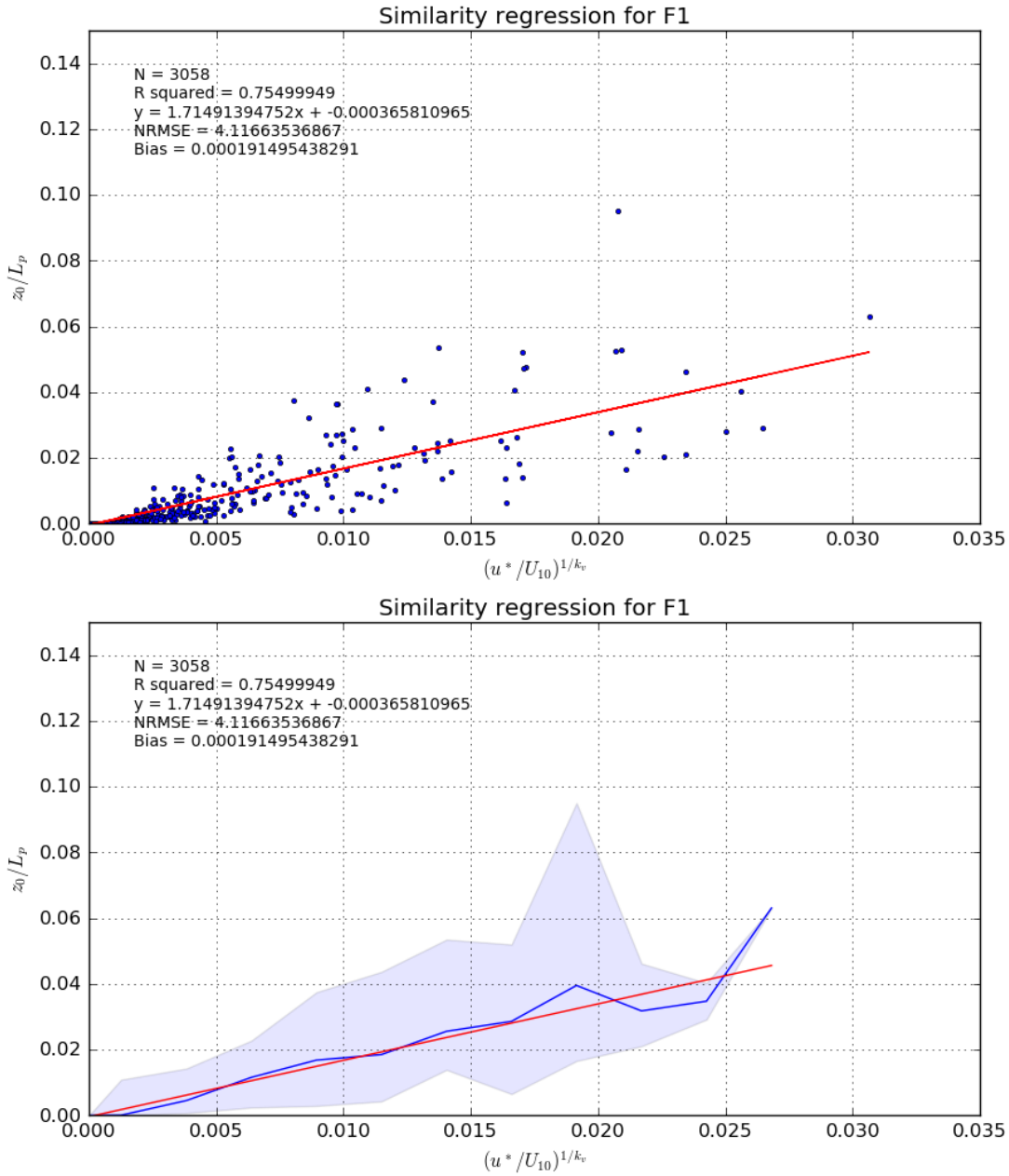

Figure 6.16. Regression for F1 with von Karman constant as k_v. The red lines are the regression lines, and the blue line is the mean value for each bin. The purple light area shows the interval of values for each bin.

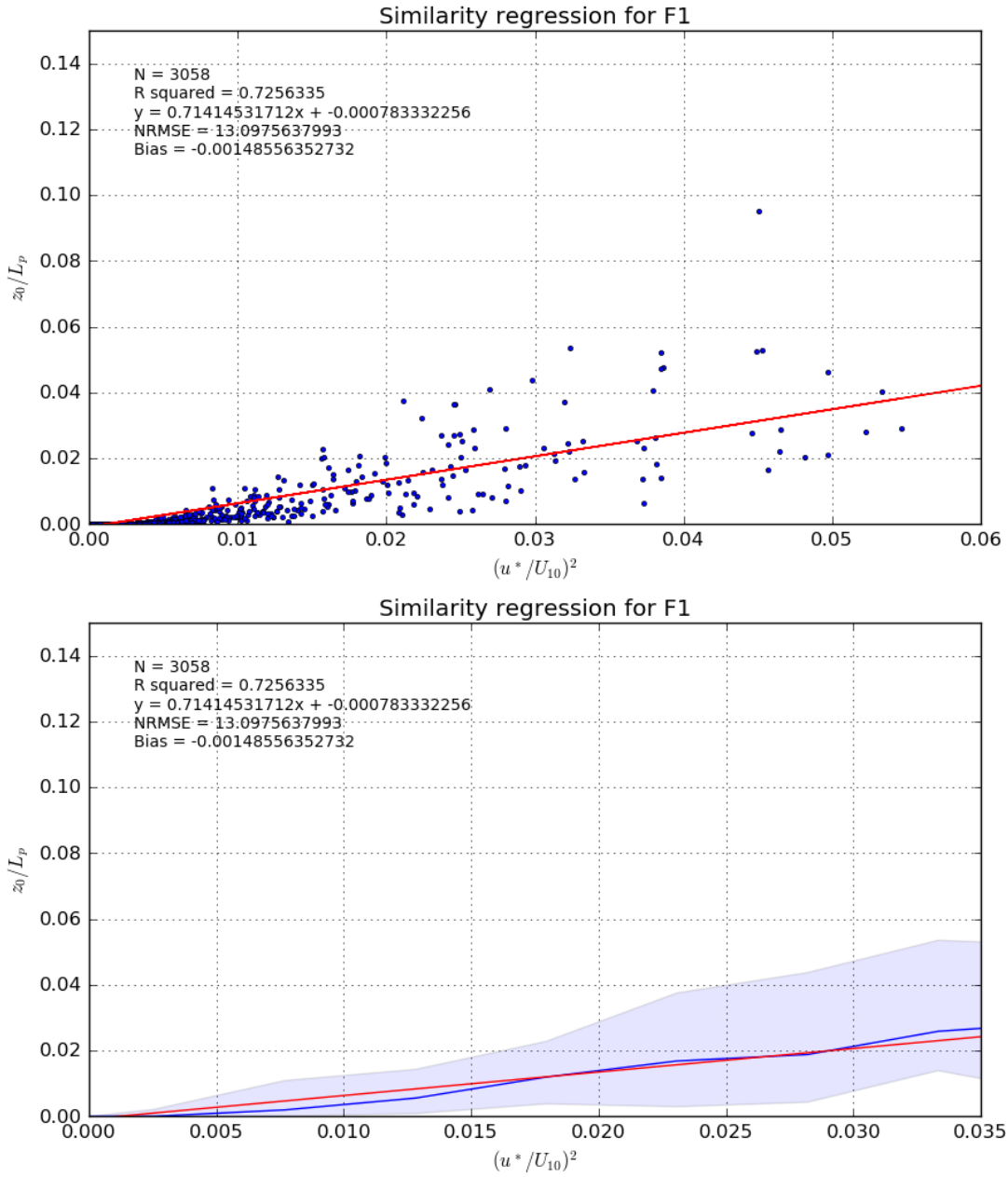

Figure 6.17. Regression for F1 without the von Karman constant. The red lines are the regression lines, and the blue line is the mean value for each bin. The purple light area shows the interval of values for each bin.

On the first figure, Figure 6.14, a good correlation was observed with an R^2 of 0.805. However the slope of the equation is four times higher the perfect slope, 1; plus the NRMSE is very high, 162,058. On the other hand, the second plot showing the interval revealed that the regression line is very close to the mean values. Some disagreement was found for high values, but it could be due to the low number of points for that area. Comparing with

results from Figure 6.15, when the von Karman constant was not used, the correlation coefficient was a bit lower than Figure 6.14. The slope of the regression line and NMRSE showed lower values and therefore better results. Again, the regression line followed the pattern of the mean values line.

Unlike EZ, a different trend was observed for F1 dataset. The correlation coefficient is still higher when κ was included, 0.754 in Figure 6.16 against 0.725 in Figure 6.17. However, the NRMSE was lower for the expression with von Karman constant. The NRMSE's were 4.116 and 13.096 in Figures 6.16 and 6.17 respectively. Only the agreement between regression line and mean values line was better for the normal expression of the drag coefficient. Again, this is probably due to the low number of points for high values.

In summary, a linear correlation between z_0/L_p and $(u_*/U_{10})^{1/\kappa}$ was proved to be fair. Nevertheless, the slopes for EZ and F1 datasets are significantly different and showed scatter for high values. More variables should be included in the study before empirical parameters are removed. In the following sections some suggestions are tested.

6.6.2 Wavelength as cw

After the results in the sensibility analysis section and the analysis by similarity theory, *cw* was substituted by L_p. The results of this substitution are shown in Fig. 6.18. At first glance, there was more scatter than regressions from Fig. 6.9. R^2 pointed to the presence of correlation with an important decrease in comparison to previous regressions; 0.71, 0.77 and 0.58 for EZ, EZS, and F1 respectively. The slope of the linear regression was also reduced to 0.60 and 0.58 for EZ and EZS but increased for F1 with 1.77. Even so, these regressions still achieved a higher R^2 than any other previous method included in this study. Hence, it was considered to achieve a reasonable correlation.

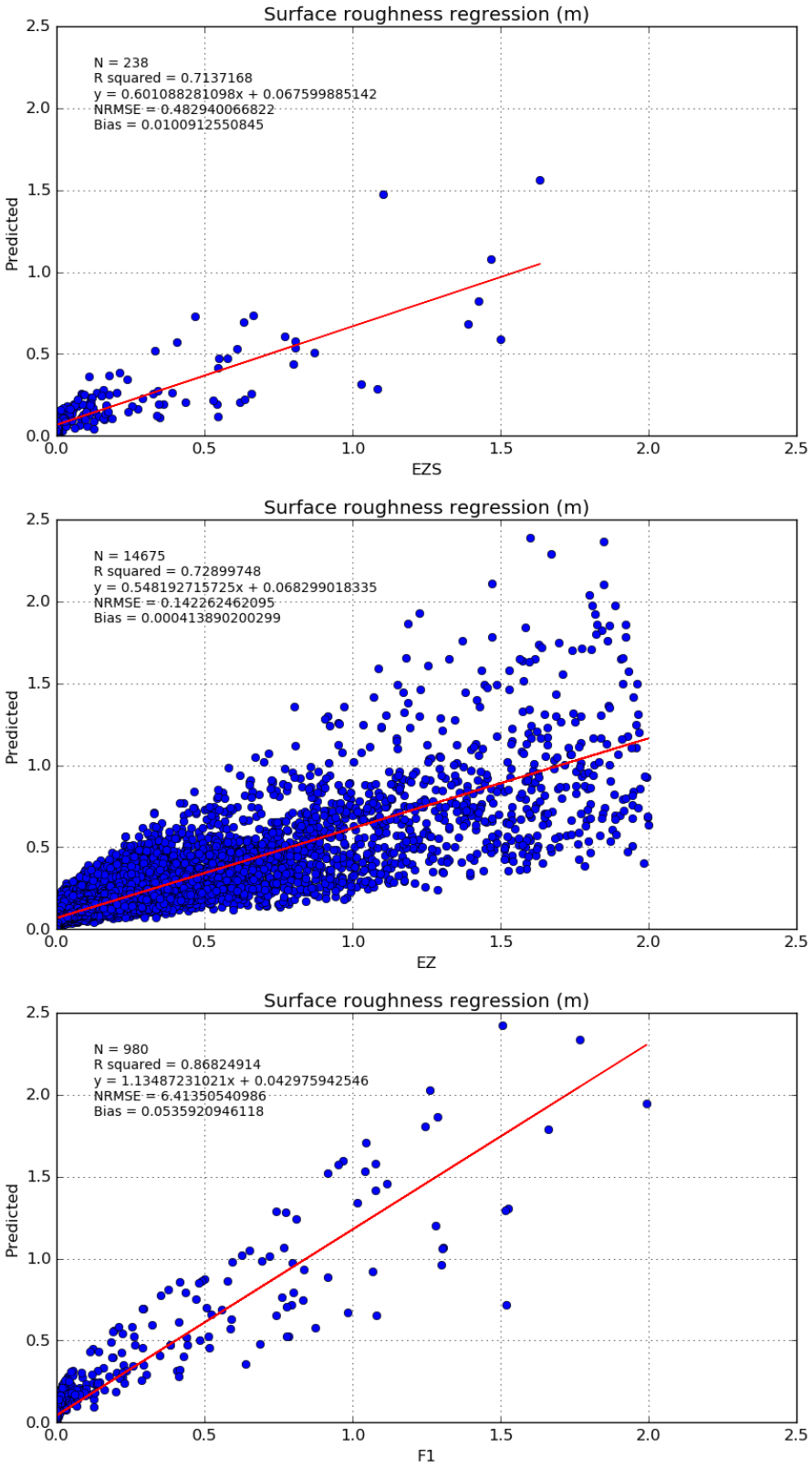

Figure 6.18. Surface roughness regressions between in situ z_0 and Eq. 6.14 model with cw=L_p coefficients for three different datasets: EZS, EZ, and F1.

6.6.3 Substitution of α

After the analysis by similarity theory, α was substituted by 2.5. Then, the expression for C_d in Eq. 6.7 was rewritten as shown in Eq. 6.16.

$$C_d = \left(\frac{u_*}{U_{10}}\right)^{(2.5)} \qquad (6.16)$$

Usually, the exponent in drag coefficient formula is 2 as shown in Eq. 6.7. This exponent was suggested by Taylor, [135], where the relation was also set by similarity theory. The drag of the atmosphere against the earth's surface could be described by the velocity squared, and so, it could be expressed by the wind stress too. Since then, researchers applied Eq. 6.7 in their studies. However, as explained, the drag coefficient is still a field of research. Even so, it is agreed that C_d associates the frictional drag related to the surface layer and the mean wind, i.e. u_* and U_{10}.

On the other hand, κ is described as a universal constant related to the turbulent flow near a surface. In [136], κ was interpreted as a geometric structural parameter, at least in the logarithmic law region. To be more precise, κ was described as the sinus of the angle between the streak ejected from the turbulent flow near a wall parallel to the fluid motion, and the wall. Hence, κ is here used as a parameter to describe the relation between frictional drag and the mean wind. This fact suggests the possibility that α is related to $1/\kappa$. However, more research will be necessary to prove this relationship. Hence, it was not included into new formulations.

As found in the previous section, the higher the α exponent, the lower the slope of the regression line in z_0 graphs. Once, α was substituted by 2.5, cw cannot be equal to L_p. As explained and observed in the second sensitivity analysis for cw, this value must be higher. Nevertheless, because of the agreement found in Fig. 6.18 and the analysis by similarity theory, cw should be still related to L_p. Also, it was proposed to keep working with wave asymmetry or wave age parameters. Therefore, an equation was derived as appears in Eq. 6.17.

$$z_0 = 0.11\frac{\nu}{u_*} + \left[\frac{u_*}{U_{10}}\right]^{(2.5)} L_p\left[1 + \left(H_s/a_T\right)\right]|\cos\theta| \qquad (6.17)$$

Once again, the first results to analyse were z_0 regressions. In Fig. 6.19 four different graphs are shown, one for each dataset plus a repetition of the EZS dataset against the predicted z_0 without the incidence angle correction included in Eq. 6.17. As it occurred with the substitution of cw by L_p, there was an obvious correlation but also some scatter was found. Comparing the results with Fig. 6.18, R^2 decreased for EZ and EZS; however, it increased slightly for F1 and more significantly for EZS without the incidence angle correction. The reduction of the independent value from the regression line was a generalized enhancement. This fact was also observed in the second sensitivity analysis for cw. Bias and NRMSE were nearer to 1 in Fig. 6.18 than Fig. 6.19. Only observing these two statistics plus R^2, the agreement between in situ and predicted z_0 fell for all Egmond aan Zee regressions. However, their results showed a small improvement for F1, even when its slope increased widening the distance to unity.

Wind speed regressions in Fig. 6.20 followed the same trend as correlations from Fig. 6.13. The extrapolated wind speed was generally underestimated again. In detail, there was a small drop in R^2 which means a reduction in the correlation. On the other hand, bias and NRMSE were also reduced meaning an increment of correlation. The main reason to underestimate wind speed was still the same. At low levels, when z_0<0.4, predicted z_0 is overestimated in the region with more data density in Fig. 6.19. In order to explain this fact and observe it more clearly, another regression was undertaken; a comparison between the natural logarithm of in situ z_0 and predicted z_0. Furthermore, results in Fig. 6.21 and z_0 calculations became comparable with those from [126]. Here only R^2 was calculated as a parameter to represent the quality of correlation.

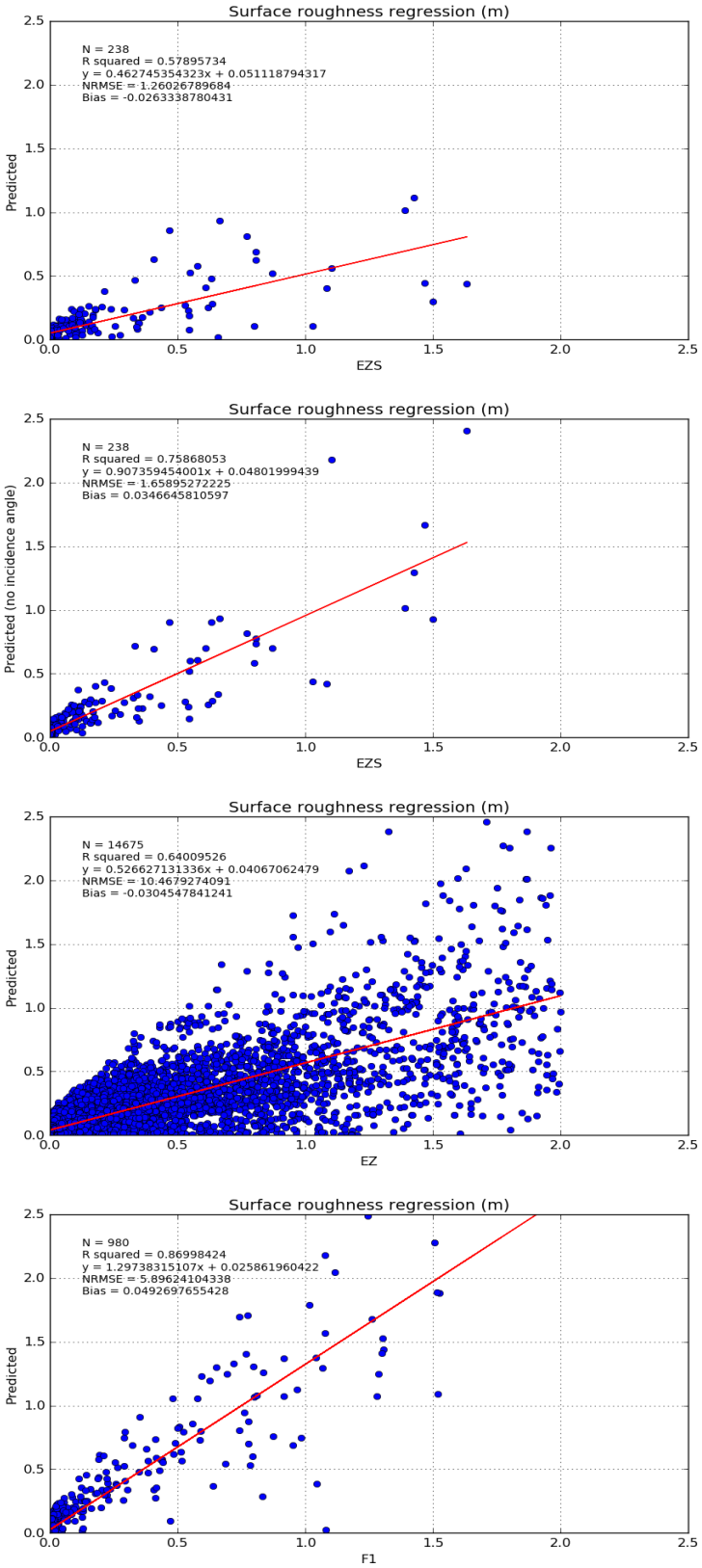

Figure 6.19. Surface roughness regressions between in situ z_0 and Eq. 6.17 model for three different datasets: EZS, EZ, and F1.

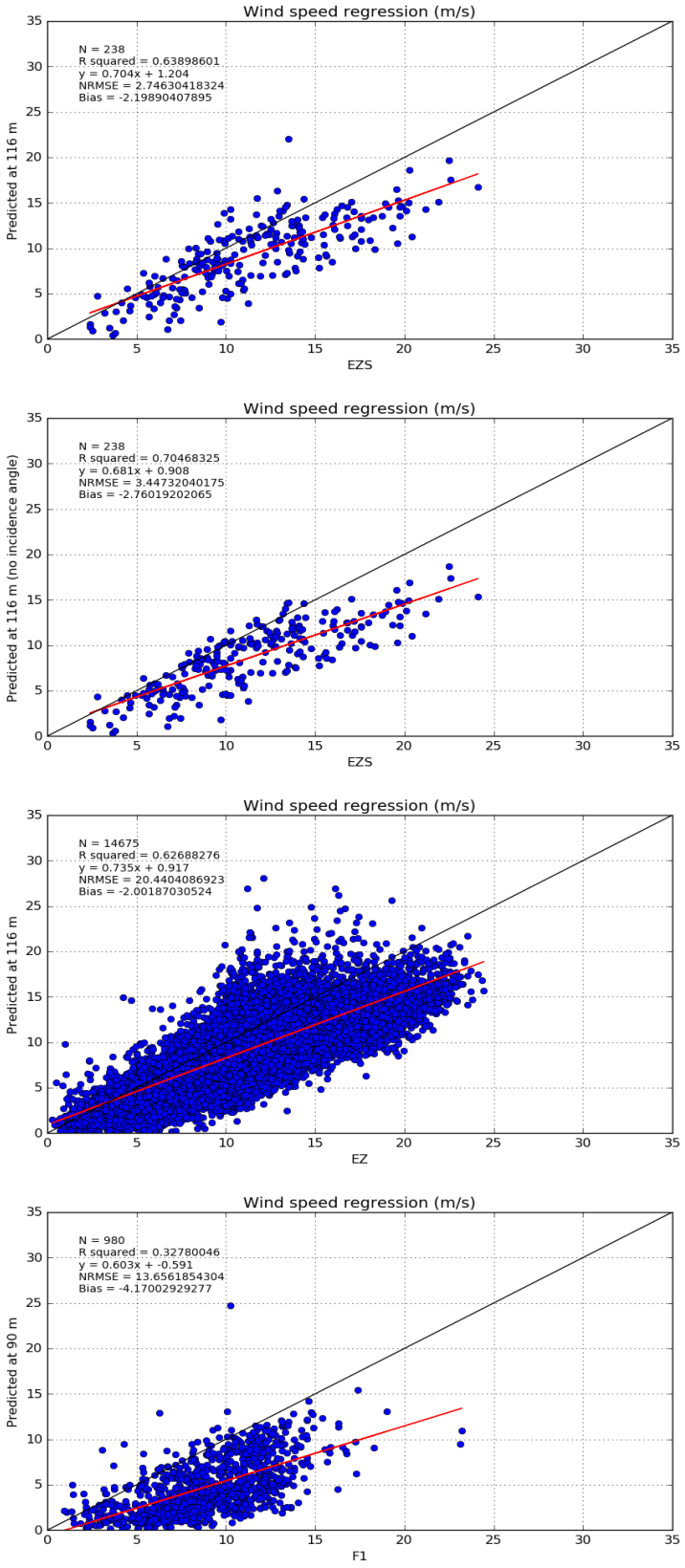

Figure 6.20. Extrapolated wind speed regressions between in situ z_0 and Eq. 6.17 model for three different datasets: EZS, EZ, and F1.

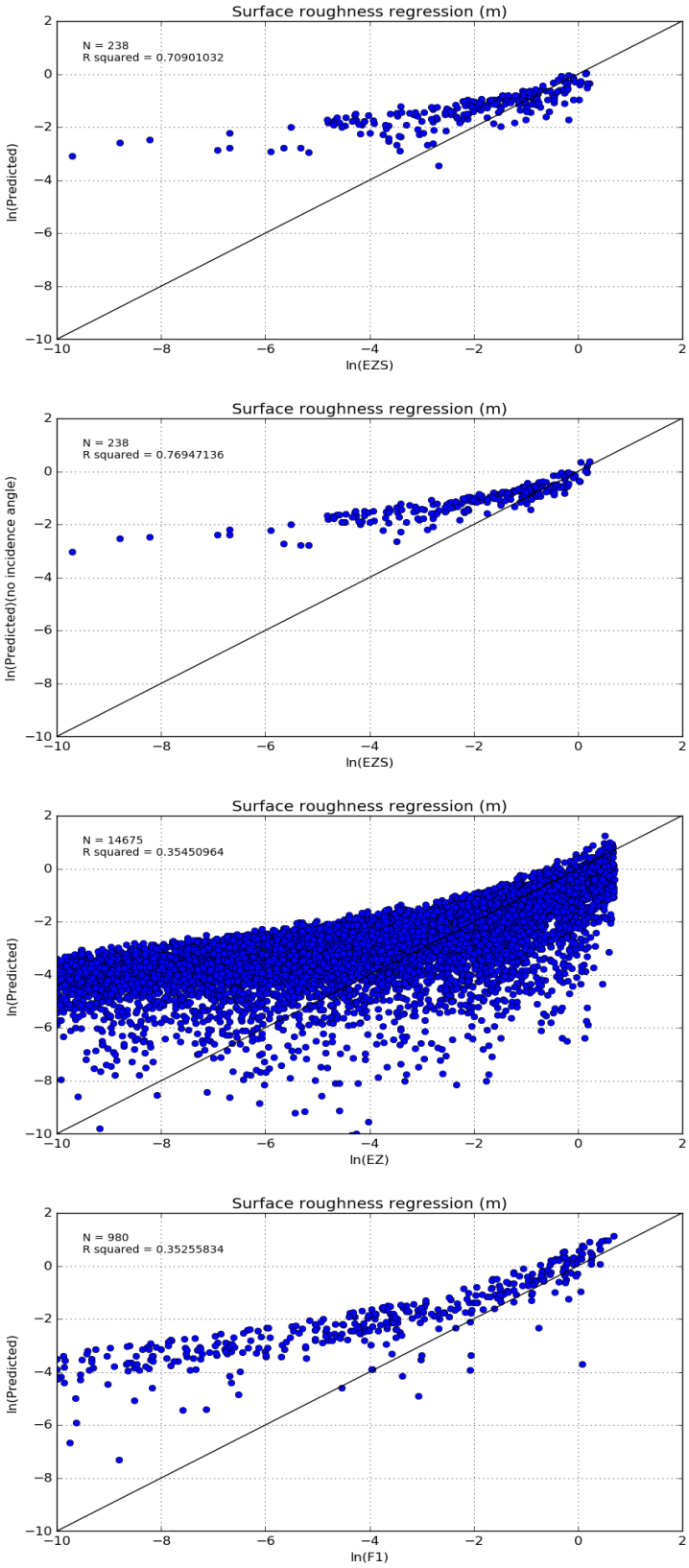

Figure 6.21. Natural logarithm of surface roughness regressions between in situ z_0 and Eq. 6.17 model for three different datasets: EZS, EZ, and F1.

This was higher for EZS regressions than EZ and F1 with more points included. The best result was found to be EZS without incidence angle correction achieving an R^2 of 0.769. Similarly, in [126] where onshore roughness is calculated, an R^2 of 0.756 was achieved for the method based on Lettau's equation and also validated against a meteorological mast. The contrast is the absence of bias in [105]. In Fig. 6.21 there is an obvious bias when $\ln(z_0)<-2$. According to results predicted z_0 was never smaller than 0.0001 for EZS. Although that was not the case for EZ and F1, it was obvious that predicted z_0 was overestimated when z_0 is smaller than 0.01.

6.6.4 No incidence angle and average *Lp*

The last improvement was applied to the developing equation. Eq. 6.17 was modified to remove the incidence angle correction and short-term L_p was substituted by average or long-term L_p.

$$z_0 = 0.11\frac{\nu}{u_*} + \left[\frac{u_*}{U_{10}}\right]^{(2.5)} \overline{L_p}\left[1 + \left(H_s/a_T\right)\right] \qquad (6.18)$$

In this first analysis, the long-term wavelength comprised between the beginning and end of data availability, more than 3 years for EZ. The results in Fig. 6.18 showed a drastic reduction in scatter. As a consequence, an improvement in correlation was found for the z_0 regression. However, there is still an overestimation of z_0 when $z_0<0.4$. This was observed in the second regression of Fig. 6.22, for $ln(z_0)$.

Hence, in order to test the developed equation, the method was analysed only when $z_0>0.4$. Those points were overlapping the ideal correlation line in Fig. 6.22, right graph. These points are also shown in Fig. 6.23 the z_0 regression where R^2 rises from 0.404 to 0.975; and so proving an almost ideal correlation. As explained, validation is proven by comparison of extrapolated wind speeds with measured wind speed. The results for the wind speed regression demonstrated a near-perfect correlation with R^2=0.954. The slope of the correlation line was low, 0.909, although near to unity. NRMSE and bias achieved the lowest values for any wind speed regression in this study and, in the case of bias, close to zero.

Following Fig. 6.23, when perfect correlation in the $ln(z_0)$ regression was achieved, a perfect wind speed correlation was reached. Eq. 6.18 results provided almost perfect agreement between predicted and measured data when z_0>0.4.

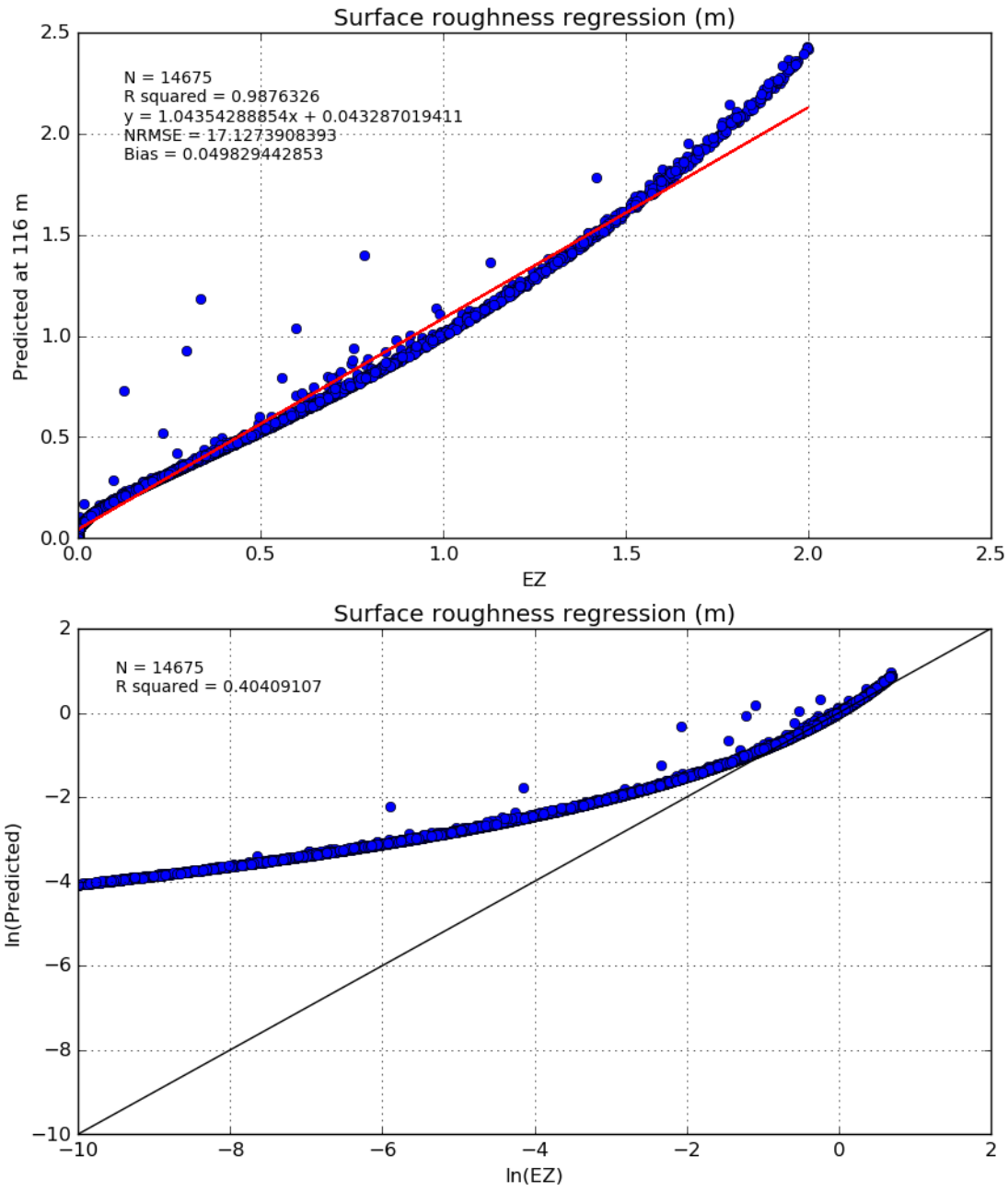

Figure 6.22. Surface roughness regressions between in situ z_0 and Eq. 6.18 model for EZ.

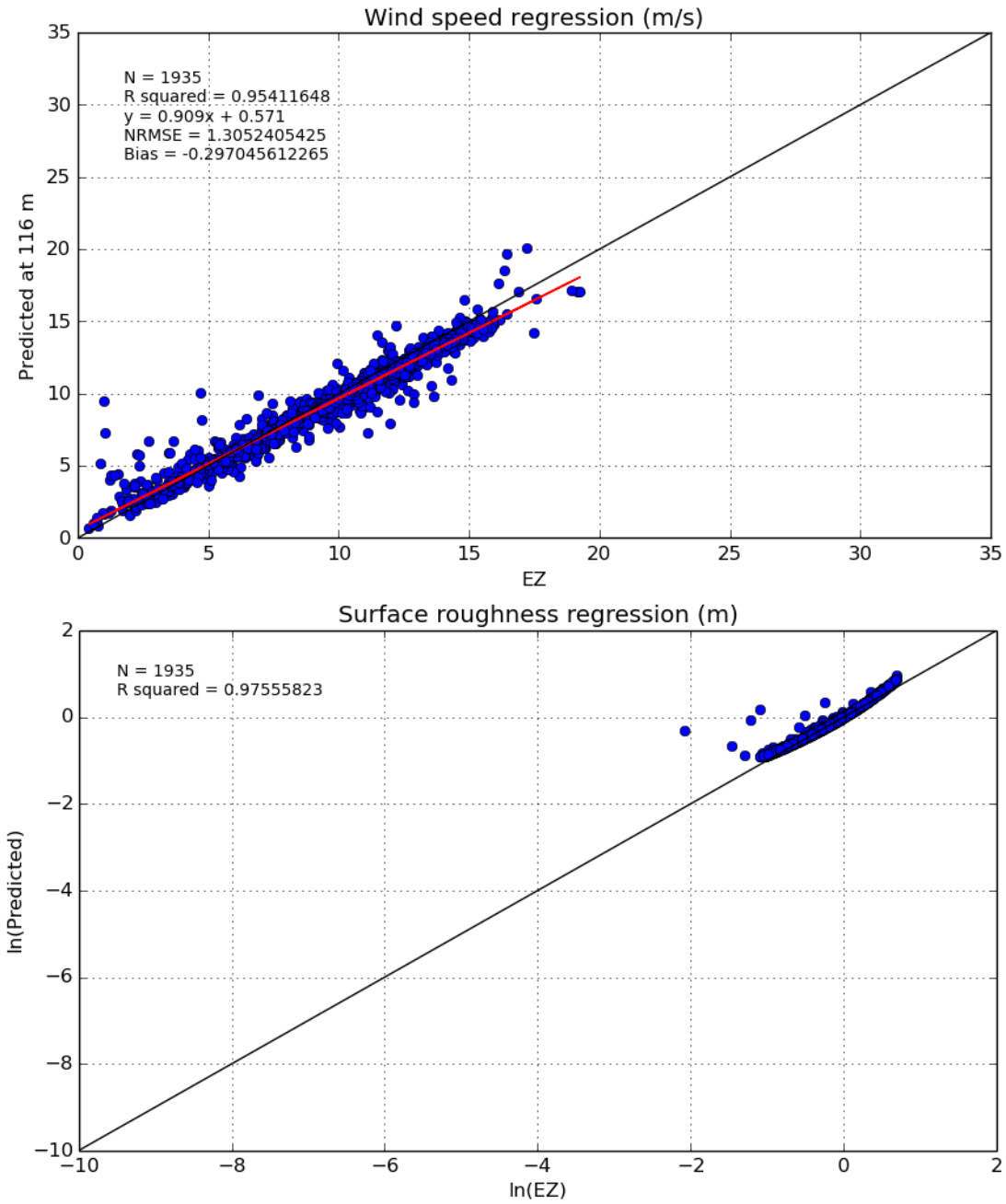

Figure 6.23. Wind speed and surface roughness regressions when z_0>0.4 between in situ z_0 and Eq. 6.18 for EZ.

6.7 Analysis of wave age, height and wind speed

As studied in chapter 5, the z_0 method was analysed under different wave ages, wave heights and wind speed conditions. All three parameters have an effect on z_0, directly or indirectly. The aim was to find an optimal interval or by contrast those intervals where the developed equation does not

adequately represent the real roughness. Perhaps, there was also the possibility to find the conditions for low z_0 where predicted roughness is overestimated. Furthermore, there are some sea conditions for which it should be easier than others to calculate z_0; e.g. wind generated, fully developed seas. Testing the method under these conditions and comparison with chapter 5 could bring some light and new ideas to find the z_0 calculation method valid for all conditions.

6.7.1 Wave age

Three different intervals were studied; $c_p/u_* < 5$, $5 \leq c_p/u_* \leq 32$, $c_p/u_* > 32$ as observed in Fig. 6.24. These intervals represent calm, growing and decaying seas respectively. For calm seas, a $z_0 > 0.01$ was practically always found. This agrees with the common idea of the younger the waves, the rougher the sea. In fact, this idea was proved to be right since higher values for z_0 were found for calm and growing seas and only low z_0 values were present for decaying seas. Even so, young and decaying seas only represented 16% of the data reflecting low representativeness. Another interesting point was the range of wind speed for each wave age interval. For calm seas, medium wind speed was found, from 7 to 16 m/s; for young seas, a wide range of wind speed was observed and finally, for decaying seas, low winds were found as expected. Calm sea conditions achieved the highest correlation coefficient, 0.947, and most of its points were located over the perfect correlation line. Therefore, predicted wind speed also achieved a high correlation with R^2, slope, NRMSE, and bias near their optimal values and low scatter was found, as shown in Fig. 6.25. This trend was already observed for high z_0 in the previous section. As z_0 dropped, the correlation also decreased, as shown in Fig. 6.24, 0.889 and 0.539 for young and decaying seas. By simple observation of z_0 regressions in Fig. 6.24 it was obvious that correlation decreased with increasing wave age. As z_0 correlation fell, the wind speed correlation also fell. This fact reflected the importance of z_0 parameterization to accurately determine the wind profile. Eq. 6.18 was proven to be fully capable of predicting z_0 for calm seas or $c_p/u_* < 5$. That was not the case for young seas were only a portion of the points found agreement. Finally, there was no sign of correlation for decaying seas. This contrasts with previously proposed z_0 methods where researchers found the worst agreement under very young wave conditions, $c_p/u_* < 15$, in [106], [107] and [108].

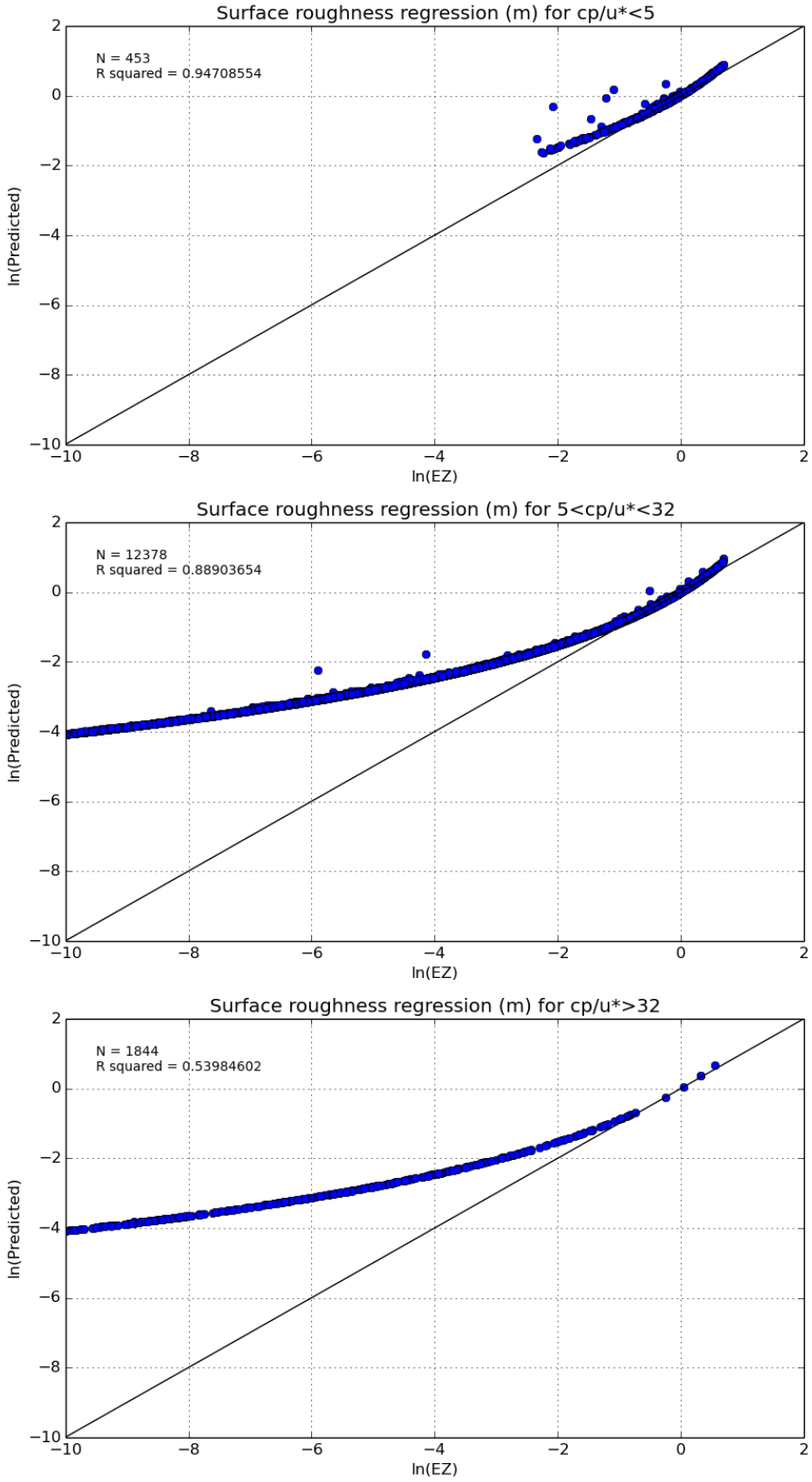

Figure 6.24. Surface roughness regressions between in situ z_0 and Eq. 6.18 for EZ under different wave ages.

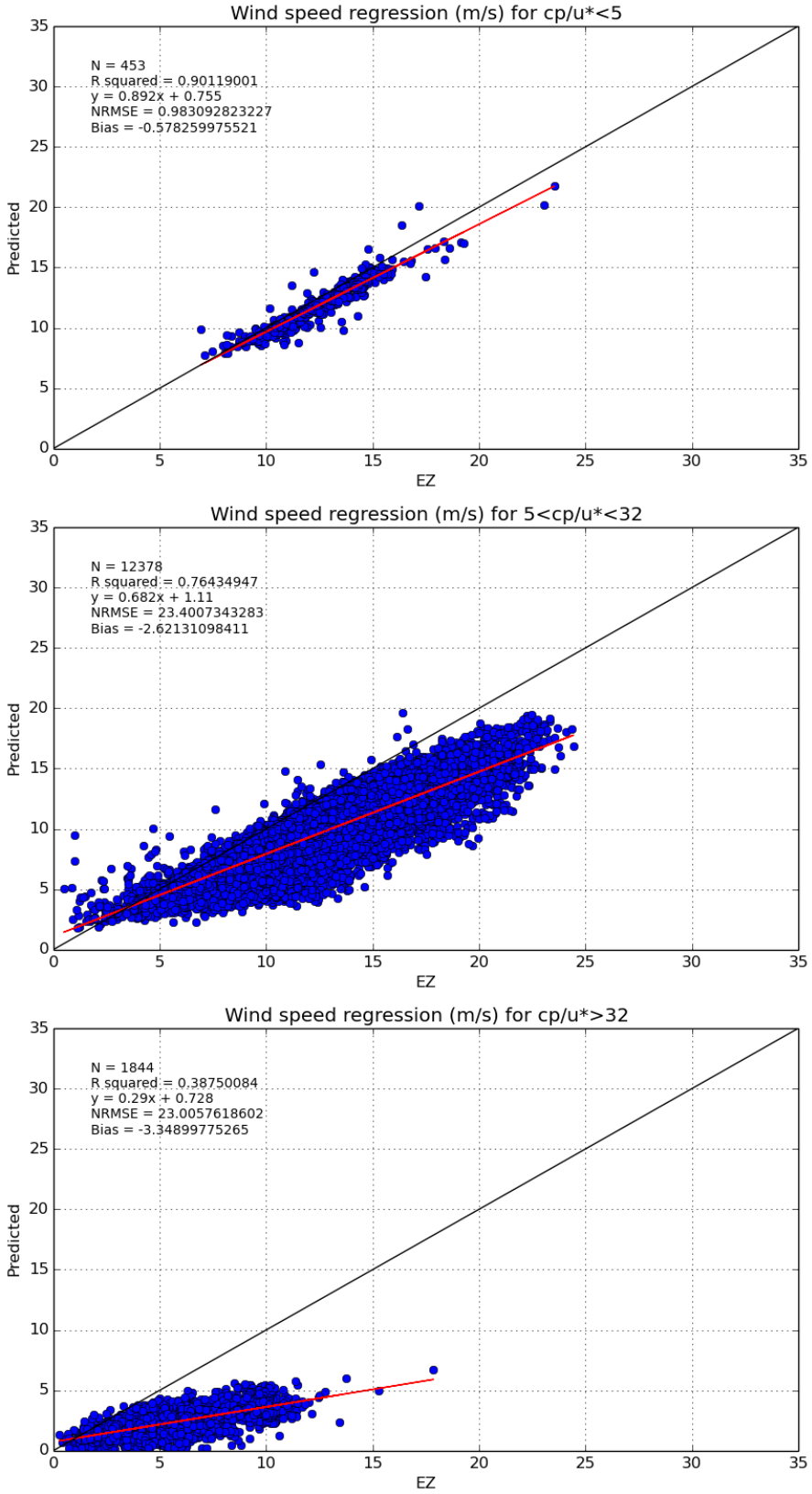

Figure 6.25. Wind speed regressions between in situ measurements and predicted wind by Eq.6.18 and logarithmic law for EZ under different wave ages.

6.7.2 Wave height

The chosen intervals to analyse were H_s<1 m, 1≤H_s≤2 m, H_s>2 m as shown in Fig. 6.26. The first two cases, where significant wave height was lower than 2 meters, reached similar results. Both cases grouped a similar number of measurements, 6,976 and 5,118 and showed a low level of correlation, R^2 was equal to 0.450 and 0.334 for H_s<1 m, 1≤H_s≤2 m respectively. Wind speed regressions achieved better correlation for both, however, the wind speed was underestimated. As explained previously the reason was an overestimated z_0. The only relevant point in this analysis was the low z_0 observed when H_s>2 m. Seemingly contradictory to common sense, higher waves do not mean higher z_0, in fact, the higher the waves the lower the surface roughness. In Fig. 6.27, this idea was proven by the decreasing slope observed for wind speed regressions; 0.908, 0.841 and 0.776 for the 1 m, 1-2 m and more than 2 m of H_s. If z_0 is overestimated then the wind speed will be underestimated as happened in Fig. 6.26. Although, this effect did not produce big differences in z_0 between cases. This only means a poor dependence of z_0 on wave height.

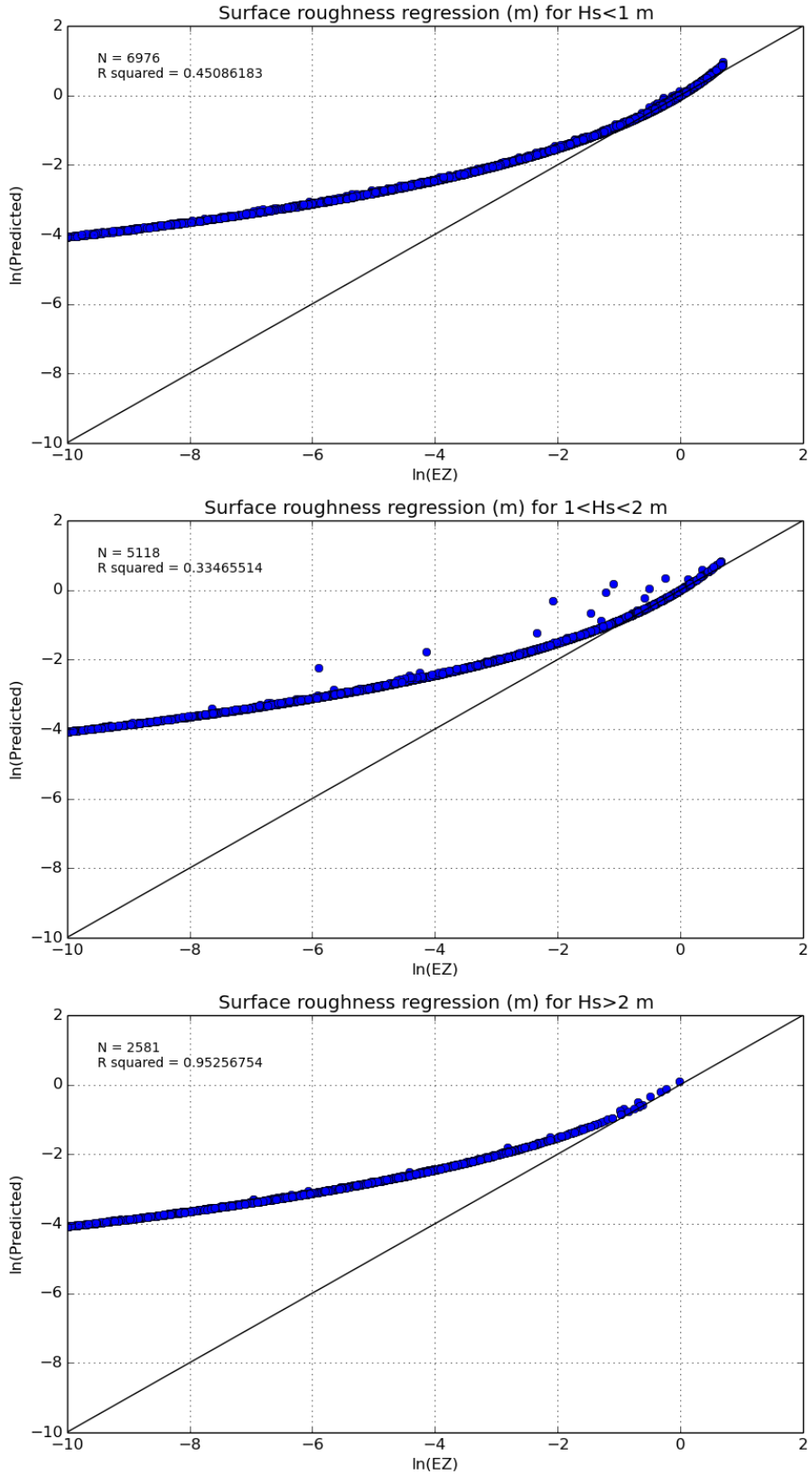

Figure 6.26. Surface roughness regressions between in situ z_0 and Eq. 6.18 for EZ under different wave heights.

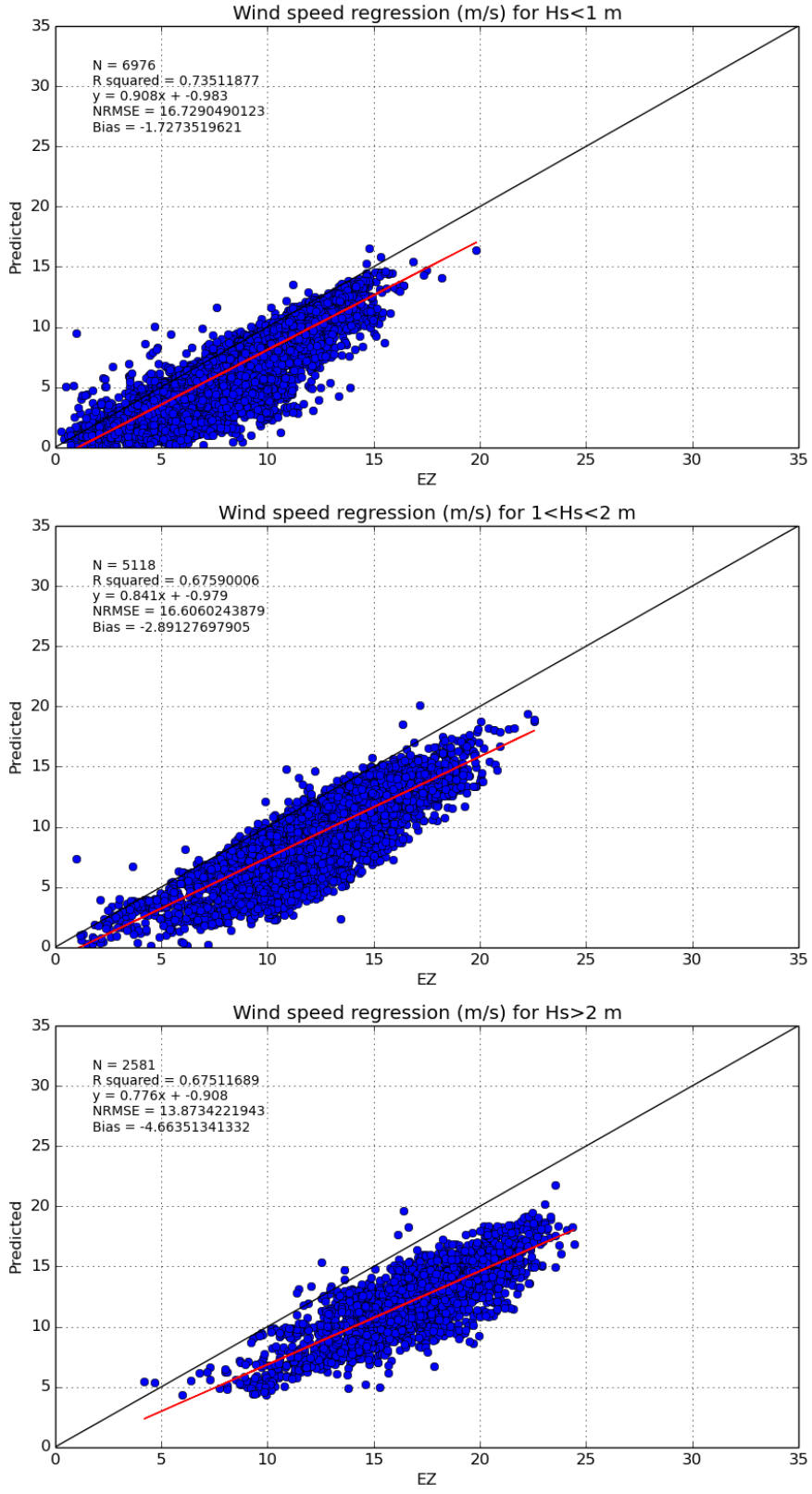

Figure 6.27. Wind speed regressions between in situ measurements and predicted wind by Eq.6.18 and logarithmic law for EZ under different wave heights.

6.7.3 Wind speed

In this section different wind speed at 10 m intervals were analysed. As shown in Fig. 6.28 these intervals are U<5 m/s, 5≤U≤15 m/s and U>15 m/s for low, medium and high wind speed. Most of the measurements were taken under medium wind speed conditions since the number of points was 11,076 out of 14,675. Even so, low and medium winds achieved the same low correlation in z_0 regressions, R^2≈0.45. Nevertheless, low winds reached better correlation in wind speed regression where R^2 and slope where 0.807 and 1.047 respectively. Both statistics were lower for medium winds as shown in Fig. 6.28. The case of high wind speed regressions brought another interesting point in Fig. 6.29. All z_0 values during high wind conditions were under 0.001 according to EZ, so can be fairly considered to be low roughness. It is well known that wind produces waves over the ocean, plus the younger waves, the rougher sea as explained in the previous section. Thus, it can be observed, comparing Fig. 6.24 for calm seas and Fig. 6.28 for high winds, the very young waves produce the highest roughness. High roughness does not correspond to high winds. Furthermore, when high winds over the ocean are reached, wave height is probably above 2 m since regressions for H_s>2 m in Fig. 6.26 and high winds in Fig. 6.28 did not show points for high z_0. Therefore, a new conclusion can be drawn; the older sea, the higher waves or the higher wind speed, the lower aerodynamic surface roughness length. Under all these three conditions Eq. 6.18 was unable to calculate z_0 with accuracy.

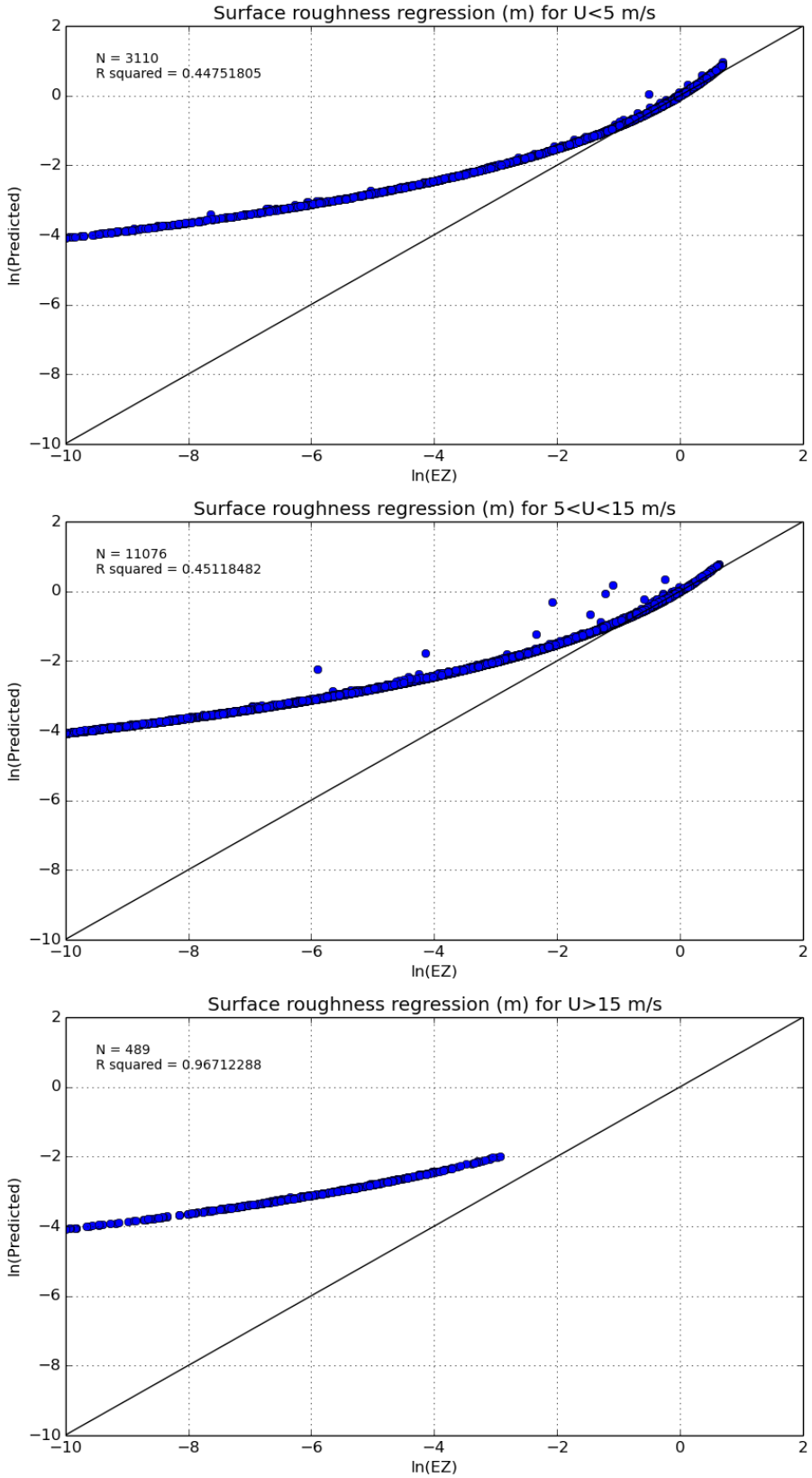

Figure 6.28. Surface roughness regressions between in situ z_0 and Eq. 6.18 for EZ under different wind speed conditions.

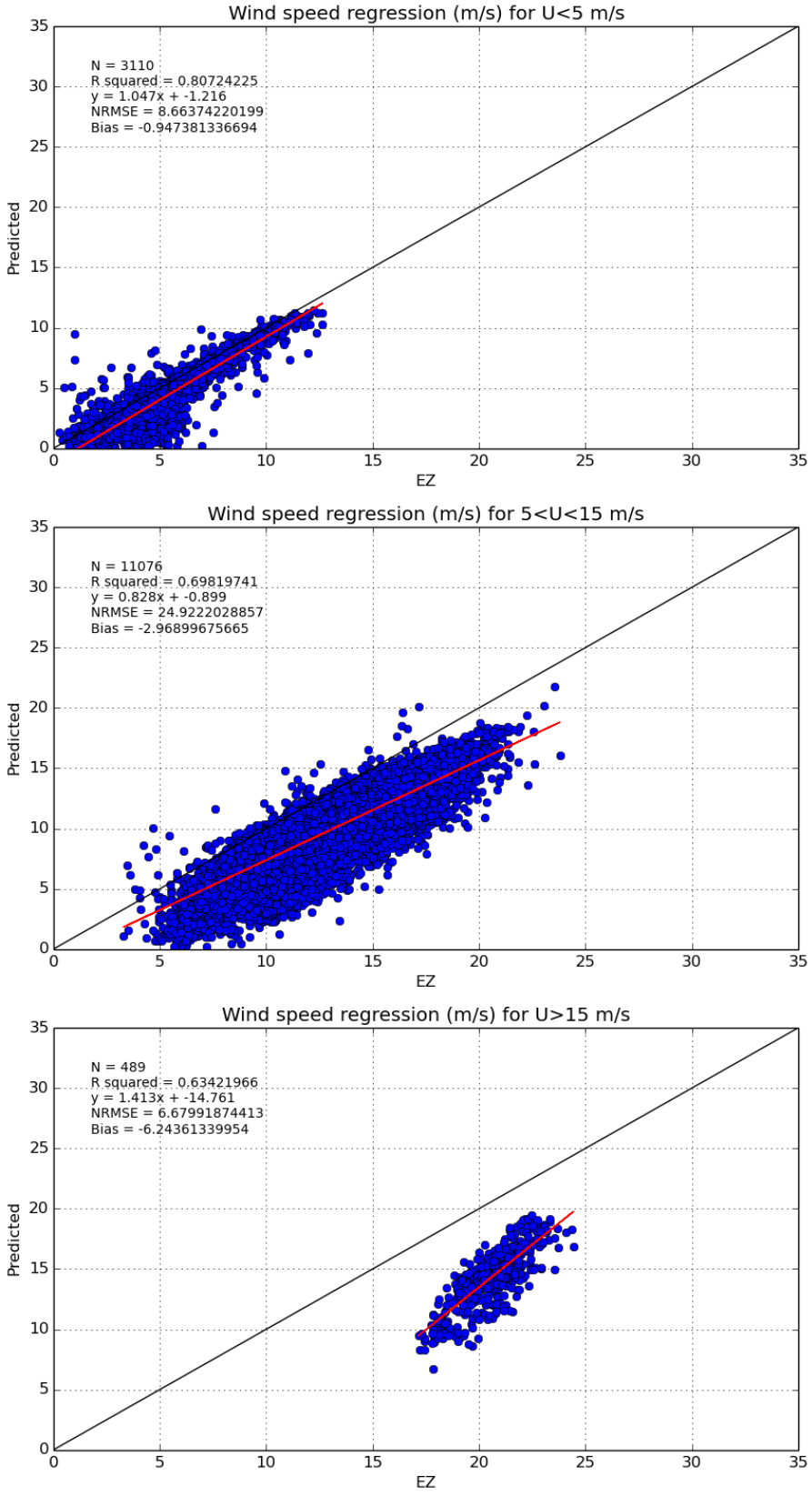

Figure 6.29. Wind speed regressions between in situ measurements and predicted wind by Eq.6.18 and logarithmic law for EZ under different wind speed conditions.

6.8 Analysis of the atmospheric stability

Normally, the expected aerodynamic surface roughness length over the sea is within the range from 0.01 m to 0.0001 m, [134]. The z_0 regressions previously shown in chapters 4 and 5 and the present chapter, pointed to higher values than the expected range. Sometimes, z_0 reached 2 metres, a value that is expected for cities with skyscrapers. Two possible reasons for it could be the atmospheric stability and the possible wake effect from the meteorological mast itself.

It must be remembered that the meteorological mast dataset was filtered in chapter 5 and 6 to avoid stable and unstable atmospheric conditions. The chosen method for filtering was the comparison between T_{SEA} and T_{AIR}. When both temperatures were almost equal, neutral stability was assumed. This method is the most straightforward, but at the same time it is the less precise. Instead of measured temperatures the virtual potential temperatures, Θ_v, should be compared at different heights which also depend on the pressure and humidity. Here is the set of equations, Eq. 6.19 – 6.23, to calculate virtual potential temperature, [134].

$$\Theta_v = \Theta(1 + 0.61r) \qquad (6.19)$$

$$\Theta = T\left(\frac{P_0}{P}\right)^{0.286} \qquad (6.20)$$

$$r = \frac{0.622 e_p}{P - e_p} \qquad (6.21)$$

$$e_p = e_s \frac{RH}{100} \qquad (6.22)$$

$$e_s = 0.6112\ exp\left[\frac{17.67(T-273.16)}{T-29.66}\right] \qquad (6.23)$$

Where r is the mixing ratio of unsaturated air, g/g, P_o is the reference pressure, 100 kPa, RH is the relative humidity, %, e_p is the partial pressure of water vapor, and e_s the saturated vapor pressure. In Eq. 6.23, temperature has units of degrees Kelvin and e_s is calculated in kPa.

When $\Delta\Theta_v = 0$, it could be expected to find a static neutral stability if vertical convection is null. But, when there is adiabatic lapse rate equal to 0, it could be vertical wind speed producing turbulence. Hence, the most precise way to represent atmospheric stability is through the heat flux parameterization,

expressed as $\overline{w'\Theta'_v}$. The overbar means the average over a period of time, the apostrophe means the fluctuation term, and w represents the vertical speed. Thus, when the heat flux is negative, the boundary layer is stable, a positive heat flux means unstable stability, and in cases where the heat flux is equal to 0 there is neutral stability. In order to quantify the atmospheric stability the Obukhov length, L_s, is commonly used.

$$L_S = -\frac{u_*^3 \Theta_v}{\kappa g \overline{w'\Theta'_v}} \qquad (6.24)$$

Therefore, the Obukhov length was calculated in order to verify that the z_0 high values are not a consequence of the atmospheric stability. In table 6.1, the range according to stability is indicated.

		$\overline{\Theta_v}$ **profile (K)**	$\overline{w'\Theta'_v}$ **($ms^{-1}K$)**	z/L_s	L_s **(m)**	$1/L_s$ **(m^{-1})**
Stable		$\overline{\Theta_{v1}} < \overline{\Theta_{v2}}$	< 0	> 0	≤ 200	≥ 0.005
Neutral	Near neutral/stable	$\overline{\Theta_{v1}} \cong \overline{\Theta_{v2}}$ If there is no convection	≅ 0	≅ 0	200 ≤ *L* ≤ 500	0.002 < *1/L* < 0.005
	Neutral				|*L*|≥*500*	0.002 ≥ *1/L* ≥ -0.002
	Near neutral/unstable				-500 ≥ *L* ≥ -200	-0.005 ≤ *1/L* ≤ -0.002
Unstable		$\overline{\Theta_{v1}} > \overline{\Theta_{v2}}$	> 0	< 0	≥ -200	≤ -0.005

Table 6.1. Summary of the range of values for different parameters according to atmospheric stability. The virtual potential temperature profile must be calculated at two different heights where z1<z2. [134] and [137].

All measurements included in the stability quantification were taken at 21 metres height from the sea surface. In this section, stability conditions were filtered out after calculating L_s. Hence, the friction velocity could not be

parameterized from the wind speed at two different heights. In this case, the ultrasonic anemometer at 21 metres was used to calculate friction velocity. Since this kind of anemometer allows the measurement of vertical, lateral and horizontal speeds, u_* was solved by Eq. 6.25. Where u', v' and w' stand for horizontal, lateral and vertical speed fluctuation respectively.

$$u_*^2 \equiv \left[\overline{(u'w')}^2 + \overline{(v'w')}^2\right]^{1/2} \qquad (6.25)$$

A 50-min period was used in this study to calculate the heat flux and friction velocity. This period was the shortest possible to calculate fluctuations with confidence. The aerodynamic surface roughness was calculated by Eq. 2.6. Again, the wind speeds used to calculate aerodynamic surface roughness were 50-min averaged values. Thus, results from a 50-min averaged dataset can be compared with the EZ and EZS datasets results. The F1 dataset could not be used in this section because, due to the large number of gaps in the F1 dataset, it was not possible to calculate fluctuations.

In Fig. 6.30 the surface roughness was plotted against the inverse of the Obukhov length. In the graph, only measurements under neutral or near neutral conditions were included. The total number of points was 11,152. Compared with the EZ dataset, the number of measurements was reduced by 3,500 points. The difference increases if only neutral conditions are included for comparison with only 5,613 points under neutral conditions. Therefore, the 1°C of difference between sea and air temperatures was covering neutral and near neutral measurements plus some stable and unstable conditions. In summary, neutral and near neutral conditions were included (76% of time) and stable plus unstable conditions also included (24% of time).

In this section, with more rigorous criteria for stability, many high z_0 values were also found as shown in Fig. 6.30. These high values were seen under near neutral conditions, but also under strict neutral conditions. Even when $1/L_s$ was close to 0, many z_0 values were higher than 0.1 metres. With these results, atmospheric stability was discarded as a reason for high surface roughness values.

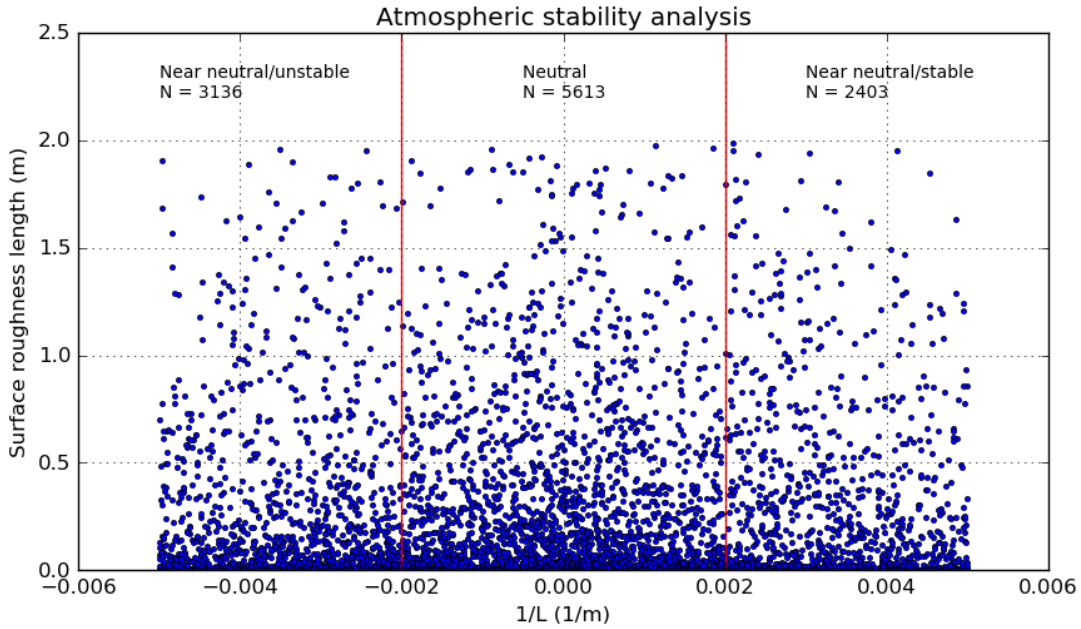

Figure 6.30. Analyses of surface roughness length under different stability conditions. *N* stands for number of points.

Another possible reason was the wake effect from meteorological mast. If this was the reason, high z_0 values should only appear for one or two sectors. In order to check this possibility, the stability was also studied according to the wind direction as shown in Figures 6.31 and 6.32. Only six sectors of 60° each were included here. The results showed that high z_0 values were measured within all the sectors. This fact dismisses the idea of a possible wake effect from the meteorological mast itself.

However, there is another possible source of wind shear, the wind turbines installed at the Egmond aan Zee offshore wind farm. These are located at North, North-East and South-East of the met mast, as shown in Figure 6.33. Hence, within these three sectors the turbulence could be the cause for an unusual wind profile and therefore unusual calculated values of z_0. On the other hand, the South, South-West and North-West sectors should not experience such wake effect from wind turbines. Within these three wake-free sectors high z_0 values were also observed under neutral conditions as shown in Figure 6.32.

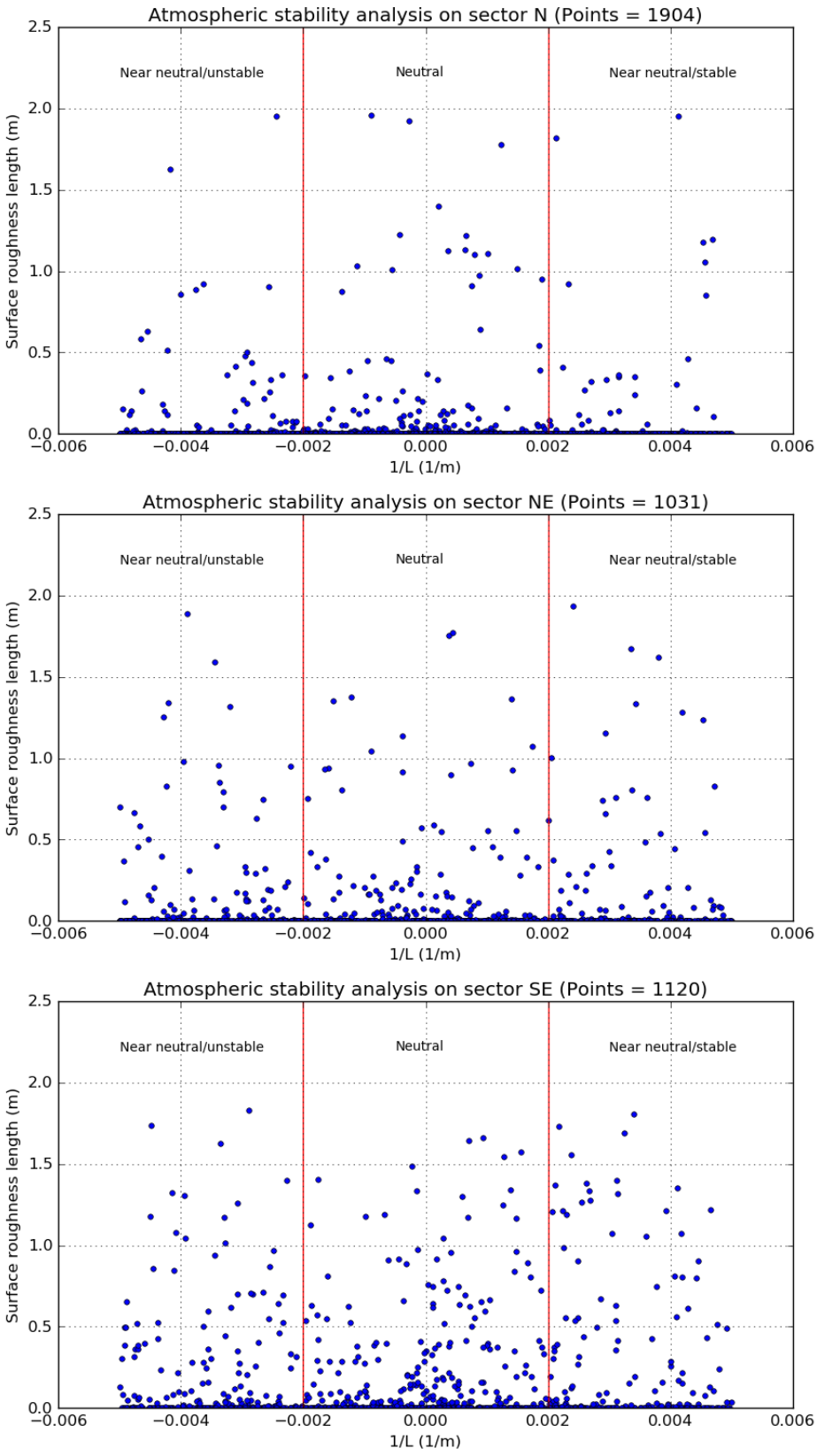

Figure 6.31. Analyses of surface roughness length under different stability conditions for the 3 sectors under a possible wake effect from wind turbines.

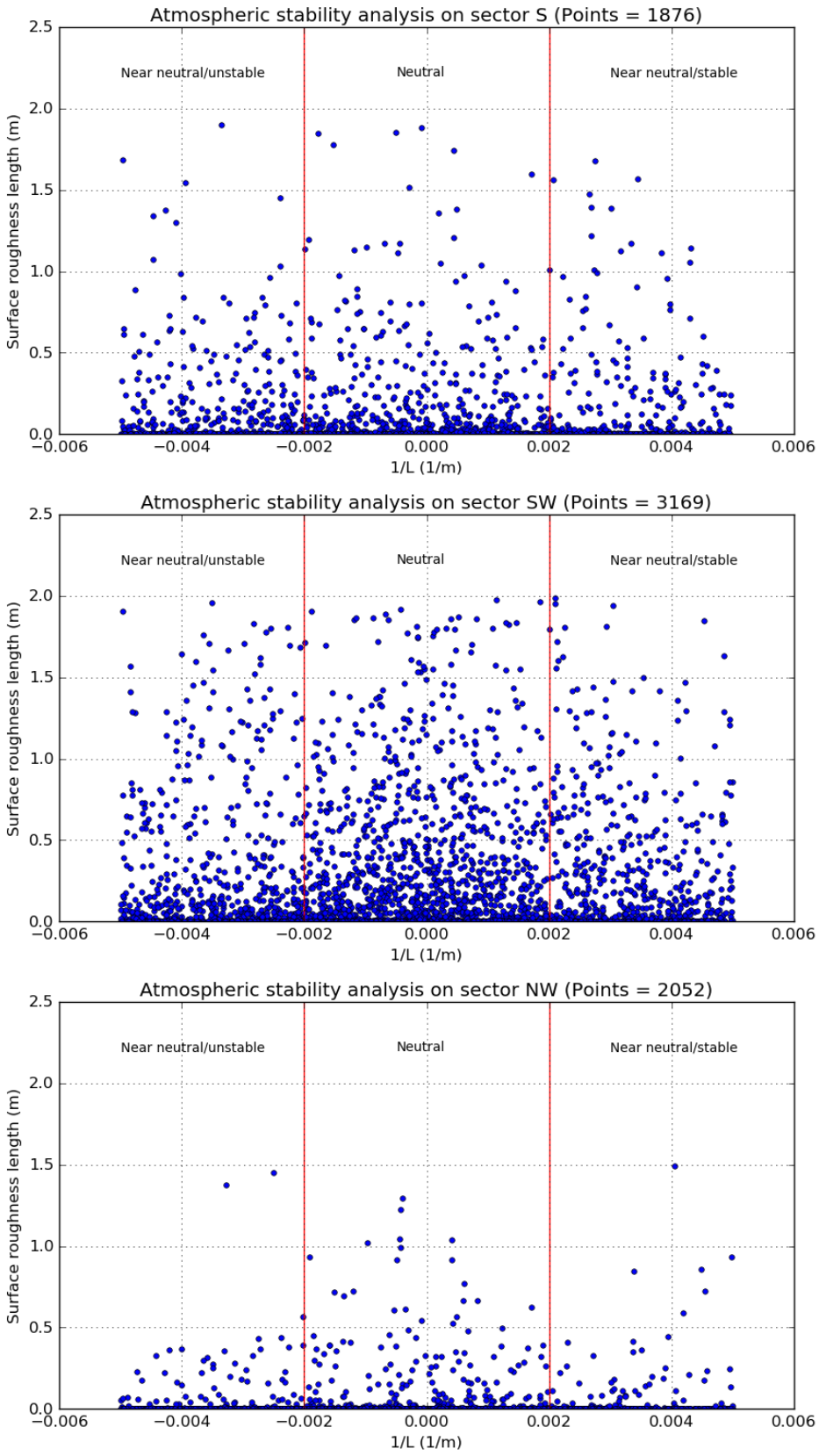

Figure 6.32. Analyses of surface roughness length under different stability conditions for the 3 assumed wake-free sectors.

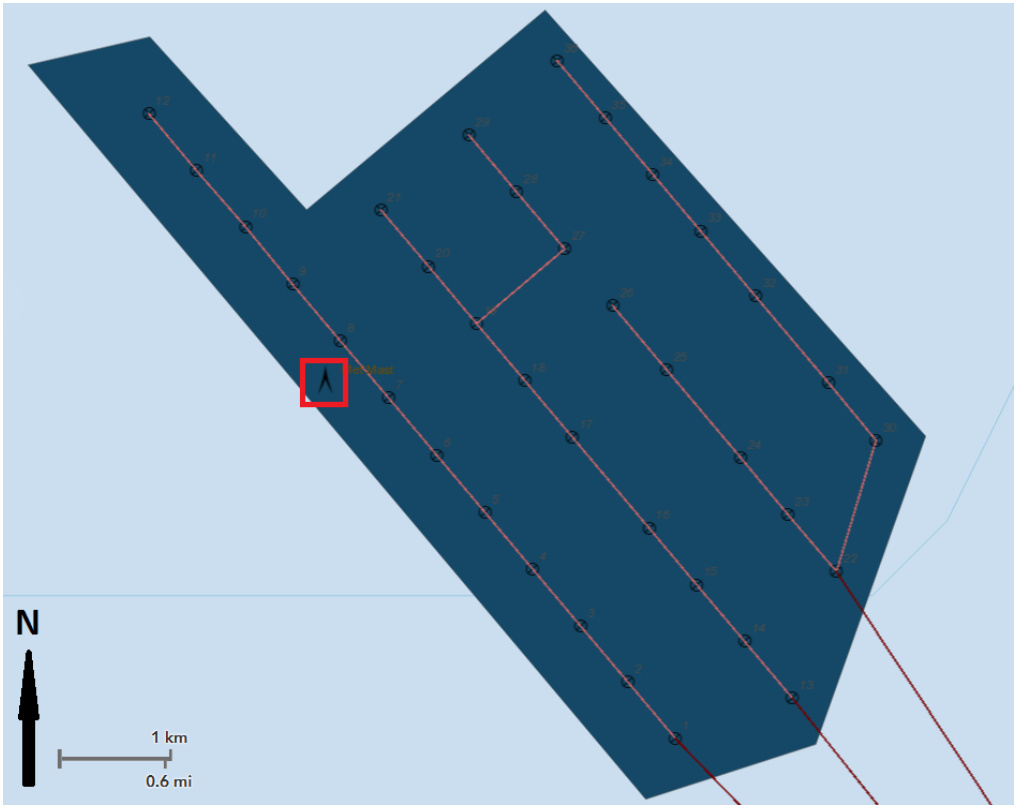

Figure 6.33. Egmond aan Zee offshore wind farm map. The red square represents the location of the meteorological mast. All red lines represent electric cables and black circles over the lines are the wind turbines, [138].

6.9 Discussion on high z_0 values

The previous section was an analysis to discover the reasons for high z_0 values. Firstly, the atmospheric stability was checked. Since the method to filter neutral conditions was too simple, comparing air and sea temperatures, it was suspected that the stability could be a reason. It has been demonstrated that this was not the case. Many high z_0 values were also found when $1/L_s \approx 0$, i.e. under neutral conditions. Another possibility was a wake effect from an obstacle, such as the meteorological mast or a wind turbine. This was also not the reason since high z_0 values were found for all sectors under neutral conditions. In this section a possible reason is discussed, although not demonstrated.

In the boundary layer there are two sources of turbulence, these are buoyancy and wind shear. The first one, buoyancy, is caused by differences of air density at different heights. These are produced by changes in

temperature, humidity and pressure. In other words, the atmospheric stability depends on buoyancy. The second source, wind shear, is a mechanical production by the obstacles in the direction of the wind. Thus, under null buoyancy, turbulence and instability can be caused by wind shear. The following explanations of this section are written under the assumption of neutral buoyancy.

The (kinetic) energy that is mechanically produced as turbulence is lost from the mean flow, and vice versa, [134]. It will be expected to have more losses when there are more obstacles on the surface, i.e. the surface is rougher. Therefore, the higher the losses, the rougher the surface. This is true onshore, where there is only one fluid, the wind, and a solid ground. These conditions are different offshore and over lakes. The turbulence mechanically produced by the surface is expected to be lower than onshore since the obstacles are smaller. Thus, the amount of losses from the mean flow by the increment of turbulence is low. However, there is another source of losses. Unlike onshore, offshore there is an interaction between two fluids. The fact that the ocean waves are produced by the wind proves that there is a kinetic energy transfer from the wind to the sea. In other words, in offshore environments the mean flow experiences losses by wind shear and wave production. If there is an increase of losses, it must be expected that there will be an increase in the aerodynamic surface roughness. This is especially true if z_0 is calculated through the wind profile.

The high z_0 values shown in this thesis could be produced by losses due to wave production. The analysis on wave age, Figure 6.24, revealed that the highest roughness appears for the smaller wave ages; i.e. when the wave production starts. A reasonable idea is to expect the highest kinetic energy transfer from the wind to the sea at the beginning of the wave production.

The losses in the mean flow, the wind, by wave production were studied in [139], [140], [141], and [142]. The growth rate of wave energy has been found to be higher for young waves than mature waves, [143]. This fact is demonstrated in Figure 6.34. At the same time, it has been demonstrated in Figure 6.35 that the non-dimensional wind energy is lower under young seas than mature seas. Both facts prove that the energy transfer from wind to waves is higher in the presence of young waves rather than mature waves.

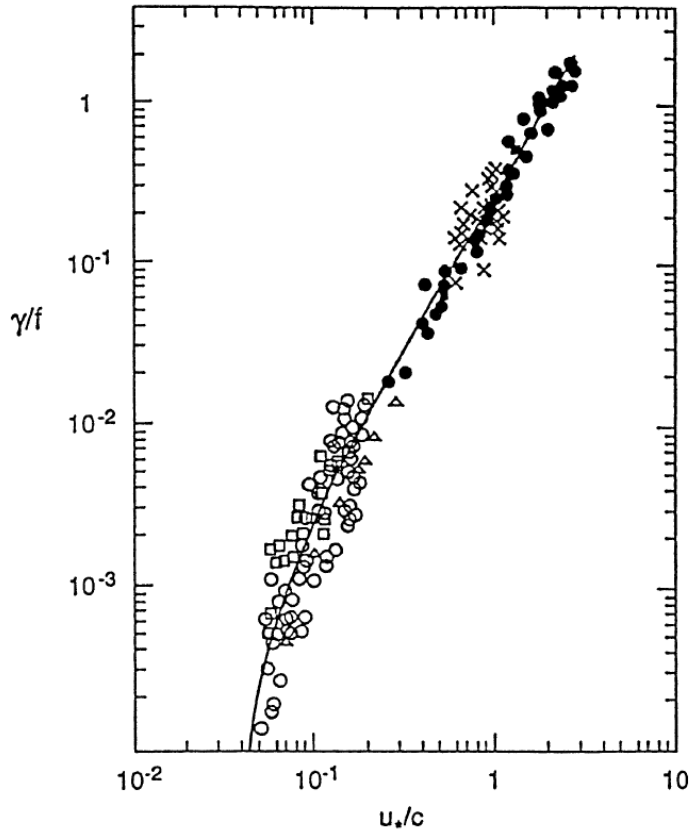

Figure 6.34. Observed non-dimensional wind wave growth rates (vertical axe) against the inverse wave age (horizontal axe). Open circles and squares are field data, others are laboratory data. γ represents the non-dimensional wind input growth rate, f is the wave frequency, and c is the phase speed. Source: [142].

Another question is: Why these high z_0 values have not been observed in previous studies? All the literature consulted for this thesis found small values for z_0. However, all the literature consulted used a long period to calculate aerodynamic surface roughness. The usual approach is to calculate z_0 from mean wind speed values for periods over months or years. This approach is correct for places with steady surface, i.e. onshore. With a non-static surface, which can change significantly within a period of minutes or hours, the usual approach is inaccurate. Analysing parameters under long period terms in offshore environments may lead to miss uncommon situations. Since the analyses in this thesis were realised with 50 minutes periods, some unusual situations were observed. Therefore, the calculated z_0 in this thesis may not be wrong; it may be showing some situations of high kinetic energy transfer from the wind to the sea.

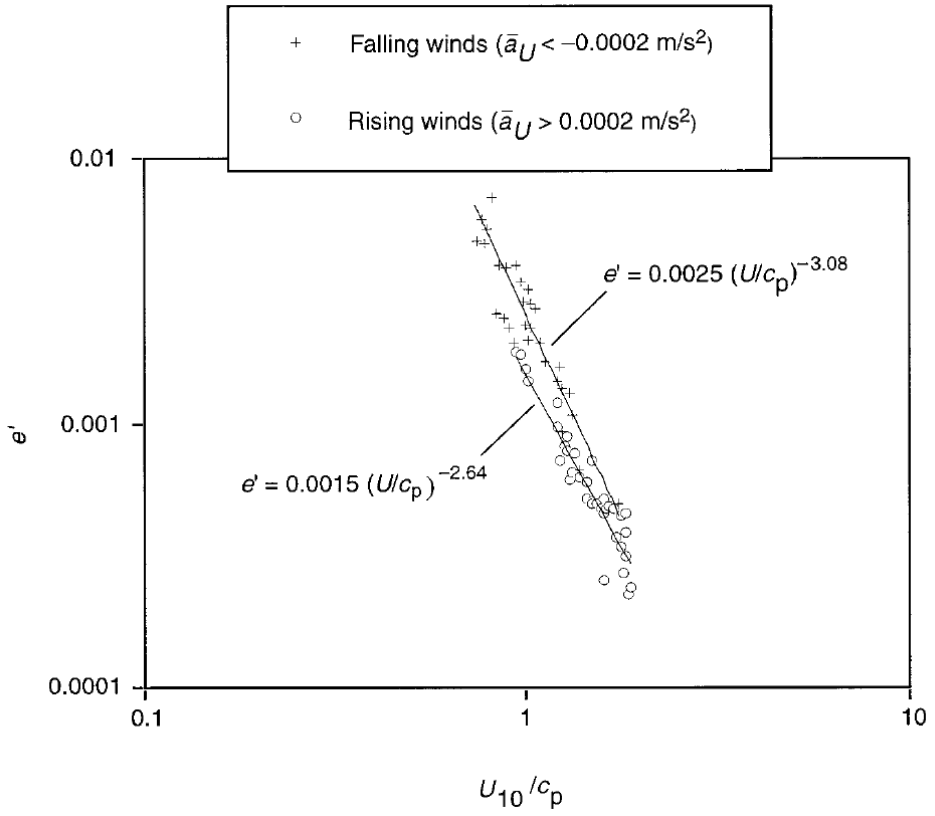

Figure 6.35. Non-dimensional wind energy (e') in falling and rising wind conditions against the inverse wave age. Source: [139].

The reason for high z_0 values discussed above should modify the logarithmic law for offshore and lake environments. Here there are two options. The first one is to switch the aerodynamic z_0 to a virtual z_0, Eq. 6.18. The virtual z_0 must incorporate the common aerodynamic surface roughness length plus another length parameter representing the kinetic energy transfer from the wind to the sea. The second option is to incorporate a dimensionless parameter similar to the atmospheric stability correction, the energy transfer correction. This parameter should be dependent on the wave age, and perhaps on a ratio of kinetic energy from the sea and kinetic energy from the wind. With this second option, z_0 may be independent of the wave age. If that was the case, the z_0 could be calculated by the adoption of Lettau's equation to the sea, as shown in Eq. 6.12. The z_0 could still be only dependant on the drag coefficient and the quantity and size of obstacles. Obviously, this is still a theory which needs to be proved, and it should be tested in future research.

6.10 Summary

This chapter explains the development of a new formulation to calculate z_0. The study began with a tested method, Lettau's method. This method was already validated onshore in the presence of only one type of obstacle over a domain. Over deep waters, it is expected to find only one type of obstacle, consecutive waves forming straight lines. Hence the adaptation of Lettau's method seemed reasonable. A straightforward formulation was achieved. However, results did not show a remarkable agreement when compared with the wind profile measured in situ. Nevertheless, a direct relation between z_0 and C_d was observed.

Following the improvement found, in comparison with previous methods tested in chapter 5, a sensitivity analysis was undertaken. The objective of the sensitivity analysis was to find the appropriate empirical coefficients for the equation derived from Lettau's research. Once both parameters, α, and cw, were found some interesting findings were achieved. The first finding is the relation between α and κ. For many researchers, α always takes a value of 2. In this study, it was suggested that α could be strongly related to von Karman's constant, κ. The second finding was the similarity of cw with L_p. This fact was also analysed and a high correlation was observed in the z_0 correlation. Due to both findings, empirical coefficients were successfully removed from the formulations.

The final equation, 6.18, was proven by different wave age, wave height, and wind speed conditions as was also studied in chapter 5. The reason to complete such analysis was to find a physical meaning to the new method for z_0. It was found that the new equation reached high agreement only under certain conditions.

Finally, a last analysis was undertaken due to the observed high z_0 values along with this thesis. The atmospheric stability was studied and plotted against z_0. This analysis was repeated for six different sectors according to the wind direction. Thus, any possible the wake effect could be checked.

7. Conclusions

7.1 Identification of advantages and disadvantages of satellite wind retrievals for the wind industry

Satellite datasets have a great potential to reduce costs in offshore wind resource assessment, not only for wind farms but also for other applications. Merging different satellites can be the solution to increase temporal coverage. However, satellites will always require the support of in situ devices to achieve high accuracy. It is known that all satellites studied here and in other studies present bias under certain conditions such as rain or high winds but this study also showed a small difference was observed for low wind speeds. The bias must be studied and corrected for each satellite before using it for a wind resource assessment. Clearly, satellites should be inter-calibrated, but even so, some satellites showed positive bias when others showed negative bias in comparison with the meteorological mast. Hence, and to achieve accuracy, all satellite data in an HDDC should be divided by satellite and analysed separately. To solve this issue, satellites should be correlated with in situ measurements, such as floating LIDAR or buoys but not meteorological masts in order to avoid the need for expensive mast foundations in the sea.

A correlation with in situ devices could increase accuracy and, perhaps, satellite data could be used as an historical data source involved in the Measure-Correlation-Prediction technique which is common in wind resource assessments. Future studies should contemplate this possibility since it could be the first use by offshore wind farm developers. Before that an improvement in surface roughness and atmospheric stability parameterization is necessary. This will require the insertion of new methods into the software tool developed by the author of this thesis and an expansion of the database made in order to include more atmospheric and oceanic parameters.

Differences related to the extrapolation methodology need to be removed and an accurate method for extrapolation determined. Wind assessment on a short-term basis seems to be the most realistic method and for the extension it should be the most accurate. However, the amount of data and parameters

involved in short-term calculations can be a real challenge. The long-term basis should still be kept in mind because it could be a fair approximation before undertaking an accurate resource assessment in detail.

Only SAR's seems to match wind industry requirements when building wind maps for small areas with high resolution. In order to improve coastal observations, the inclusion of computational fluid dynamics could increase coastal coverage and also resolution. Although it was not included in this thesis, daily and seasonal variations must be studied. Otherwise, wind climatology will be biased due to a higher amount of data acquired during the daytime.

7.2 Analysis of different methodologies for offshore wind vertical extrapolation

Vertical extrapolation of wind speed over the ocean is challenging when the wind profile is unknown. Satellite wind retrievals give information in two dimensions in a plane parallel to the ocean surface. All wind data, independently of spacecraft device type, is calculated at 10 meters over the ocean by its characteristic GMF. Meteorological masts and Lidars also monitor wind vectors but in a single dimension, along with the altitude, unlike satellite data. Transformation of satellite data from 2D to 3D was undertaken through knowledge in wind profile, i.e. the logarithmic law shown in Eq. 2.5. Since U_{10} is monitored by satellites, only u_* and z_0 must be parameterized.

All results highlighted underestimation of u_* by various methods when compared with in situ measurements. The same problem appeared for all z_0 regressions pointing to the fact that z_0 calculated by all different methods was also underestimated. These two facts were proven to compensate each other by the nature of the logarithmic law. Wind speed regressions after extrapolation were found to be in good agreement. However, those regressions were not sufficient to validate the methods. Only the agreement between u_* and z_0, plus a posterior agreement in extrapolated wind speed, could validate a methodology.

The main problem found was with the z_0 method rather than u_* parameterization. This fact was proved with the combination of different z_0

methods and directly measured u_*. A combination of the z_0 equation and the logarithmic law can be solved by iteration. However, as long as a z_0 method underestimate z_0, u_* will also be underestimated. The research needed to be directed towards the resolution of z_0. This one should reach a proper agreement with z_0 from a measured wind profile, or at least some correlation. In chapter 5, that correlation was completely missing for z_0. Since measurement or calculation errors were discarded in the surface roughness crosscheck, the most probable reason for such underestimation was the use of empirical coefficients in both u_* and z_0 methods. A new method without the use of empirical coefficients was deemed to be necessary. The new relation must include sea state parameters in order to include all possible sea conditions, such as the calm sea, growing sea, and the presence of swell. Any method relying only on wind speed will only represent fully developed, wind dominated seas which are not common conditions. The inclusion of satellite data into wind industry will not occur unless this new method is found and a vertical extrapolation is successfully achieved. In that sense, there is still a second challenge. This challenge is building climatology from satellite data, which should be remembered.

7.3 The developed method for surface roughness length parameterization

Two different locations were chosen for validation; however, Egmond aan Zee presented better data consistency over time. Hence, higher valid data were found despite a shorter survey period. Data quality in offshore environments was a big issue since a lack of quality can drastically reduce the volume of data as occurred with the Fino-1 mast. The synergy between different monitoring devices was another cause of data leakage. The third dataset of overlapping satellites and Egmond aan Zee measurements was a proof of this. Due to the amount of valid data Egmond aan Zee dataset covered a wide range of atmosphere and sea state conditions achieving high representativeness. Under neutral conditions, the logarithmic law was proven to be valid by reaching accurate, predicted wind profiles when compared with a meteorological mast. This fact was key in order to establish control u^* and z_0 parameters for validation.

The study from chapter 6 pursued a new formulation for z_0 avoiding the use of empirical coefficients. Lettau's equation was adapted to sea parameters following wave dynamics and wave amplitude theories. Incidence angle and different z_0 regimes were also included. Two big assumptions were made in order to simplify this; the proposed formulation was only written for deep waters and excluded breaking waves. As an output Eq. 6.12 was proposed, its results showed a poor correlation in z_0 regression. Even so, better correlation than previous methods proposed in the literature was achieved with a correlation coefficient of 0.750. Three sensitivity analyses helped to make some changes and the final Eq. 6.18 was created. Furthermore, a slightly different formulation for drag coefficient was proposed, Eq. 6.16, but not validated. Finally, two sources of scattering were removed, incidence angle correction and instantaneous wavelength. A possible cause of error was that the wind direction measurements were taken at an excessive height where Ekman's spiral effects could be present, leading to an unrealistic incidence angle correction. On the other hand, the instantaneous wavelength was substituted by long-term wavelength. Although the z_0 formulation achieved a good correlation overall, it tends to overestimate z_0 for low ranges, z_0<0.4. Most of the measurement points were found to be located within this low range. This fact led to an underestimation of the wind profile which was compared with measured wind speed by an offshore meteorological mast.

A deeper analysis of Eq. 6.18 for different wave ages, wave heights and wind speeds brought shed some light on this. The best correlation was surprisingly found under very young waves conditions when a better agreement was expected for fully developed seas. In fact, Eq. 6.18 was capable of determining z_0 for such range of wave age where no other formulation in the literature was capable. It was also found that most of the decaying seas presented low roughness. Wave height analysis only showed that the higher the wave height, the lower the roughness. Similarly, wind speed analysis reflected that the higher the wind speed, the lower the roughness. Surface roughness regressions were more illustrative when the natural logarithm was plotted. According to previous z_0 methods, these found correlation at very low z_0; the proposed formulation covered high z_0 but medium to low z_0 has not been successfully parameterized by any other equation. Further

research should keep studying z_0 as a function of drag coefficient as Lettau's equation and the present study since it found almost a perfect agreement in the overall regressions. Plus, there are still possibilities for improvement of the proposed formulation from this study.

High z_0 values were showed in the last chapter. These values are unexpectedly high for offshore environments. Hence, the atmospheric stability was analysed. This was discarded as a reason for such values. A possible wake effect was neither the cause. The energy transfer between wind and sea was demonstrated to be the reason. Since this energy transfer is not reflected in the logarithmic law expression, neither the z_0, the energy transfer needs to be integrated into the logarithmic law to represent with confidence the offshore wind profile over short periods in offshore environments.

This research was part of a bigger project, the development of a satellite-enabled tool for offshore wind resource optimisation. Following the project line, a proper parameterization of z_0 could improve satellite wind retrievals. Their lack of accuracy for low and high winds could be due to a loss in translation from measured wind stress to calculated wind speed at 10 meters above sea level. A proper parameterization of z_0 plus the use of wind stress, retrieved from satellites, should allow the calculation of wind speed at any given height. This hypothesis will only stand under neutral conditions, to cover all atmospheric stability conditions, stability correction must be applied.

7.4 Thesis objectives achievement

After making conclusions from the analyses covered in chapters 4, 5 and 6, it is necessary to evaluate the fulfillment of the thesis objectives detailed in section 1.1. These objectives were split into two different blocks. First, the WindRes related objectives; and second, the further research for improvement of satellite retrievals or matching wind industry requirements.

The analysis undertaken in chapter 4 was focused on the achievement of WindRes objectives. The benefits of satellite datasets for the wind industry were highlighted in section 7.1. The developed tool is capable of creating a wind atlas from any source of wind information, remote sensing or in situ. A

preliminary wind assessment can also be undertaken. This includes Weibull parameters, energy density, wind roses and other statistics. However, the software is not operational or ready to commercialize. The main reason for that is the further research required to improve the accuracy of the wind speed extrapolation.

Advantages and disadvantages of the satellite wind retrievals were explained as well as the fields of research to match industry requirements. These are the capability to vertically extrapolate winds, calculate friction velocity and surface roughness length, plus the possibility to build climatology. From these four different research fields, surface roughness parameterization has been identified as essential.

This fact led to the research undertaken and explained in chapters 5 and 6. These two chapters are focused on friction velocity and surface roughness methods. As explained in section 7.3, it is possible to take friction velocity directly from satellite measurements. But, surface roughness length must be known before calculating the wind speed. In this thesis, a new formulation for surface roughness length has been suggested as well as a new method for drag coefficient estimation. However, the new methods have been proved to work only under low wave age conditions. Nevertheless, the method is free of empirical coefficients and describes surface roughness length with accuracy for conditions where no other known formulation does.

Even so, surface roughness length is not well parameterized under all conditions. Furthermore, a method to build climatology from satellites measurements has not been investigated yet. Thus, more research is needed to be carried out for confident parameterizations; details of this are explained in the next section.

7.5 Future work

This thesis followed the development of a tool which, while fully functional, is not yet fully operational. Before releasing any software to the market, it is still necessary to undertake further studies. Furthermore, some technical issues must be faced too. Here it is presented a list of the tasks in the future as follows.

1. **Finish the development of a z_0 model.** Once a z_0 model is achieved, it will be automatically possible to calculate wind vectors in 3 dimensions from satellite retrievals and buoy (or other in situ devices) measurements.

2. **Calculation of the wind vector from wind stress.** Satellites (scatterometers and SAR's) are really measuring wind stress instead of wind speed. The actual algorithm, GMF, for conversion uses empirical coefficients resulting in a lack of accuracy for low winds (< 5 m/s), high winds (>15 m/s) and coastal areas. Applying an accurate z_0 method plus the measured u^* by satellites, could enhance accuracy.

3. **The inclusion of atmospheric stability correction.** In this thesis, only measurements under neutral conditions were used. This was so to simplify calculations and analyze z_0 methods independently. With the inclusion of atmospheric stability correction into the algorithms, it will be possible to use measurements under all atmospheric conditions.

4. **Satellite wind climatology.** The first use of satellite data by wind developers should be as support during the planning stage. Hence it would necessary to study how to use satellite data as historical data. Representativeness of daily, season and year variabilities by satellite data must be analyzed.

5. **Testing phase.** In previous steps, results will be validated and compared with in situ devices. Even so, a testing stage where the methodology is applied in different points of the globe will be necessary. Hence, it will be required to acquire data from all over the world. There is another possibility; it could use ERA and MERRA databases. These databases contain data from ground and satellite measurements, plus parameters calculated trough Numerical Weather Prediction models.

6. **Build the satellite DB.** This database can include gridded data from satellites, including scatterometers, radiometers, SAR's and perhaps altimeters. Otherwise, the database could be a short register of

datasets per area including a link to original satellite DB. Thus, it will not be necessary to hold a large DB; however, analysis speed will drop due to required time to download datasets. A third and ambitious option is to build a massive DB with any ocean measurement from any remote sensing device onboard a satellite.

7. **Build in situ devices DB.** This second and parallel database is the exact same idea but here only including in situ devices such as buoys, meteorological masts, offshore platforms, etc. Again, ERA and MERRA databases could be used as well.

8. **Further software development.** The very last step before launching the software. The goal is to improve the output layout, build a user interface, etc.

8. References

[1] L. Fried, L. Qiao, S. Sawyer, S. Shukla. *Global Wind Report. Annual market update, 2014.* Global Wind Energy Council (GWEC). 2014

[2] A. Arapogianni, A.B. Genachte, R. M. Ochagavia, J.P. Vergara, D. Castell, A.R. Tsouroukdissian, J. Korbijn, N.C.F. Bolleman, F.J. Huera-Huarte, F. Schuon, A. Ugarte, J. Sandberg, V. de Laleu, J. Maciel, A. Tunbjer, R. Roth, P. de la Gueriviere, P. Coulombeau, S. Jedrec, C. Philippe, S. Voutsinas, A. Weinstein, L. Vita, E. Byklum, W.L. Hurley, H. Grubel. *Deep Water. The next step for offshore wind energy.* European Wind Energy Association (EWEA). 2013.

[3] A. Arapogianni, J. Moccia, J. Wilkes, A.B. Genachte. *Where is the money coming from? Financing offshore wind farms.* European Wind Energy Association (EWEA). 2013.

[4] Oldbaum Services, Institut für Solare Energieversorgungstechnik e. V (IWES), Kjeller Vindteknikk (KVT), DTU Wind Energy, University of Strathclyde, GL Garrad Hassan Germany, Scottish Enterprise, Dong Energy, Nautilus Associates, Statoil Hydro ASA, 3E, CLS France, Institute of Physical Energetics, SSE, Faculdade de Ciências da Universidade de Lisboa, Koninklijk Nederlands Meteorologisch Instituut, SmartWIND, LNEG, EDP renewables, Danish Technical University IMM Denmark, GL Garrad Hassan UK, 2012: NORSEWInD. Oldbaum Services, February 2015, http://www.norsewind.eu/norse/.

[5] Energy Sector management Assistance Program. Best Practice Guidelines for Mesoscale Wind Mapping projects for the World Bank. October 2010.

[6] J.F. Manwell, J,G McGowan, A.L. Rogers. *Wind Energy explained, theory, design and application*. Second edition, Ed.Wiley, 2009.

[7] G.M. Joselin Herbert, S. Iniyan, D. Amutha. *A review of technical issues on the development of wind farms*. Renewable and Sustainable Energy Review, 32, 619-641, 2014.

[8] Mathworks, Wind Resource Assessment: http://www.mathworks.co.uk/discovery/wind-resource-assessment.html (January 2015)

[9] A.M. Sempreviva, R.J. Barthelmie, S.C. Pryor. *Review of methodologies for offshore wind resource assessment in European Seas*. Surv. Geophys. 29: 471-497, 2008.

[10] World Bank Group, Energy Sector Management Assistance Program, Technical University of Denmark, VORTEX. Global Wind Atlas. March 2016. https://globalwindatlas.info/.

[11] A.K. Azad, M.G. Rasul, M.M. Alam, S.M. Ameer Uddin, S.K. Mondal. *Analysis of Wind Energy Conversion System Using Weibull Distribution.* J. of Procedia Engineering, vol. 90, 725-732, 2014. DOI: 10.1016/j.proeng.2014.11.803.

[12] L. Botsis. What Particular spatial, environmental and public constraints are presented for the UK wind projects' developments and success? Can be managed? CarbonDescent.org.uk, July 2011.

[13] A. L. Rogers, J. W. Rogers, J. F. Manwell, *Comparison of the performance of four measure-correlate-predict algorithms*. Journal of Wind Engineering and Industrial Aerodynamics, 243-264, 2005.

[14] P. Beaucage, M.C. Brower, J. Tensen. *Evaluation of four numerical wind flow models for wind resource mapping.* J. of Wind Energy, 17, 197-208, 2014. DOI: 10.1002/we.1568.

[15] DTU Wind Energy. WAsP: Wind energy industry-standard software. January 2016. http://www.wasp.dk/.

[16] Wind Power Program. March 2016. http://www.wind-power-program.com/mean_power_calculation.htm.

[17] C. B. Hasager, A.Pena, M. B. Christiansen, P. Astrup, M. Nielsen, F. Monaldo, D. Thompson, P. Nielsen. *Remote Sensing Observation Used in Offshore Wind Energy*. IEEE Journal of selected Topics in Applied Earth Observations and Remote Sensing, Vol. 1, No. 1, March 2008.

[18] M.B. Christiansen, W. Koch, J.Horstmann, C.B. Hasager. *Wind resource assessment from C-Band.* Remote Sensing of Environment, 105, 68-81, 2006.

[19] M.B. Christiansen, C.B. Hasager. *Wake Effects of large offshore wind farms identified from satellite SAR*. Remote Sensing of Environment, 98, 251-68, 2005.

[20] P.P. Mathieu, C.B. Hasager. *Winds of change from space*. In the Full Picture, pp 202-203, Genova, Tudor Rose, 2008.

[21] M.B. Christiansen, C.B. Hasager, D.R. Thompson, F. Monaldo. *Ocean winds from synthetic aperture radar*. In Ocean Remote Sensing,: Recent Techniques and Applications, eds R. Niclos and V. caseles, Research Singpost Editorial, 2008.

[22] R.J. Barthelmie, J. Badger, S. Pryor, C.B. Hasager, M.B. Christiansen B.H. Jorgensen. *Offshore coastal wind speed gradients: issues for the design and development of large offshore windfarms*. Wind Engineering , 31, n0. 6, 369-82, 2007.

[23] P. Beaucage, M. Bernier, G. Lafrange, J. Choisnard. *Regional mapping of the offshore wind resource: Towards a significant contribution from space-borne Synthetic Aperture Radar*. IEEE Journal of selected Topics in Applied Earth Observations and Remote Sensing, 1, N0. 1, 45-56, 2008.

[24] C.B. Hasager, R.J. Barthelemie, M.B. Christiansen, M. Nielsen, S.C. Pryor. *Quantifying offshore wind resources from satellite wind maps: study area the North Sea*. Wind Energy, 9, 63-74, 2006.

[25] C.B. Hasager, N. Nielsen, P. Astrup, R.J. Barthelemie, E. Dellwik, N.O. Jensen, B.H. Jorgensen, S.C. Pryor, O. Rathman, B. Furevik. *Offshore wind resource estimation from satellite SAR wind field maps*. Wind Energy, 8, 403-19, 2005.

[26] Y. Quilfen, C. Prigent, B. Chapron, A.A. Mouche, N. Houti. The potential of quikSCAT and WindSat observations for the estimation of sea surface wind vector under severe weather conditions. Journal of geophysical Research-Oceans, 112, no.C9, 2007.

[27] F. Pimenta, W. Kempton, R. Garvine. Combining meteorological stations and satellite data to evaluate the offshore wind power resource of Southeastern Brazil. Renewable energy 33, 2008.

[28] F.M. Monaldo, X. Li, W.G. Pichel, C.R. Jackson. *Ocean wind speed climatology from spaceborne SAR imagery.* American meteorologiacal society, April 2014.

[29] M.B. Christiansen. Wind Energy Applications of Synthetic Aperture Radar. Risø-PhD-27(EN), 2006.

[30] F.M. Monaldo, D.R. Thompson, N.S. Winstead, W.G. Pichel, P. Clemente-Colon, M.B. Christiansen. *Ocean Wind Field Mapping from Synthetic Aperture Radar and its Application to Research and Applied Problems.* Johns Hopkins APL Technical Digest, volume 26, number 2, 2005.

[31] P.D. Mourad, D.R. Thompson, D.C. Vandemark. *Extracting Fine-Scale Wind Fields from Synthetic Aperture Radar images of the Ocean Surface.* Johns Hopkins APL Technical Digest, volume 21, number 1, 2000.

[32] J. Horstmann, W. Koch. High resolution ocean surface wind fields retrieved from spaceborne Synthetic Aperture Radars operating at C-Band. Institute for Coastal Research, GKSS Research Center, Germany.

[33] H.G. Kim, H.J. Hwang, S.H. Lee, H.W. Lee. Evaluation of SAR wind retrieval algorithms in offshore areas of the Korean Peninsula. Renewable Energy 65, 2014.

[34] C.B. Hasager, A. Mouche, M. Badger, F.Bingol, I. Karagali, T. Driesenaar, A. Stoffelen, A. Peña, N. Longepe. *Offshore wind climatology based on synergetic use of Envisat ASAR, ASCAT and QuikSCAT.* Remote Sensing Environment 156, 2015.

[35] P. Chang, P.W. Gaiser, K. St Germain, L. Li. Multi-Frequency Polarimetric Microwave Ocean Wind Direction retrievals. NRL, NOAA and JPL.

[36] Iain H. Woodhouse. *Introduction to Microwave Remote Sensing*. Taylor & Francis Group. 2015.

[37] D. Vandemark, P.W. Vachon, B. Chapron. Assessment of ERS-1 SAR wind speed estimates using an airbone altimeter.

[38] S. Jin, A. Komjathy. GNSS Reflectometry and Remote Sensing: New Objectives and Results. Advances in Space Research 46. 2010.

[39] CEOS, ESA. The CEOS Database. January 2016. http://database.eohandbook.com/database/missiontable.aspx.

[40] Ocean Vector Wind Science Team, Climate Working Group. Evaluating and Extending the Ocean Wind Climate Data Record. 2016

[41] European Space Agency: http://earth.esa.int/services/(September 2016)

[42] European Organisation for Meteorological Satellites (EUMETSAT). September 2016. https://www.eumetsat.int/website/home/index.html.

[43] National Aeronautics and Space Administration (NASA). September 2016. https://www.jpl.nasa.gov/missions/.

[44] Indian Space Research Organisation (ISRO). September 2016. https://www.isro.gov.in/.

[45] Canadian Space Agency (CSA). September 2016. http://www.asc-csa.gc.ca/eng/Default.asp.

[46] US Naval Research Laboratory. September 2016. https://www.nrl.navy.mil/WindSat/.

[47] J.P. Hollinger, J.L. Pierce, G.A. Poe. *SSM/I Instrument Evaluation.* IEEE Transactions on geoscience and remote sensing, volume 28, number 5, September 1990.

[48] S.H. Yueh, W.J. Wilson, F.K. Li, S.V. Nghiem, W.B. Ricketts. *Polarimetric Measurements of Sea Surface Brightness Temperatures Using an Aircraft K-Band Radiometer.* IEEE Transactions on geoscience and remote sensing, volume 33, number 1, January 1995.

[49] K St Germain, G.A. Poe, P.W. Gaiser. Polarimetric Emission model of the sea at microwave frequencies and comparison with measurements. Progress In Electromagnetics Research 37, 2002.

[50] P.W. Gaiser. *WindSat-Remote Sensing of Ocean Surface Winds.* Naval Research Laboratory-Remote Sensing Division.

[51] Ian S. Robinson. Measuring the Oceans from Space: The principles and methods of satellite oceanography. Springer. 2004.

[52] S. Soisuvarn, Z. Jelenak, P.S. Chang, S.O. Alsweiss, Q. Zhu. *CMOD5.H – A High Wind Geophysical model Function for C-band Vertically Polarized Satellite Scatterometer Measurements.* IEEE Transactions on Geoscience and Remote Sensing, vol. 51, no. 6, 3744-3760, June 2013.

[53] A. Resti, J.Benveniste, M. Roca, G. Levrini. *The Envisar Radar Altimeter System (RA-2).* ESA bulletin 98. June 1999.

[54] C. Zuffada, T. Elfouhaily, S. Lowe. *Sensitivity analysis of wind vector measurements from ocean reflected GPS signals.* Remote Sensing of Environment 88, 341-350, 2003.

[55] A. Komjathy, V.U. Zavorotny, P. Axelrad, G.H. Born, J.L. Garrison. *GPS Signal Scattering from Sea Surface: Wind Speed Retrieval using Experimental Data and Theoretical Model*. Remote Sensing of Environment 73, 162-174, 2000.

[56] E. Cardellach, G. Ruffini, D. Pino, A. Rius, A. Komjathy, J.L. Garrison. *Mediterranean Ballon Experiment: ocean wind speed sensing from the stratosphere using GPS reflections*. Remote Sensing of Environment 88, 351-362, 2003.

[57] D. Mickler, P. Axelrad, G. Born. *Using GPS reflections for satellite remote sensing.* Acta Austronautica 55, 39-49, 2004.

[58] E. Cardellach, A. Rius. A new technique to sense non-Gaussian features of the sea surface from L-band bi-static GNSS reflections. Remote Sensing of Environment 112, 2927-2937, 2008.

[59] V.U. Zavorotny, A.G. Voronovich. *Scattering of GPS Signals from the Ocean with Wind Remote Sensing Application.* IEEE Transactions on Geoscience and Remote Sensing, Vol. 38, No. 2, March 2000.

[60] S. Gleason, S. Hodgart, Y. Sun, C.Gommenginger, S. Mackin, M. Adjrad, M. Unwin. *Detection and Processing of Bistatically Reflected GPS Signals From low earth Orbit for the Purpose of Ocean Remote Sensing.* IEEE Transactions on Geoscience and remote sensing, Vol. 43, No. 6, June 2005.

[61] K. Yu, C. Rizos, D. Burrage, A.G. Dempster, K. Zhang, M. Markgraf. *An overview of GNSS remote sensing.* Journal on Advances in Signal Processing, 2014.

[62] C.S. Pryor, M. Nielsen, R.J. Barthelmie, J. Mann. Can satellite sampling of offshore wind speeds realistically represent wind speed distributions? Part II: quantifying uncertainties associated with distribution fitting methods. Journal of Applied Meteorology, 43, 739-750, 2004.

[63] M.B Ben Ticha, T. Ranchin, L. Wald. *Using several data sources for offshore wind resource assessment*. Copenhague Offshore Wind conference, 2005.

[64] N. Fichaux, T. Poglio, T. ranchin. *Mapping offshore wind resources: synergetic potential of SAR and scatterometer data.* IEEE Journal of oceanic engineering, Vol 30, No3, 516-525, 2005.

[65] P. Beaucage, G. Lafrance, J. Choisnard, M. Bernier. *Synthetic aperture radar satellite data for offshore wind assessment : a strategic sampling approach*. J. Wind. Eng. Ind. Aerodyn. 99, p27-36, 2011.

[66] University of Regina, Getting your imagery at the right level: http://uregina.ca/piwowarj/Think/ProcessingLevels.html (March 2015)

[67] C. B Hasager, M. Badger, A. Mouche, A. Stoffelen, T. Driesenaar, I. Karagali, F. Bingol, A. Pena, P. Astrup, M. Nielsen, A. Hahman, P. Costa, E. Berge, R. E. Bredesen. *Report from DTU Wind Energy E-0007(EN)*. Sept. 2012, ISBN 978-87-92896-12-4.

[68] K.F. Dagestad, J. Johannessen, G. Hauge, V. Kerbaol, F. Collard. *Automated high resolution wind field retrievals off the norvegian coast by combined use of Envisat Asar and numerical models*. Proc. Envisat Symposium 2007, Montreux, Switzerland, 23-27 April 2007.

[69] A. Mouche, F. Collard, B. Chapron, K.F. Dagestad, G. Guillon, J. Johannessen, V. Kerbaol and M.W. Hansen. *On the use of Doppler shift for sea surface wind retrieval from SAR*. IEEE Transactions on Geoscience and Remote Sensing, DOI: 10.1109/TGRS.2011.2174998, 2012.

[70] A. Pena, T. Mikkelsen, S.E. Gryning, C. Hasager, A.N. Hahman, M. Badger, I. Karagali, M. Courtney. *Offshore Vertical Wind shear*. DTU Wind Energy-E-Report-0005(EN), August 2012.

[71] C. Draxl, A. N. Hahman, A. Pena G. Giebel. Evaluating winds and vertical wind shear from Weather Research and Forecasting model forecasts using seven planetary boundary layer schemes. Wind Energy, Vol 17, pp 39-55, 2014.

[72] M. Badger, A. Pena, R. E. Bredesen, E. Berge, A. Hahman, J. Badger, I. Karagali, C. Hasager, T. Mikkelsen. *Bringing satellite winds to hub-height*. EWEA, 2012.

[73] R.J. Barthelmie, S.C. Pryor. Can Satellite of Offshore Wind Speeds Realistacally Represent Wind Speed Distributions? American Meteorological Society, 2003.

[74] P. Beaucage, G. Lafrance, J. Lafrance, J. Choisnard, M. Bernier. *Synthetic aperture radar satellite data for offshore wind assessment: A strategic sampling approach.* J. Wind Eng. Ind. Aerodyn. 99, 2011.

[75] PO.DAAC. Cross-Calibrated, Multi-Platform Ocean Surface Wind Velocity Product (MEaSUREs Project). 2009.

[76] L. Ricciardulli, F.J. Wentz. A Scatterometer Geophysical Model Function for Climate-Quality Winds: QuikSCAT Ku-2011. American meteorological society. October, 2015.

[77] HZG Centre for materials and Coastal Research: http://w3g.gkss.de/G/Mitarbeiter/horstmann.html/hur_sar.htm (September 2016)

[78] NOAA Ocean Remote Sensing: http://fermi.jhuapl.edu/sar/stormwatch/ (September 2016)

[79] Brest Operational Observation Systems and Technologies: http://www.boost-technologies.com(September 2016)

[80] Edinburgh Earth Observatory, University of Edinburgh. March 2016. http://www.eeo.ed.ac.uk/.

[81] DTU Wind Energy, Technical University of Denmark. March 2016. http://www.vindenergi.dtu.dk/english.

[82] Institut français de recherché pour l'exploitation de la mer (IFREMER). March 2016. https://wwz.ifremer.fr/.

[83] The Royal Netherlands Meteorological Institute (KNMI). March 2016. https://www.knmi.nl/home.

[84] Remote Sensing Systems (RSS). March 2016. http://www.remss.com/.

[85] Collecte Localisation Satellites (CLS). March 2016. https://www.cls.fr/es/.

[86] European Centre for Medium-Range Weather Forecasts (ECMWF). March 2016. https://www.ecmwf.int/.

[87] C.B. Hasager, P. Astrup, R. Zhu, R. Chang, M. Badger, A.N. Hahmann. *Quarter-Century Offshore Winds from SSM/I and WRF in the North Sea and South China Sea.* J. of Remote Sensing, 8, 769, 2016. DOI: 10.3390/rs8090769.

[88] I. Karagali, A. Peña, M. Badger, C.B. Hasager. *Wind characteristics in the North and Baltic Seas from the QuikSCAT satellite.* J. of Wind Energy, 17, 123-140, 2014. DOI: 10.1002/we.1565.

[89] Chang, R., Zhu, R., Badger, M., Hasager C.B., Xing, X., Jiang, Y., 2015: Offshore wind resources assessment from multiple satellite data and WRF modelling over South China Sea. *J. of Remote Sensing*, **7**, 467-487, doi:10.3390/rs70100467.

[90] Musial, W.; Butterfield, S.; Ram, B. Energy from Offshore Wind. Offshore Technology Conference, Houston, Texas, USA, May 2006, National Renewable Energy Laboratory: Golden, Colorado, USA.

[91] Peña, A.; Hasager, C.B.; Lange, J.; Anger, J.; Badger, M.; Bingöl, F.; Bischoff, O.; Cariou, J. ; Dunne, F. ; Emeis, S.; Harris, M.; Hofsäss, M.; Karagali, I.; Laks, J.; Larsen, S.E.; Mann, J.; Mikkelsen, T.K.; Pao, L.Y.; Pitter, M.; Rettenmeier, A.; Sathe, A.; Scanzani, F.; Schlipf, D.; Simley, E.; Slinger, C.; Wagner, R.; Würth, I. *Remote Sensing for Wind Energy;* DTU Wind Energy (DTU Wind Energy E; No. 0029 (EN)): Roskilde, Denmark, 2013.

[92] Fino 1 Research Platform. Available online: www.fino1.de (May 2016)

[93] Meissner, T.; Rcciardulli, L.; Wentz, F. All-Weather Wind Vector Measurements From Intercalibrated Active and Passive Microwave Satellite Sensors. IGARSS, Vancouver, Canada, 2011.

[94] Ricciardulli, L.; Meissner, T.; Wentz, F. Towards a Climate Data Record of Satellite Ocean Vector Winds. IGARSS, Munich, Germany, 2012.

[95] Badger, M.; Pena, A.; Hahmann, A.N.; Mouche, A.A.; Hasager, C.B. Extrapolating Satellite Winds to Turbine Operating Heights. *Journal of Applied Meteorology and Climatology, 2016, Volume 55,* pp. 975-991, DOI: 10.1175/JAMC-D-15-0197.1

[96] Brettle, M., 2001. Wind direction profiles and yacht sails. Weather Journal, 56, 161-171.

[97] Doubrawa, P.; Barthelmie, R.J.; Pryor, S.C.; Hasager, C.B.; Badger, M.; Karagali, I. Satellite winds as a tool for offshore wind resource assessment: The Great Lakes Winds Atlas. *Remote Sensing of Environment,* 2015, *Volume 168,* pp. 349-359, DOI:10.1016/j.rse.2015.07.008

[98] Smedman, A.S.; Larsen, X.G.; Hogstrom, U. Is the Logarithmic Wind Law Valid Over the Sea?. In Wind over Waves II: Forecasting and Fundamentals of Applications, Wind Over Waves Conference, Cambridge, UK, 2001; Horwood Publishing Limited: Chichester, UK, 2003.

[99] Papadimitrakis, I.; Papaioannou A.I. Sea Surface Roughness Parameterization. In Wind over Waves II: Forecasting and Fundamentals of Applications, Wind Over Waves Conference, Cambridge, UK, 2001; Horwood Publishing Limited: Chichester, UK, 2003.

[100] Smith S.D., Anderson R.J., Oost W.A., Kraan C., Maat N., DeCosmo J., Katsaros K.B., Davidson K.L., Bumke K., Hasse L., Chadwick H.M., 1992: Sea surface wind stress and drag coefficients: The hexos results. *J. of Boundary-layer Meteorology*, 60, 109-142, doi: 10.1007/BF00122064.

[101] Drennan W.M., Graber H.C., Donelan M.A., 1999: Evidence for the effects of swell and unsteady winds on marine wind stress. *J. of physical oceanography*, 29, 1853-1864, doi: 10.1175/1520-0485(1999)029.

[102] Wu, J., 1980: Wind-stress coefficients over sea surface near neutral conditions: A revisit. *J. of physical oceanography,* 10, 727-740, doi: 022-3670/80/050727-14.

[103] Bourassa, M.A., Vincent, D.G., Wood, A.L., 2001: A sea state parameterization with nonarbitrary wave age applicable to low moderate winds speeds. *J. of physical oceanography,* 31, 2840-2851, doi: 10.1175/1520-0485(2001)031.

[104] Veiga, J.A.P., Queiroz, M.R., 2015: Impact of the waves on the sea surface roughness under uniform wind conditions: Idealized cases for uniform winds (Part I). *J. of atmospheric and climate sciences*, **5**, 317-325, doi: 10.4236/acs.2015.53024.

[105] Veiga, J.A.P., Queiroz, M.R., 2015: Impact of the waves on the sea surface roughness length under idealized like-hurricane wind conditions. *J. of atmospheric and climate sciences,* **5**, 326-335, doi: 10.4236/acs.2015.53025.

[106] Edson, J.B.; Jampana, V.; Weller, R.A.; Bigorre, S.P.; Plueddemann A.J.; Fairwall C.W.; Miller S.D.; Mahrt, L.; Vickers, D.; Hersbach, H. On the Exchange of Momentum over the Open Ocean. *Journal of Physical Oceanography, 2013, Volume 43,* pp. 1589-1610, DOI: 10.1175/JPO-D-12-0173.1

[107] Astrup, P., Larsen, S.E., 1999: WAsP engineering flow model for wind over land and sea. (Denmark. Forskningscenter Risoe. Risoe-R, No. 117 (EN))

[108] Taylor, P.K., Yelland, M.J., 2001: The dependence of sea surface roughness on the height and steepness of the waves. *J. of physical oceanography*, **31**, 572-590, doi: 10.1175/1520-0485(2001)031.

[109] Bretschneider, C.L., 1964: Generation of waves by wind: state of the art. *Netherlands University international cooperation and North Atlantic treaty organization*. NESCO Report SN-134-6, 106 pp.

[110] Wu, J., 1982: Wind-stress coefficients over sea surface from breeze to hurricane. *J. of geophysical research*, **87**, 9704-9706, doi: 0148-0227/82/002C-0800.

[111] Maat, N., Kraan, C., Oost, W.A., 1991: The roughness of wind waves. *J. of boundary-layer meteorology*, 54, 89-103, doi: 10.1007/BF00119414.

[112] Toba, Y., 1972: Local balance in the air-sea boundary processes: I. On the growth process of wind waves. *J. of the oceanographical society of Japan*, 28, 109-121, doi: 10.1007/BF02109772.

[113] Portabella, M., Stoffelen, A., 2009: On Scatterometer Ocean Stress. *J. of Atmospheric and Oceanic Technology*, **26**, 368-382, doi: 10.1175/2008JTECHO578.1.

[114] Ricciardulli, L., Wentz, F., 2011. Reprocessed QuikSCAT (V04) Wind Vectors with Ku-2011 Geophysical Model Function. Remote Sensing Systems, Santa Rosa, California, USA.

[115] Figa-Saldana, J., Wilson, J.J., Attema, E., Gelsthorpe, R., Drinkwater, M.R., Stoffelen, A., 2002: The advanced scatterometer (ASCAT) on meteorological operational (MetOp) platform: A follow on for European wind scatterometers. *Canadian Journal of Remote Sensing*, **28**, 404-412, doi: 10.5589/m02-035.

[116] Hersbach, H., 2011: Sea surface roughness and drag coefficient as functions of neutral wind speed. *J. of physical oceanography*, **41**, 247-251, doi:10.1175/2010JPO4567.1.

[117] Toba, Y., Iida, N., Kawamura, H., Ebuchi, N., Jones, I.S.F., 1990: Wave dependence of sea-surface wind-stress. *J. of physical oceanography*, **20**, 705-721, doi: 10.1175/1520-0485(1990)020.

[118] B. Lange, S. Larsen, J. Højstrup, R. Barthelmie. *Importance of thermal effects and sea surface roughness for offshore wind resource assessment*. J. of Wind Engineering and Industrial Aerodynamics, 69, 959-988, 2004. DOI: 10.1016/j.jweia.2004.05.005.

[119] Hasselmann, K., Barnett, T.P., Bouws, E., Carlson, H., Cartwright, D.E., Enke, K., Ewing, J.A., Gienapp, H., Hasselmann, D.E., Kruseman, P., Meerburg, A., Müller, P., Olbers, D.J., Richter, K., Sell, W., Walden, H, 1973: Measurements of wind-wave growth and swell decay during the Joint North Sea Wave Project (JONSWAP). *Erganzungsheft zur Deutschen Hydrographischen Zeitschrift*, Reihe A (8) 12, 93 pp.

[120] Paskyabi, M.B.; Flugge, M.; Edson, J.B.; Reuder, J. Wave-induced characteristics of atmospheric turbulence flux measurements. *Energy Procedia, 2013, Volume 35,* pp.102-112, DOI: 10.1016/j.egypro.2013.07.163

[121] Hare, J.E., Hara, T., Edson, J.B., Wilczak, J.M., 1997: A similarity analysis of the structure of airflow over surface waves. *J. of physical oceanography*, 27, 1018-1037.

[122] Fairall, C.W., Grachev, A.A., Bedard, A.J., Nishiyama, R.T., 1996: Wind, wave, stress, and surface roughness relationships from turbulence measurements made on R/P flip in the scope experiment. *NOAA*, P.ETL.2090, 41 pp.

[123] Oost, W.A., Komen, G.J., Jacobs, C.M.J., van Oort, C., Bonekamp, H., 2001: Indications for a wave dependent Charnock parameter from measurements during ASGAMAGE. *J. of Geophysical Research Letters*, 28, 2795-2797, doi:0094-8276/01/2001GL013035

[124] Peña, A., Gryning, S.E., 2008: Charnock's roughness length model and non-dimensional wind profiles over the sea. *J. of Boundary-Layer Meteorology*, 128, 191-203, doi: 10.1007/s10546-008-9285-y.

[125] Lettau, H., 1969: Note on aerodynamic roughness-parameter estimation on the basis of roughness-element description. *J. of Applied Meteorology*, 8, 828-832.

[126] Nield, J.M., King, J., Wiggs, G.F.S., Leyland, J., Bryant, R.G., Chiverrell, R.C., Darby, S.E., Eckardt, F.D., Thomas, D.S.G., Vircavs, L.H., Washington, R., 2013: Estimating aerodynamic roughness over the complex surface terrain. *J. of Geophysical Research: Atmospheres*, 118, 12,948-12,961, doi: 10.1002/2013JD020632.

[127] Tseng, R.S., Hsu, Y.H.L., Wu, J., 1992: Methods of measuring wind stress over a water surface: discussions of displacement height and von Karman constant. *J. of Boundary-Layer Meteorology*, 58, 51-68.

[128] Charnock, H., 1955: Wind stress on a water surface. Quart. *J. Roy.Meteor. Soc.*, 81, 639–640.

[129] Donelan, M. A., 1990: Air-sea interaction. The Sea, B. LeMehaute and D. M. Hanes, Eds., *Ocean Engineering Science*, Vol. 9, Wiley and Sons, 239–292.

[130] Fenton, J.D., 1985: A fifth-order Stokes theory for steady waves. *J. of Waterway, Port, Coastal, Ocean Engineering*, 111, 216-234.

[131] Le Mehaute, B., 1969: An introduction to hydrodynamics and water waves volume I: Fundamentals. *Pacific Oceanographic Laboratories*, Miami, Florida, U.S., ERL 118-POL 3-1.

[132] M. Toffolon. *Ekman circulation and downwelling in narrow lakes.* J. of Advances in Water Resources, 53, 76-86, 2013.

[133] Pierson, W., Neumann, G., James, R., 1955: Practical methods for observing and forecasting ocean waves. U.S. *Naval Oceanographic Office*, Washington D.C., U.S.

[134] Stull, R. B., 1988: An Introduction to Boundary Layer Meteorology. Kluwer Academic.

[135] Taylor, G.I., 1916: Conditions at the surface of a hot body exposed to the wind. *Brit. Adv. Com. Aero. Rep. and Memor.*, 272.

[136] Trinh, K.T., 2010: On the Karman constant. *Massey University.*

[137] A. Peña. Sensing the wind profile. Risø-PhD-45(EN), 2009.

[138] Global Offshore Wind Farms Database. June 2018. https://www.4coffshore.com/windfarms/.

[139] J.L. Hanson, O.M. Phillips. *Wind Sea Growth and Dissipation in the Open Ocean.* J. of Physical Oceanography, vol. 29, 1633-1648, 1999.

[140] M.L. Banner, J.B. Song. *Determining the Onset and Strength of breaking for Deep Water Waves. Part II: Influence of Wind Forcing and Surface Shear.* J. of Physical Oceanography, vol. 32, 2559-2570, 2002.

[141] M. Donelan , M. Skafel , H. Graber , P. Liu , D. Schwab & S. Venkatesh. *On the growth rate of wind-generated waves, Atmosphere-Ocean*, 30:3, 457-478, 1992. DOI: 10.1080/07055900.1992.9649449

[142] Komen, G. J., L. Cavaleri, M. Donelan, K. Hasselmann, S. Hasselmann, and P. A. E. M. Janssen. *Dynamics and Modelling of Ocean Waves*. Cambridge University Press, 532 pp, 1994.

[143] M. Brunetti, N. Marchiando, N. Berti, J. Kasparin. *Nonlinear fast growth of water waves under wind forcing.* J. of Physics Letters A, 378, 1025-1030, 2014.

Appendix A. Software user guide

Software installation

For any of the following installation instructions it is essential to have connection to Internet since all libraries, packages and repositories will be downloaded from Internet platforms.

MySQL installation

There are two ways of installing *MySQL* and *MySQL Workbench*. The first is the use of the *Ubuntu software center*. The second is the directly from the command prompt. The first option is really straightforward, thus only the second way will be explained.

Open the command prompt and type the following steps:

1. To refresh the *apt* package cache to make the new software packages available.

   $ sudo apt-get update

2. Install *MySQL server.*

   $ sudo apt-get mysql-server

   Here it will be necessary to introduce twice the new password for the user "root".

3. Testing *MySQL.*

   $ mysqladmin –u root –p version

   The password for user "root" will be asked. In the previous command, *-u root* refers to user, *-p* refers to the password. The output will be information about the *MySQL* version.

4. Install *MySQL Workbench.*

   $ sudo apt-get mysql-workbench

5. Run *Mysql.*

    $ mysql –u root –p

As step 3, the password for user "root" will be asked.

Python 2.7 version installation

Ubuntu OS, by default, contains *Python 3.6*, but the tool was designed in *Python 2.7*. Hence, it is necessary to install the correct version of *Pyhton.*

1. Refresh repositories.

    $ sudo apt-get update

2. Update all the software

    $ sudo apt-get dist-upgrade

3. Install *Python 2.7* and *pip.*

    $ sudo apt-get install python2.7 python-pip

Python packages installation

Here is the list of the *Python* packages included in the software; *pandas, numpy, scipy, MySQLdb, netCDF4, xml, gzip, openpyxl, windrose, matplolib* and *basemap*. All these packages are available through *PiPY*, the online repository for *Python*. There are two ways of installation, through *pip* or from the command line. It is recommended to install all packages via command line. Furthermore, some packages may need the installation of other python packages. These will be installed automatically after the user agreement. Some others may need the previous installation of *Linux* libraries. In these cases, instructions of installation are indicated in *PiPY* repository.

1. Installation via command line (recommended).

    $ sudo apt-get install python-package_name

2. Installation via *pip*.

    $ sudo pip install package_name

MySQL change of data directory

The DB size will be large, an important space is needed plus more space for the downloaded satellite datasets and *csv* files created prior to insertion into DB. Hence, installing an extra hard drive to the computer hosting the DB would be recommended. Thus, operating system and DB would be located in different hard drives. Once the large hard drive is installed and set to initiate when the computer turns on, the data directory can be changed. In the next steps, *path2* will refer to the new directory.

1. Stop the *mysql server.*

    $ sudo stop mysql

2. Create the new directory.

    $ sudo mkdir /path2/mysql

3. Copy over only the database folders.

    $ sudo cp –R /var/lib/mysql /path2/mysql

    $ sudo cp –R /var/lib/mysql/users /path2/mysql

4. Copy the *ibdata** and *ib_logfile** files. It is necessary to copy the *InnoDB* tables; otherwise it will not be possible to use the tables.

    $ sudo cp –p /var/lib/mysql/ib /path2/mysql/*

5. Backup the *my.cnf* file.

    $ sudo cp /etc/mysql/my.cnf /root/my.cnf.backup

6. Edit the *my.cnf* file.

    $ sudo gedit /etc/mysql/my.cnf

    Here, it is essential to change all mentions of the old data directory and socket to the new location. For example,

datadir=/path2/mysql

socket=/path2/mysql/mysql.sock

7. Update the directory permissions.

   $ sudo chown –R mysql:mysql /path2/mysql

   $ sudo chmod 771 /path2/mysql

   It may be necessary to change the permissions of each folder in the directory or path to the new containing folder.

8. Rename the old directory.

   $ mv /var/lib/mysql /var/lib/mysql-old

9. Let the *apparmor* know about the new data directory.

   $ gedit /etc/apparmor.d/usr.sbin.mysqld

   As step 5, change any mention of the old directory for the new directory. This is to avoid a future issue when *MySQL* receives an update.

10. Reload the *apparmor* profile.

    $ sudo /etc/init.d/apparmor reload

11. Restart *MySQL*.

    $ sudo /etc/init.d/mysql restart

In case of the hard drive (for the new location of the DB) is not launched when the computer initiates, it will not be possible to connect with the DB. An error message will appear similar to:

/var/run/mysqld/mysql.sock doesn't exist and nor does the directory

In order to solve this issue every time the computer is initiated the steps 1, 10 and 11 must be repeated in order; i.e. stop *MySQL*, reload *apparmor* and restart *MySQL*.

Software code

As explained in chapter 3, the software has not been deployed and the user interface has not been designed. The user interaction with the software has been already well explained in section 3.5.2. Hence, there is no need of further explanations. However, the code has not been showed in this thesis. Due to size of the code, this is not included in the appendix. The code has been published through *Github*, it is open source and freely available. For those readers interested in the code, here is the link:

https://github.com/SatelliteApplicationsCatapult/WindRes

Appendix B. Regressions from table 5.1 plus z_0 regressions

I. For Hersbach friction method

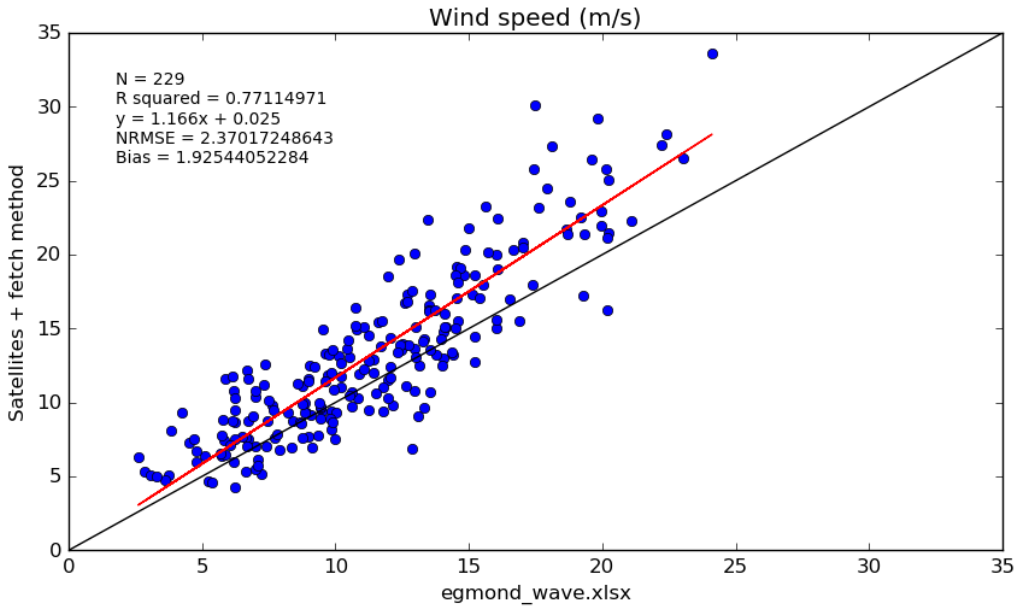

B. 1. Wind speed regression for method Hersbach & Fetch combination.

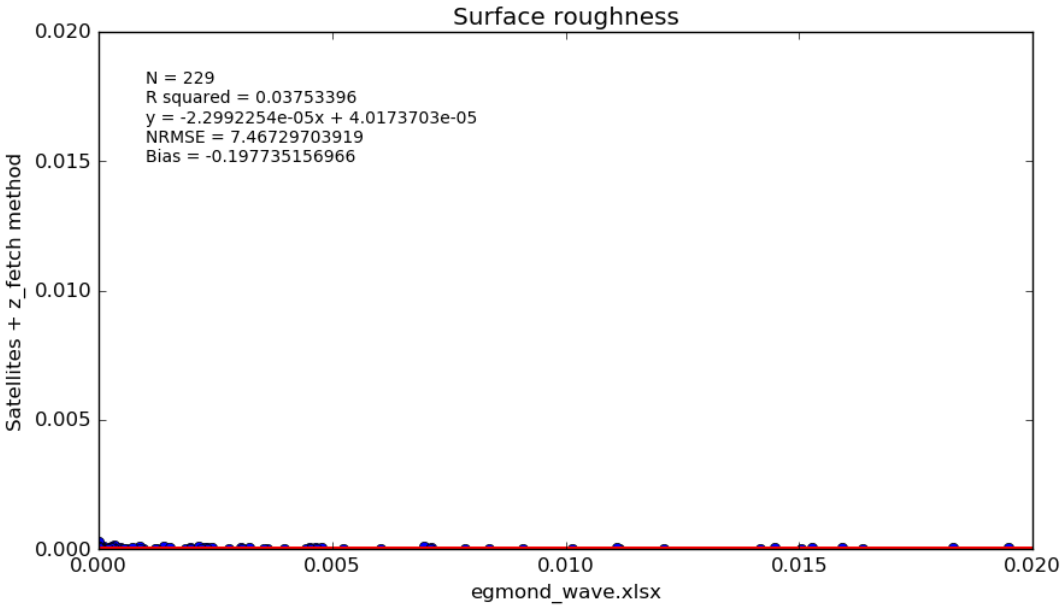

B. 2. Surface roughness regression for method Hersbach & Fetch combination.

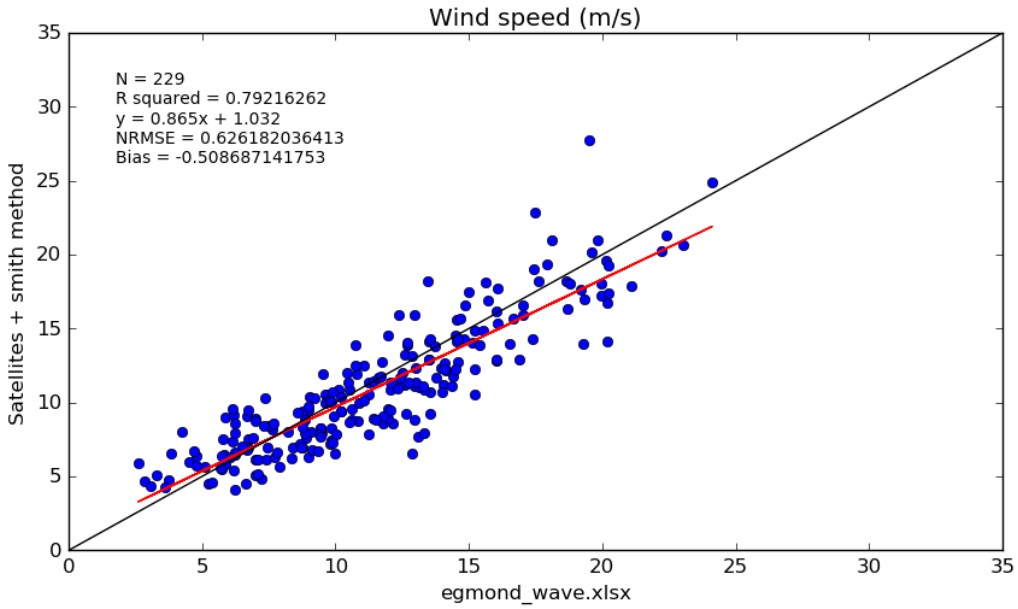

B. 3. Wind speed regression for method Hersbach & Smith combination.

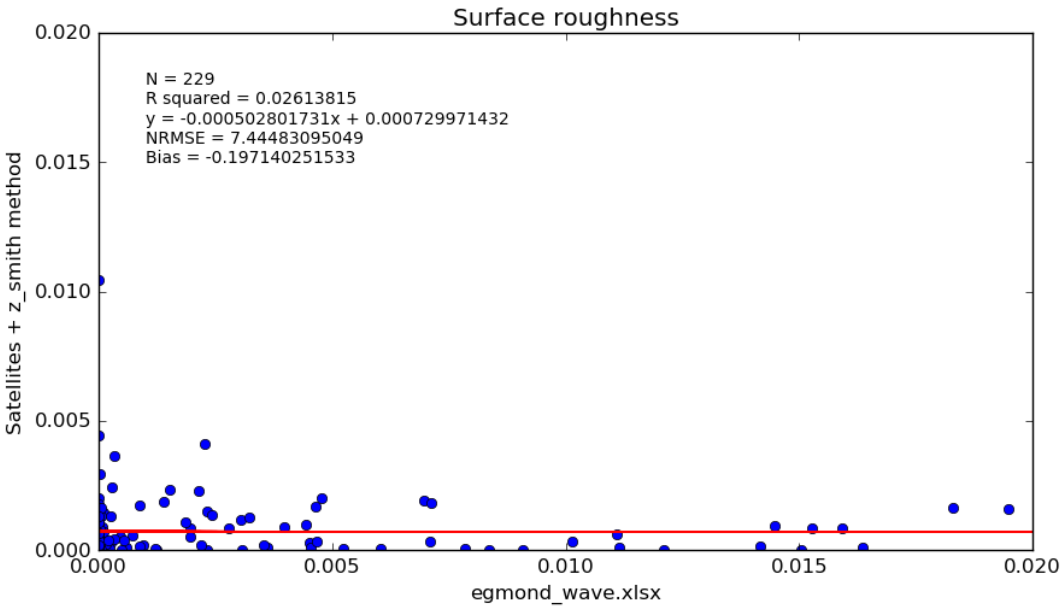

B. 4. Surface roughness regression for method Hersbach & Smith combination.

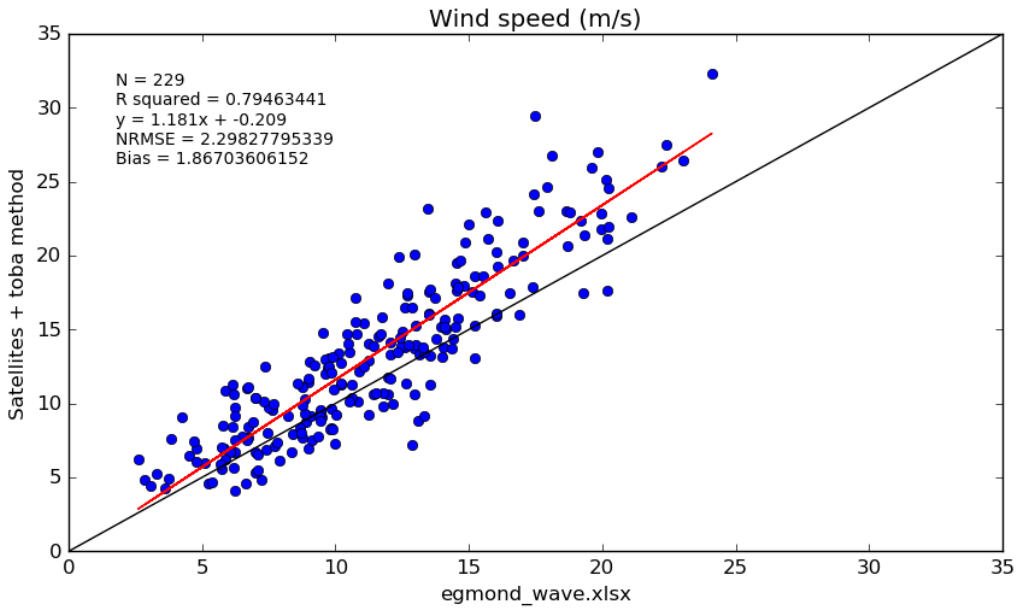

B. 5. Wind speed regression for method Hersbach & Toba combination.

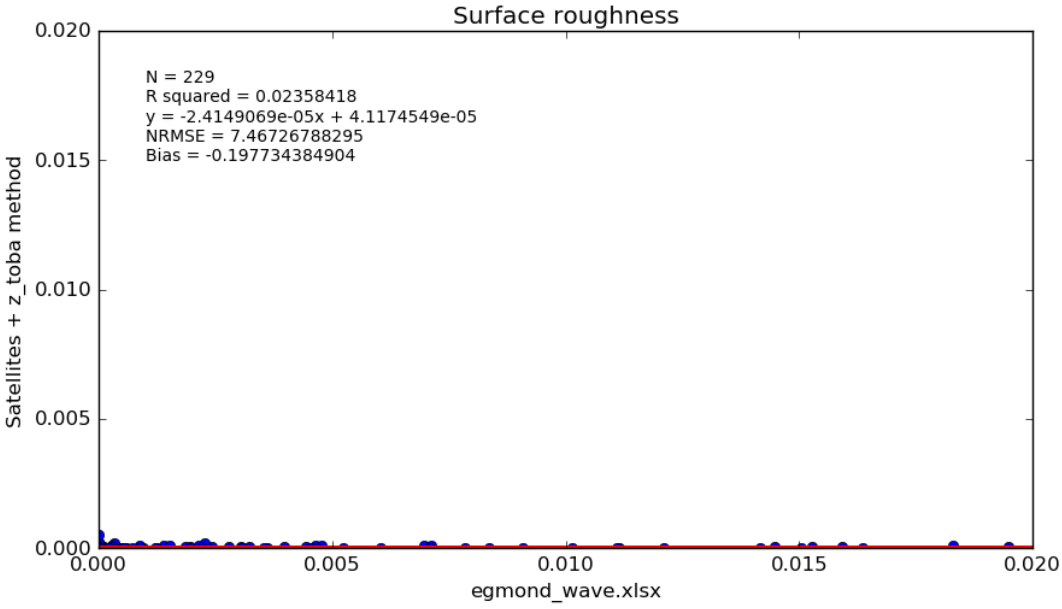

B. 6. Surface roughness regression for method Hersbach & Toba combination.

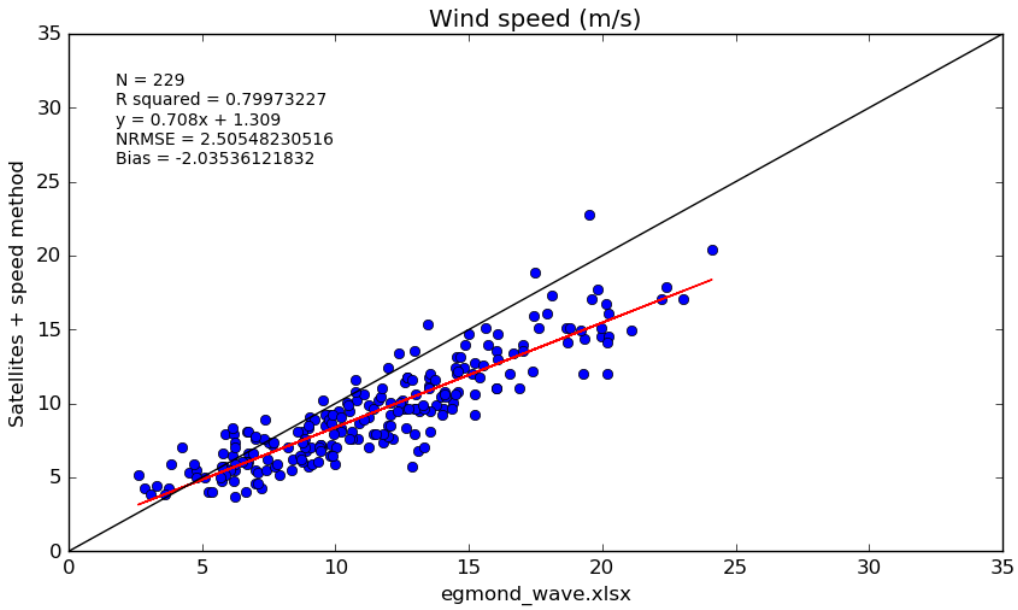

B. 7. Wind speed regression for method Hersbach & Edson_Speed combination.

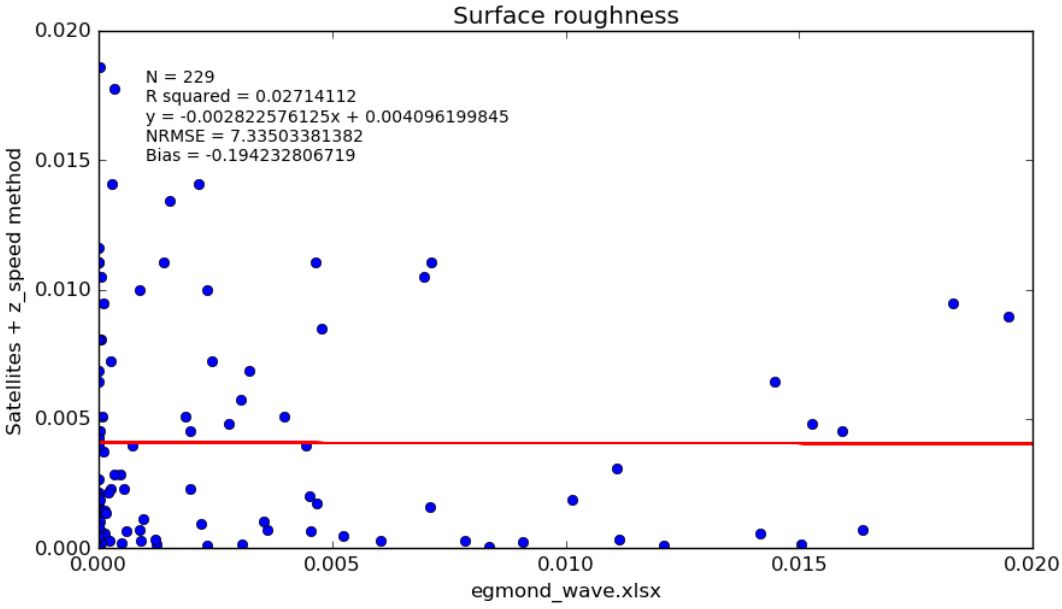

B. 8. Surface roughness regression for method Hersbach & Edson_Speed combination.

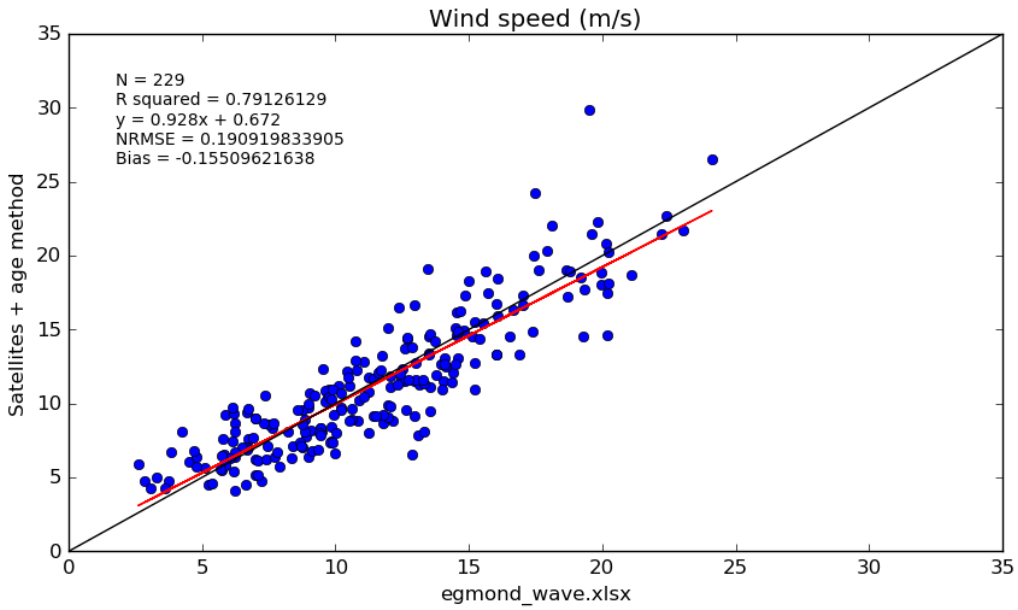

B. 9. Wind speed regression for method Hersbach & Edson_Age combination.

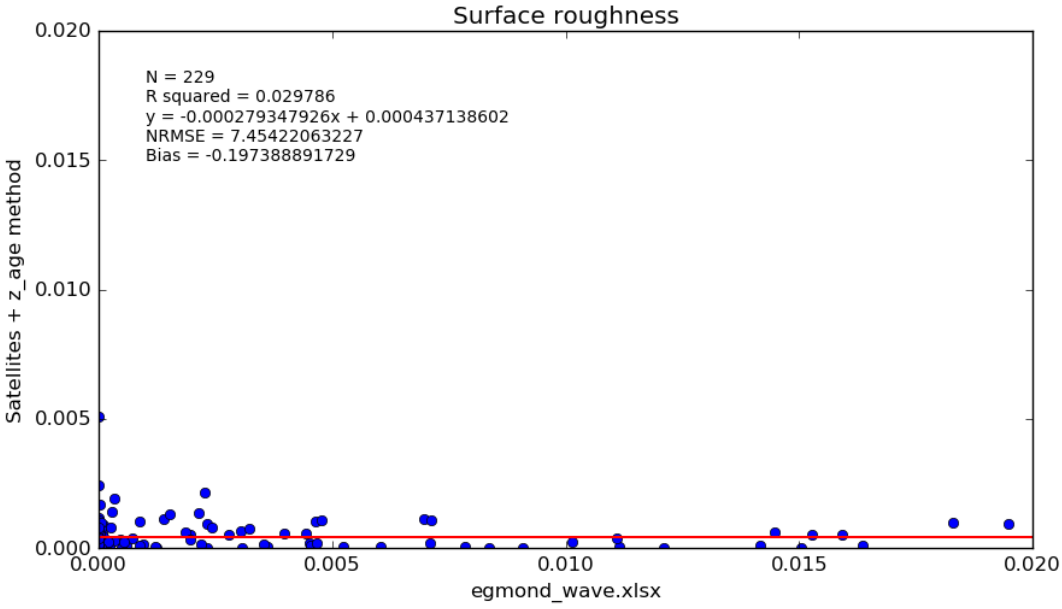

B. 10. Surface roughness regression for method Hersbach & Edson_Age combination.

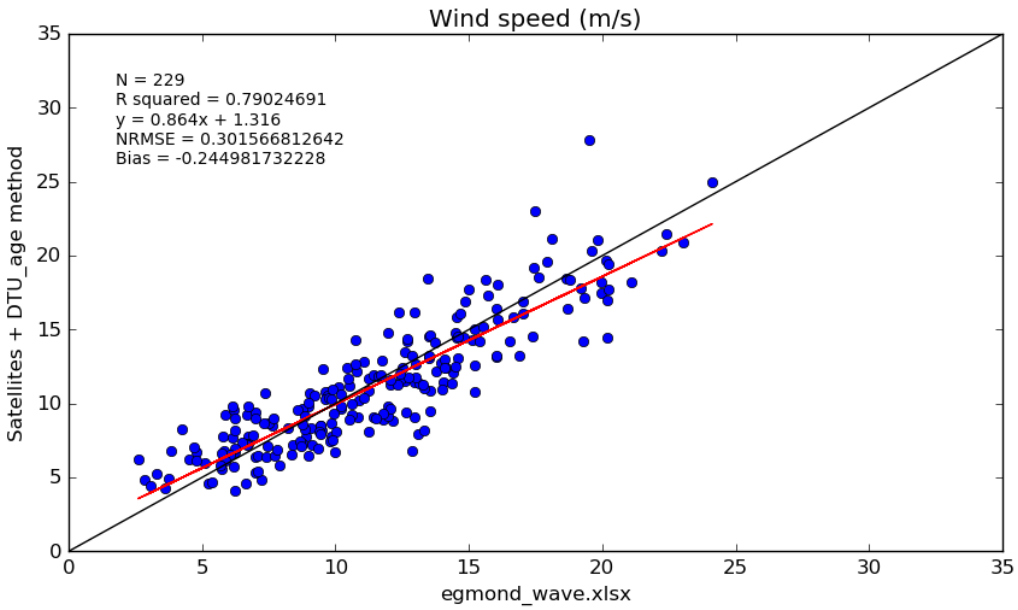

B. 11. Wind speed regression for method Hersbach & DTU_Age combination.

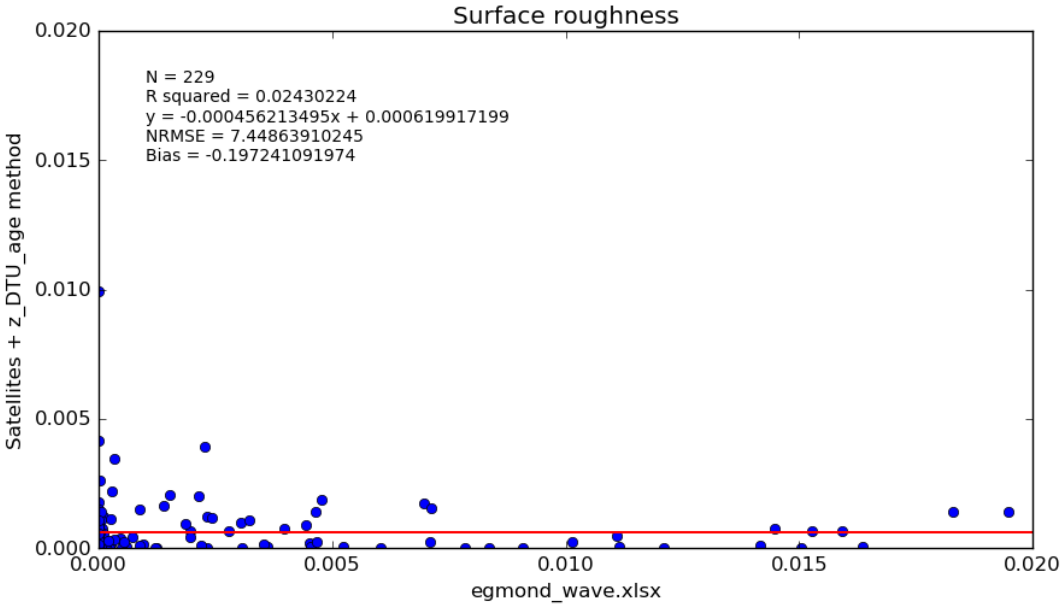

B. 12. Surface roughness regression for method Hersbach & DTU_Age combination.

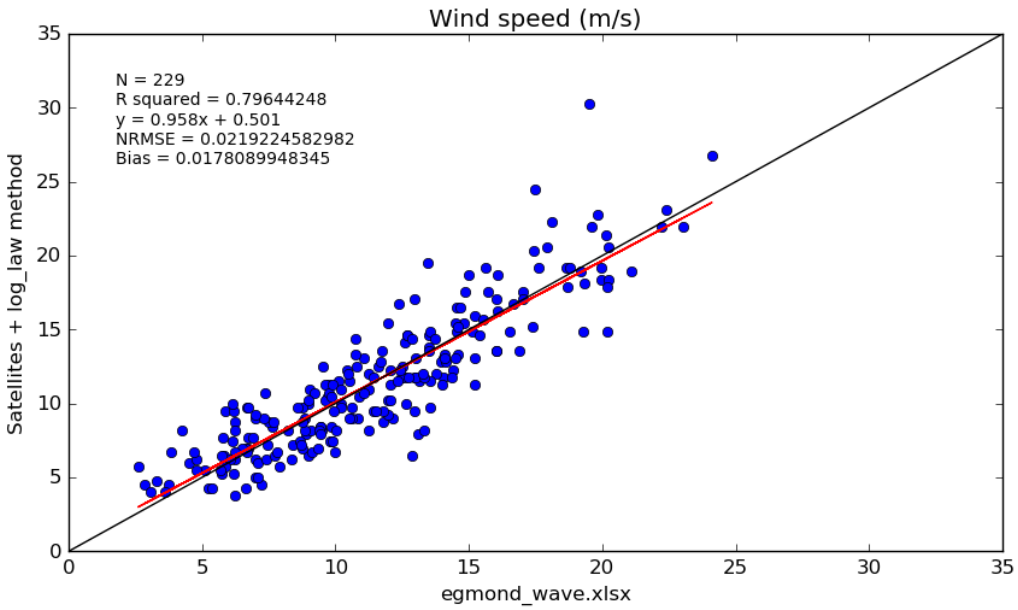

B. 13. Wind speed regression for method Hersbach & Log_law combination.

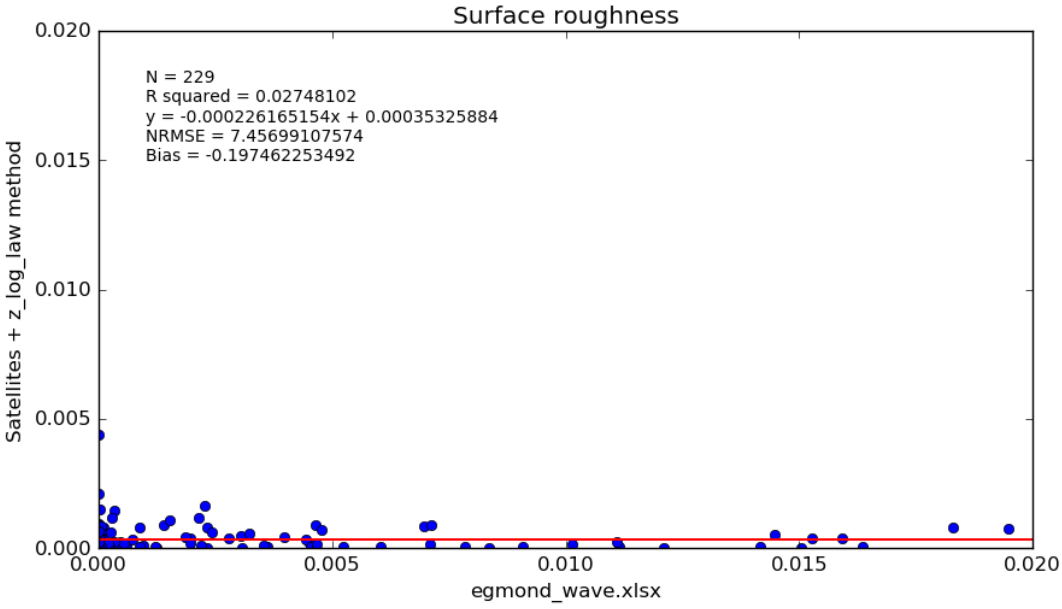

B. 14. Surface roughness regression for method Hersbach & Log_law combination.

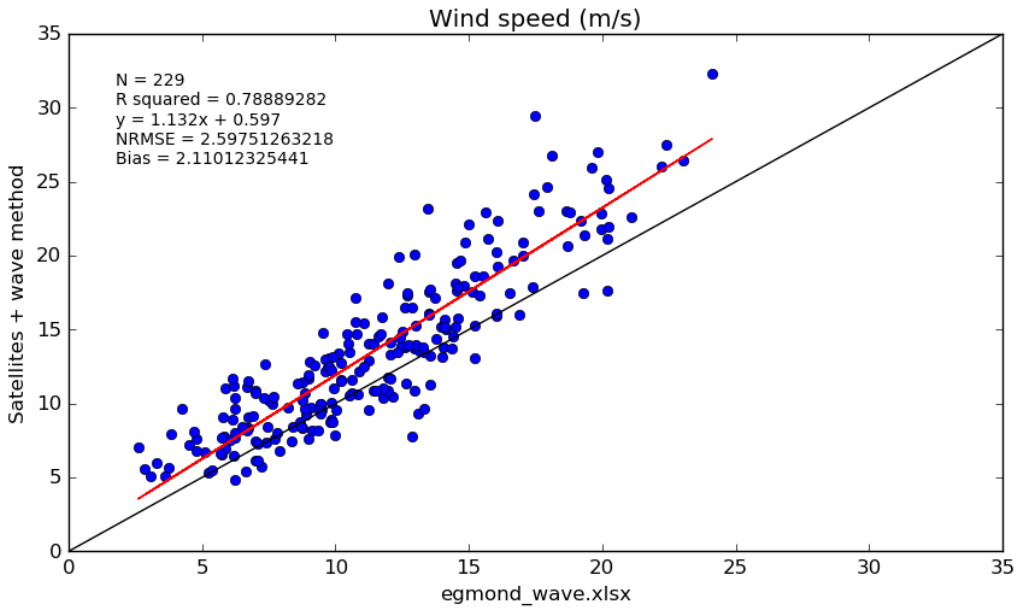

B. 15. Wind speed regression for method Hersbach & Edson_wave combination.

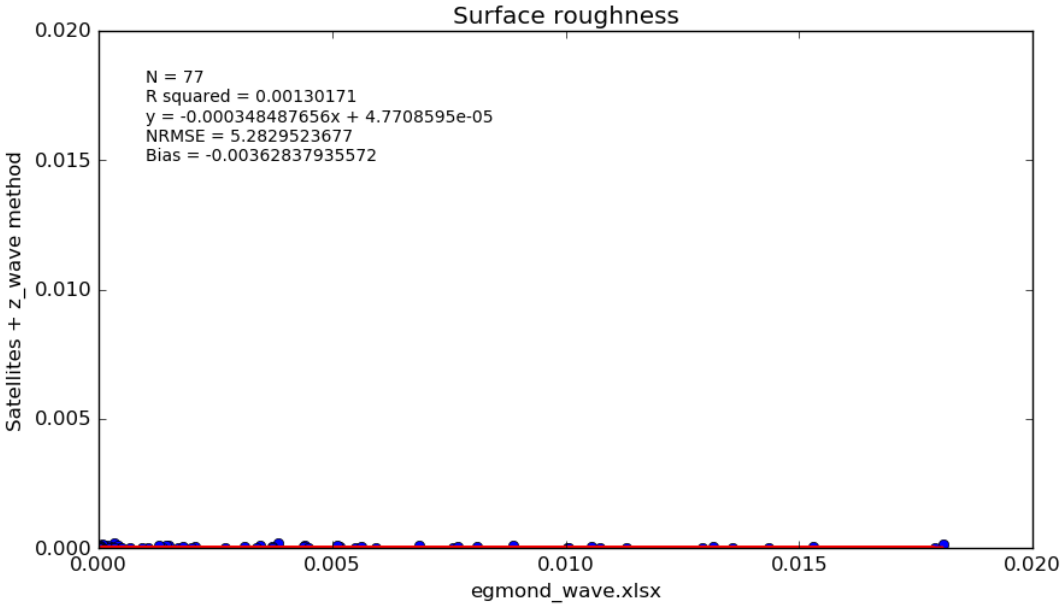

B. 16. Surface roughness regression for method Hersbach & Edson_wave combination.

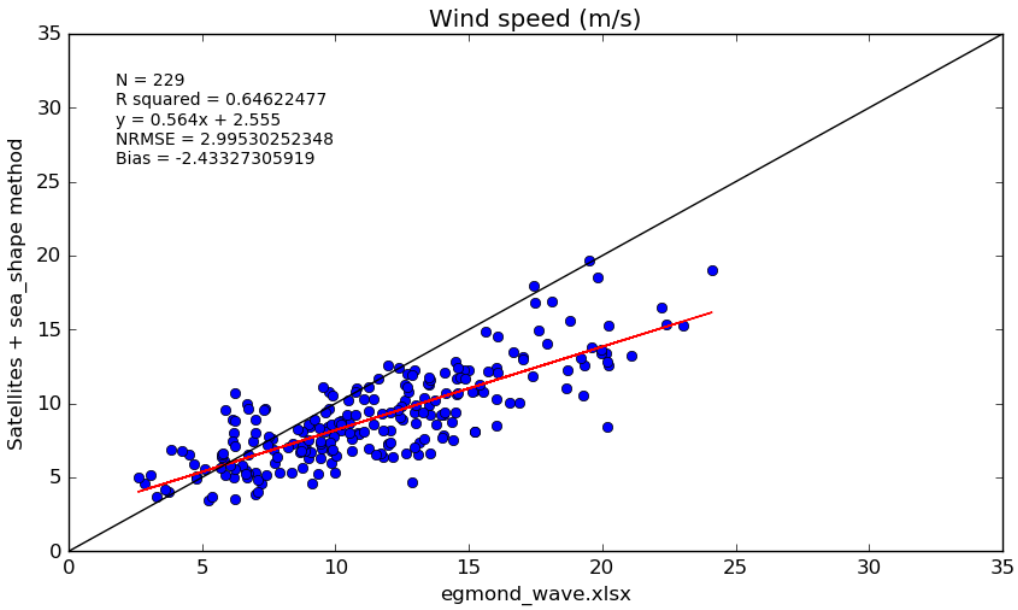

B. 17. Wind speed regression for method Hersbach & Taylor combination.

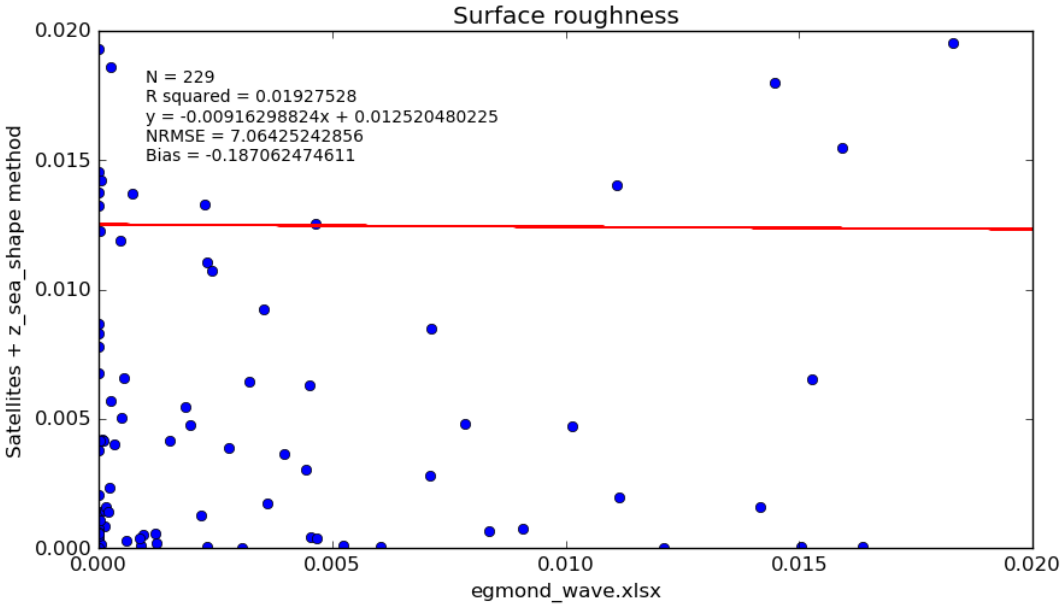

B. 18. Surface roughness regression for method Hersbach & Taylor combination.

II. For Wu friction method

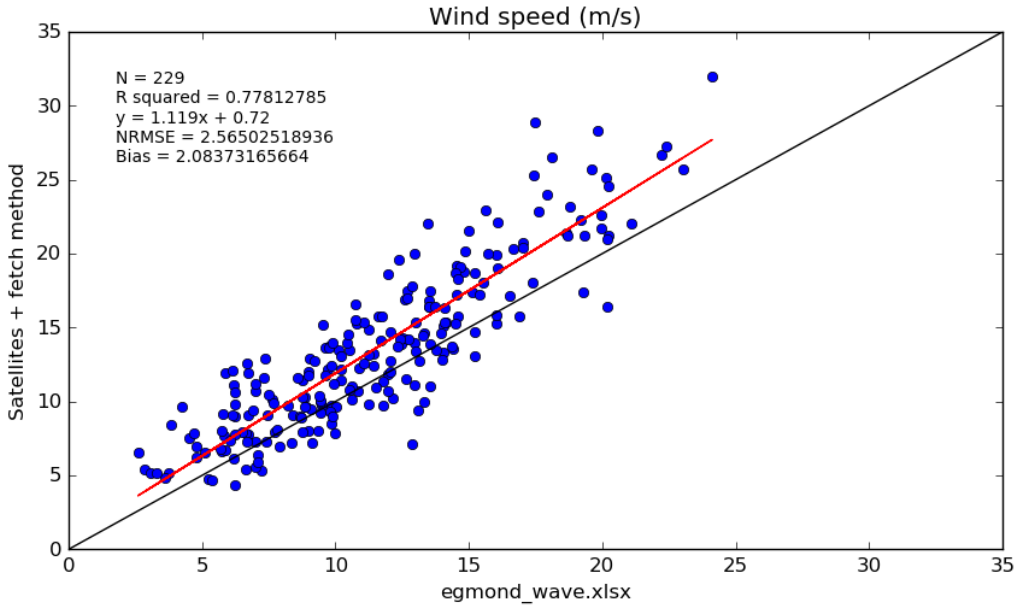

B. 19. Wind speed regression for method Wu & Fetch combination.

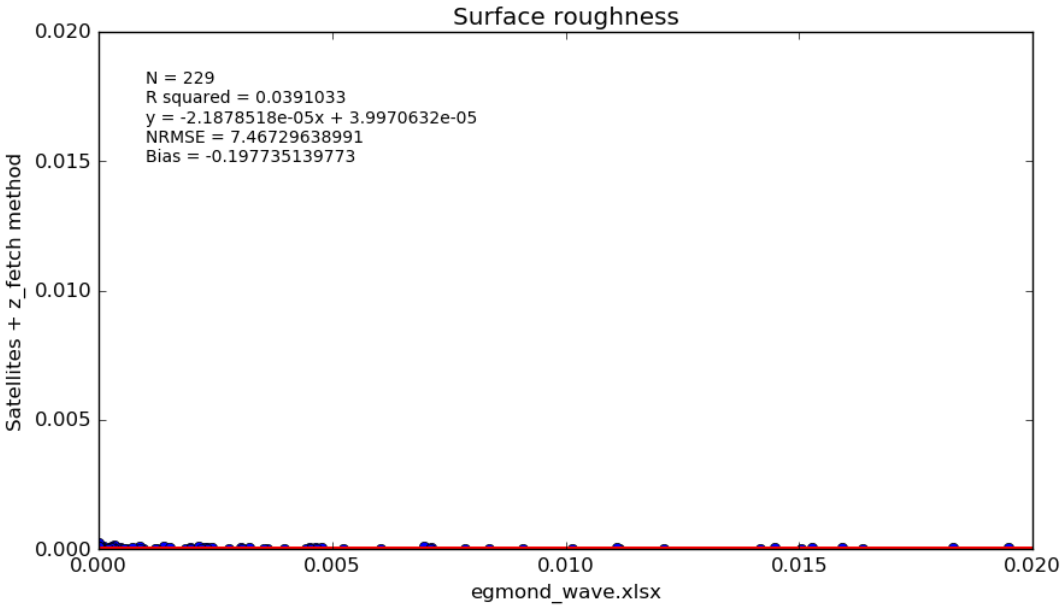

B. 20. Surface roughness regression for method Wu & Fetch combination.

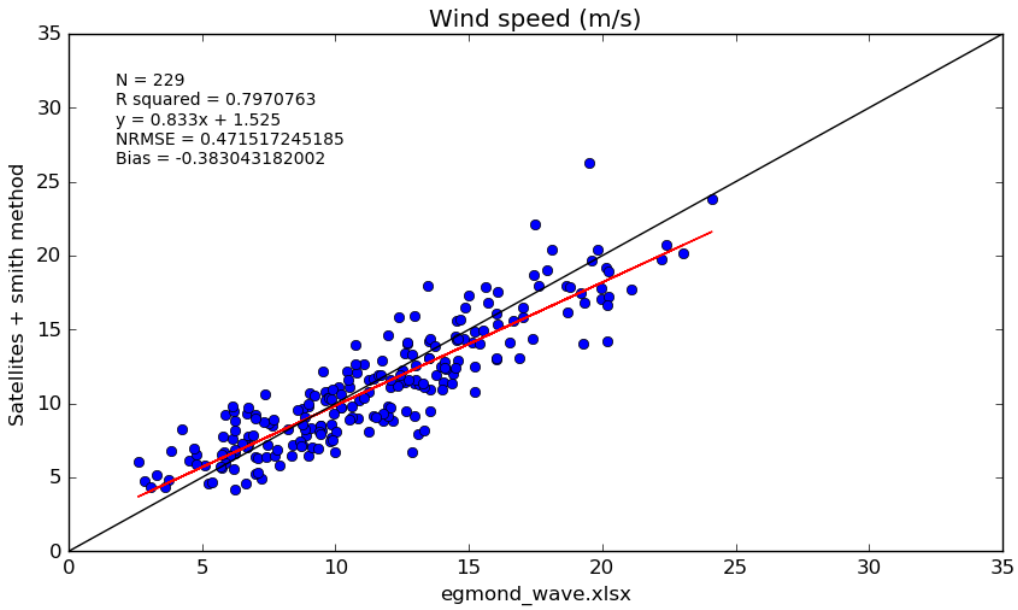

B. 21. Wind speed regression for method Wu & Smith combination.

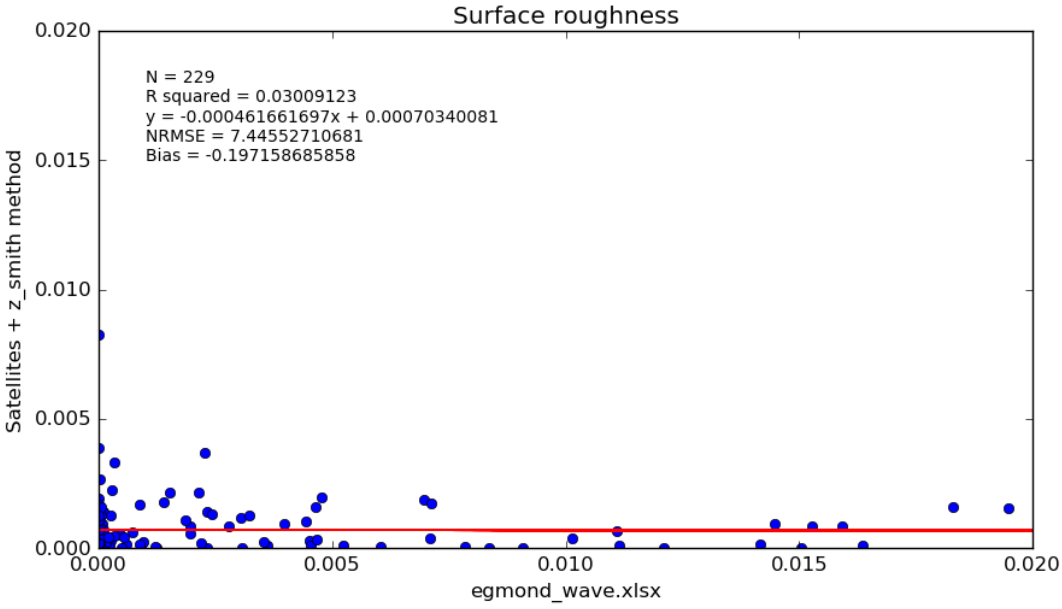

B. 22. Surface roughness regression for method Wu & Smith combination.

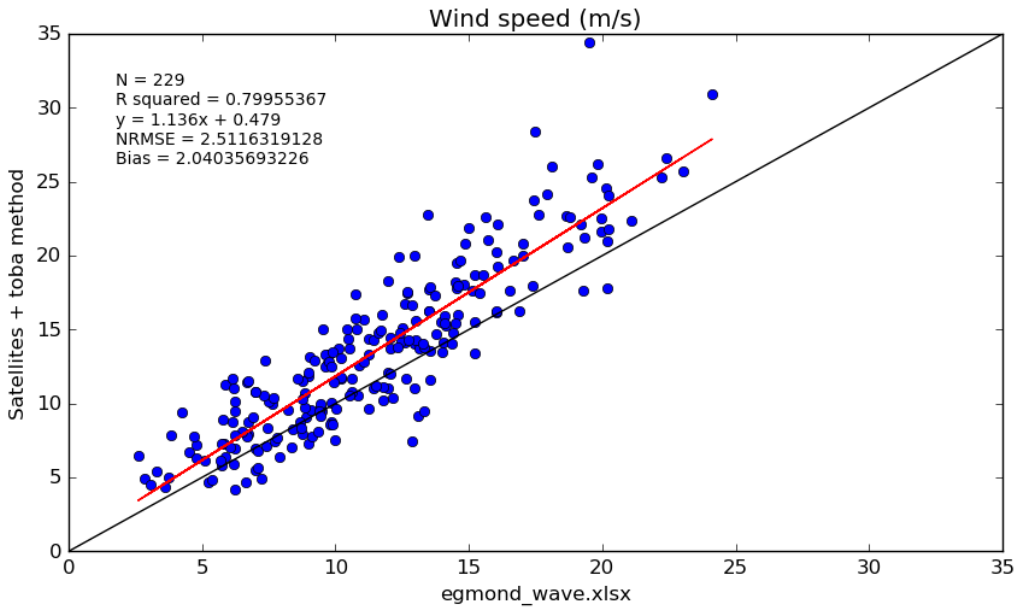

B. 23. Wind speed regression for method Wu & Toba combination.

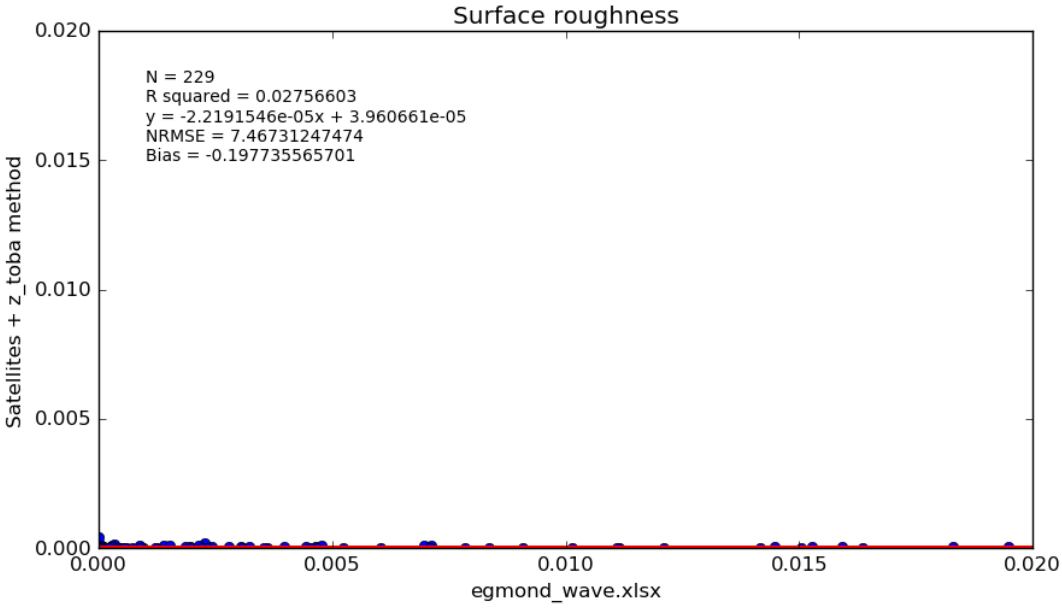

B. 24. Surface roughness regression for method Wu & Toba combination.

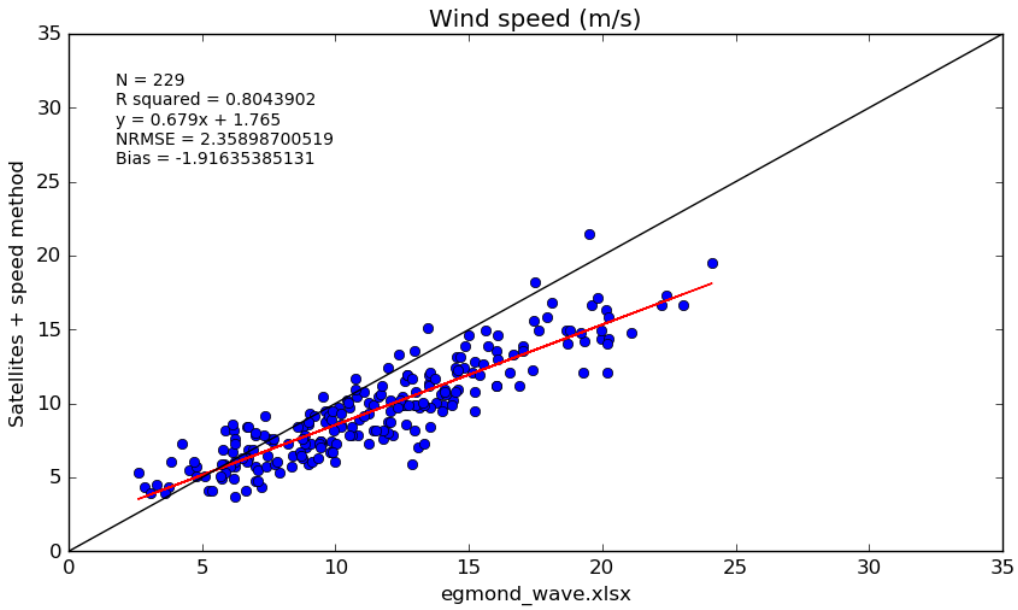

B. 25. Wind speed regression for method Wu & Edson_Speed combination.

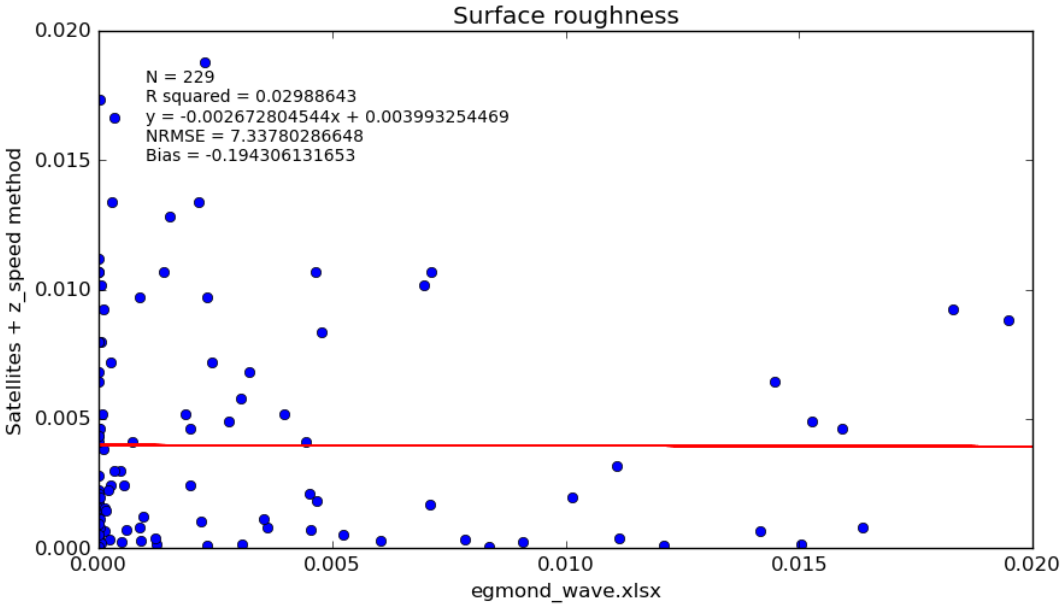

B. 26. Surface roughness regression for method Wu & Edson_Speed combination.

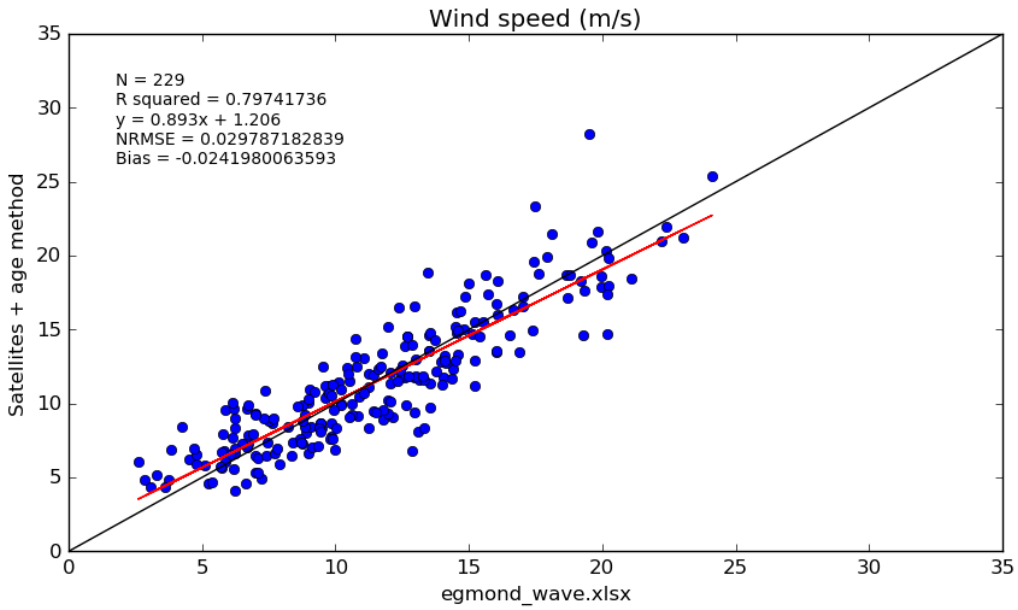

B. 27. Wind speed regression for method Wu & Edson_Age combination.

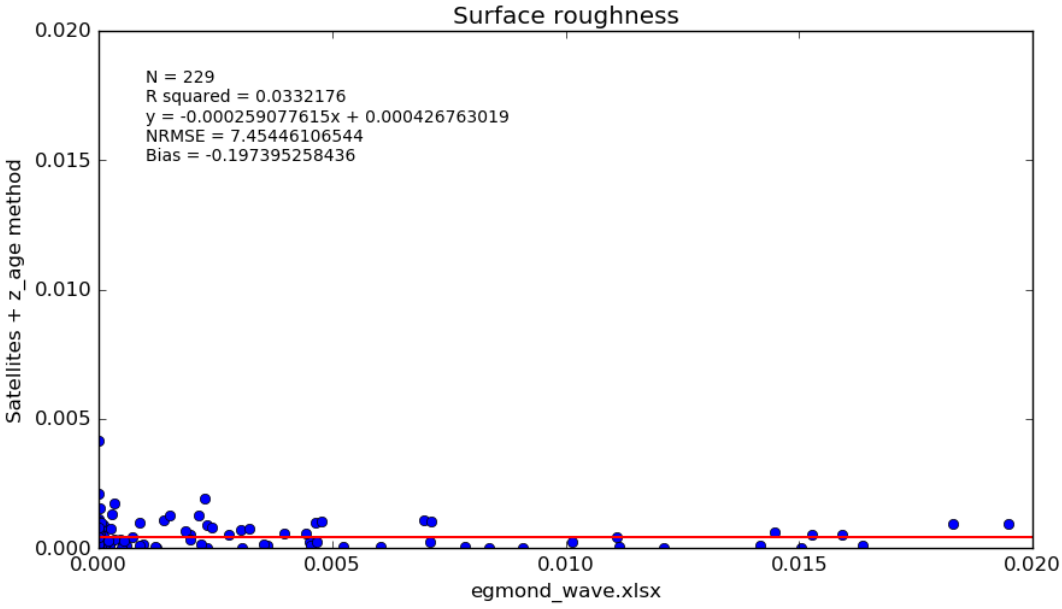

B. 28. Surface roughness regression for method Wu & Edson_Age combination.

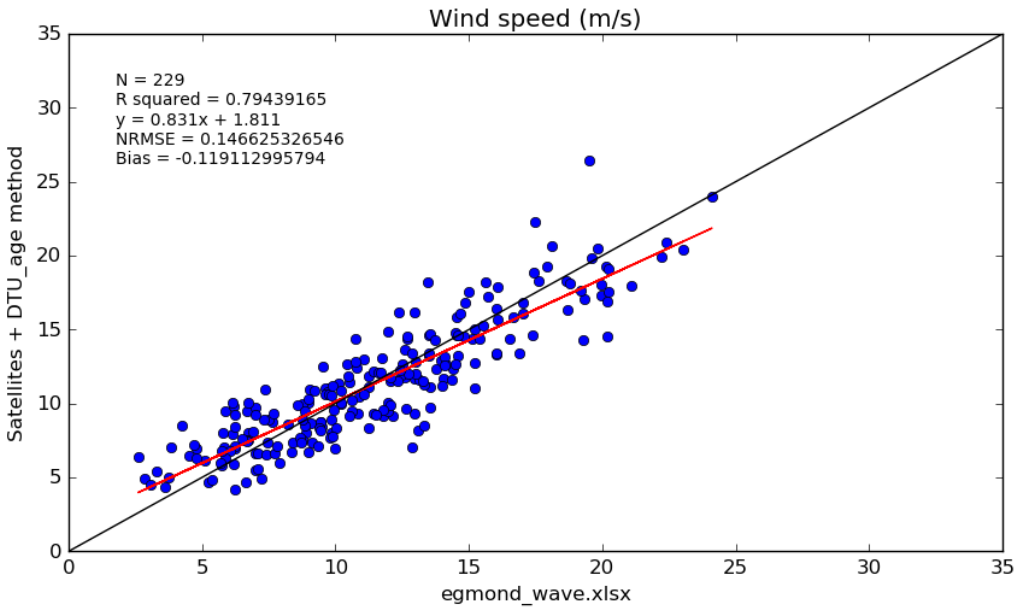

B. 29. Wind speed regression for method Wu & DTU_Age combination.

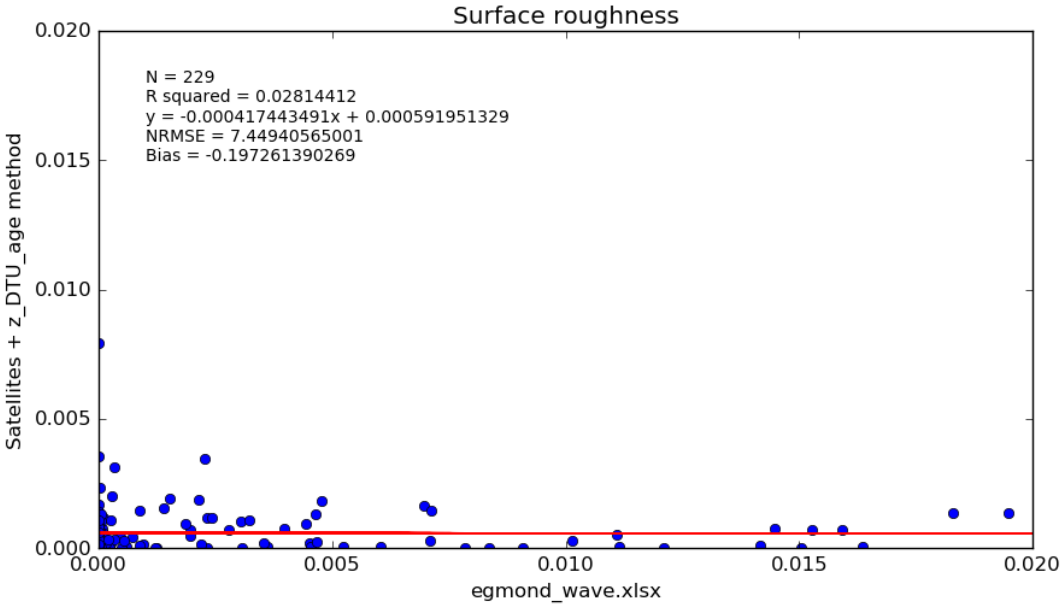

B. 30. Surface roughness regression for method Wu & DTU_Age combination.

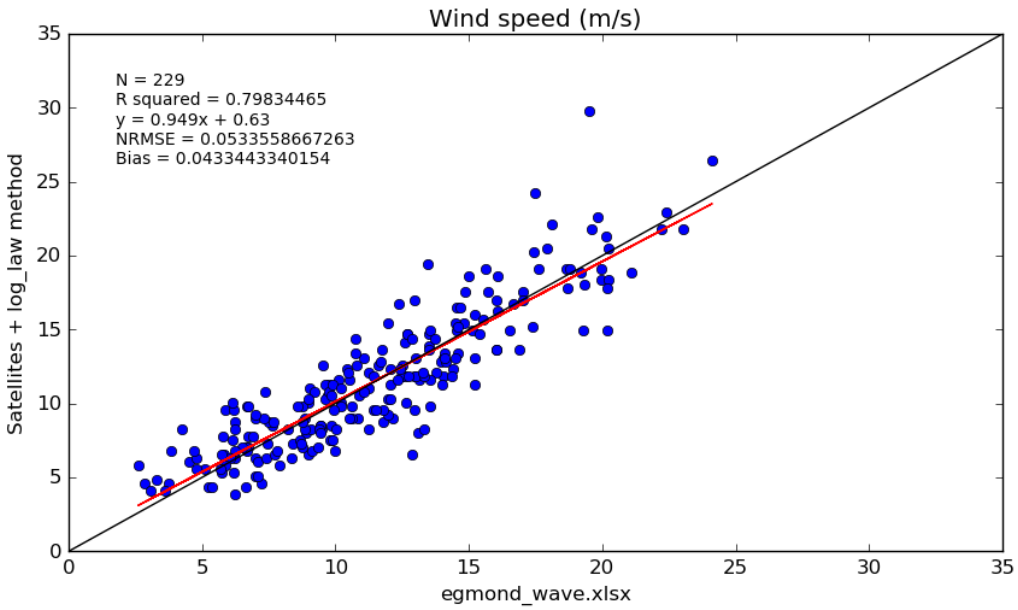

B. 31. Wind speed regression for method Wu & Log_law combination.

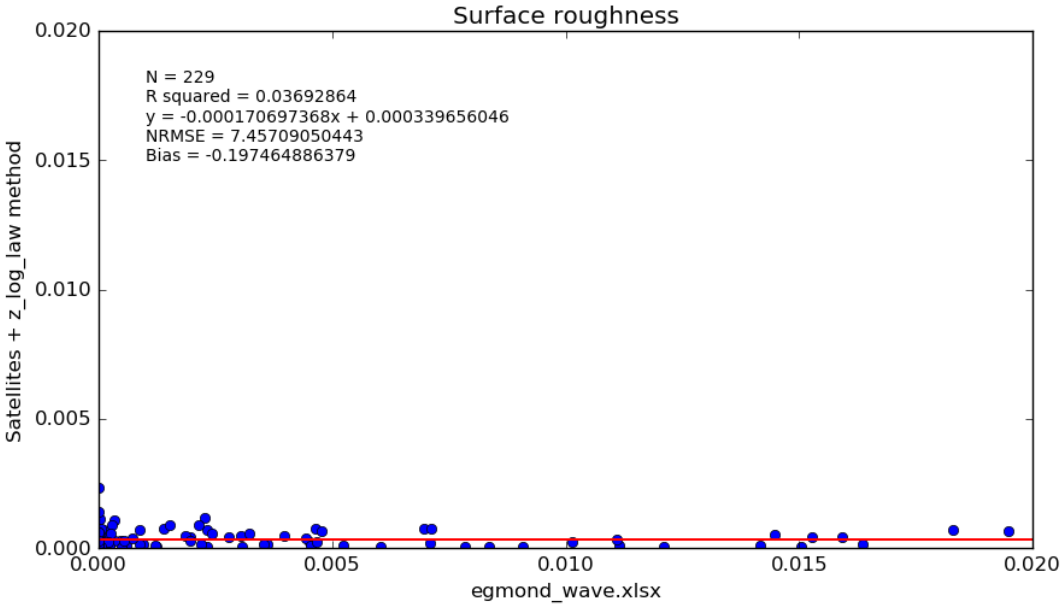

B. 32. Surface roughness regression for method Wu & Log_law combination.

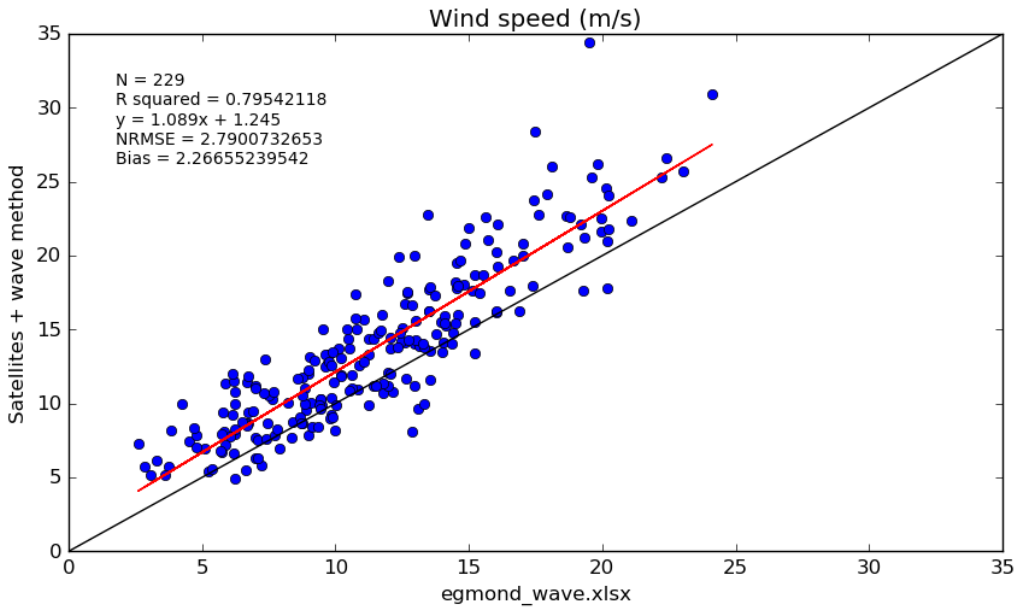

B. 33. Wind speed regression for method Wu & Edson_wave combination.

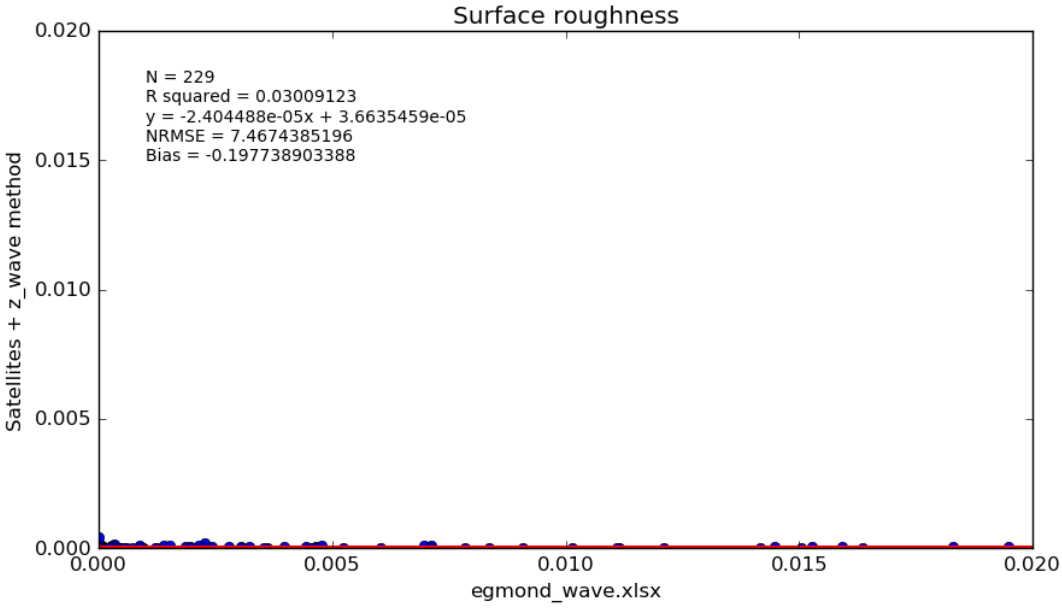

B. 34. Surface roughness regression for method Wu & Edson_wave combination.

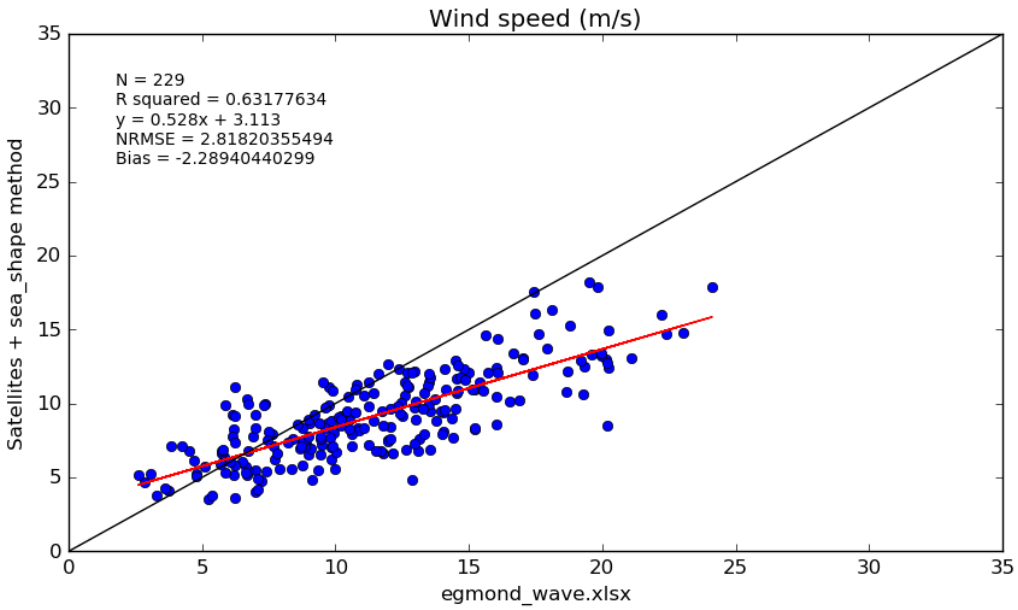

B. 35. Wind speed regression for method Wu & Taylor combination.

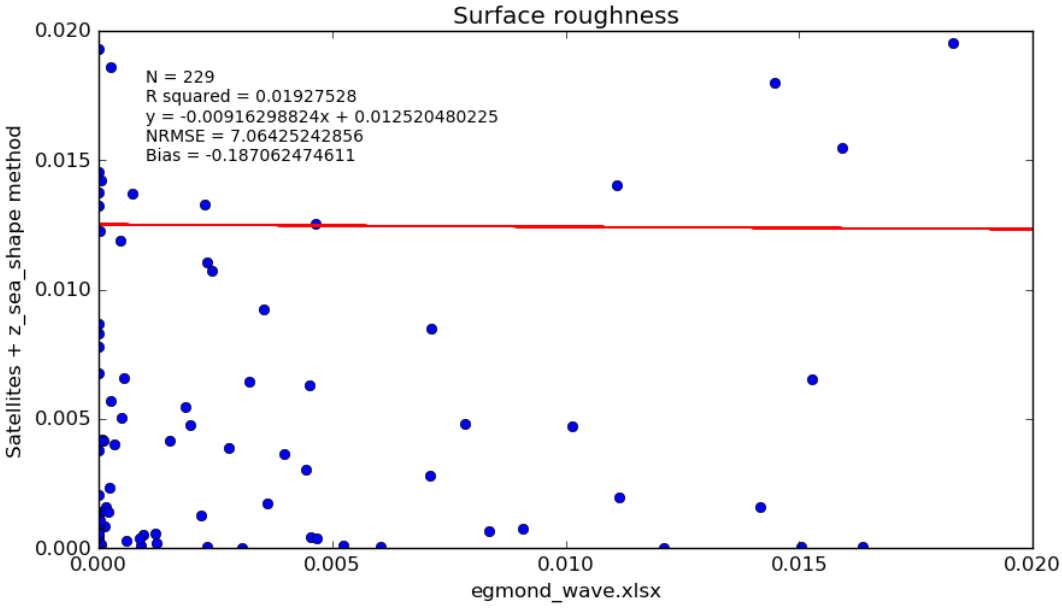

B. 36. Surface roughness regression for method Wu & Taylor combination.

III. For Maat friction method

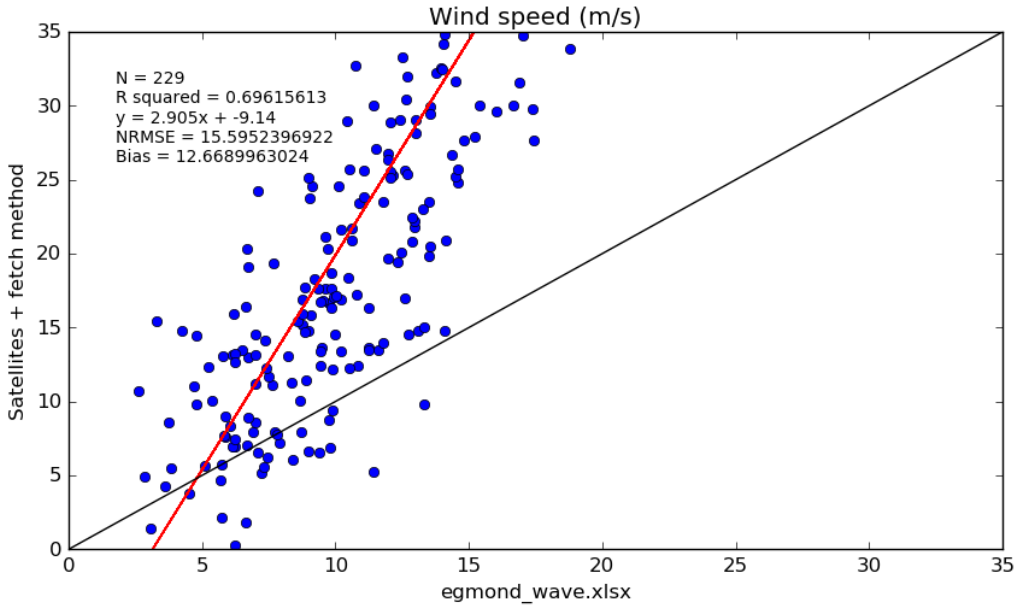

B. 37. Wind speed regression for method Maat & Fetch combination.

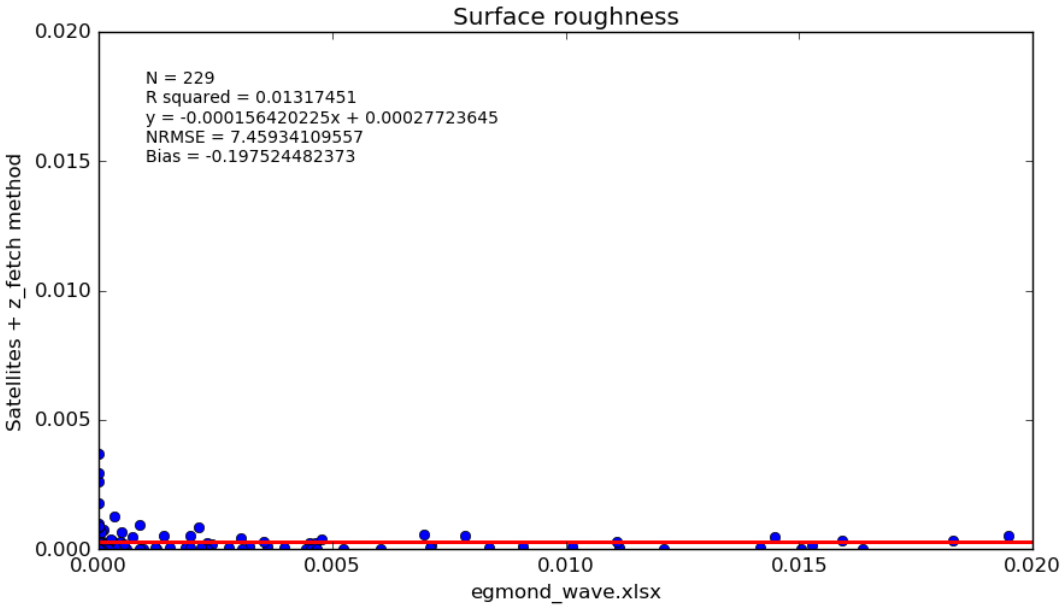

B. 38. Surface roughness regression for method Maat & Fetch combination.

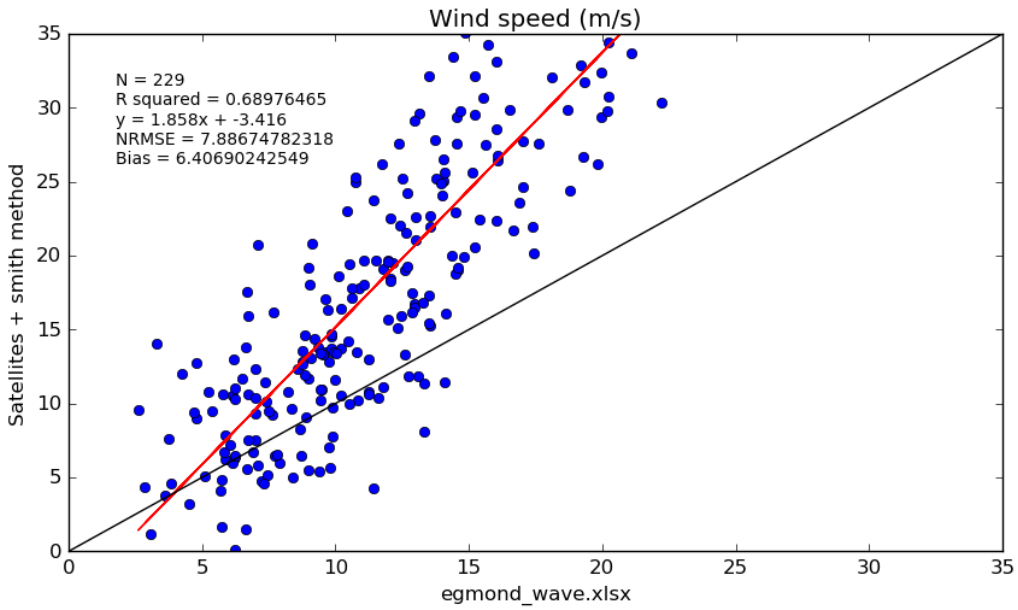

B. 39. Wind speed regression for method Maat & Smith combination.

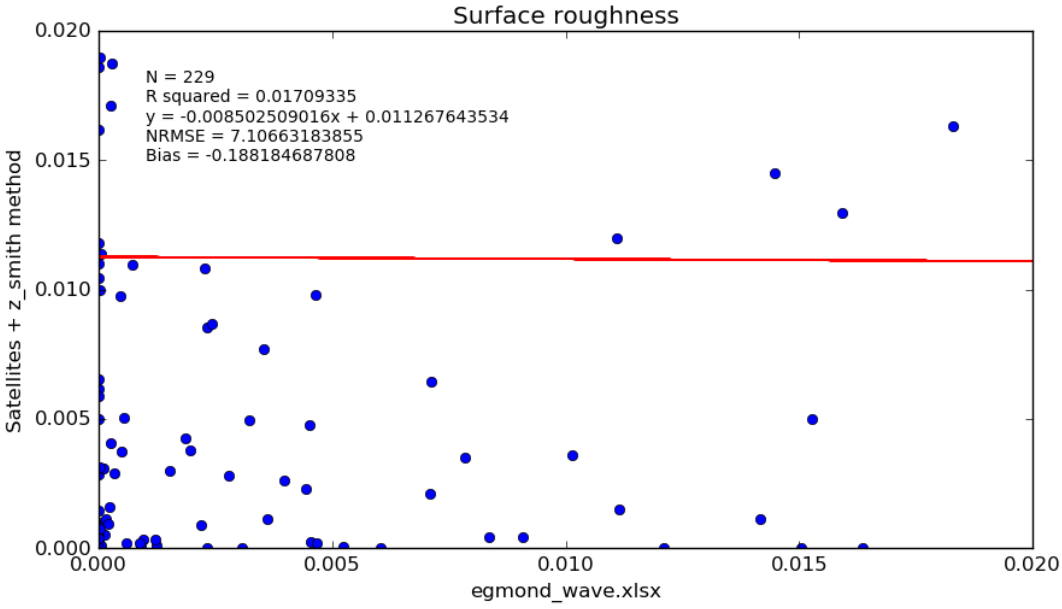

B. 40. Surface roughness regression for method Maat & Smith combination.

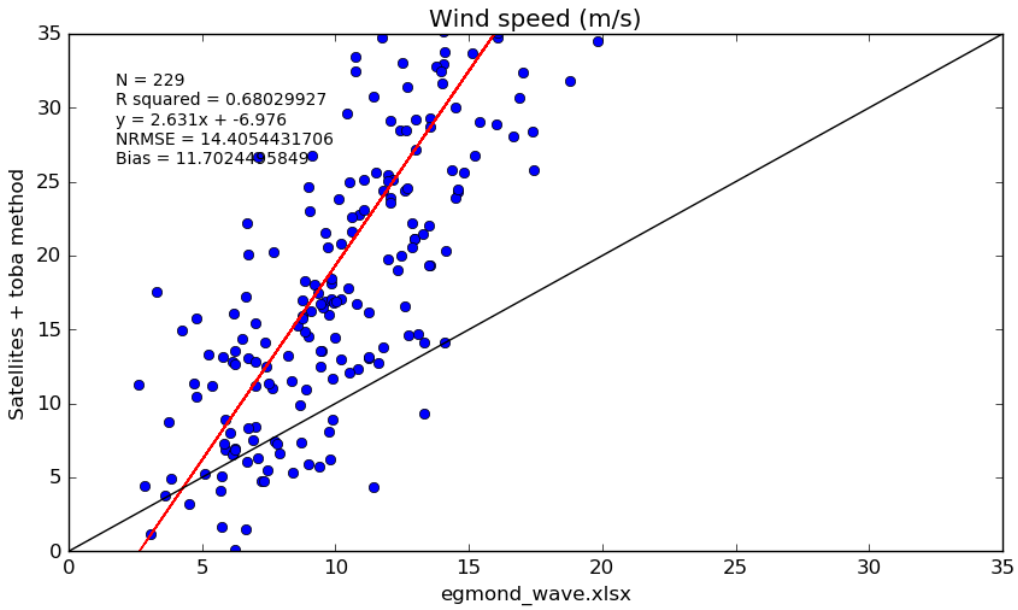

B. 41. Wind speed regression for method Maat & Toba combination.

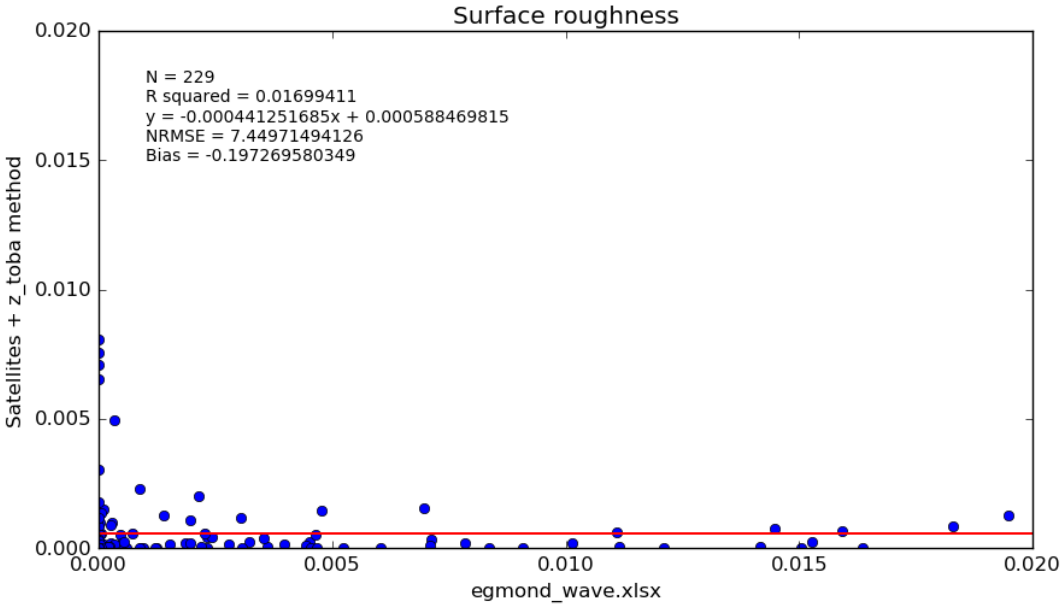

B. 42. Surface roughness regression for method Maat & Toba combination.

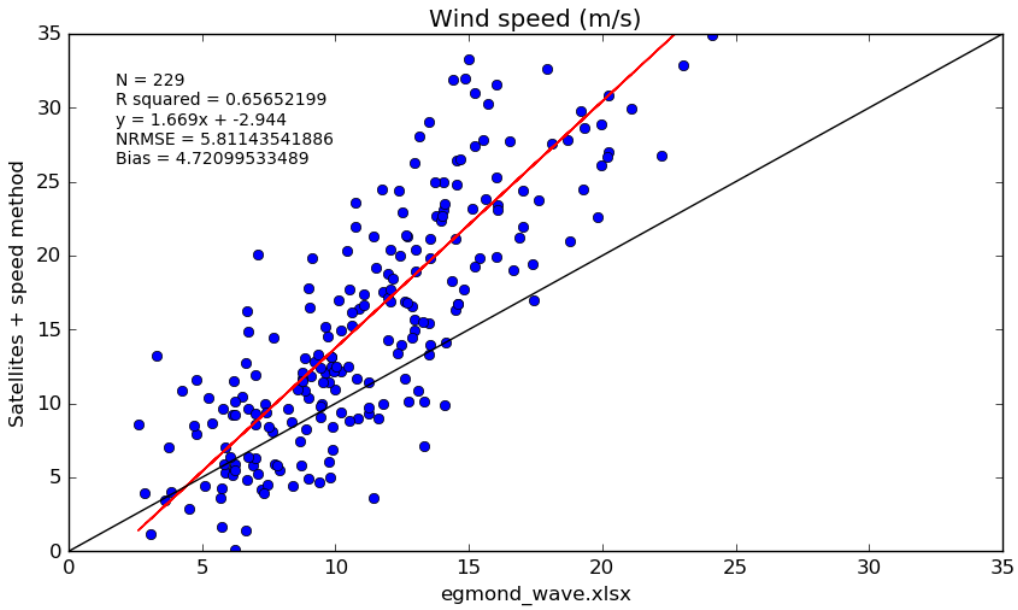

B. 43. Wind speed regression for method Maat & Edson_Speed combination.

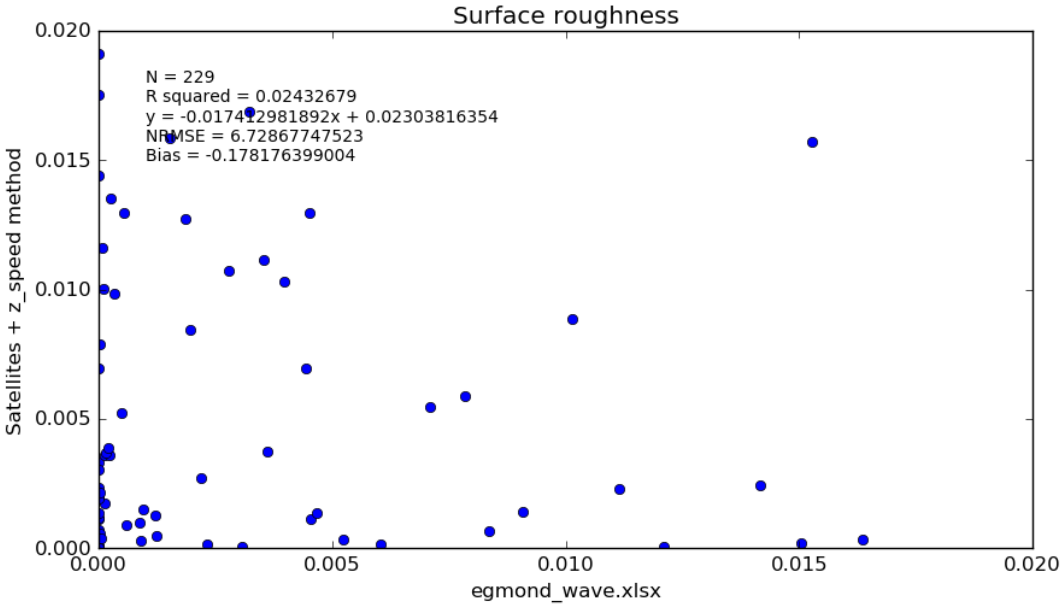

B. 44. Surface roughness regression for method Maat & Edson_Speed combination.

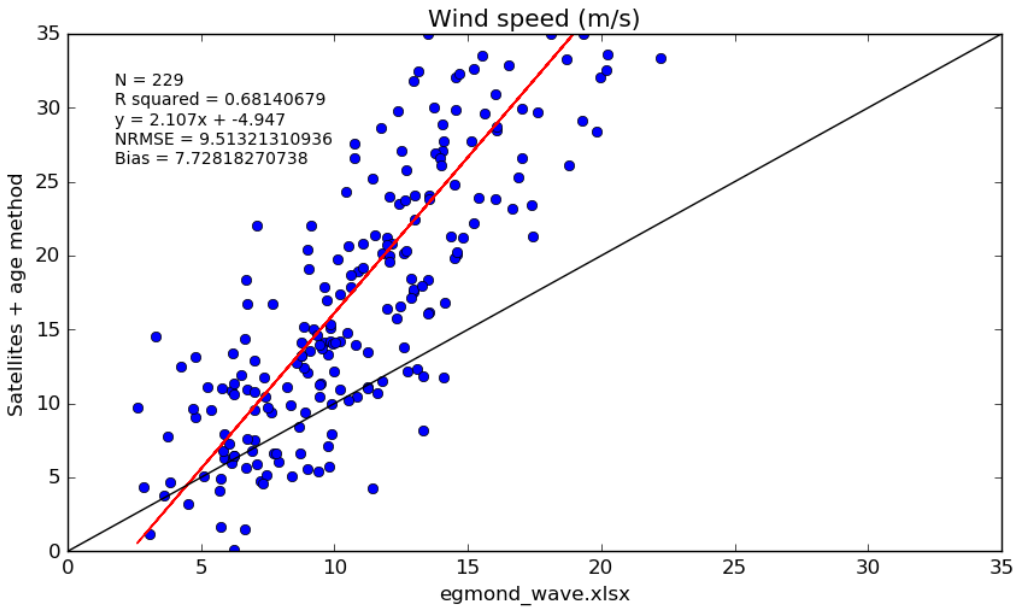

B. 45. Wind speed regression for method Maat & Edson_Age combination.

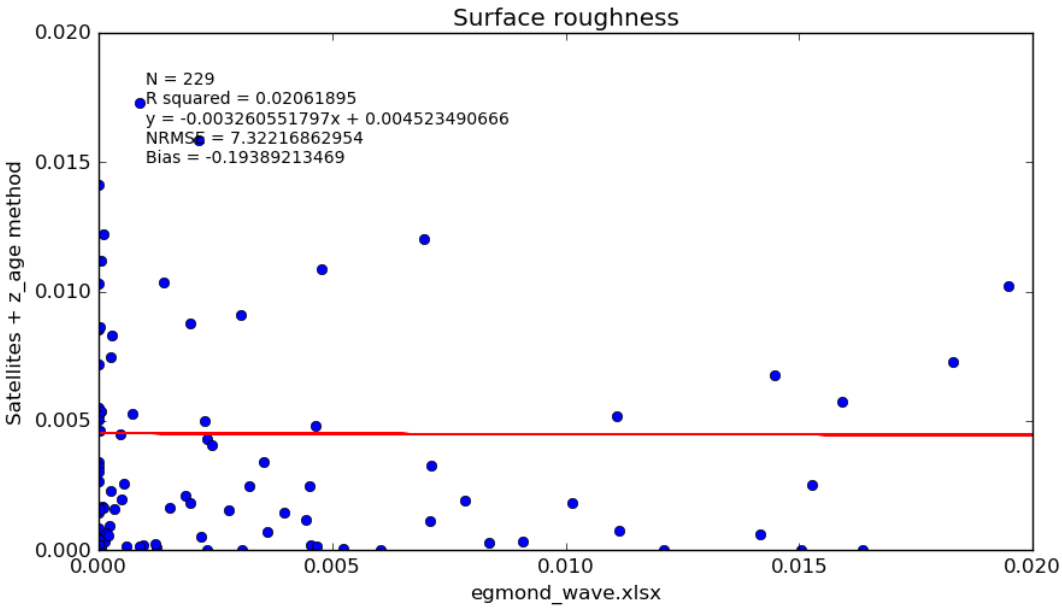

B. 46. Surface roughness regression for method Maat & Edson_Age combination.

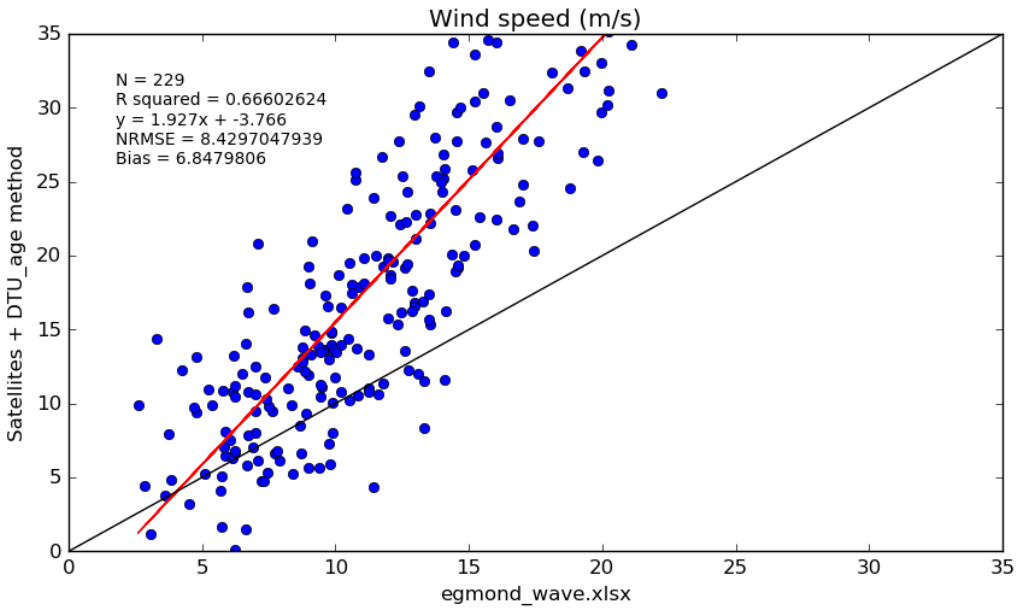

B. 47. Wind speed regression for method Maat & DTU_Age combination.

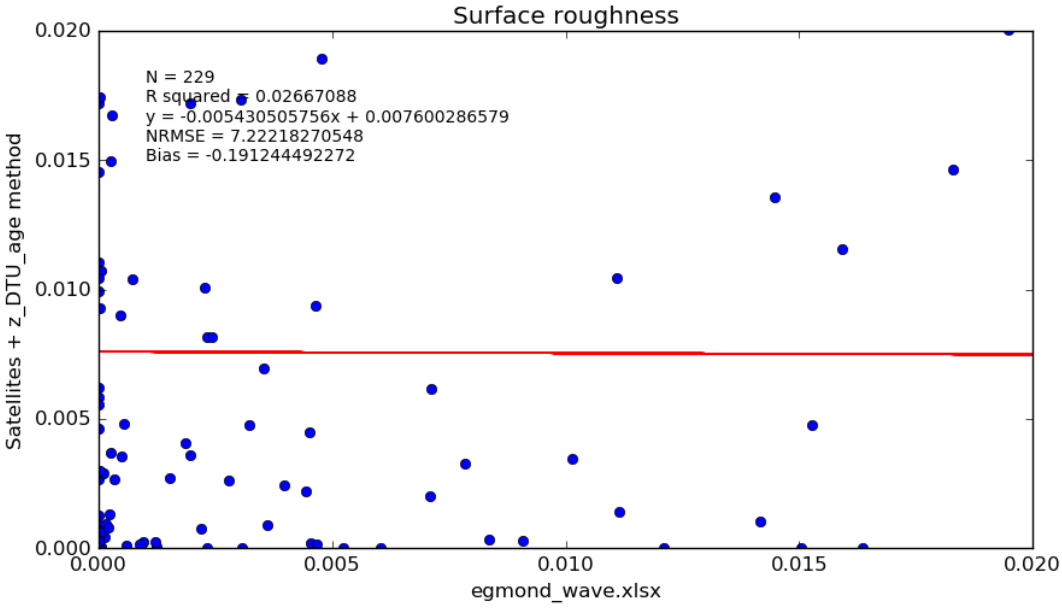

B. 48. Surface roughness regression for method Maat & DTU_Age combination.

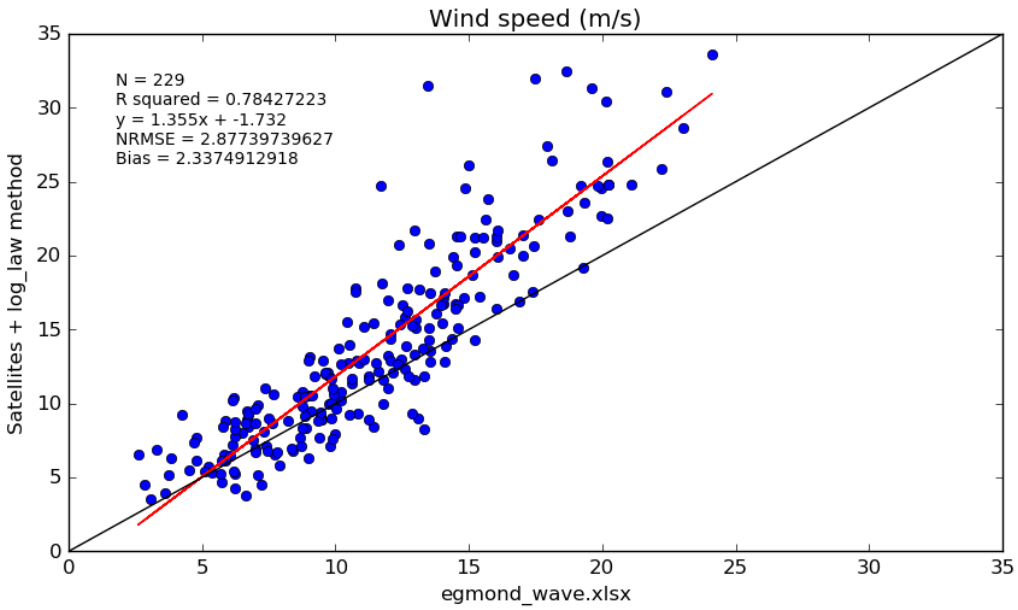

B. 49. Wind speed regression for method Maat & Log_law combination.

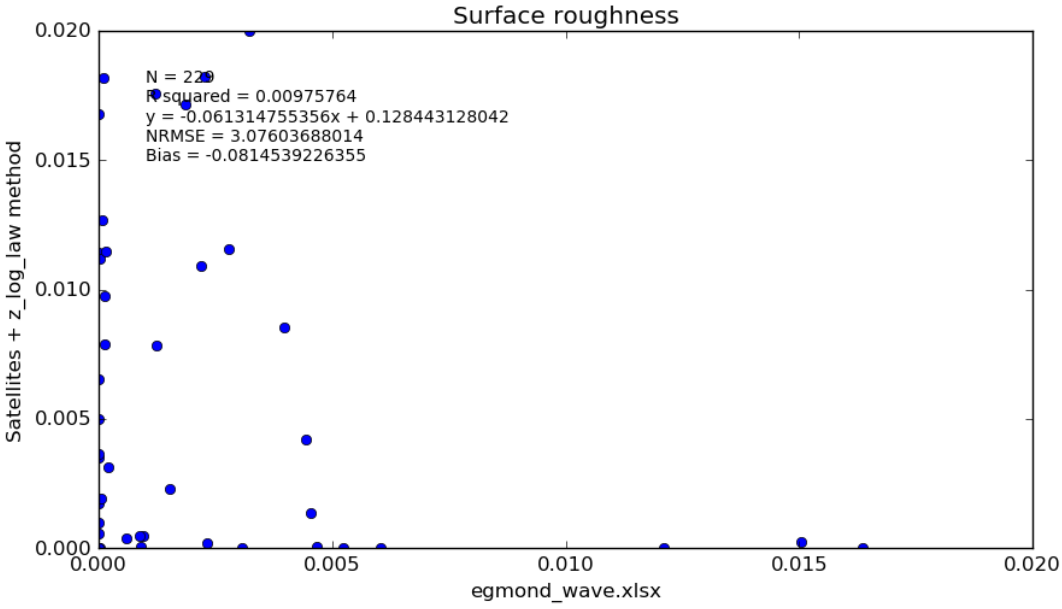

B. 50. Surface roughness regression for method Maat & Log_law combination.

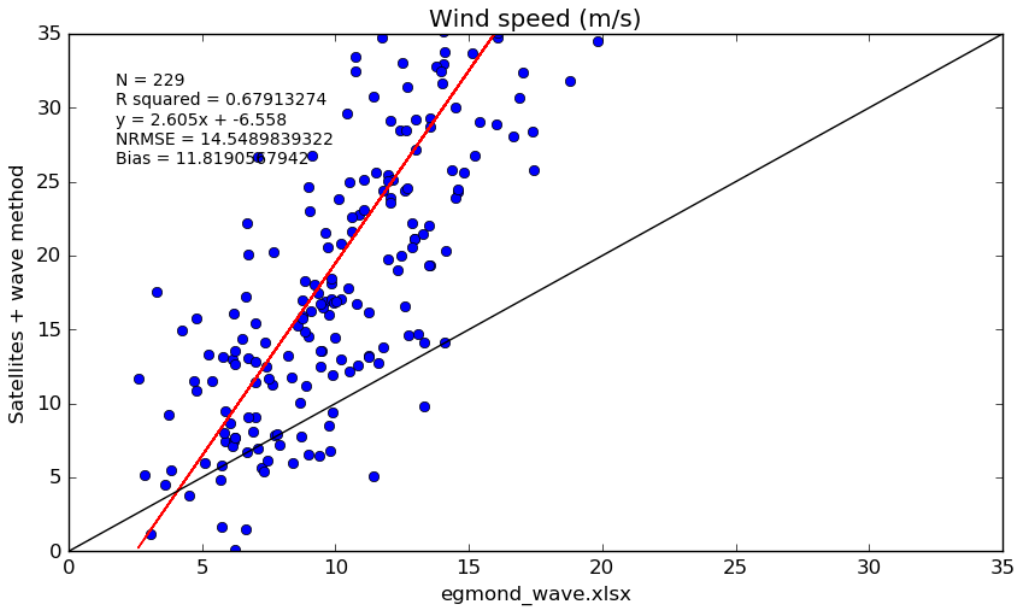

B. 51. Wind speed regression for method Maat & Edson_wave combination.

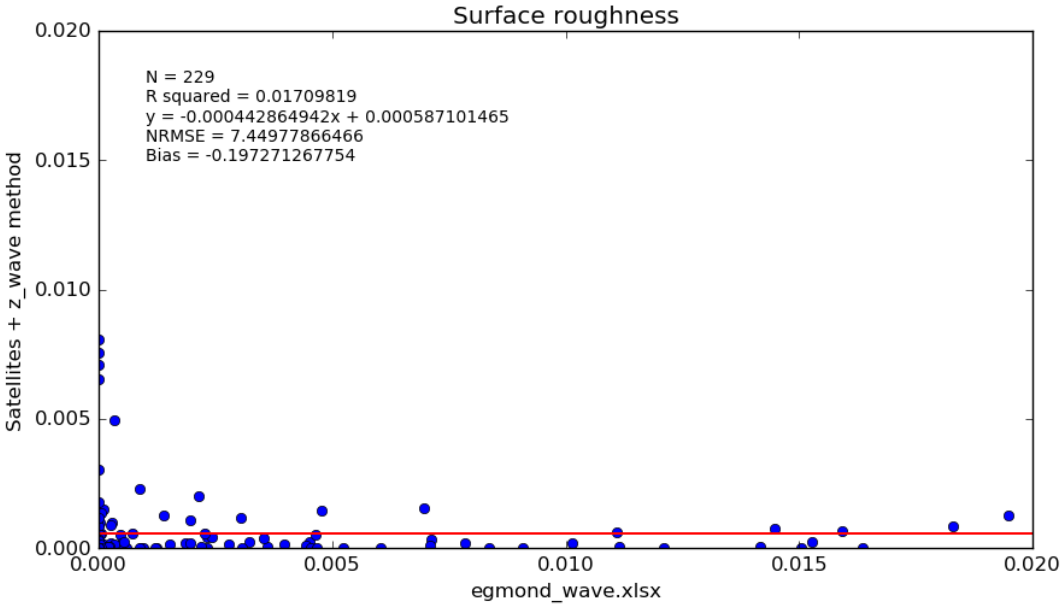

B. 52. Surface roughness regression for method Maat & Edson_wave combination.

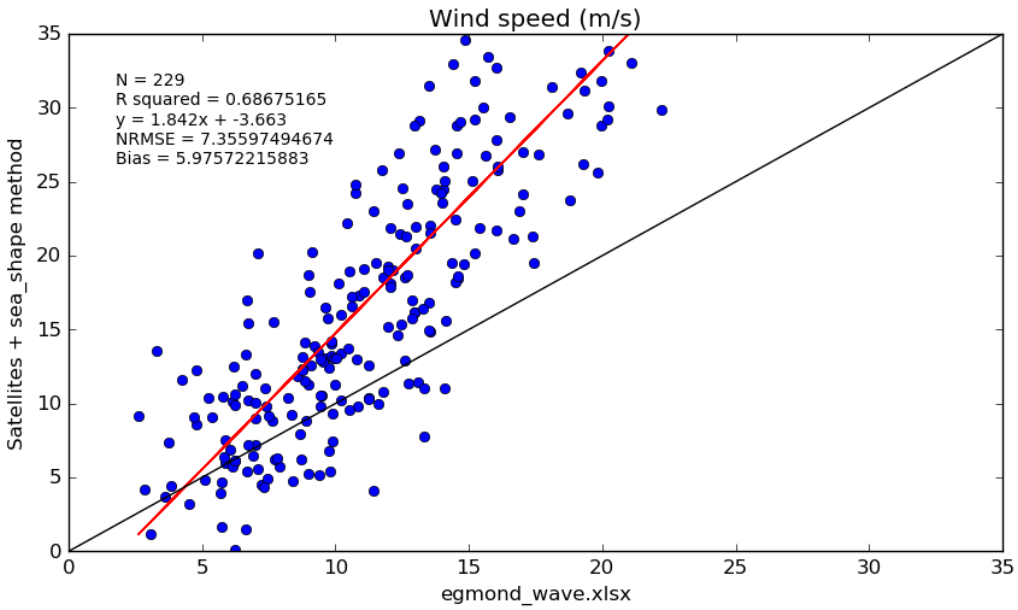

B. 53. Wind speed regression for method Maat & Taylor combination.

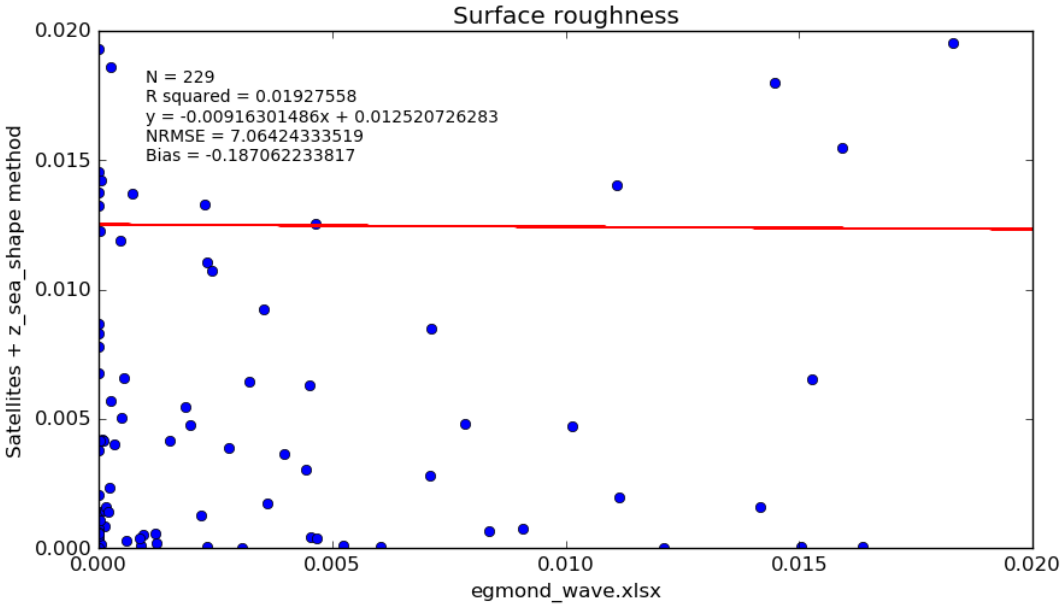

B. 54. Surface roughness regression for method Maat & Taylor combination.

IV. For Toba friction method

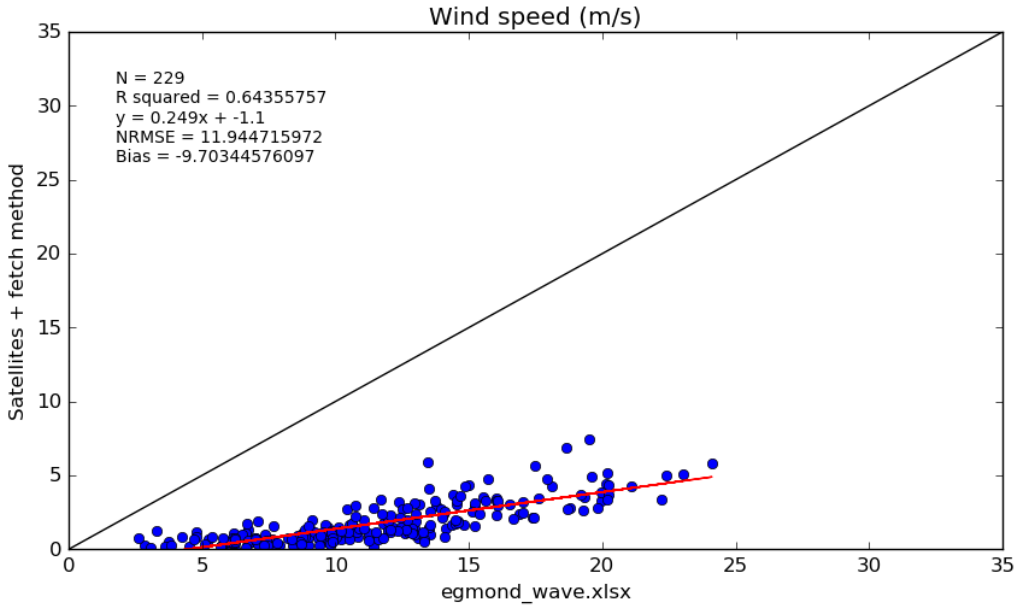

B. 55. Wind speed regression for method Toba & Fetch combination.

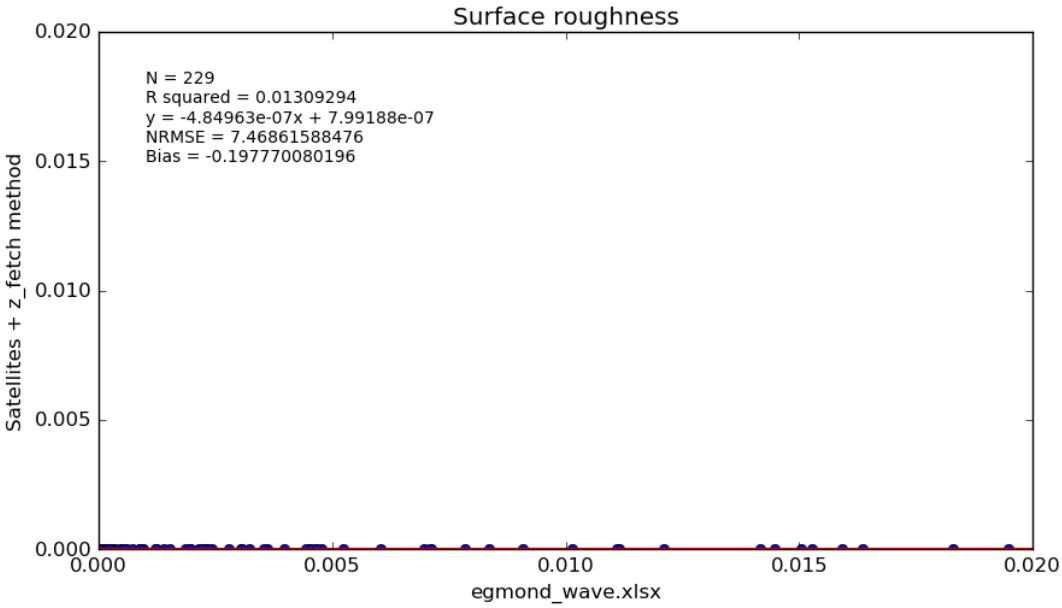

B. 56. Surface roughness regression for method Toba & Fetch combination.

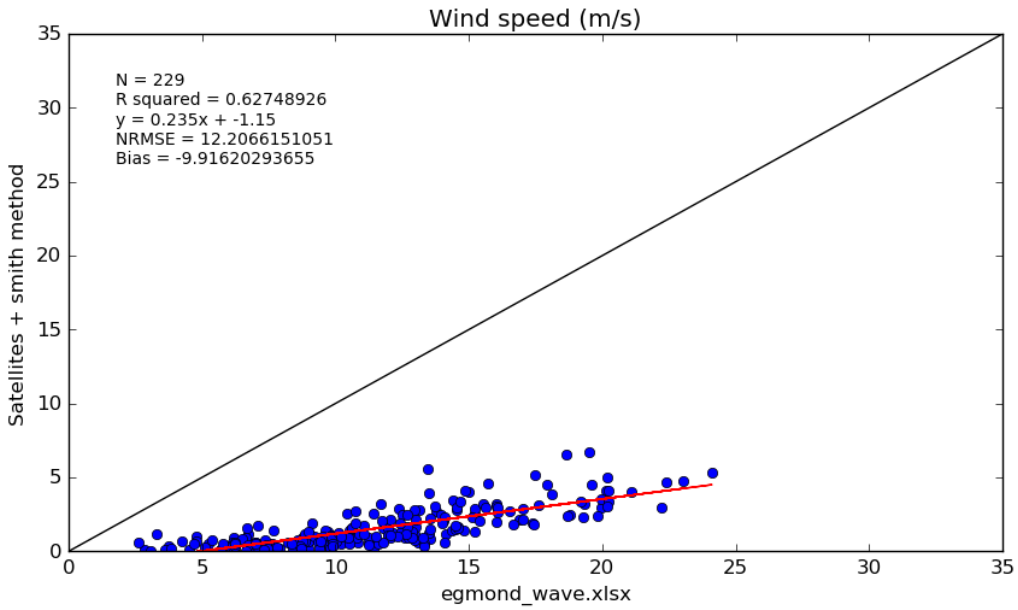

B. 57. Wind speed regression for method Toba & Smith combination.

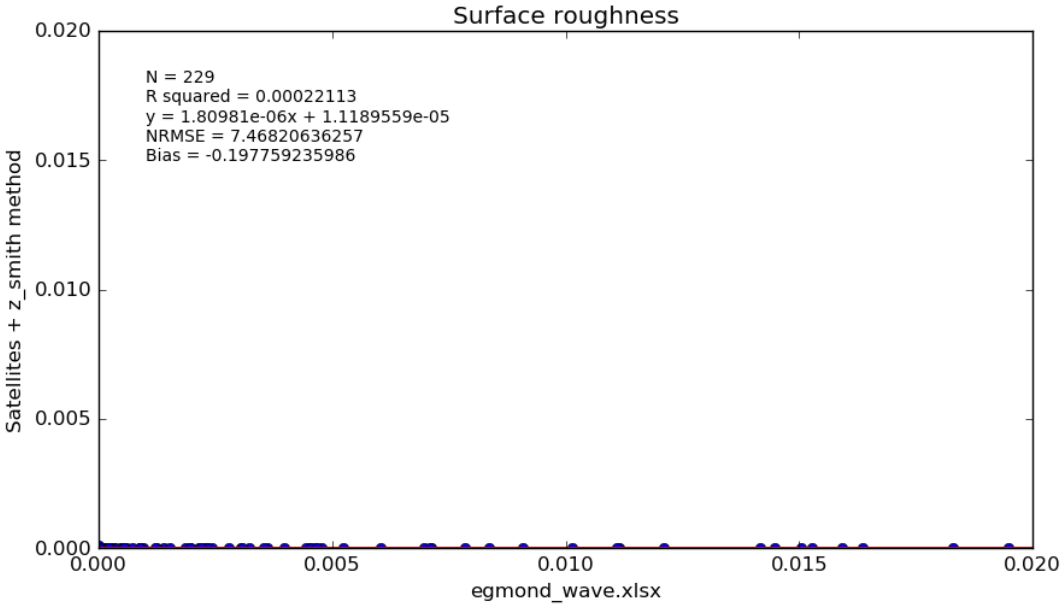

B. 58. Surface roughness regression for method Toba & Smith combination.

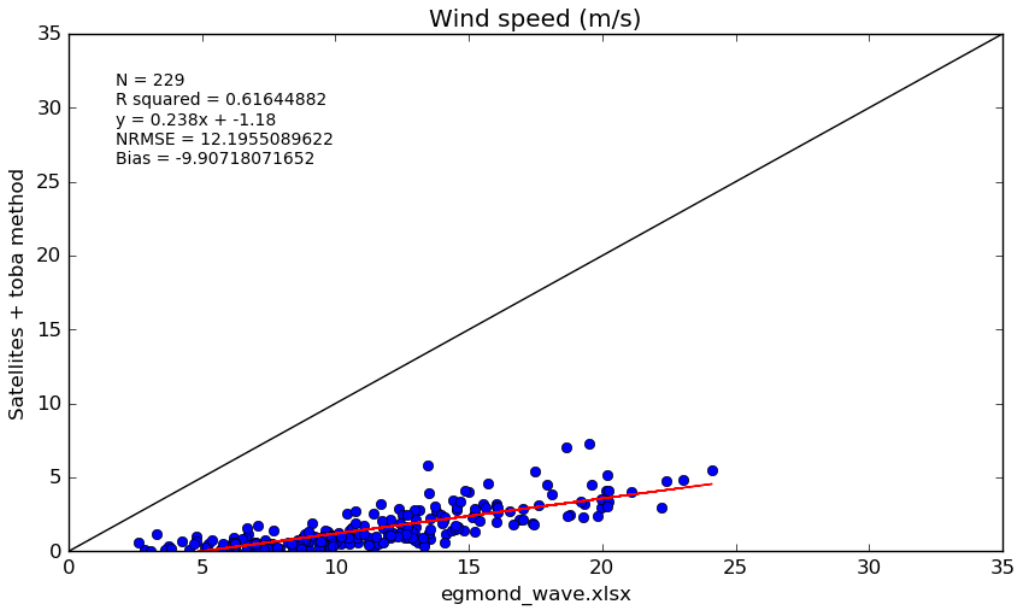

B. 59. Wind speed regression for method Toba & Toba combination.

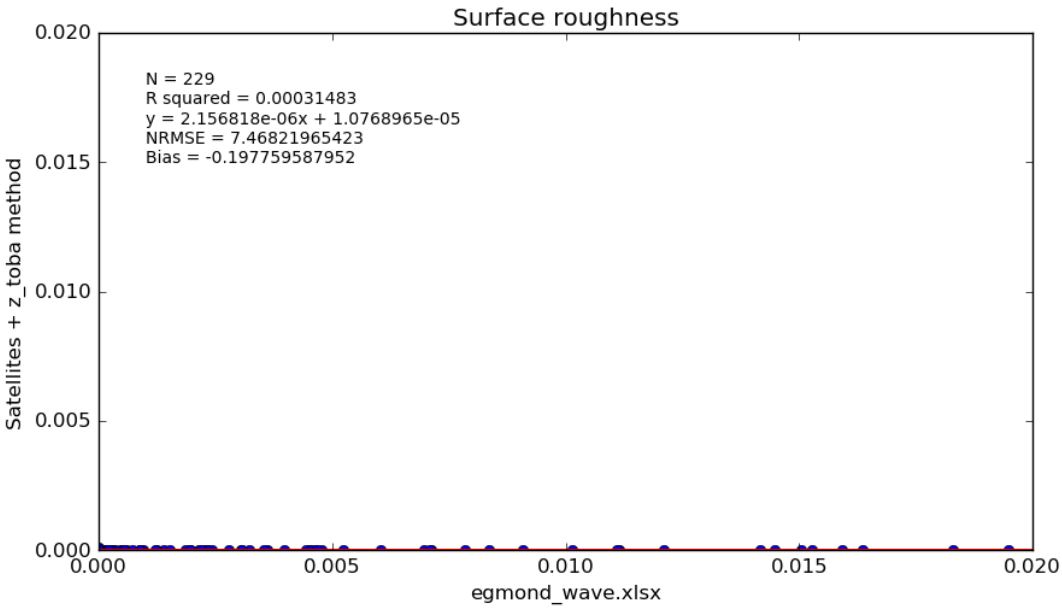

B. 60. Surface roughness regression for method Toba & Toba combination.

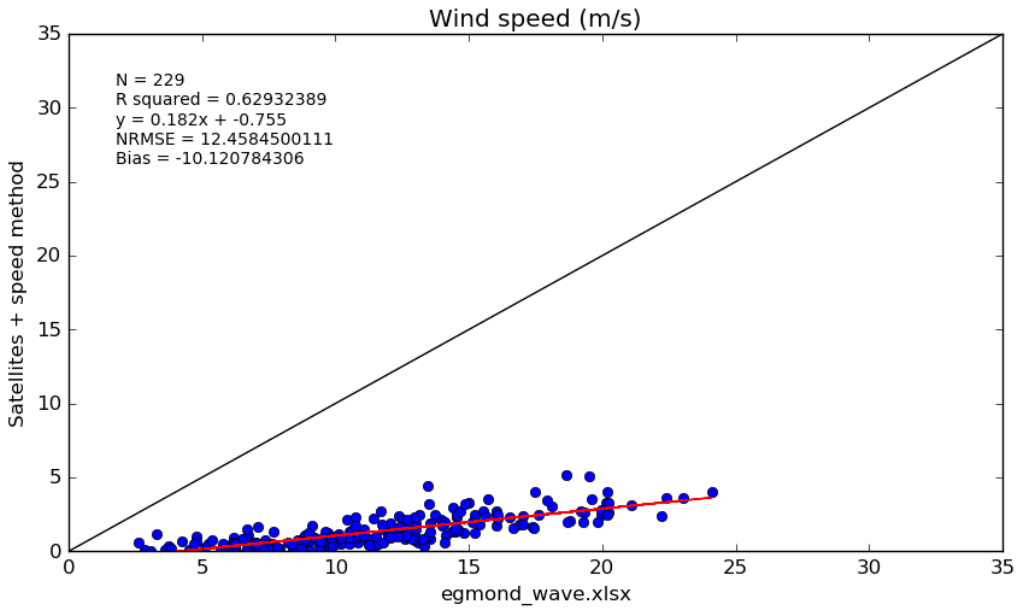

B. 61. Wind speed regression for method Toba & Edson_Speed combination.

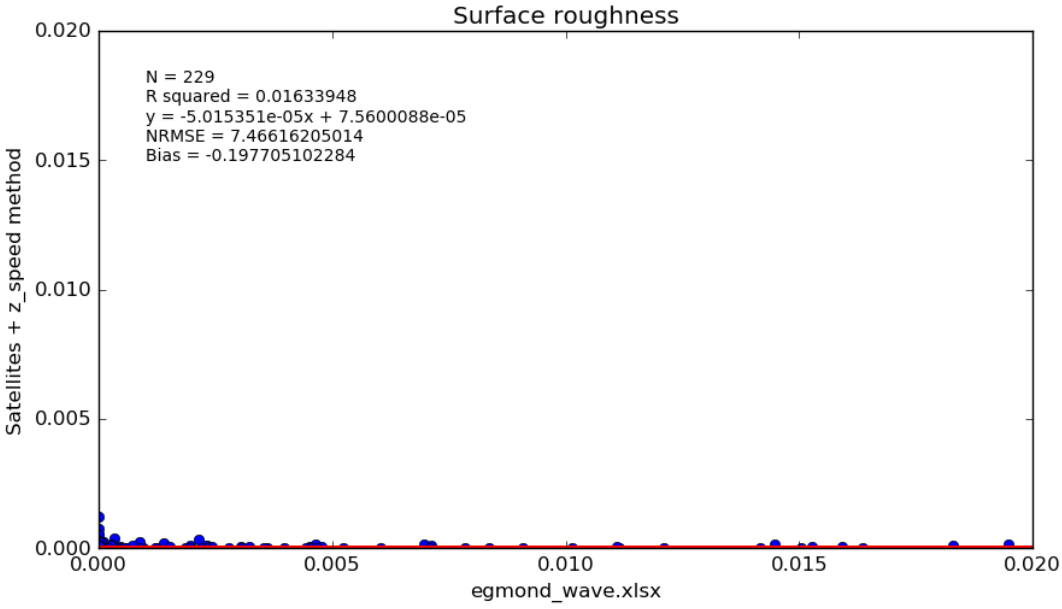

B. 62. Surface roughness regression for method Toba & Edson_Speed combination.

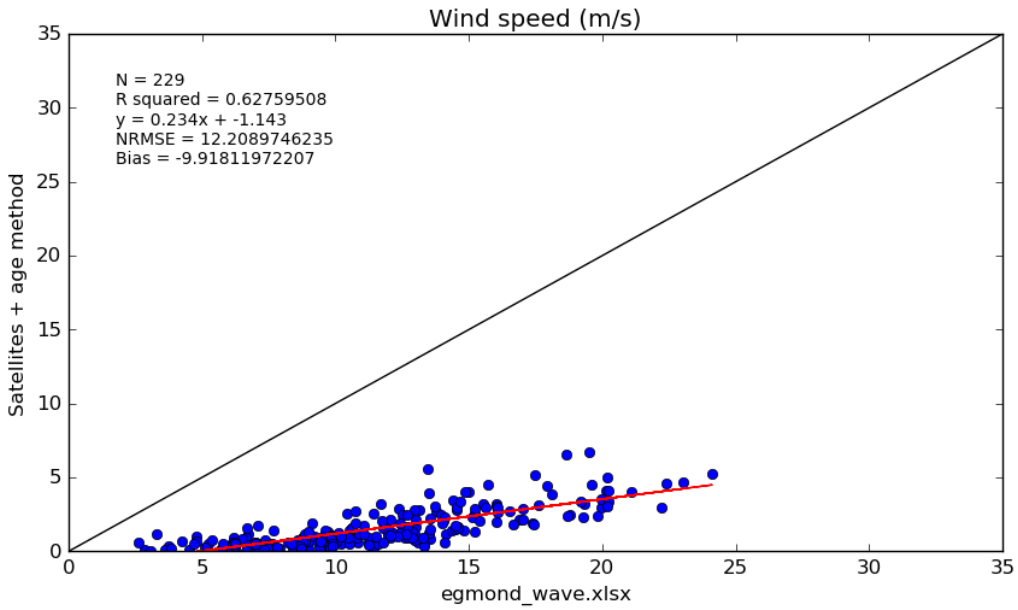

B. 63. Wind speed regression for method Toba & Edson_Age combination.

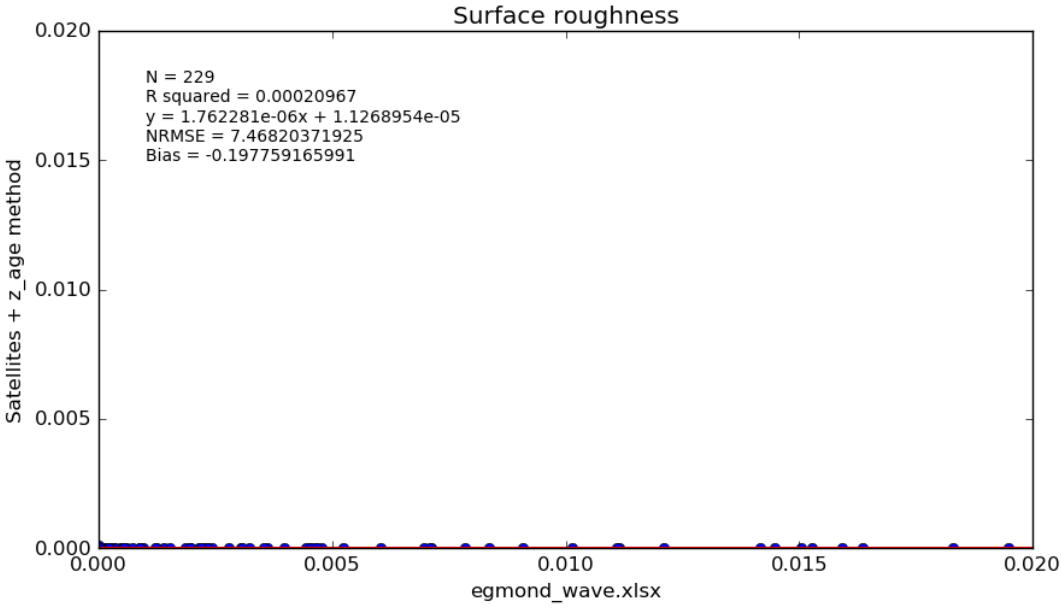

B. 64. Surface roughness regression for method Toba & Edson_Age combination.

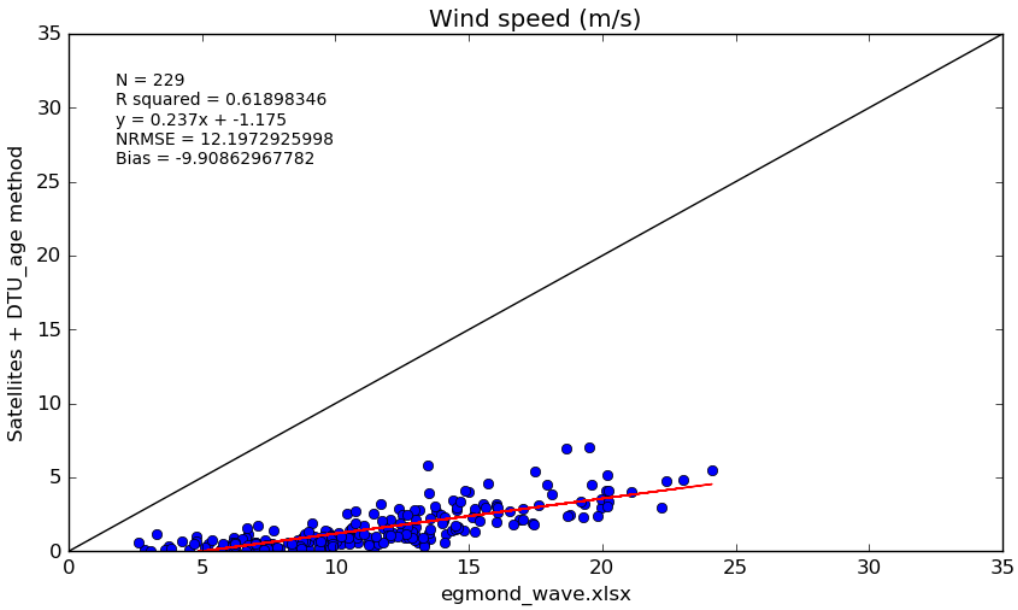

B. 65. Wind speed regression for method Toba & DTU_Age combination.

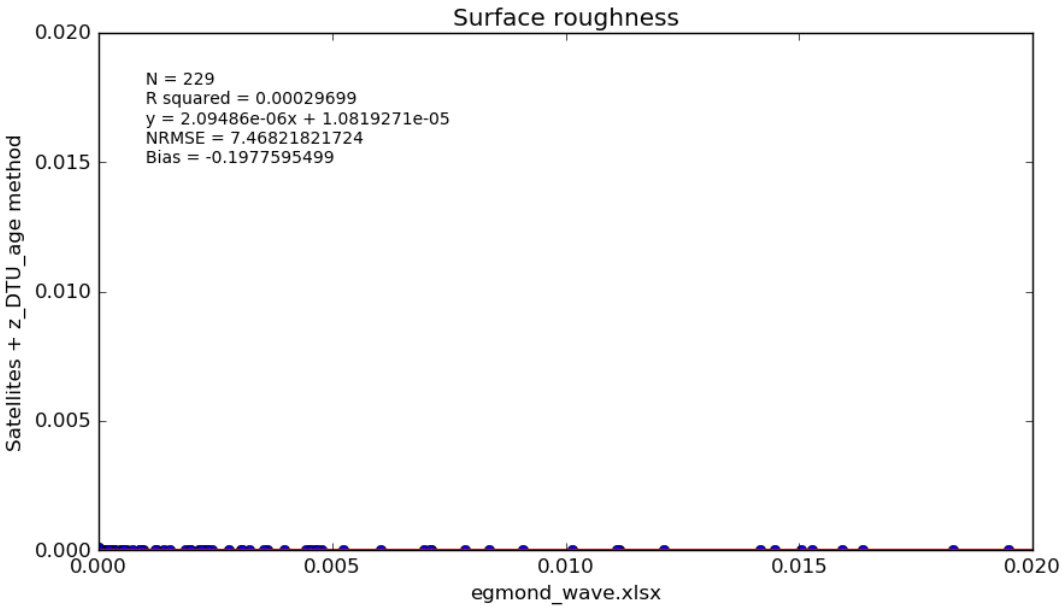

B. 66. Surface roughness regression for method Toba & DTU_Age combination.

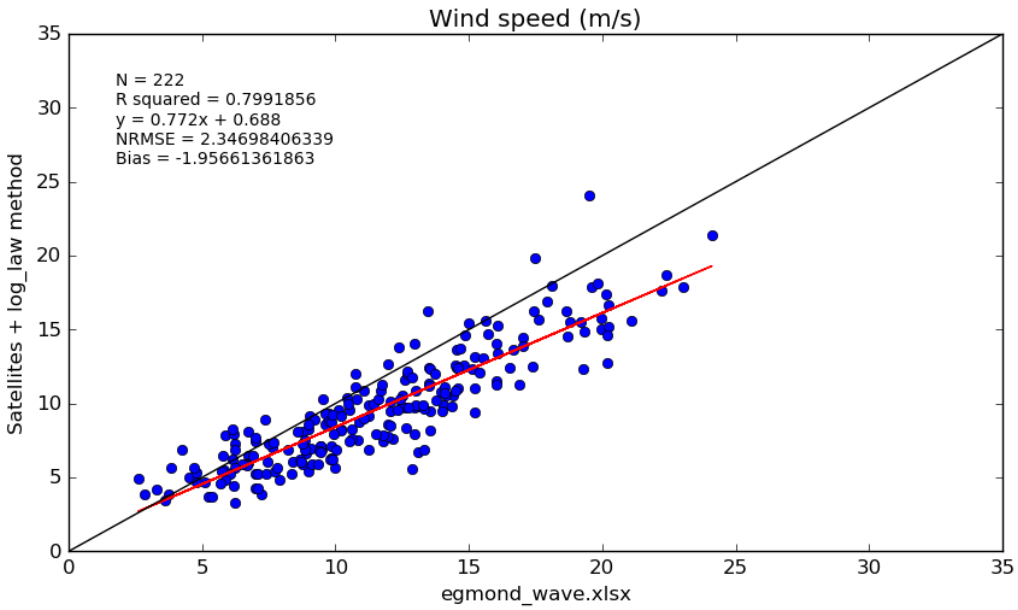

B. 67. Wind speed regression for method Toba & Log_law combination.

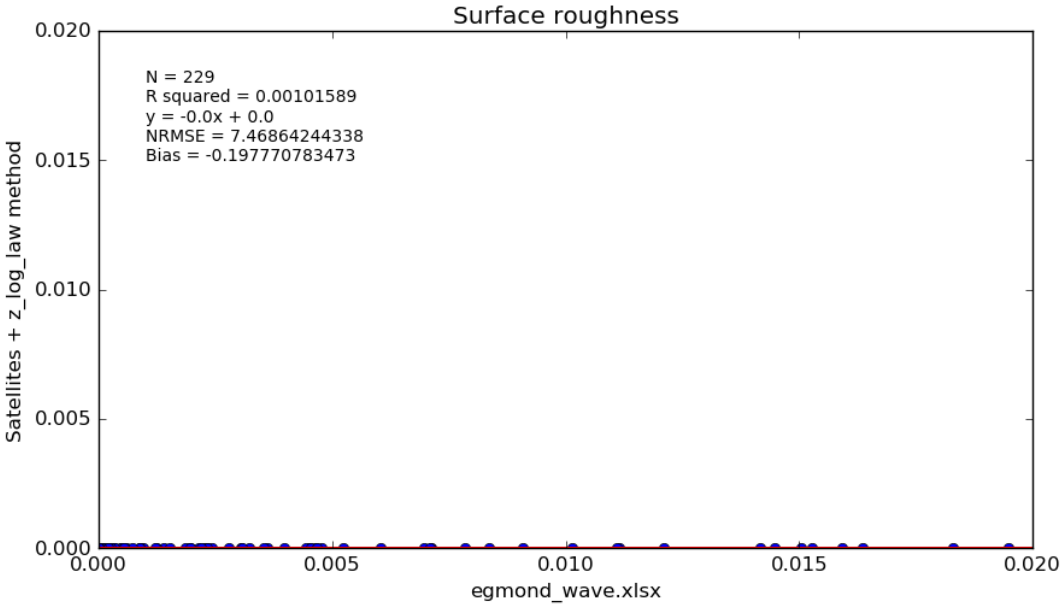

B. 68. Surface roughness regression for method Toba & Log_law combination.

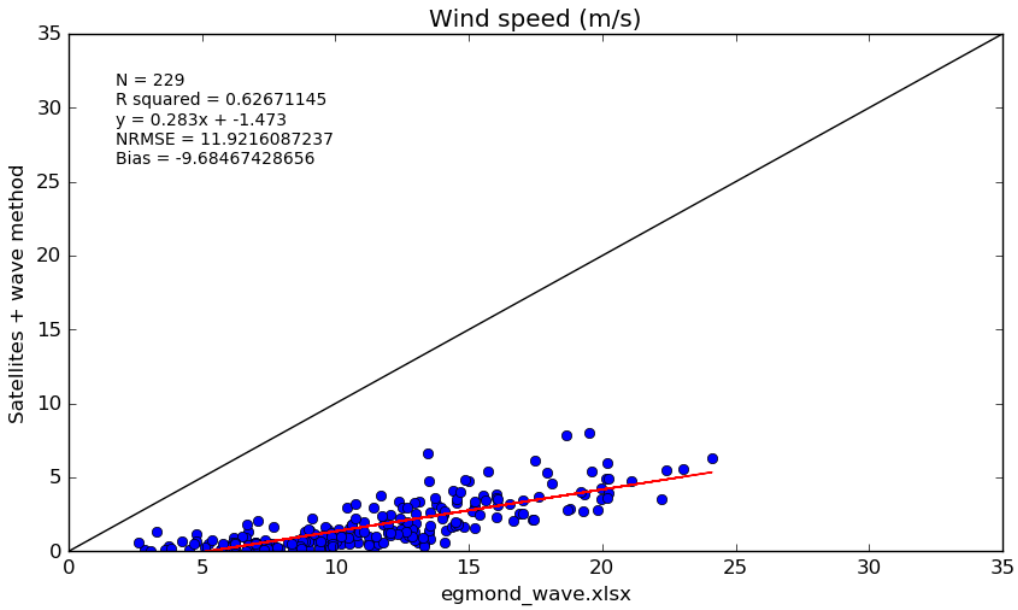

B. 69. Wind speed regression for method Toba & Edson_wave combination.

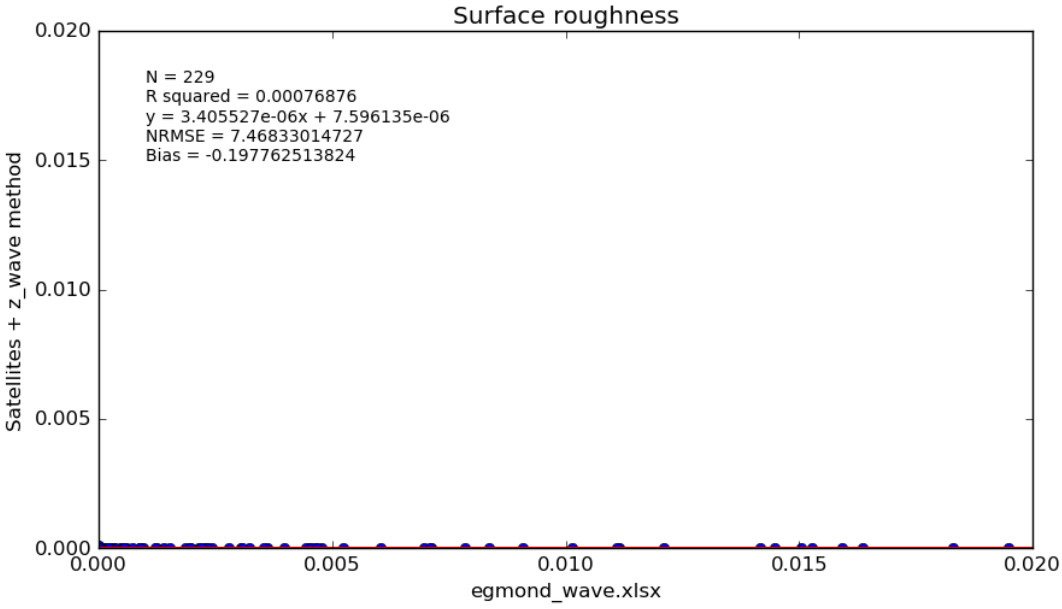

B. 70 Surface roughness regression for method Toba & Edson_wave combination.

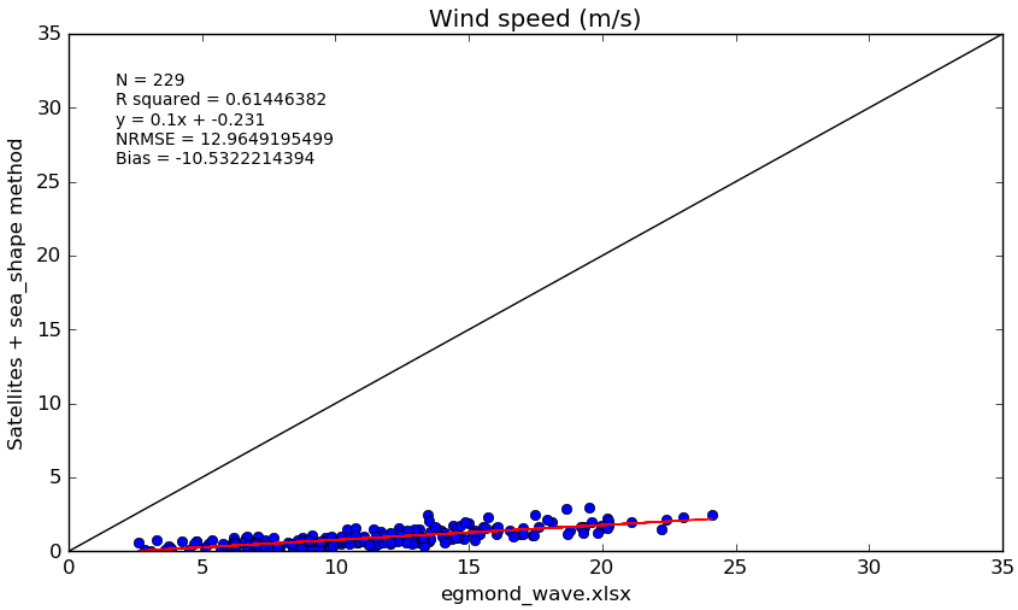

B. 71. Wind speed regression for method Toba & Taylor combination.

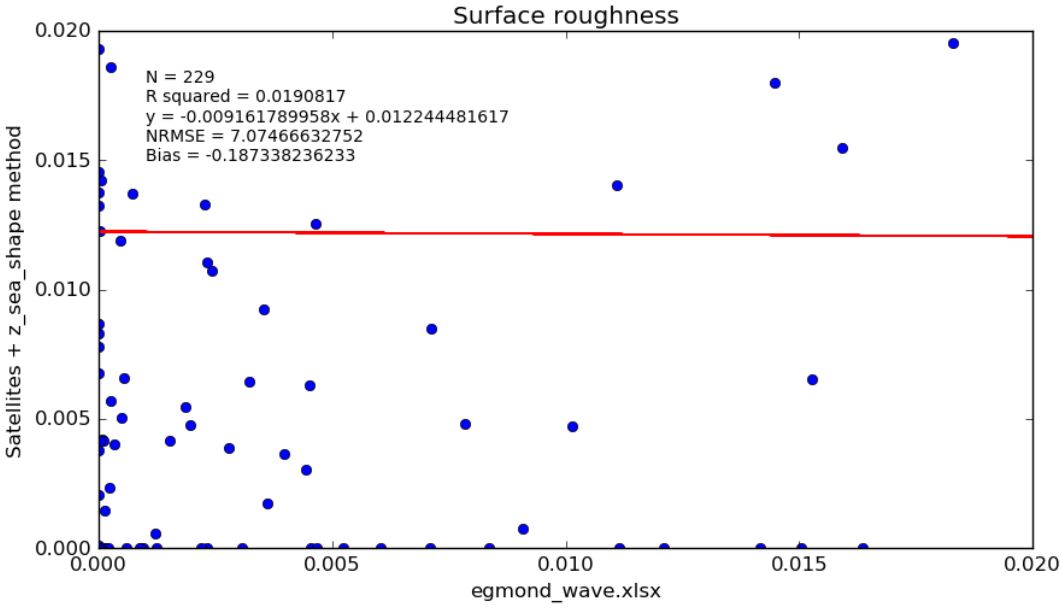

B. 72. Surface roughness regression for method Toba & Taylor combination.

V. For Insitu friction method

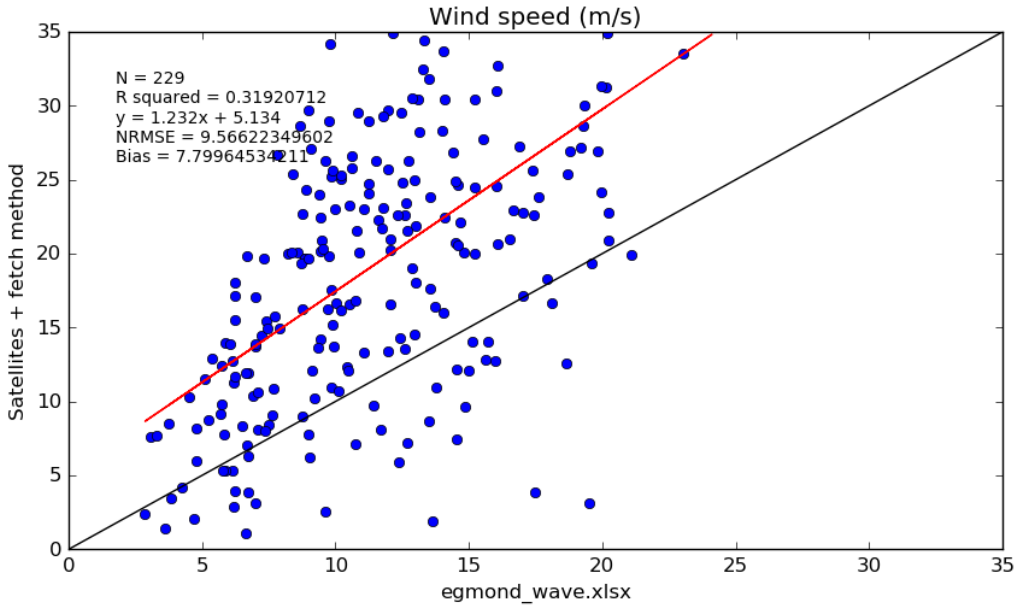

B. 73. Wind speed regression for method Insitu & Fetch combination.

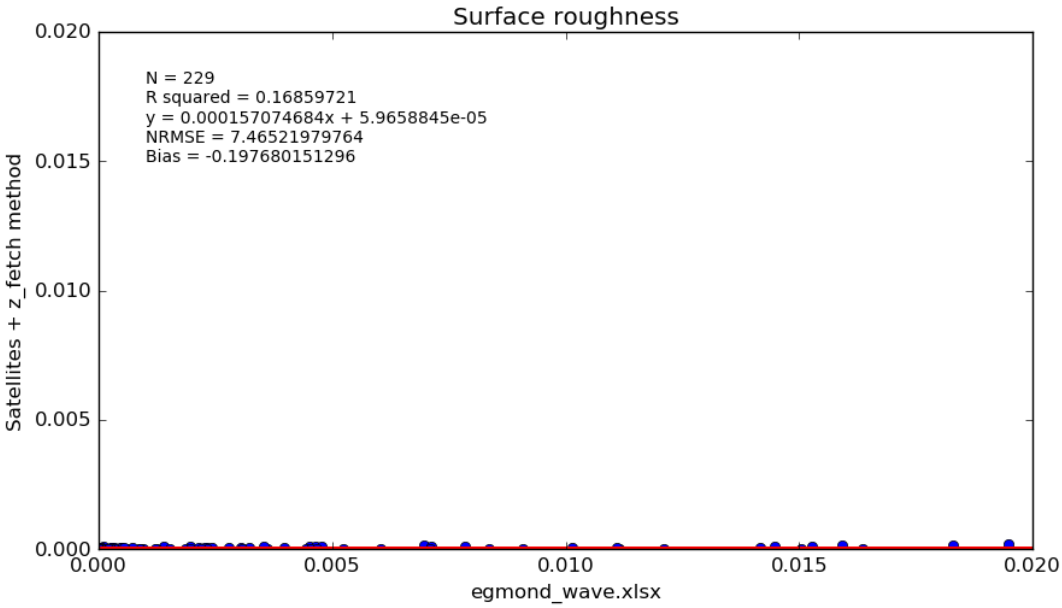

B. 74. Surface roughness regression for method Insitu & Fetch combination.

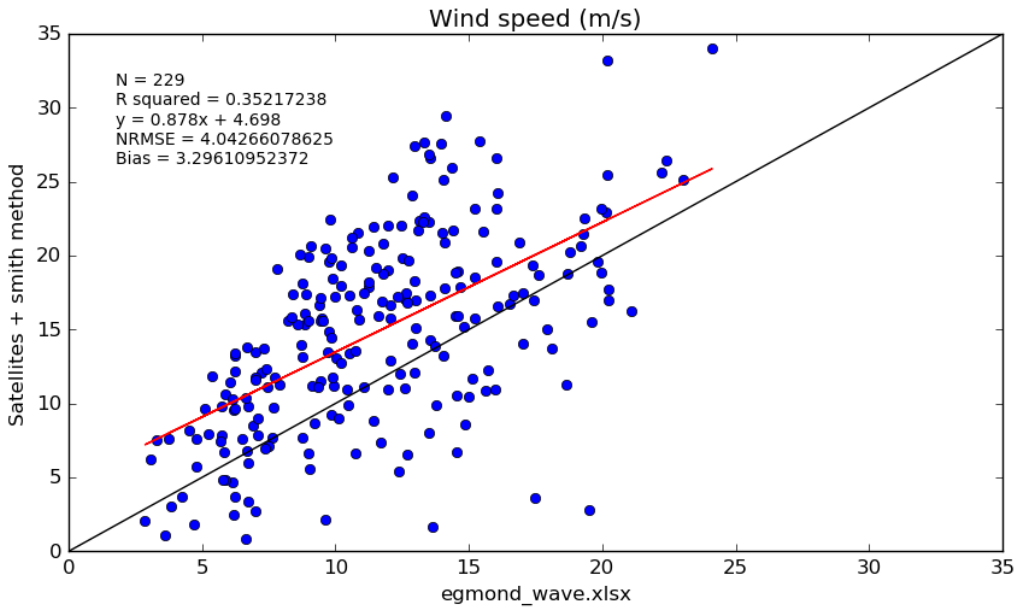

B. 75. Wind speed regression for method Insitu & Smith combination.

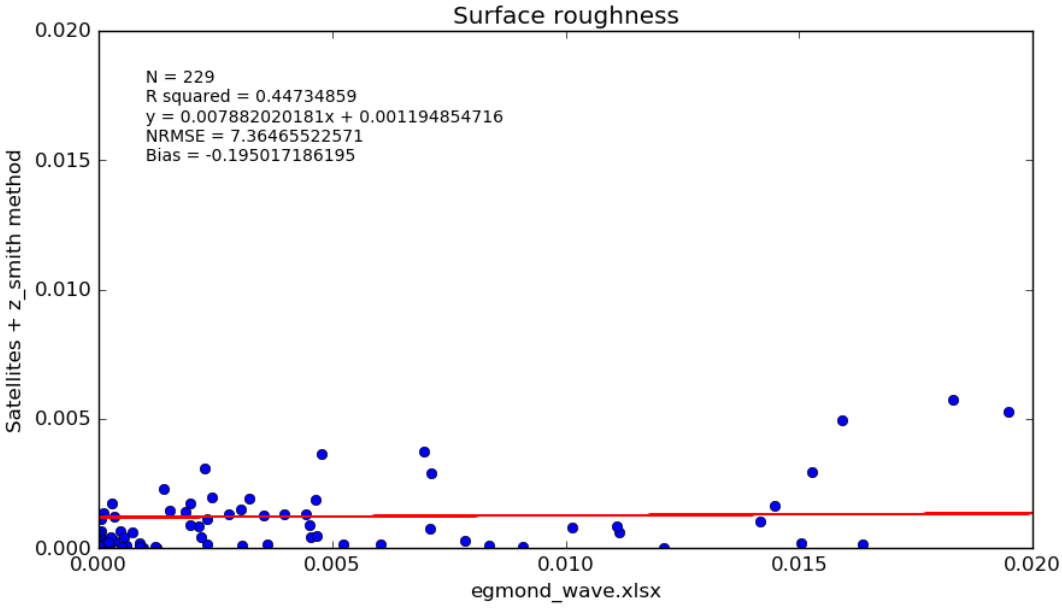

B. 76. Surface roughness regression for method Insitu & Smith combination.

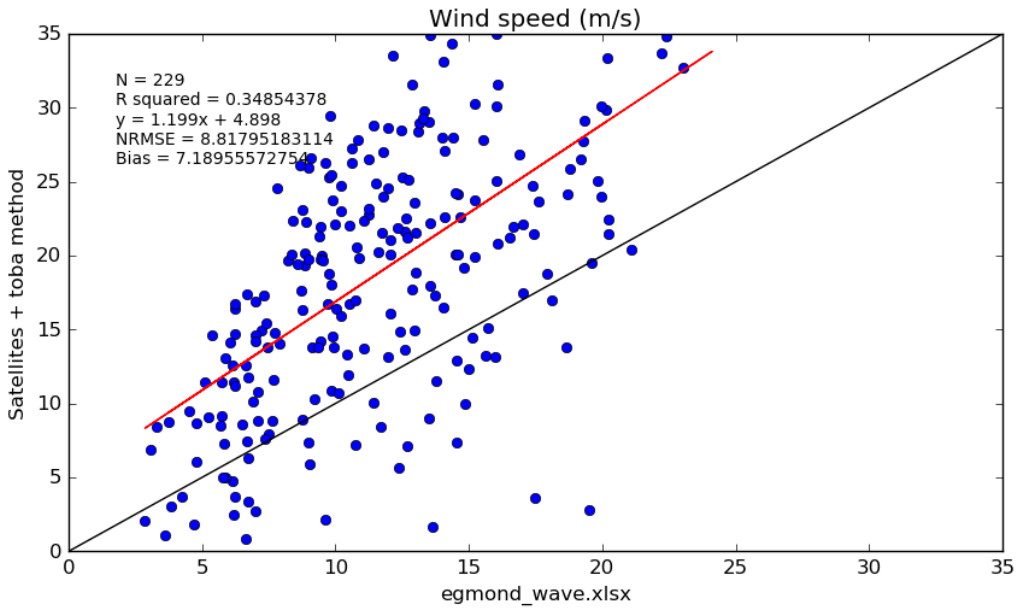

B. 77. Wind speed regression for method Insitu & Toba combination.

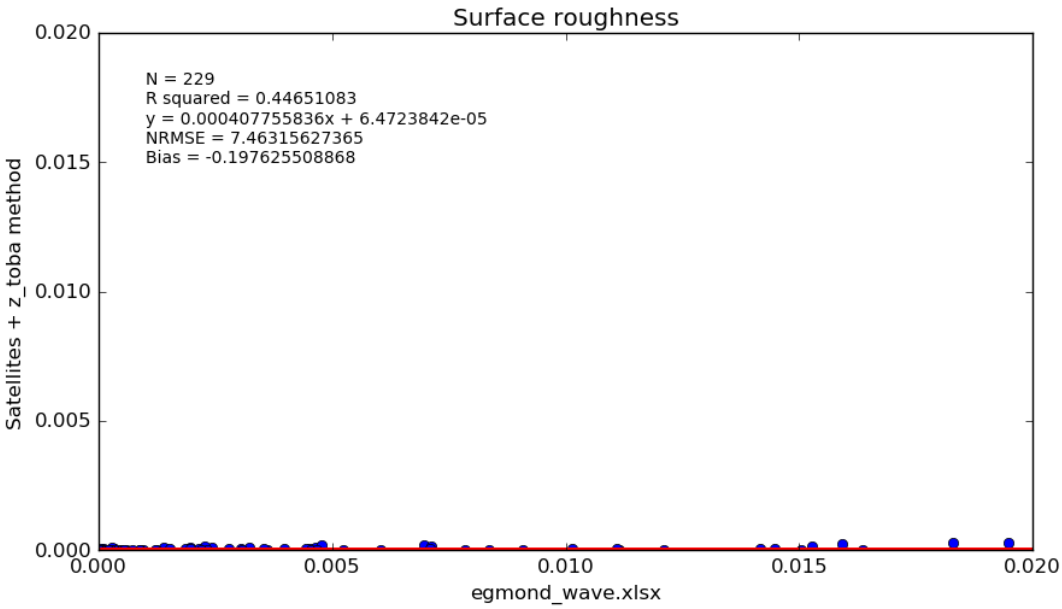

B. 78. Surface roughness regression for method Insitu & Toba combination.

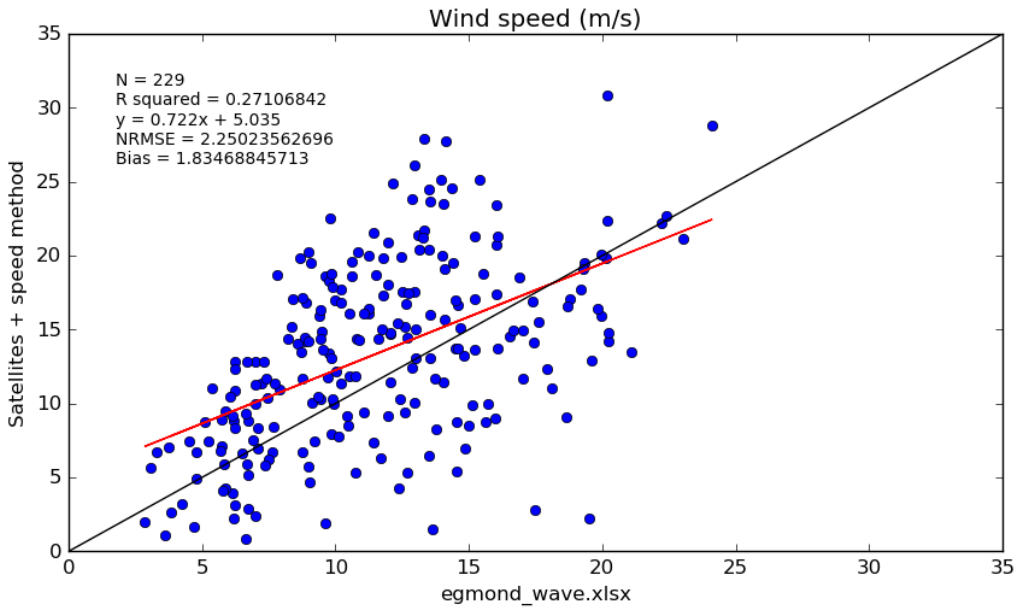

B. 79. Wind speed regression for method Insitu & Edson_Speed combination.

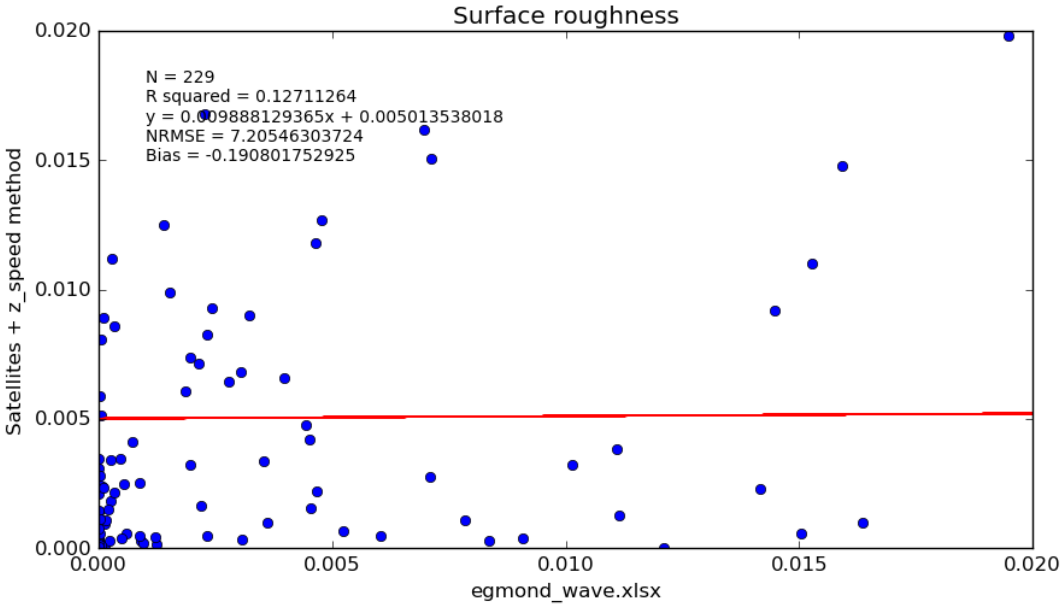

B. 80. Surface roughness regression for method Insitu & Edson_Speed combination.

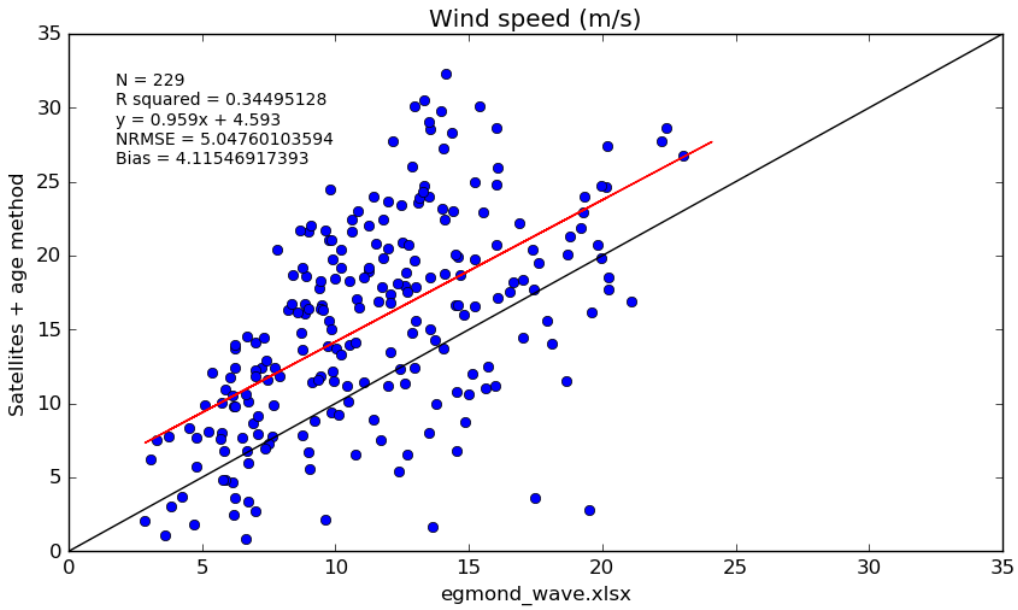

B. 81. Wind speed regression for method Insitu & Edson_Age combination.

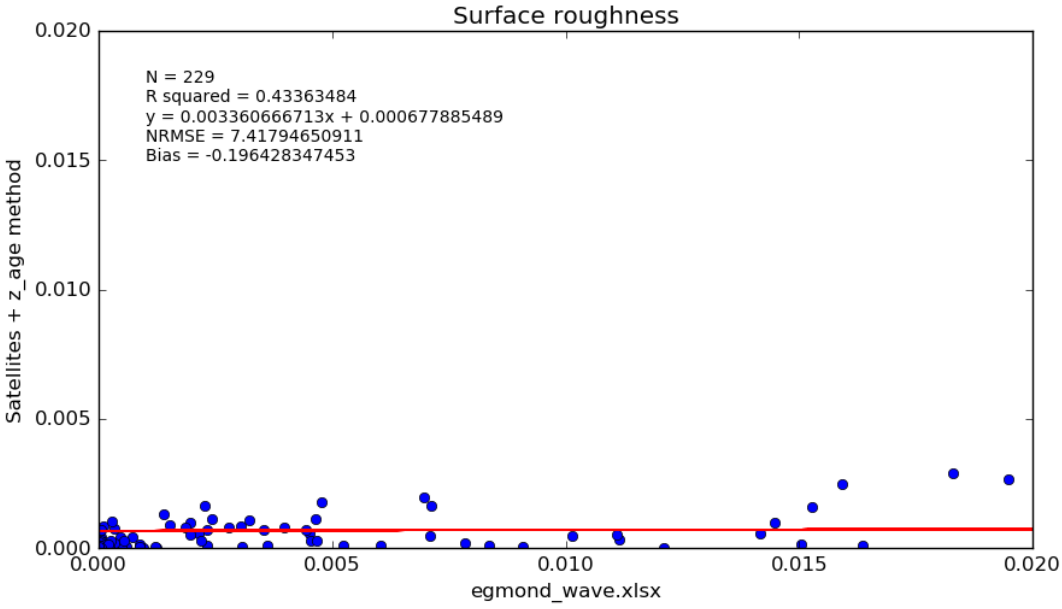

B. 82. Surface roughness regression for method Insitu & Edson_Age combination.

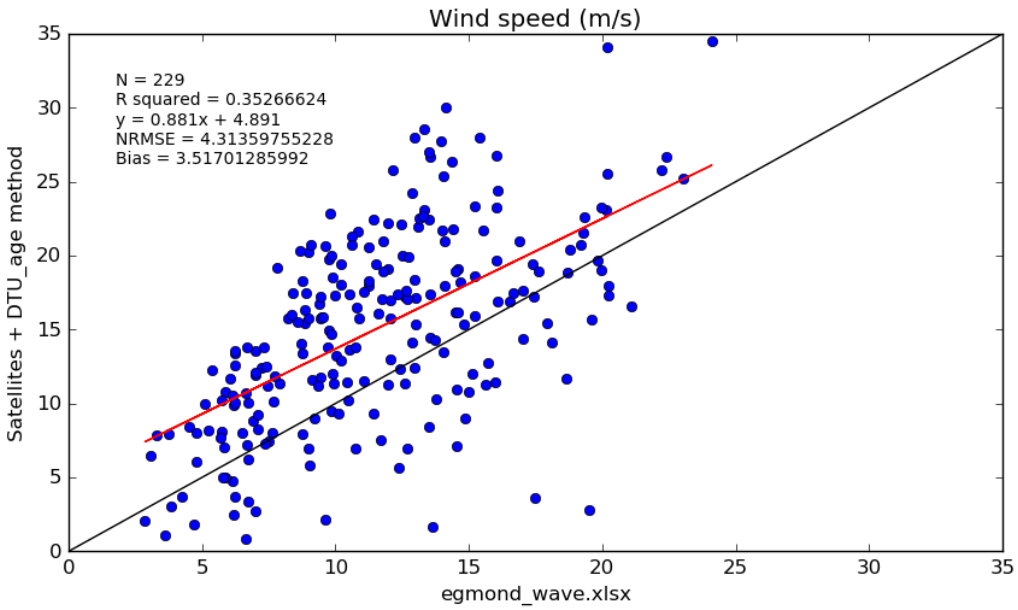

B. 83. Wind speed regression for method Insitu & DTU_Age combination.

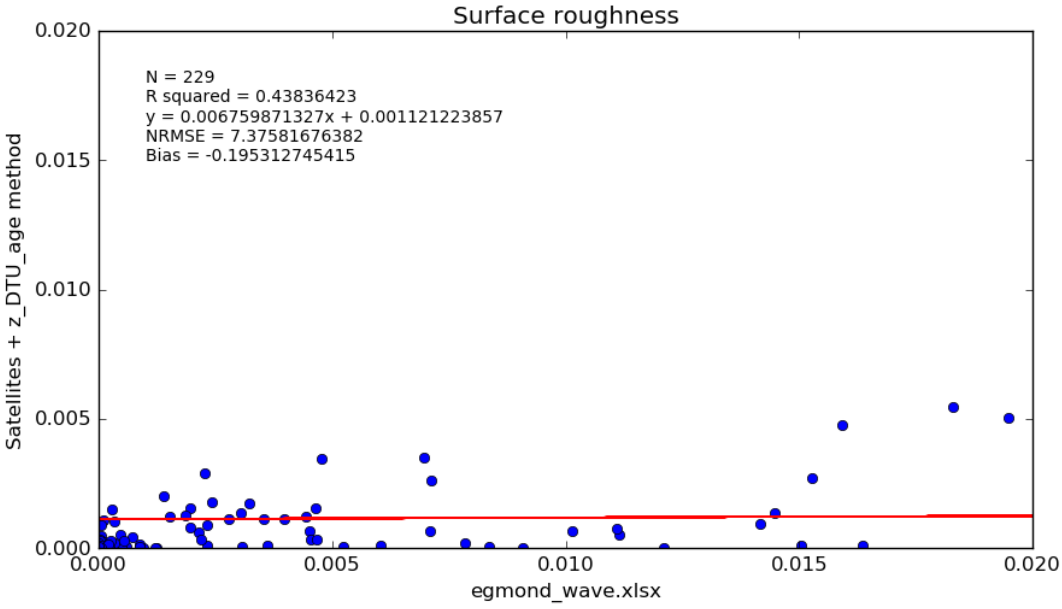

B. 84. Surface roughness regression for method Insitu & DTU_Age combination.

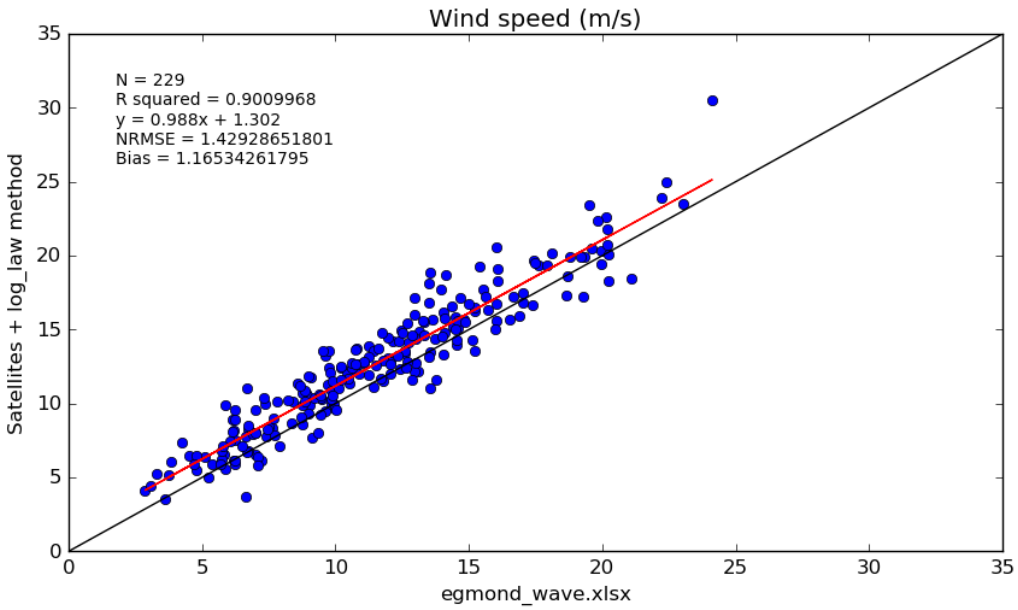

B. 85. Wind speed regression for method Insitu & Log_law combination.

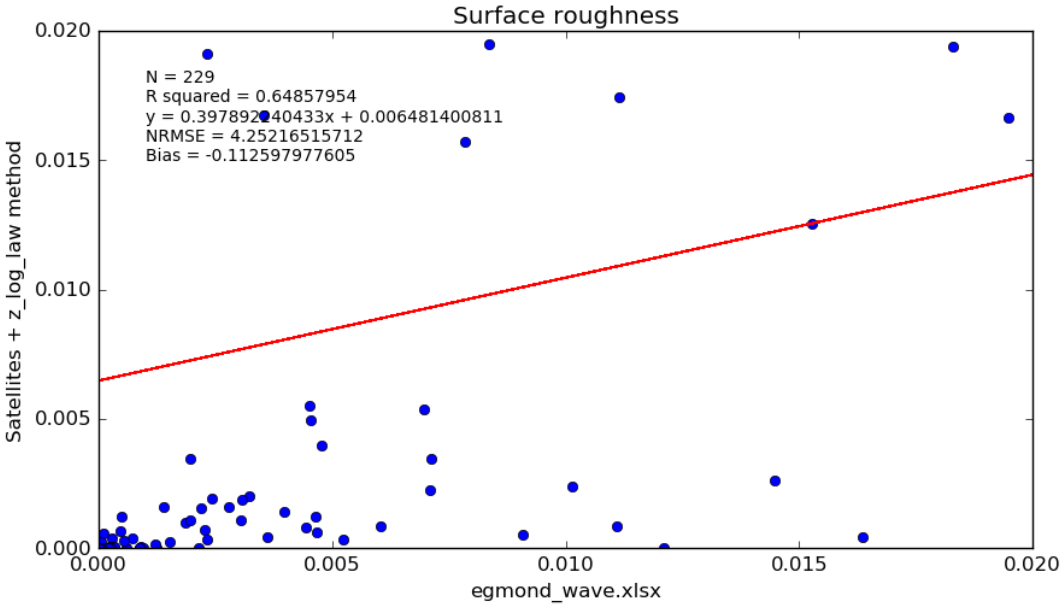

B. 86. Surface roughness regression for method Insitu & Log_law combination.

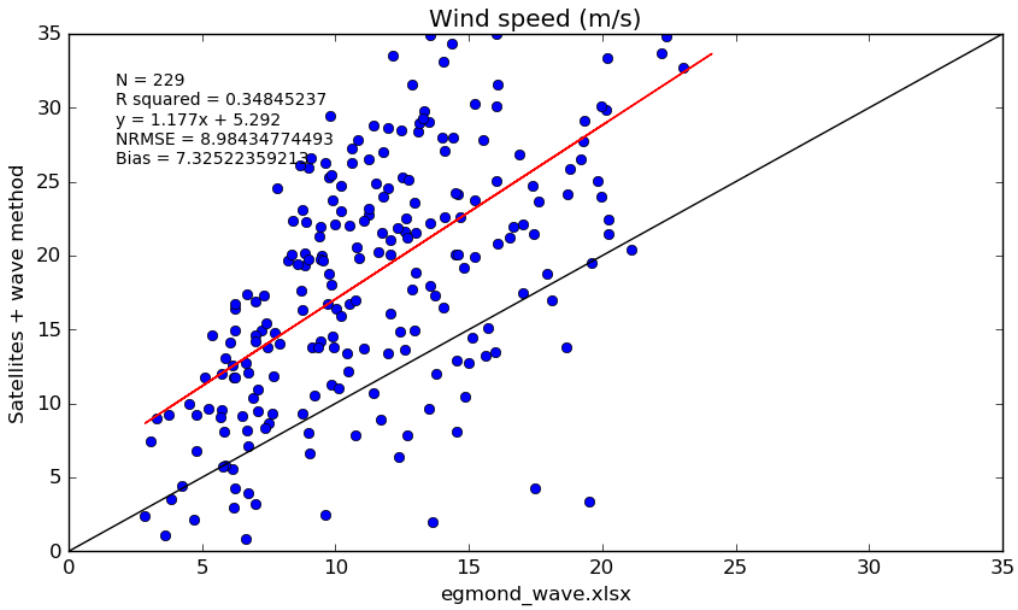

B. 87. Wind speed regression for method Insitu & Edson_wave combination.

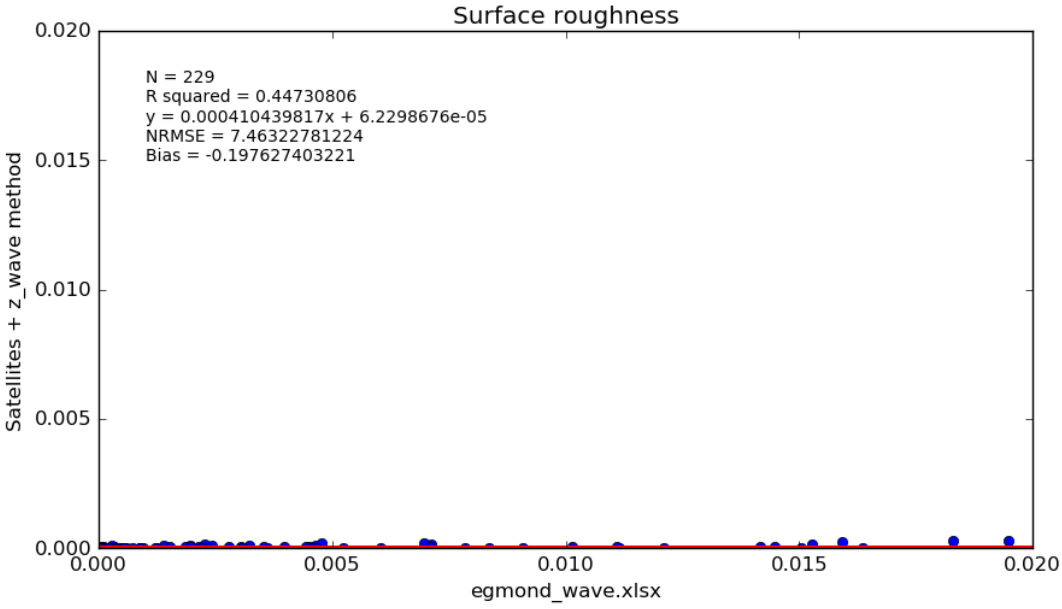

B. 88. Surface roughness regression for method Insitu & Edson_wave combination.

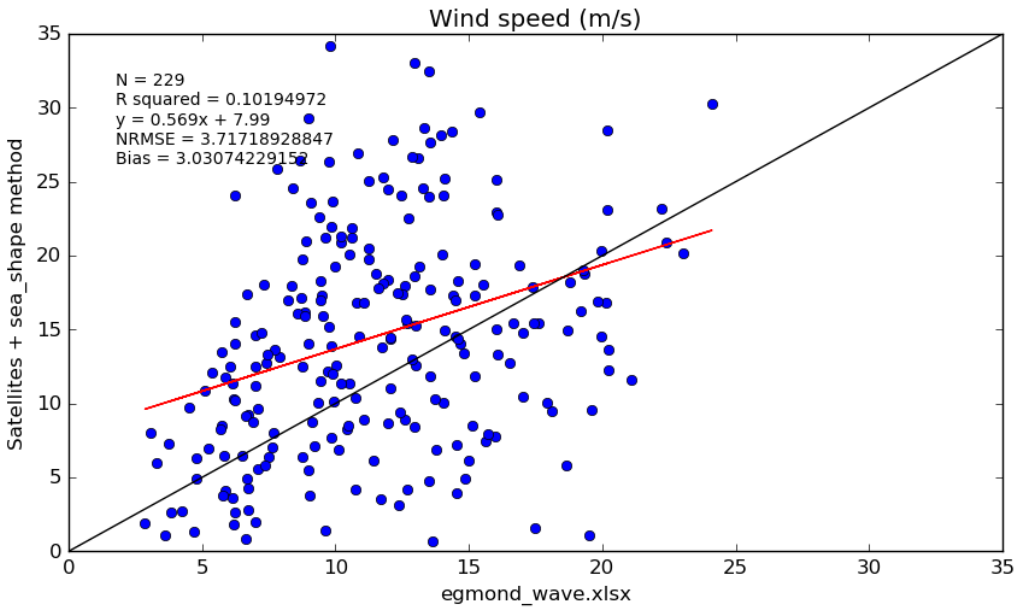

B. 89. Wind speed regression for method Insitu & Taylor combination.

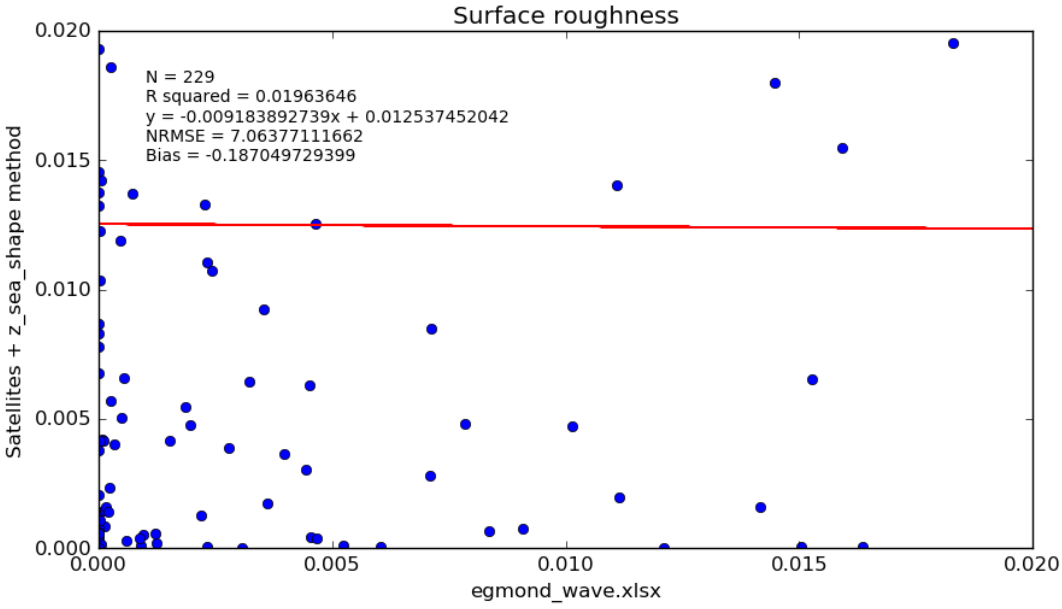

B. 90. Surface roughness regression for method Insitu & Taylor combination.

VI. For iterated methods

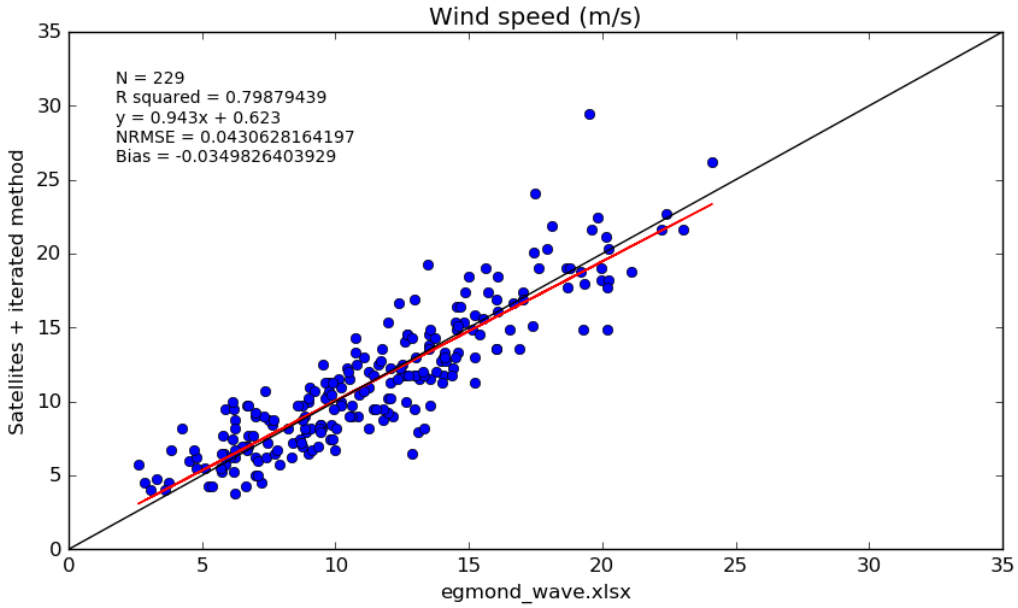

B. 91. Wind speed regression for Iteration method.

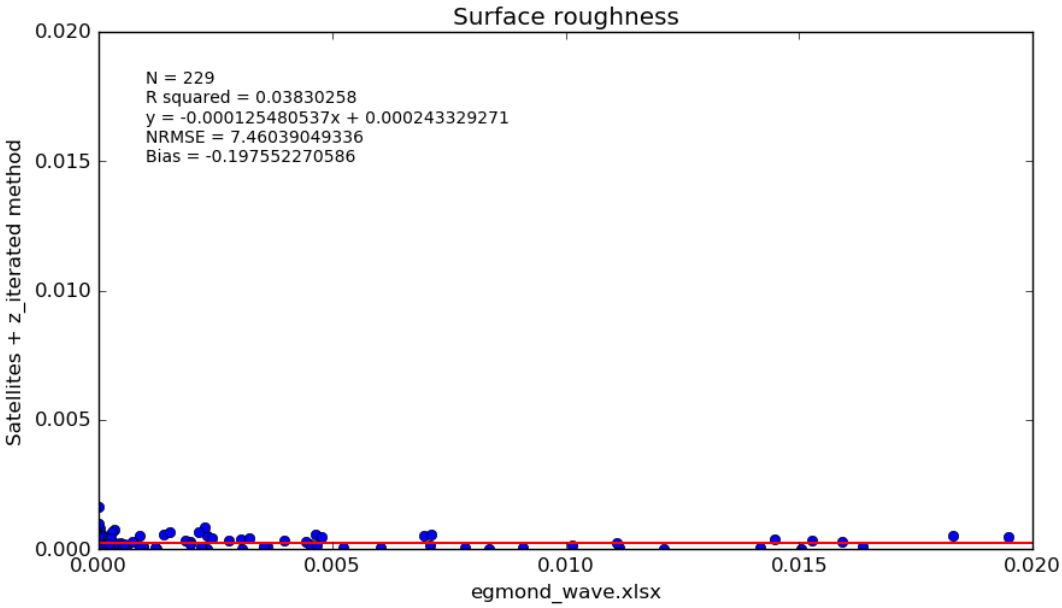

B. 92. Surface roughness regression for Iteration method.

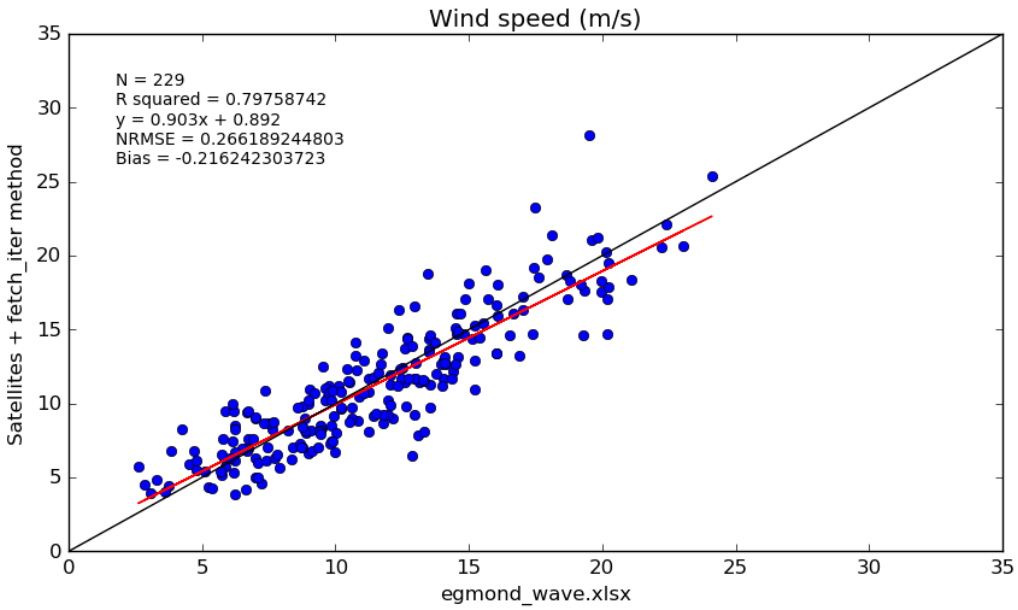

B. 93. Wind speed regression for Fetch_iteration method.

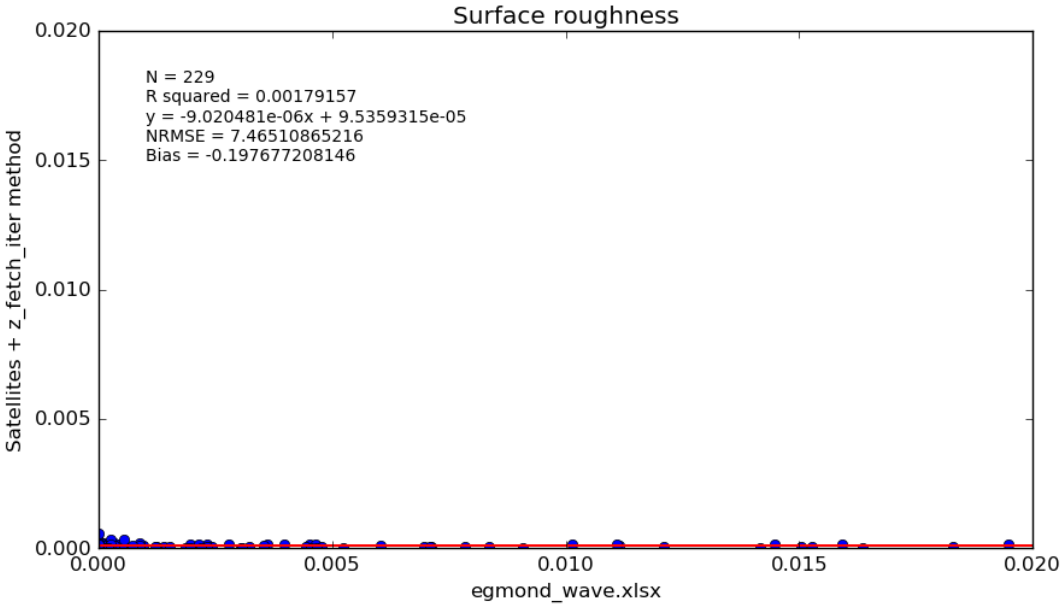

B. 94. Surface roughness regression for Fetch_iteration method.

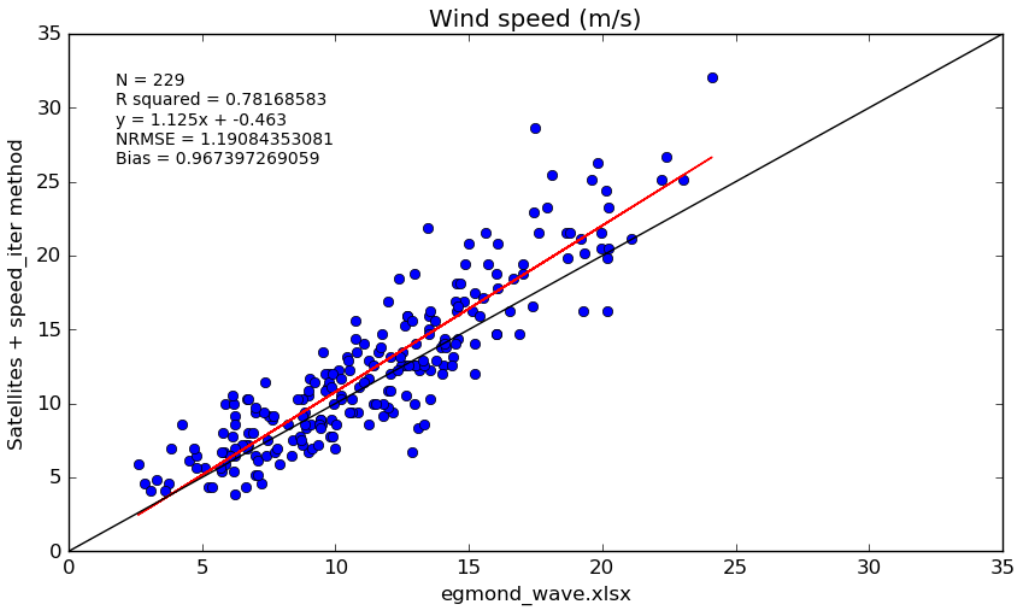

B. 95. Wind speed regression for Speed_iteration method.

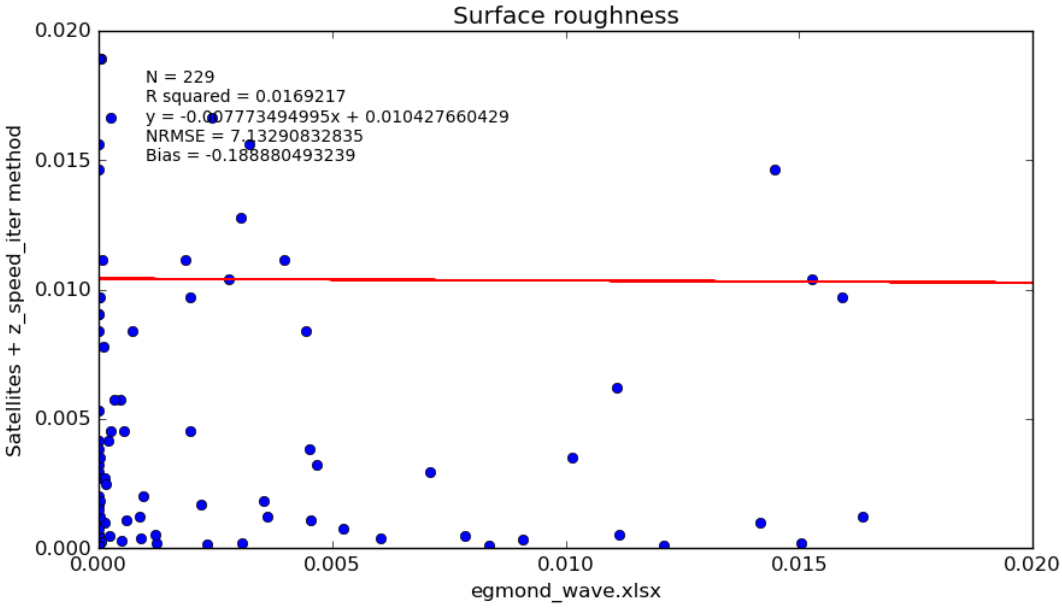

B. 96. Surface roughness regression for Speed_iteration method.

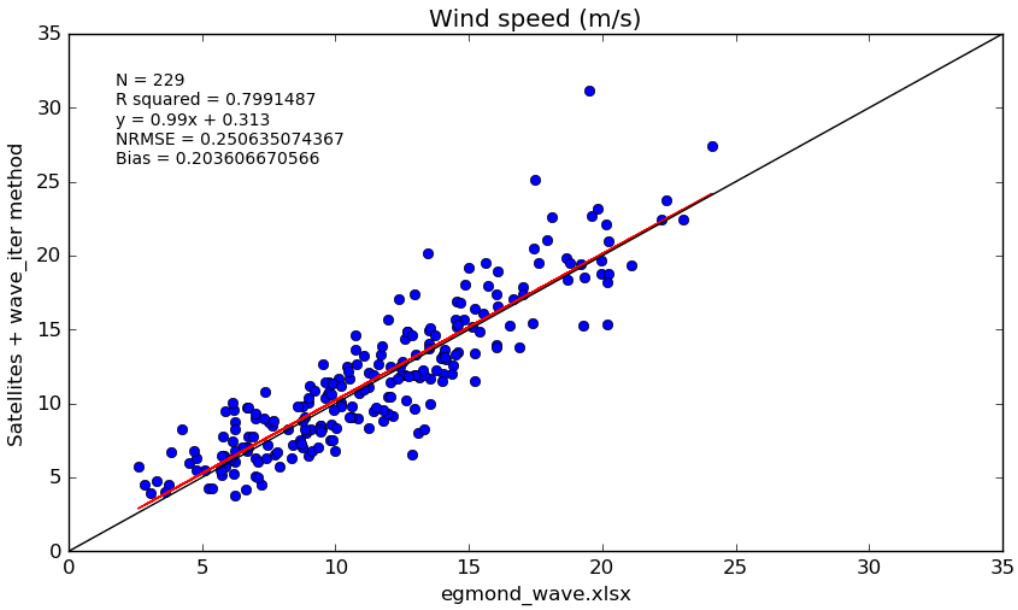

B. 97. Wind speed regression for Wave_iteration method.

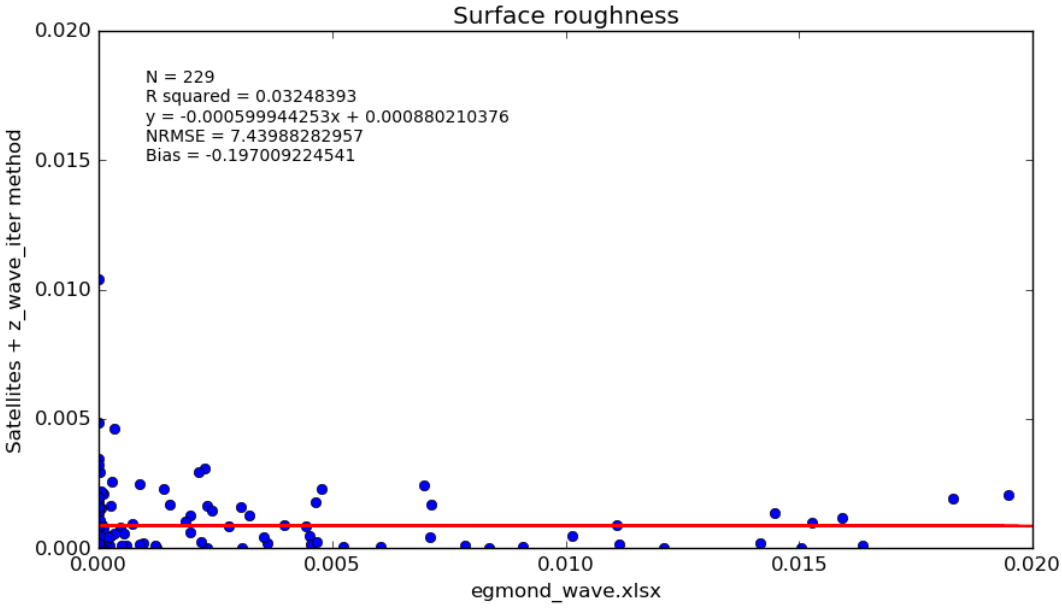

B. 98. Surface roughness regression for Wave_iteration method.

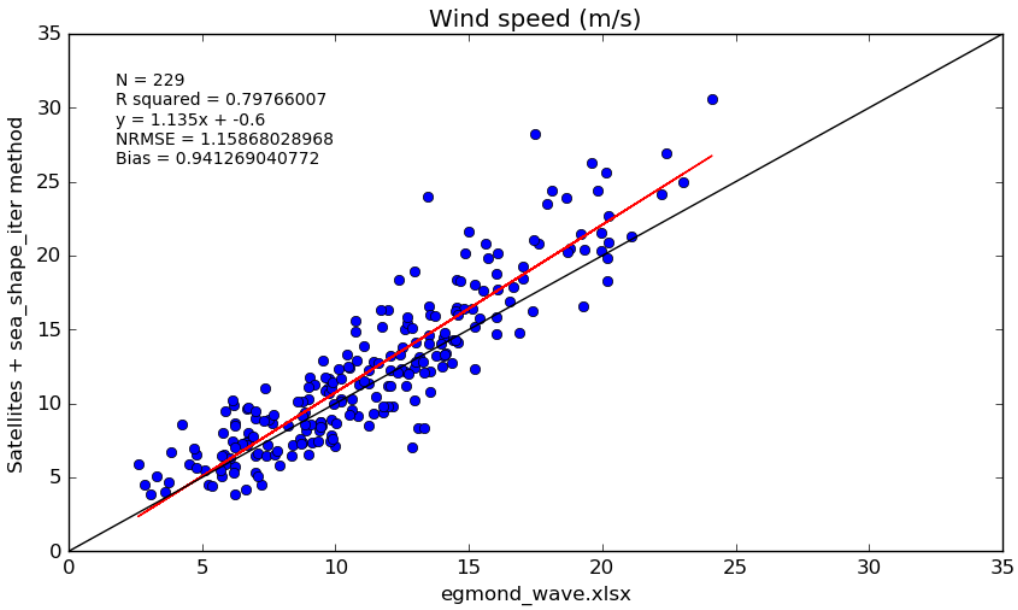

B. 99. Wind speed regression for Taylor_iteration method.

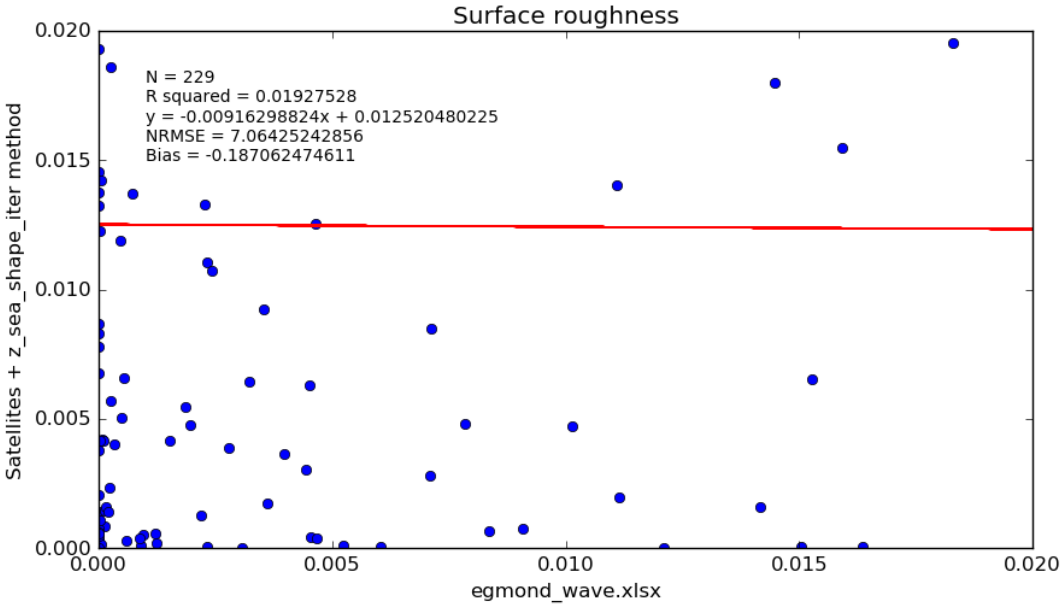

B. 100. Surface roughness regression for Taylor_iteration method.